



Université
de Toulouse

THÈSE

En vue de l'obtention du

DOCTORAT DE L'UNIVERSITÉ DE TOULOUSE

Délivré par :

Institut National Polytechnique de Toulouse (Toulouse INP)

Discipline ou spécialité :

Génie des Procédés et de l'Environnement

Présentée et soutenue par :

M. MARCO AVILA LOPEZ

le jeudi 16 juillet 2020

Titre :

Energy dissipation and mixing characterization in continuous oscillatory baffled reactor

Ecole doctorale :

Mécanique, Energétique, Génie civil, Procédés (MEGeP)

Unité de recherche :

Laboratoire de Génie Chimique (LGC)

Directeur(s) de Thèse :

MME MARTINE POUX

MME JOELLE AUBIN

Rapporteurs :

M. GIUSEPPINA MONTANTE, UNIVERSITA DEGLI STUDI DE BOLOGNE

M. LAURENT FALK, CNRS

Membre(s) du jury :

Mme CATHERINE XUEREB, TOULOUSE INP, Président

M. CLAUDIO FONTE, UNIVERSITY OF MANCHESTER, Membre

M. DAVID FLETCHER, UNIVERSITY OF SYDNEY, Invité

Mme JOELLE AUBIN, TOULOUSE INP, Membre

Mme MARTINE POUX, TOULOUSE INP, Membre

M. SEBASTIEN ELGUE, , Invité

Remerciements

Avant toute chose, je tiens à remercier à CONACYT pour le support financier reçu et SIIES Yucatán pour m'avoir donné les différents moyens qui m'ont permis finir cette thèse de manière satisfaisante.

Je remercie à mes encadrantes, Martine Poux et Joëlle Aubin, qui m'ont donné l'opportunité de réaliser ma thèse et faire partie de leur équipe, pour m'avoir accueilli si chaleureusement durant ces quasiment 4 ans et d'avoir fait que tout se soit aussi bien passé.

Je remercie aux membres de jury : aux rapporteurs Giuseppina Montante et Laurent Falk pour avoir accepté rapporter cette thèse et leurs remarques ; à Claudio Fonte et Sébastien Elgue pour votre participation le jour de la soutenance et vos discussions et commentaires ; à Catherine Xuereb pour ton encadrement au long de la thèse et tes remarques et conseils qui ont enrichi cette travail ; et finalement à David Fletcher pour m'avoir formé en ANSYS, tout ton encadrement sur les simulation numériques et pour m'avoir accueilli si chaleureusement le temps que nous avons dépensé ensemble pendant mon séjour à Sydney.

Je remercie à tout le personnel du LGC, qui m'ont aidé au quotidien, à résoudre des problèmes ou tout simplement pour les conversations aux couloirs : Dany, Claudine, Angelique, Jean-Luc, Patricia, Maria, et un remerciement très spécial à Alain, pour tout le temps que nous avons partagé et pour ton amitié honnête et sincère.

Je tiens à remercier aussi au chercheurs du LGC : Joël Bertrand, Philippe, Séverine, à tout le département STPI et au service technique : Maïko, Franck, Bruno, Lahcen et Jean-Louis qui m'ont aidé à résoudre tous les problèmes que j'ai rencontré et pour le bon accueil qu'ils m'ont réservé.

Un énorme merci à mes amis du LGC qui sont parti du labo avant moi : Alex, Doriane, Kevin, Marwa, Marina, Fatine, Omar, Claire Lafossas, Melissa, Pierre, Mathieu, Lucille, Freddy, Carlos et Francisco, Clementine, Hassan, Freyman, Robbie, Hanbin (pour avoir partagé le bureau avec moi et ton énorme patience avec toutes les personnes qui passaient me voir et dépenser énormément de temps dans notre bureau) et très spécialement à Léo et Flavie, les meilleurs (et seuls) colocos que j'ai eu et pour tous les soirée et moments que nous avons partagé autant que coloc et amis; à mes amis de Ranguel : Julien, Christophe, Paul, Ranine et Fatma ; et à ceux de Labège : Youssef, Juliano, Sergio, Adriana, Alessandro, Florent, Milad, Sabine, Margot, Thibaut, Konstantina, Dihia, Aloysius, Vincent, Beatrice, Morgane, Julien, Cedric, Emma, Pierre Champigneux, Paul, Pierre Albina (merci pour les soirées films et jeux de société), Thomas, et Sid Ahmed (le roi de conseil et règles bizarres d'UNO).

A mes amis de l'équipe Alambic, pour toutes les activités que nous avons organisées et le temps que nous passons ensemble : Florian, Chams, Yosra, et très particulièrement à Lucas et Pierre, pour partager avec moi notre amour pour la NFL et notre ligue de fantasy, même si je finissais à la dernière place.

A l'équipe sportif des doctorants « J'aime ma thèse » : Lise, Eduardo, Carlos, Yohann, Michelle (merci pour avoir baptiser notre team), et très spécialement à Thomas, pour tous les différents moments

que nous avons partagés et à Claire-Salomé pour ton ENORME énergie, et pour me convaincre des faibles des activités sportifs un jour en avance, et toutes les aventures que nous avons passées.

Je n'oublie pas mes « préfères » du laboratoire : Garima, Benoit, Emilien, Thomas, Alexandre et tes colocos Max, Sam, Guillaume, et surtout à Hélène, Claire Malafosse et Astrid, pour toutes les pause-café, soirées, mots d'encouragements, conversations (sérieux et pas sérieux), crises et pour leur amitié.

Je remercie à mes amis qui ne font pas partie du LGC : Anabel, Geoffrey, Mauricio, Marcela, Antonella, Tim, Vivien et Audrey, merci pour être partie de ma vie, et m'avoir encouragé et soutenu.

A ma famille latine à Toulouse, pour les repas, soirées, voyages et soutien: Pedro et Leticia (mes brésiliens préfères), Belen, Gaby, Monica, Nydia, Christopher, Ada, Jésus, Emanuel, Ceci, Lilia, Isaura, Lucila et Chucho. Un grand merci à Magno, Rosaura et Caro, pour les soirées films, jeux vidéo et geeks, et surtout à Andres pour tous les débats et discussions geeks (inutiles) que nous avons partagés. Un énorme merci à Silvia, Lucero et Lauren, pour votre amitié sincère, vos conseils, votre aide, le temps et moments très précieux que nous avons partagés ensemble. Je serai toujours remercié avec vous.

Finalmente, quiero darle los más grandes agradecimientos a toda mi familia, mis tíos y primos de todo México, pero sobre todo a mi papá, mi mamá, mis hermanos Cielito y Nacho, y mi hermano “adoptivo” Enrique, quienes siempre han creído en mí (más de lo que yo mismo creo) y por su apoyo en todo lo que proponga a hacer en mi vida. Gracias por su amor, su confianza y sus palabras de aliento para hacer ser siempre ser una mejor persona. Una vida no es suficiente para agradecerles todo lo que han hecho por mí; todo lo que he logrado y lo que soy es gracias a todos ustedes.

Table of contents

Chapter 1. Introduction	1
Chapter 2. Literature review	3
Part I: Oscillatory baffled reactors: characterisation, applications and limitations – state of the art	3
2.I.1. Introduction	3
2.I.2. Flow and reactor design	6
2.I.2.1. Description of flow.....	6
2.I.2.2. Geometries and configurations.....	7
2.I.2.3. Geometrical parameters.....	10
2.I.2.4. Dimensionless groups in continuous oscillatory flow.....	13
2.I.3. Process enhancements using OBR	15
2.I.3.1. Macromixing.....	15
2.I.3.2. Micromixing.....	18
2.I.3.3. Shear and strain rate.....	19
2.I.3.4. Heat transfer.....	20
2.I.3.5. Energy dissipation.....	23
2.I.3.6. Multiphase systems.....	26
2.I.4. Scale-up	33
2.I.5. Applications and industrial processes	34
2.I.6. Limitations of recommended operating conditions	38
2.I.7. Summary and conclusions	41
Part II: Context and general objectives	43
References	46
Chapter 3: Description of the numerical modelling approaches used	61
3.1. Introduction	61
3.2. The Navier-Stokes equations	61
3.3. Solvers	63
3.3.1. Pressure-velocity coupling.....	65
3.4. Discretization methods	68
3.4.1. Discretization of governing equations.....	68
3.4.2. Discretization schemes.....	69
3.5. Conclusion	74
3.6. References	75
Chapter 4: Predicting power consumption in continuous oscillatory baffled reactors	77
4.1. Introduction	77

4.2. Power dissipation characterization	77
4.3. Numerical method	79
4.3.1. Geometry and operating conditions.....	79
4.3.2. Meshing.....	81
4.3.3. Implications for the calculation of <i>PME</i>	89
4.4. Results and discussion	90
4.5. Conclusions	95
4.6. References	96
Chapter 5: Mixing performance in continuous oscillatory baffled reactors	97
5.1. Introduction	97
5.2. Characterization of mixing performance	97
5.2.1. Statistical analysis of concentration distribution.....	97
5.2.2. Areal distribution of mixing intensity.....	98
5.3. Numerical method	98
5.3.1. Geometry and operating conditions.....	98
5.3.2. Meshing and solution independence.....	102
5.4. Results and discussion	104
5.4.1. Flow and tracer patterns.....	104
5.4.2. Mixing performance.....	106
5.4.3. Power dissipation.....	116
5.5. Conclusions	118
5.6. References	119
Chapter 6. Experimental characterization of mixing	121
Part I: Micromixing characterization in a continuous oscillatory baffled reactor	121
6.I.1. Introduction	121
6.I.2. Materials and methods	123
6.I.2.1. Experimental rig.....	123
6.I.2.2. Test reactions and quantification of micromixing.....	124
6.I.3. Results and discussions	134
6.I.3.1. Influence of oscillatory conditions.....	134
6.I.3.2. Influence of feed flow rate.....	135
6.I.3.3. Micromixing time.....	138
6.I.4. Conclusions	140
Part II: Visual analysis of a passive tracer upstream of the baffled zone	141
6.II.1. Introduction	141
6.II.2. Materials and methods	141
6.II.2.1. Experimental rig.....	141

6.II.2.2.	Fluids and operating conditions.....	141
6.II.3.	Observations	143
6.II.3.1.	Initial experiments on macromixing.....	143
6.II.3.2.	Influence of the frequency and amplitude	143
6.II.3.3.	Influence of the inlet orientation	146
6.II.3.4.	Influence of the viscosity.....	148
6.II.4.	Conclusions	152
	General conclusions	153
	References	154
Chapter 7.	Conclusion and future work	159
Appendix 1:	Velocity vectors over one oscillation period	163
Appendix 2:	Areal distribution of mixing intensity averaged over one oscillation period	172
Appendix 3:	Absorbance calibration and experiments	188
Appendix 4:	Matlab script code for the determination of micromixing time	191

List of tables

Table 2.1: Different baffled geometries used in OBRs.	8
Table 2.2: Summary of main geometrical parameters in oscillatory baffled reactor design.	11
Table 2.3: Summary of main dimensionless groups in oscillatory baffled reactor design.	14
Table 2.4: Correlations for tube-side Nusselt number found the literature.	24
Table 2.5: Mean droplet size correlations for oscillatory baffled reactors.	30
Table 2.6: Scale-up correlations forms found the literature.	34
Table 2.7: Examples of OBR applications	38
Table 4.1: Simulation conditions proposed.	81
Table 4.2: Characteristics of different meshes used for the mesh and time step independency study. .	84
Table 4.3: Quantification of the effect of body mesh, inflation layers and time step on the axial velocity and pressure at different monitor points (M0-M3) with the MADP.....	85
Table 4.4: Influence of the body mesh, inflation layers, time step and power calculation method on power dissipation and MADP values.	88
Table 4.5: Contribution of the individual terms of equation (4.10) on power dissipation PME	89
Table 5.1: Experimental conditions proposed by $2k$ factorial design.	100
Table 6.1: Operating conditions studied.....	128
Table 6.2: Reactant concentrations.....	129
Table A.1: Molar extinction coefficient for $I3^-$ – found in the literature	189

List of figures

Figure 2.1: Schematic diagram of a continuous oscillatory baffled reactor with a single orifice plate baffles.....	4
Figure 2.2: Van Dijck (1935) patent design of (a) reciprocating plate column, and (b) pulsed plate column.....	5
Figure 2.3: Number of research publications on oscillatory flow from 1970 to 2019. Data obtained from Web of Science using the keywords “oscillatory flow reactor”.....	6
Figure 2.4: Eddy formation in oscillatory baffled reactor (McDonough et al., 2015).....	6
Figure 2.5: Axial to radial velocity ratio (RV) as function of oscillatory Reynolds number for different fluids (green and white legend in the plot refer to low and high viscosity non-Newtonian fluids, respectively) (Manninen et al., 2013).....	16
Figure 2.6: The dependency of the tanks-in-series model parameter, N , on the oscillatory Reynolds number for different net Reynolds (Ni et al., 2003b).....	17
Figure 2.7: Influence of oscillatory conditions and baffle geometry on the mean shear strain rates (Mazubert et al., 2016b).....	20
Figure 2.8: Heat transfer enhancement in oscillatory baffled tubes (Ni et al., 2003b).....	21
Figure 2.9: kLa against power density for a single orifice baffle 50 mm OBR and a STR at constant superficial gas velocity (Hewgill et al., 1993).....	27
Figure 2.10: (a) mean droplet size as function of oscillatory velocity, with $A = x_0$, (b) droplet size distribution for different net flowrate and same oscillatory conditions ($x_0 = 52$ mm and $f = 1.17$ Hz) (Lobry et al., 2013).....	29
Figure 2.11: Comparison of power density and length to diameter ratio behaviour for OBRs and turbulent flow reactor (Stonestreet and Harvey, 2002).....	35
Figure 3.1: Overview of the Pressure-Based Solution Methods (a) Segregated algorithm (b) Coupled algorithm (ANSYS Inc., 2019).....	65
Figure 3.2: Non-Iterative Time Advancement Solution algorithm (ANSYS Inc., 2019).....	67
Figure 3.3: Control volume definition (a) cell-centred formulation, (b) vertex-centered formulation (Acharya, 2016).....	69
Figure 3.4: Illustration of spatial discretization of the control volume defined by Fluent ANSYS (ANSYS Inc., 2019).....	70
Figure 3.5: One-dimensional control volumes showing cell locations used in the QUICK scheme (ANSYS Inc., 2019).....	70
Figure 3.6: Illustration of spatial discretization of the control volume defined In ANSYS CFX (ANSYS Inc., 2017).....	72
Figure 4.1: (a) Photograph of the NiTech® COBR and (b) the geometry of the COBR simulated by CFD.....	80
Figure 4.2: Example of tetrahedral mesh and inflation layers employed.....	82
Figure 4.3: Locations of the monitor points and lines. M0: tube centerline, 8.45 mm upstream of the first orifice. M1 & L1: tube centerline, 8.45 mm upstream of the third orifice. M2: tube centerline, in the third orifice of the geometry. M3 & L2: tube centerline, at 8.45 mm downstream of the third orifice. 82	
Figure 4.4: Images of the meshes used for the mesh and time step independency study: (a) Mesh 1, (b) Mesh 2, (c) Mesh 3, (d) Mesh 4, (e) Mesh 5.....	83
Figure 4.5: Comparison between power dissipation calculation methods for the three different mesh sizes.....	86

Figure 4.6: Comparison between power dissipation calculation methods for different numbers of inflation layers.....	87
Figure 4.7: Power dissipation profiles determined via the integral of viscous dissipation at L2 as a function of the radius for three different numbers of inflation layers at $t/T = 0.60$	87
Figure 4.8: Comparison between power dissipation calculation methods for different time steps.....	89
Figure 4.9: Power density as function of Reo	90
Figure 4.10: Power density as a function of velocity ratio (ψ).....	91
Figure 4.11: Power density as function of ReT	93
Figure 4.12: Dimensionless power density as a function of ReT	94
Figure 5.1: Geometry of the COBR simulated by CFD with the location of tracer sources and monitoring planes.....	99
Figure 5.2: Radial variation of (a) axial velocity and scalars released (b) at the axis (Source 0) and (c) mid-baffle (Source 1) at one quarter of the time through the first period for Case 1. The legend gives the mesh size in microns.	103
Figure 5.3: Velocity vectors during the oscillatory flow for Case 5 ($Renet = 6, f = 1$ Hz, $xo = 5$ mm): (a) $t/T = 0.00$, (b) $t/T = 0.25$, (c) $t/T = 0.55$, (d) $t/T = 0.6$, (e) $t/T = 0.75$, (f) $t/T = 0.95$, (g) normalized inlet velocity over an oscillatory period for Case 5 with the representation of the positions of the different times t/T during the period.	105
Figure 5.4: Effect of source position on tracer patterns over a flow period (T) for Case 1 ($Renet = 27, f = 1$ Hz, $xo = 5$ mm): (a) Source 0, (b) Source 1, (c) Source 2.....	107
Figure 5.5: Tracer profiles from Source 2 over a flow period (T) at Plane 4 for Case 1 ($Renet = 27, f = 1$ Hz, $xo = 5$ mm).	108
Figure 5.6: Areal distribution of mixing intensity averaged over one oscillation period at Plane 4 for Source 1: (a) Case 1, (b) Case 2, (c) Case 3, (d) Case 4, (e) Case 5, (f) Case 6, (g) Case 7, (h) Case 8.	109
Figure 5.7: Areal distribution of mixing intensity averaged over one oscillation period at Plane 4 for Source 2: (a) Case 1, (b) Case 2, (c) Case 3, (d) Case 4, (e) Case 5, (f) Case 6, (g) Case 7, (h) Case 8.	110
Figure 5.8: Area fraction of Planes 1, 2, 3, and 4 (averaged over one oscillation period) where $> 90\%$ mixing is achieved for Cases 1 to 8. (a) Source 0; (b) Source 1; (c) Source 2.	113
Figure 5.9: Tracer patterns over a flow period (T) for Case 7 ($Renet = 6, f = 2$ Hz, $xo = 5$ mm): (a) Source 0, (b) Source 1, (c) Source 2.....	114
Figure 5.10: Tracer patterns over a flow period (T) for Case 8 ($Renet = 6, f = 2$ Hz, $xo = 10$ mm): (a) Source 0, (b) Source 1, (c) Source 2.	115
Figure 5.11: Area fraction of Planes 4 (averaged over one oscillation period) where $> 90\%$ mixing is achieved as a function of the power dissipation. (a) Source 0; (b) Source 1; (c) Source 2.	117
Figure 6.1: Photograph of the baffles in the NiTech® COBR.....	123
Figure 6.2: (a) Schematic diagram of the experimental setup containing the Nitech® reactor R-01. V-01 to V-03 are valves, FV-01 and FV-02 are feed vessels, P-01 to P-03 are gear pumps, F-01 is the flowmeter and SV-01 is the sample vessel. (b) Schematic diagram of the entries from P-01 (bulk flow), P-02 (side injection flow) and P-03 (oscillatory flow) to the Nitech® reactor.	124
Figure 6.3: Photograph of the presence of iodide (I_2) in the experiments without oscillations, with an acid concentration $H_2SO_4 = 1$ mol L^{-1}	130
Figure 6.4: Absorption spectra obtained for experiments without oscillations using an acid concentration $H_2SO_4 = 1$ mol L^{-1}	131
Figure 6.5 : Schematic diagram of the incorporation model.	133

Figure 6.6: Example curve of segregation index as function of the calculated micromixing time for $R = 7$ and $[H_2SO_4] = 0.015 \text{ mol L}^{-1}$	133
Figure 6.7: Segregation index as function of oscillatory Reynolds number for $H_2SO_4 = 0.015 \text{ mol L}^{-1}$, $R = 7$ and $Renet = 125$	135
Figure 6.8: Segregation index as function of oscillatory Reynolds number for different acid flow rates.	136
Figure 6.9: Schematic diagram of the acid-buffer contacting zone; the grey zone is the volume used for the calculation of specific power density.	137
Figure 6.10: Segregation index as function of the specific power density. Dashed lines denote the positive and negative deviation from the trendline (solid line): $\pm 50\%$. Open symbols correspond to acid concentration $[H_2SO_4] = 0.015 \text{ mol L}^{-1}$ and $R = 7$; filled symbols correspond acid concentration $[H_2SO_4] = 0.0075 \text{ mol L}^{-1}$ and $R = 3.5$. Symbol shapes represent the operatory conditions: $\diamond \blacklozenge$ ($x_0 = 0 \text{ mm}$, $f = 0 \text{ Hz}$, $Re_o = 0$), $\triangle \blacktriangle$ ($x_0 = 3 \text{ mm}$, $f = 1.5 \text{ Hz}$, $Re_o = 400$), \otimes ($x_0 = 4.5 \text{ mm}$, $f = 1 \text{ Hz}$, $Re_o = 400$), $\diamond \blacklozenge$ ($x_0 = 6.5 \text{ mm}$, $f = 1 \text{ Hz}$, $Re_o = 600$), $\square \blacksquare$ ($x_0 = 13 \text{ mm}$, $f = 0.5 \text{ Hz}$, $Re_o = 600$), ∇ ($x_0 = 13 \text{ mm}$, $f = 1 \text{ Hz}$, $Re_o = 1200$) and $\circ \bullet$ ($x_0 = 13 \text{ mm}$, $f = 1.5 \text{ Hz}$, $Re_o = 1800$).	138
Figure 6.11: Theoretical (dash-dotted line) and calculated (open/filled symbols) micromixing time as function of the specific power density. Dashed lines denote the positive and negative deviation from the trendline (solid line): $\pm 40\%$. Open symbols correspond to acid concentration $[H_2SO_4] = 0.015 \text{ mol L}^{-1}$ and $R = 7$; filled symbols correspond acid concentration $[H_2SO_4] = 0.0075 \text{ mol L}^{-1}$ and $R = 3.5$	139
Figure 6.12: Schematic diagram of the entries from P-01 (bulk flow), P-02 (side injection flow) and P-03 (oscillatory flow) to the Nitech® reactor.	142
Figure 6.13: Images for the different inlets orientations: (a) top entry, (b) bottom entry. Blue tube feed the bulk flow, and the red tube feed the secondary injection – the distance between the tubes is 30 cm.	142
Figure 6.14: Tracer patterns for (a) Case 1 and (b) Case 2.	143
Figure 6.15: Results of the central passive injection for the inlets top entry orientation using water as the working fluid.	146
Figure 6.16: Results of the central passive injection for the inlets bottom entry orientation using water as the working fluid.	148
Figure 6.17: Results of the central passive injection for the inlets bottom entry orientation using a solution of 69% wt. glycerol/water as the working fluid.	151
Figure 6.18: Inlet zone between the net flow (blue pipe) and the system, with the oscillations being provided through the white pipe.....	151

Nomenclature

A	OBR cross-section area (m^2)
A_t	actual value at time t
C	species concentration (kg m^{-3})
C^*	dimensionless tracer concentration (-)
C_i	local scalar concentration of the tracer at the time t (kg m^{-3})
C_i^*	local dimensionless tracer concentration at the time t (-)
C_i	molar concentration of ion i (mol L^{-1})
\bar{C}	fully mixed concentration (kg m^{-3})
C_D	orifice discharge coefficient (-)
C_0	concentration of tracer in the injection source (kg m^{-3})
Co	Courant number, $v \Delta t / \Delta x$ (-)
C_p	fluid specific heat ($\text{J kg}^{-1} \text{K}^{-1}$)
C_{X-}	lower limit of mixedness ranges (-)
C_{X+}	upper limit of mixedness ranges (-)
c_{i10}	concentration of the specie i in the surrounding fluid (mol L^{-1})
D	OBR diameter (m)
d	OBR orifice diameter (m)
D_{ax}	axial dispersion coefficient ($\text{m}^2 \text{s}^{-1}$)
D_f	diffusion coefficient ($\text{m}^2 \text{s}^{-1}$)
D_h	hydraulic diameter (m)
d_{32}	Sauter mean diameter (m)
$d_{v,0.5}$	mean particle size (m)
F_t	forecast value at time t
f	oscillation frequency (Hz)
f_s	frequency of vortex shedding (Hz)
h_{OBR}	OBR-side transfer coefficient ($\text{W m}^{-2} \text{K}^{-1}$)
I	ionic strength (mol L^{-1})
K_B	Equilibrium constant of reaction (R3)
k_1	reaction rate coefficient of reaction (R1) ($\text{L mol}^{-1} \text{s}^{-1}$)
k_2	reaction rate coefficient of reaction (R2) ($\text{mol}^{-4} \text{s}^{-1}$)
k_{3f}	reaction rate coefficient of reaction (R3)
k_{3b}	reaction rate coefficient of reaction (R3)
k	thermal conductivity of the process fluid ($\text{W m}^{-1} \text{K}^{-1}$)

k_L	liquid-side mass transfer coefficient (m s^{-1})
$k_L a$	volumetric mass transfer coefficient (s^{-1})
l	mixing length (m)
l	optical path length (m)
l^*	mixing length proposed by Jimeno et al. (2018b) (m)
l_b	distance between baffles (m)
l_b^{opt}	optimum distance between baffles (m)
L	reactor length (m)
n	number of baffles (-)
\mathbf{n}	normal vector (-)
\dot{n}	molar flow rate (mol m^{-3})
N	number of theoretical baffles (-)
Nu	Nusselt number (-)
OD	optical density or light absorption (-)
p	pressure (Pa)
P	power dissipation (W)
Pr	Prandtl number $\left(C_p \mu / k \right)$ (-)
P_{VD}	power dissipation calculated using the viscous dissipation equation (W)
P_{ME}	power dissipation calculated using the mechanical energy equation (W)
P/V	power density (W m^{-3})
$(P/V)^*$	dimensionless power density (-)
Pe	Péclet number (-)
\dot{q}	volumetric flow rate ($\text{m}^3 \text{s}^{-1}$)
q	volumetric flow rate at the tracer inlet ($\text{m}^3 \text{s}^{-1}$)
q_{jet}	volumetric flow rate of the side injection ($\text{m}^3 \text{s}^{-1}$)
Q	volumetric flow rate at the COBR inlet ($\text{m}^3 \text{s}^{-1}$)
Q_{net}	volumetric flow rate of the main stream ($\text{m}^3 \text{s}^{-1}$)
R	radius of reactor (m)
R	volumetric flow rate ratio between the bulk and jet stream (-)
R_V	axial to radial velocity ratio (-)
Re_G	net flow Reynolds number for gas (-)
Re_{net}	net flow Reynold number (-)
Re_o	oscillatory Reynolds number (-)
Re'_o	modified oscillatory flow Reynolds number proposed by Ahmed et al. (2019) (-)
Re_{oh}	hydrodynamic oscillatory Reynolds number (-)

Re_T	total Reynolds number proposed by Jimeno et al. (2018b) (-)
r	radial coordinate (m)
r_n	radial number (-)
S	surface (m ²)
\mathbf{S}	surface vector (m ²)
Sc	Schmidt number (-)
\dot{S}_C	mass source of tracer (kg m ⁻³ s ⁻¹)
Sh	Sherwood number (-)
S_n	swirl number (-)
St	Strouhal number (-)
Δt	time step (s)
t	time (s)
t_m	micromixing time (s)
$t_{m\ theo}$	theoretical micromixing time considering only the molecular diffusion (s)
$t_{m\ cal}$	calculated micromixing time (s)
T	oscillation period (s)
u	instantaneous velocity (m s ⁻¹)
\mathbf{u}	velocity vector (m s ⁻¹)
\bar{u}	mean velocity (m s ⁻¹)
u_g	superficial gas velocity at standard pressure (m s ⁻¹)
u_{in}	initial velocity (m s ⁻¹)
$u_{i,axial}$	axial velocity in computational cell i (m s ⁻¹)
$u_{i,transverse}$	transverse velocity in computational cell i (m s ⁻¹)
u_{net}	net velocity (m s ⁻¹)
u_x, u_y, u_z	velocity components (m s ⁻¹)
V	volume (m ³)
V_2	volume of the aggregate (m ³)
V_{20}	initial value of the aggregate volume (m ³)
v_r	radial velocity (m s ⁻¹)
v_z	axial velocity (cylindrical coordinate) (m s ⁻¹)
v_θ	tangential velocity (m s ⁻¹)
x_o	oscillation amplitude (m)
We_h	hydrodynamic Weber number (-)
We_s	Weber number (-)
X	percentage of perfectly-mixed state (-)
X_s	segregation index (-)

x, y, z	cartesian coordinates (m)
Y	selectivity of the iodide reaction (-)
Y_{TS}	selectivity of iodide when there is total segregation (-)
z_i	charge number of species i (-)

Greek symbols

α	dimensionless free baffle area $\left(d/D\right)^2$ (-)
β	optimal to use baffle spacing ratio (-)
Γ	relevant effective diffusivity coefficient ($\text{m}^2 \text{s}^{-1}$)
$\dot{\gamma}$	mean shear rate (s^{-1})
δ	baffle thickness (m)
δ	unit tensor (-)
δ_0	initial striation thickness (m)
ε	specific power density per mass (W kg^{-1})
ε	molar extinction coefficient of I_3^- ions at 353 ($\text{L mol}^{-1} \text{cm}^{-1}$)
κ	dilatational viscosity (Pa.s)
λ	number of time steps in an oscillatory cycle (-)
λ	coefficient of thermal performance by Ahmed et al. (2018a) (-)
μ	dynamic viscosity (Pa.s)
ρ	fluid density (kg m^{-3})
σ	momentum flux tensor (Pa)
τ	theoretical residence time (s)
τ	shear stress vector (Pa)
ν	kinematic viscosity ($\text{m}^2 \text{s}^{-1}$)
ϕ	scalar quantity variable (-)
Φ	flux tensor (Pa)
Φ_v	dissipation function (s^{-2})
φ	correction factor (-)
ψ	velocity ratio (-)
ω	oscillation angular frequency (rad s^{-1})

List of publications

Journal papers

Avila, M., Fletcher, D.F., Poux, M., Xuereb, C., Aubin, J., 2020. Mixing performance in continuous oscillatory baffled reactors. *Chem. Eng. Sci.* 219. <https://doi.org/10.1016/j.ces.2020.115600>

Avila, M., Fletcher, D.F., Poux, M., Xuereb, C., Aubin, J., 2020. Predicting power consumption in continuous oscillatory baffled reactors. *Chem. Eng. Sci.* 212. <https://doi.org/10.1016/j.ces.2019.115310>

Conference posters

M. Avila, M Poux, C Xuereb, D. Fletcher, Joelle Aubin. Characterization of micromixing in a Continuous Oscillatory Baffled Reactor. 16th European Conference on Mixing, September 2018, Toulouse, France.

M. Avila, M Poux, C Xuereb, D. Fletcher, Joelle Aubin. Macro- and micro-mixing performance in continuous oscillatory baffled reactors. 6th European Process Intensification Conference, October 2017, Barcelona, Spain

Chapter 1. Introduction

The stirred tank reactor (STR) remain the standard approach for mixing and carrying out chemical reactions from early stage discovery to manufacture. Many areas of chemical and process industries are still dependent on this kind of reactors at plant scale. The most definite advantage of batch production is the lower initial setup cost (although this is not always true). However, continuous processing is becoming a more viable option for these industries due to advancements in design and technology. Compared with continuous processing, STR is much slower, increasing the overall cost of processing. Starting up and using batch equipment can also increase energy consumption and the quality discrepancy between batches may differ. This can lead to lost production and compromised quality if the batch process is not monitored closely and properly. Many industrial sectors are shifting from traditional batch processes to continuous processes.

For most applications, a continuous process saves time, energy, and costs and when implemented correctly, it can offer much faster operation, reduce waste, improve quality, increase productivity and adapt to the needs of customers more efficiently than batch processing. Continuous processes usually require less space than batch processes. Significant reductions in dimensions leads to high efficiency in mass and heat transfer: smaller volume means larger heat exchange surface, shorter residence time and much easier control of the process.

The transition from batch to continuous operation, aiming to reduce reactant volume and miniaturization in dimensions is an example of process intensification. Process intensification (PI) is defined as drastic improvements in chemical manufacturing and processing; substantially decreasing equipment volume, energy consumption, or waste formation; ultimately leading to cheaper, safer and sustainable technologies (Stankiewicz and Moulijn, 2000)¹. According to Stankiewicz and Moulijn, process intensification can be divided into two areas. The first is the process intensifying equipment, which are special designs that optimize critical parameters (e.g., heat transfer, mass transfer), such as novel reactors, and intensive mixing, heat-transfer and mass-transfer devices. The second area is the process intensifying methods, where multiple processing steps are integrated into a single unit operation (as hybrid separations, integration of reaction and separation, heat exchange, or phase transition), or alternative energy sources are used (light, ultrasound, etc.), and new process-control methods (such as intentional unsteady-state operation). Some examples of process intensifying equipment are spinning disk reactors, rotating packed bed, microreactors, rotor-stator devices, static mixers, compact heat exchangers, and oscillatory baffled reactors.

An oscillatory baffled reactor (OBR) is a particular type of tubular reactor, which has drawn increasing attention over the past few decades. Eddy generation due to an oscillatory flow and their

¹ Stankiewicz, A.I., Moulijn, J.A., 2000. Process Intensification: transforming chemical engineering. Chem. Eng. Prog. 96, 22–34.

interaction with internal baffles characterize the OBR. This intensified reactor has proven to globally intensify processes when compared with STRs. OBRs have been applied in several industrial sectors. However, despite being already used for industrial production, this equipment presents some limitations and today is being studied to be implemented in a wider range of operation conditions and industrial sectors.

In this context, a review of this intensified technology is presented in the next chapter, highlighting its characteristics, process enhancements, applications and the limitations found in the literature. The aim is to analyse and identified new areas of opportunities that will allow this technology to be applied in a broader range of applications for continuous processing.

Chapter 2. Literature review

This chapter focuses on a review of the OBR technology and its limitations that motivate this thesis work. The chapter is divided into two parts: Part I presents the state of the art of the most important characteristics of the OBR. Part II highlights the motivation of the research, along with the general objective and the thesis structure.

Part I: Oscillatory baffled reactors: characterisation, applications and limitations – state of the art

2.I.1. Introduction

The development of green and sustainable technologies is of prime importance for the chemical and process industries due to increasing social and environmental concerns. One of the major challenges that these industries face currently is the creation of innovative processes for the production of commodity and intermediate products that allow high product quality with specified properties and that are less polluting, as well as more efficient in terms of energy, raw materials and water management.

Stirred tank reactors (STR) and continuous stirred tank reactors (CSTR) are widely used at the industrial scale in chemical and process industries, due to their simplicity and the extensive knowledge of these reactors. Continuous processing offers many benefits over batch operation, as it minimizes waste (Schaber et al., 2011), reduces energy consumption (Yoshida et al., 2011), improves mass and heat transfer (Singh and Rizvi, 1994; Yu et al., 2012), as well as chemical conversion (Hartman et al., 2011). One of the main aims in continuous processing is the design of chemical reactors that enable plug flow. Tubular reactors offer good mixing performance and plug flow under turbulent flow conditions, however, they require long tube lengths to achieve long residence times, resulting in high-pressure drop along the reactor. Nowadays, new technologies and devices have been developed to achieve plug flow in more compact geometries, such as static in-line mixers, packed bed reactors, microreactors and oscillatory baffled reactors. In the plug flow state the fluid is perfectly mixed in the radial direction but not in the axial direction (forwards or backwards).

The oscillatory baffled reactor (OBR) is a particular type of tubular reactor, typically equipped with periodically spaced sharp-edged orifice baffles along its length, as is shown in Figure 2.1. This type of reactor operates with a periodic oscillatory or pulsed flow, which with the presence of the baffles, causes unsteadiness in the laminar flow. The oscillations are normally generated by diaphragms, bellows or pistons at one or both ends of the tube. This technology has been called pulsed flow reactor (PFR), oscillatory baffled column (OBC), or oscillatory baffled reactor (OBR) in the literature. In this chapter, the expression OBR is used to cover batch processes and continuous flow.

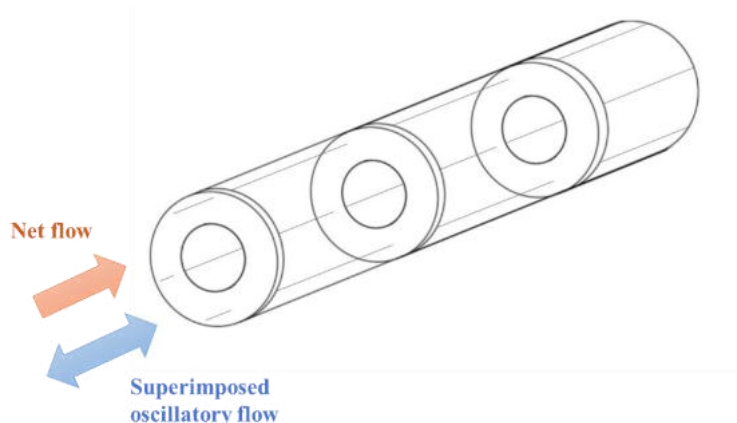


Figure 2.1: Schematic diagram of a continuous oscillatory baffled reactor with a single orifice plate baffles.

Due to the interaction of fluid pulsations with the baffles and the resulting recirculating flow (see section 2.1.2.1 for details), mixing in OBRs is independent of the net flow when operated continuously, providing a good mixing quality and long residence times (comparable with those obtained in batch reactors) with a greatly reduced length-to-diameter ratio tube (Harvey et al., 2003). Due to these characteristics, OBRs have proven to globally intensify processes, leading to operations that use less energy and produce less waste compared with processes in conventional STRs (Phan et al., 2011a; Reis et al., 2006b).

The idea of pulsed flow reactors is not new. The first apparition of oscillation conditions for industrial applications was the patent of Van Dijck (1935). The patent, as illustrated in Figure 2.2, describes vertical pulsed and reciprocating plate columns for liquid-liquid extractions that are equipped with oscillating perforated sieve plates or with immobile internals. Until the 1980s, the pulsed packed column (Baird and Garstang, 1972; Burkhart and Fahien, 1958) and reciprocating plate column (Karr, 1959), were the only equipment using oscillatory flow for enhancing heat and mass transfer. The pulsation of the fluid and the reciprocating plates have both shown to improve the dispersion of liquid phases and increase the interfacial area, providing enhanced mass transfer performance compared with conventional extraction columns. In the 1980s, the interest in the details of periodic flows increased due to the improvement of mass and heat transfer offered by oscillatory flow mixing. Knott and Mackley (1980) studied the nature of the eddies created at the sharp-edge channels under the influence of periodic flows and observed the formation and separation of vortex rings, which were explained to be the origin of the enhanced transport phenomena. Following this, a number of pioneering studies were conducted. Howes (1988) investigated the dispersion of a passive tracer in both batch and continuous OBRs and concluded that net flow, amplitude and frequency affects the axial dispersion of the passive tracer. Increasing the oscillatory velocity (i.e. $f \cdot x_o$) increases radial mixing, thereby decreasing axial dispersion. By increasing net flow, backmixing is decreased. However, for low oscillatory velocities, the net flow will increase axial dispersion since the radial mixing to counterbalance the effects of net flow. Brunold et al. (1989) studied the influence of oscillatory flow on the flow patterns in a duct

containing sharp edges. Their experimental flow observations describe the formation, development and separation of large-scale eddies in the baffle area and were found to lead to efficient mixing. Later the same year, Dickens et al. (1989) experimentally characterized the mixing performance in a horizontal OBR under laminar net flow conditions via the measurement of the residence time distribution (RTD), reporting plug flow behaviour. Mackley et al. (1990) investigated heat transfer in OBRs. Their work showed a significant increase in heat transfer in the presence of oscillations with respect to the same mass flow rate in a classical tubular reactor. Their results also demonstrated that oscillatory flow and the sharp-edged orifice baffles must be present to produce this enhancement.

The interest in oscillatory flow has been increasing over the last forty years, and particularly since the 1990s where there has been a relatively steady increase over the years as can be seen in Figure 2.3. Since then, there have been more and more in oscillatory flow for enhancing the performance chemical reactors and new areas of research have emerged, such as combined microwave heating and OBRs for the production of a metal-organic frameworks (Laybourn et al., 2019), combined heat pipes and OBRs to performing exothermic reactions, which operate through the evaporation and condensation of a working fluid (McDonough et al., 2018, 2016), as well as the development of crystallization processes using moving baffle oscillatory reactors (Raval et al., 2020).

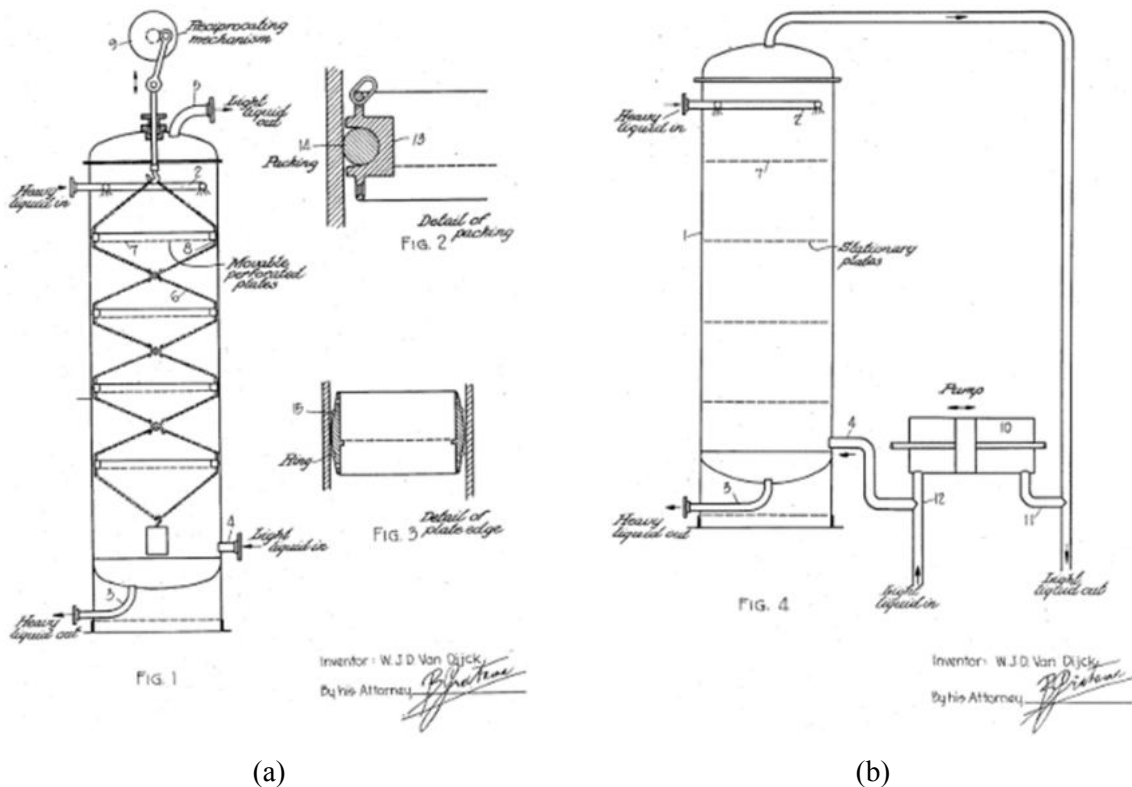


Figure 2.2: Van Dijck (1935) patent design of (a) reciprocating plate column, and (b) pulsed plate column.

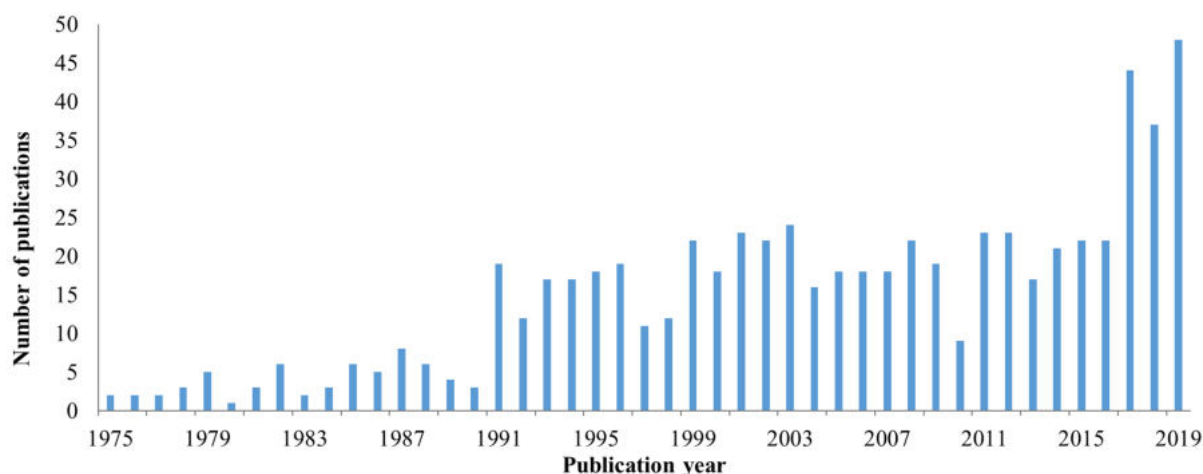


Figure 2.3: Number of research publications on oscillatory flow from 1970 to 2019. Data obtained from Web of Science using the keywords “oscillatory flow reactor”.

2.1.2. Flow and reactor design

2.1.2.1. Description of flow

The overall mechanism of eddy formation in OBRs has been described widely in the literature (Brunold et al., 1989; Gough et al., 1997; Mazubert et al., 2016a; McDonough et al., 2015; Ni et al., 2002). Typical flow patterns formed in OBRs with orifice baffles are shown in Figure 2.4. During the flow acceleration phase (Figure 2.4(a)), eddies are formed downstream of the baffles and flow separation starts. As the oscillatory velocity increases ((Figure 2.4(b)), eddies start to fill the baffle cavity. At the flow reversal phase (Figure 2.4(c)), the eddies are detached from the baffle, leaving a free vortex that is engulfed by the bulk flow and that interacts with other vortices that were generated in previous cycles (Figure 2.4(d)), before restarting the cycle again.

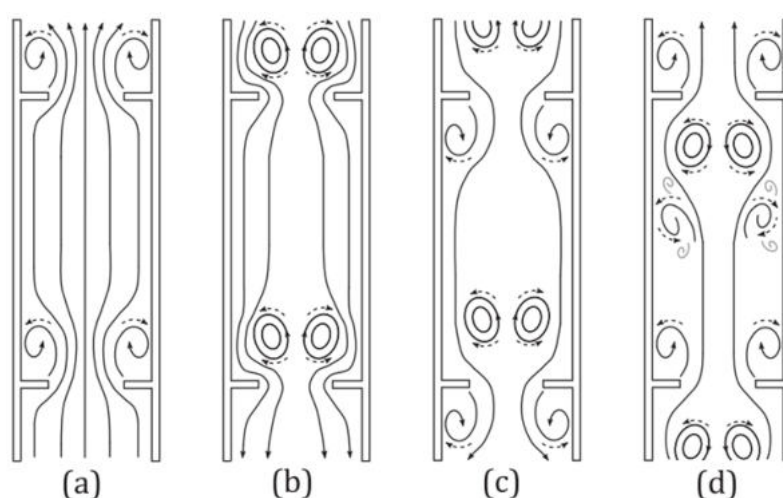


Figure 2.4: Eddy formation in oscillatory baffled reactor (McDonough et al., 2015)

2.1.2.2. Geometries and configurations

Sharp-edged single orifice baffles (as shown in Figure 2.1) are the most common baffle design used in OBR studies, however there are a number of other baffle geometries that have been studied in the literature. These geometries are shown in Table 2.1 and include periodic smooth constrictions, multi-orifice plates, disc-and-doughnuts, helical forms (round wires, sharp-edged and alternating ribbon, double ribbons, combined with a central rod), central disc baffles, and wire.

Periodic smooth constrictions are based on the single orifice plate baffle design. The main difference is that orifices in smooth constriction baffles are made by constricting the reactor tube (usually made with glass) and hence offers low and uniform shear rates, which may be advantageous for applications such as shear-sensitive bioprocesses (Reis et al., 2006a, 2006b).

Multi-orifice designs are the same as those in the pulsed and reciprocating multi-orifice plate columns. This geometry is attractive due to the ease of manufacture. The influence of the number of orifices was studied by González-Juárez et al. (2017) using numerical simulations. A higher number of orifices enhance radial mixing, thanks to the production of a larger number of small eddies. With a significant number of orifices, the reactor achieves narrower RTD curves with a more uniform concentration in the cross-section, thus improving the plug flow behaviour and the mixing quality. Ahmed et al. (2018b) studied mass transfer in air-water systems for different OBR geometries and concluded that the multi-orifice design is recommended over the smooth constrictions, single orifice and helical baffle geometries for gas-liquid mass transfer applications. Indeed, the multi-orifice geometry offers better control of the size and shape of the bubbles and microbubbles, offering a wider bubbly flow region and higher volumetric mass transfer coefficient than the other geometries.

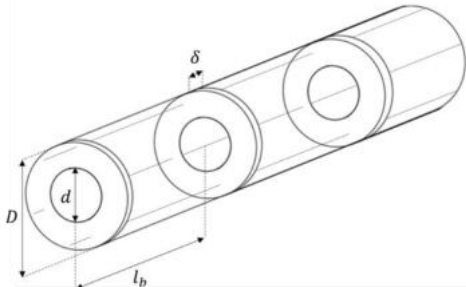
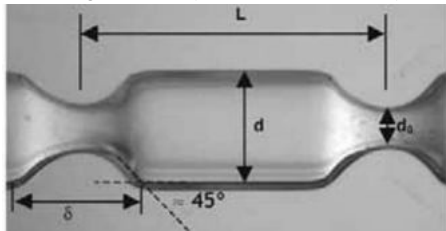
In the disc-and-doughnut geometry, the disc placed between the orifice plate acts as a barrier to the axial flow, generating additional radial flow. This design has been used largely in liquid-liquid extraction columns for a long time (Al Khani et al., 1988; Angelov et al., 1990; Laulan, 1980; Leroy, 1991; Martin, 1987) and its geometry has been employed in pulsed liquid-liquid dispersion operation (Lobry et al., 2013; Mazubert et al., 2016a). Mazubert et al. (2016a, 2016b) studied the disc-and-doughnut geometry and they found that this geometry shows the highest values of shear strain rates, pressure drop and energy dissipation (important parameters for multiphase flow applications) when compared with other geometries, such as the single orifice plate, single helical ribbon, double helical ribbon and alternating helical ribbon. However, this design does not improve radial mixing or decrease axial dispersion in comparison with the single orifice baffle.

Helical baffles have been shown that this geometry enables plug flow behaviour to be achieved over a wider range of oscillatory conditions than other geometries, due to additional “swirl motion” that is created from the interactions of the oscillatory flow and the helical baffle (Phan and Harvey, 2011a, 2010). This swirl flow has been identified by different authors using numerical simulation (Mazubert et al., 2016a, 2016b; Solano et al., 2012) and PIV experiments (McDonough et al., 2017). Different variations of this geometry exist, each one having specific properties and characteristics. There are

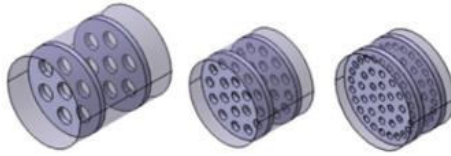
helical baffles made simply by coiling round wire, as well as sharp-edged helical baffles, alternating helical ribbons and double helical ribbons, which are variants using a coiled blade or ribbon. The sharp-edged helical baffle has shown to provide better yield in the production of biodiesel than the coiled wire helical baffle, due to the sharp baffle edge, which generates higher shear rates and enables more effective liquid-liquid phase mixing (Phan et al., 2011b). The alternating helical ribbon consists of a single blade that revolves in different directions every two periods, and in the double helical ribbon the blades revolve in opposite directions. The vortical flow is less apparent in the alternating helical blade, and streamlines appear to occupy less volume in the reactor, suggesting that flow turnover close to the walls is less efficient (Mazubert et al., 2016a). The helical baffle and alternating helical baffle provide improved plug flow behaviour compared with that generated by the single orifice and the disc-and-doughnut baffles (Mazubert et al., 2016a, 2016b). These authors also conclude that helical baffles provide lower axial dispersion, whilst maintaining significant levels of shear strain rate.

Axial circular baffles (or central baffles) are periodically spaced discs mounted on an axial rod. This geometry offers higher shear rates and pressure drop compared with the single baffle orifice and smooth constriction geometries (Ahmed et al., 2018a), making it useful for homogeneous liquid-liquid reactions (Rasdi et al., 2013; Yussof et al., 2018). The wire wool and sharp-edge helical blade with central rod geometries have also proven enhanced dispersion in liquid-liquid operations (Phan et al., 2012, 2011b). The helical coil baffle with central rod has been studied by McDonough et al. (2019a) using numerical simulation and comparing the results with PIV experiments. The presence of the central rod creates a new dual counter-rotating vortex regime, due to the significant swirl velocity generated by the helical coils.

Table 2.1: Different baffled geometries used in OBRs.

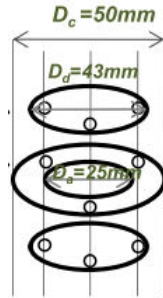
Baffled design	Reference
 <p>Single baffle orifice (plate)</p>	(Mazubert et al., 2015; Ni et al., 2003a, 1998a; Stonestreet and Van Der Veeke, 1999)
 <p>Single orifice (smooth constrictions)</p>	(Ahmed et al., 2018b; Eze et al., 2013; Phan and Harvey, 2010; Reis et al., 2005)

Multi-orifice plate baffle



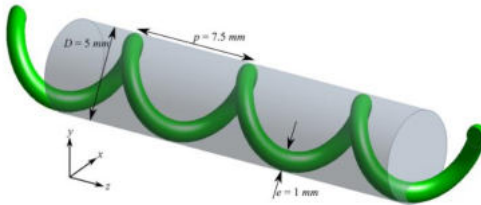
(Ahmed et al., 2018b; González-Juárez et al., 2017; Lucas et al., 2016; Palma and Giudici, 2003; Smith and Mackley, 2006)

Disc-and-doughnut baffle



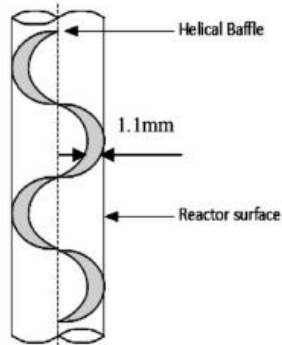
(Amokrane et al., 2014; Lobry et al., 2013; Mazubert et al., 2016a, 2016b)

Helical baffle



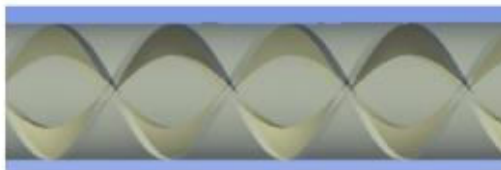
(Ahmed et al., 2018b; McDonough et al., 2019b, 2017; Phan and Harvey, 2011a, 2010)

Sharp-edged helical baffle



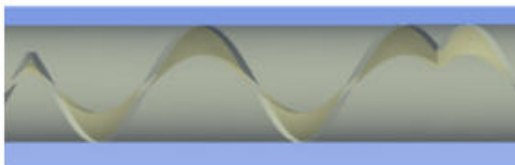
(Mazubert et al., 2016a, 2016b; Phan et al., 2011b; Phan and Harvey, 2011b)

Double helical baffle

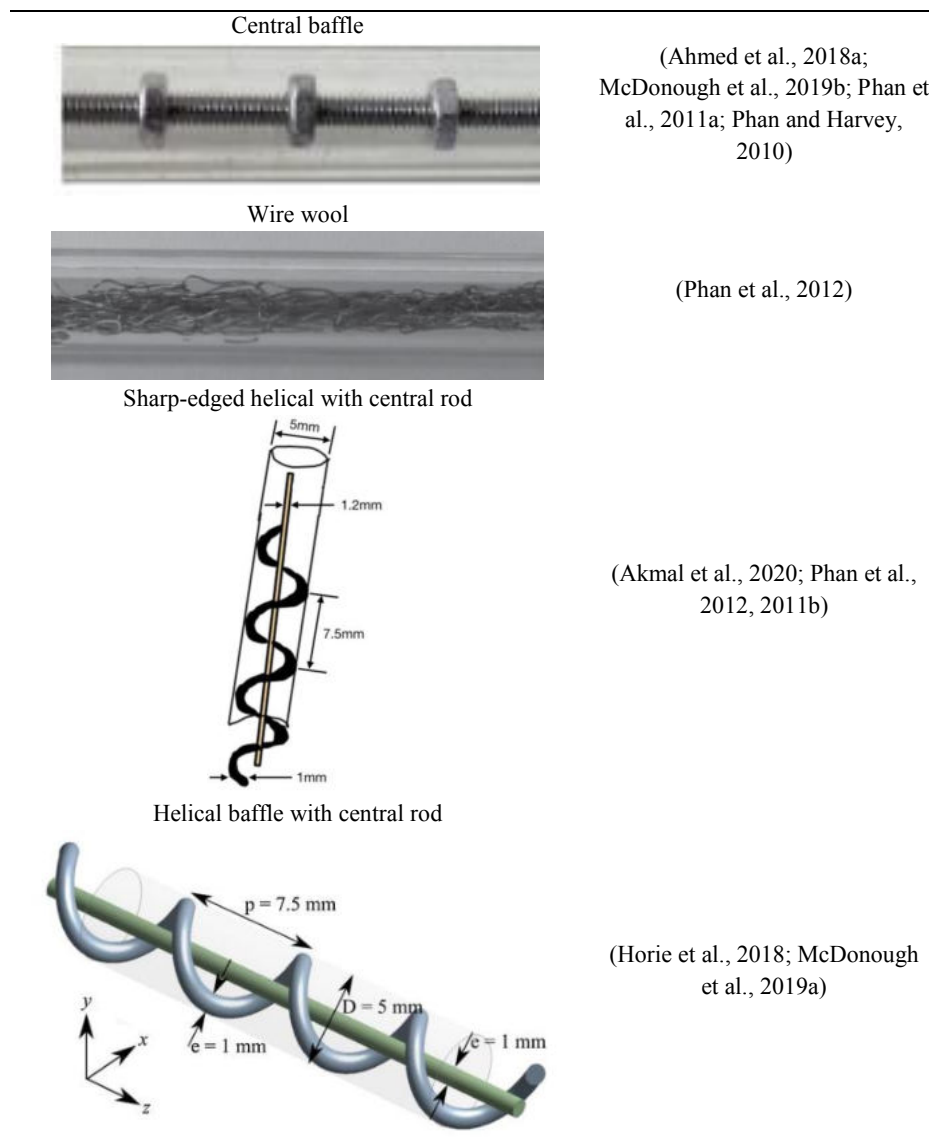


(Mazubert et al., 2016a, 2016b)

Alternating helical ribbon



(Mazubert et al., 2016a, 2016b)



2.1.2.3. Geometrical parameters

The geometrical parameters influence the shape and size of the generated vortices, which require adequate space to fully expand and spread in each baffle cavity. The main geometrical parameters in the design of oscillatory baffled reactors are based on the single orifice baffle design and are summarized in Table 2.2 and illustrated in Table 2.1. Table 2.2 gives the ranges of the most commonly used values, which were defined by the cited studies and are now often used as a design guideline. However, it should be pointed out that these ranges of values were defined for specific conditions used in the original studies and have never been optimised for a wide range of operating conditions or applications.

The selection of the OBR diameter depends on the process application and the desired production rate. In the literature, the conventional OBR diameter range is from 15 mm to 150 mm. However, it can be pointed out continuous flow OBRs offers the advantage of being able to ensure industrial-scale production even with 15 mm diameter reactors (Mazubert et al., 2015, 2014). In recent years, the interest in miniaturized OBRs (referred to meso-OBRs in literature) has increased. These miniaturized reactors

have diameters of ≤ 5 mm and they are typically operated with lower flow rates than the larger-scale OBRs, allowing reduced material inventory, as well as wastes generated in the process. These characteristics are particularly beneficial for rapid process screening and process development as explained by McDonough et al. (2015). Recent works show the feasibility of the use of meso-OBR as a reactor for multiphase reactions, such as solid-liquid carboxylic acid esterification (Eze et al., 2017), hexanoic acid esterification (Eze et al., 2013), as well as gas-liquid ozonation of water and wastewater (Lucas et al., 2016).

Table 2.2: Summary of main geometrical parameters in oscillatory baffled reactor design.

Parameter	Symbol	Most commonly used values in the literature	References
OBR diameter	D	15 – 150 mm	----
Baffle spacing	l_b	$1.5D$	(Brunold et al., 1989)
Baffle orifice diameter	d	$0.45 - 0.5D$	(Ni et al., 1998a)
Dimensionless free baffle area	α	$0.20 - 0.25$	(Ni et al., 1998a)
Baffle thickness	δ	2 – 3 mm	(Ni et al., 1998a)
Oscillation amplitude	x_o	$0.25 - 0.6l_b$	(Gough et al., 1997; Soufi et al., 2017)

The baffle spacing (l_b) is a key design parameter in an OBR as it influences the shape and length of eddies within each baffle cavity (Brunold et al., 1989; Knott and Mackley, 1980). A good value of l_b should ensure the full extension of the vortex generated behind the baffles, thus assuring its presence over the inter-baffle zone. Low values of baffle spacing cause the vortices to hit adjacent baffles before their full expansion, resulting in a constrained growth of eddies, a reduction of radial motion, as well as undesirable axial dispersion in continuous operations. For large values of baffle spacing, the vortices do not propagate through the full volume of the inter-baffle region. A spacing of $l_b = 1.5D$ has been the most commonly used value in the literature following the results reported by the flow visualizations of Brunold et al. (1989). Similar values have been recommended by others: Ni and Gao (1996b) reported a value of $l_b = 1.8D$ as the optimal in their studies of mass transfer, and Ni et al. (1998a) recommended a value of $l_b = 2D$ is needed to minimize the mixing time in a batch OBR with oscillating baffles. It should be mentioned that baffle spacing is also inherently related to oscillation amplitude and the effectiveness of eddy generation and mixing; this will be discussed later in this section.

The dimensionless free baffle area, defined as $\alpha = \left(\frac{d}{D}\right)^2$, impacts the size of eddies generated in each baffle cavity. Small values of d will constrict the fluid more as it flows through the baffles, resulting in larger vortices, and giving better mixing conditions. The dimensionless free baffle area is typically chosen in the range of 0.2–0.4 (Phan and Harvey, 2011b), but many studies have established a standardized orifice diameter of $d = 0.5D$ (Abbott et al., 2014a; Mackley and Stonestreet, 1995;

Navarro-Fuentes et al., 2019a; Ni et al., 1998a; Stonestreet and Harvey, 2002), which corresponds to a dimensionless free baffle area of $\alpha = 0.25$. Depending on if the flow is single or multi-phase, different values of α may be preferred. Ni et al. (1998a) studied the effect of dimensionless free baffle area for single phase flow on the mixing time in OBRs using either oscillating baffles or pulsed flow, over a range of $0.11 < \alpha < 0.51$. In both configurations (oscillating baffles and pulsed flow), shortest mixing times were achieved for values of $\alpha = 0.20 - 0.22$. In liquid-solid flows, Ejim et al. (2017) stated that the dimensionless free baffle area plays a dominant role in controlling solid backmixing and batch suspension of particles in meso-OBRs. In their study, a value of $\alpha = 0.12$ was found to minimize axial dispersion, resulting in a longer mean residence time of the solids.

Other geometrical parameters, such as the baffle thickness and the gap between baffle and wall, and their influence on mixing performance have also been reported. Ni et al. (1998a) studied the influence of baffle thickness on the mixing efficiency. Vortex generation is favoured by thinner baffles and they are deformed as the baffles get thicker. Thinner baffles are therefore recommended over thicker baffles, which will behave more like a step than a baffle. However, thinner baffles could negatively affect the mechanical stability of baffles, and it is expected that there would be a minimum baffle thickness to diameter ratio (δ/D) that ensures the stability of baffles and the vortex generation. The influence of the gap between the outer edge of the baffles and the tube wall on flow patterns has been studied using particle image velocimetry (PIV) (Ni et al., 2004a). It has been observed that an increased gap results in the generation of smaller eddies and an increase in the axial velocity, both leading to poor mixing performance. It is interesting to note that this study does not specify if the amount of tube cross-section open to flow was kept constant as the gap increased (i.e. by reducing the orifice diameter) or not. Indeed, this is expected to be an important parameter and for equal cross-sections open to flow, one can imagine higher axial dispersion to be obtained in geometries with no (or little) gap at the wall.

For fixed values of interbaffle spacing and orifice diameter, l_b and d , the combination of amplitude and frequency controls the generation and the propagation of eddies, producing different fluid flow behaviour. Gough et al. (1997) studied the effect of the oscillation frequency and amplitude on flow pattern by qualitative flow visualization in polymerisation suspensions in a modified OBR. It is important to point out that in this study, fluid oscillation was achieved by oscillating the baffles and not the fluid. From this study, the oscillation amplitude required to achieve similar flow patterns at those presents in a conventional OBR (where the flow is pulsed) is approximately equal to $0.25l_b$. Eventhough, the operation of the reactor used in Gough et al. (1997)'s study is rather different than both batch and continuous flow OBRs, this value of oscillation amplitude has been widely used for OBR design since that time. More recently, Reis et al. (2005) investigated a range of ratios of oscillation amplitude/baffle spacing, ranging from 0.015 to 0.85. It was shown that flow separation occurred with amplitude values lower than $0.25l_b$, the general recommendation. In an optimisation study carried out by Soufi et al. (2017), an amplitude value of $0.6l_b$ was found to give an optimal reaction yield in a mass

transfer limited liquid-liquid reaction that is significantly greater than the general design guideline. Indeed, these authors claim that the ‘optimal’ design of OBRs certainly depends on the type of application (single phase, gas-liquid, solid-liquid etc.), the process objective and the performance parameter that is being optimized.

The recommended values of geometrical parameters and the design guidelines for OBRs have mainly been based on the single orifice geometry and on the results of limited studies. It is clear that for some designs (e.g. helical baffles and wire meshes), these guidelines are for the most part not applicable or need some modification. For example, the multi-orifice plate baffle uses an equivalent diameter instead of the baffle orifice diameter to calculate the dimensionless free baffle area; helical baffles use the pitch (i.e. the axial distance of one complete helix turn) instead of the baffle spacing. Other geometries such as the disc-and-doughnut baffles have additional design parameters that need to be considered, such as the disc diameter and the distance between the disc and the orifice.

2.1.2.4. Dimensionless groups in continuous oscillatory flow

The key dimensionless groups that characterize the fluid mechanics and flow conditions in OBRs are the net flow Reynolds number (Re_{net}), oscillatory Reynolds number (Re_o), Strouhal number (St), and velocity ratio (ψ). These are presented in Table 2.3 and described briefly below.

The net flow Reynolds number controls the flow regimes of the fluids (from laminar to turbulent flow), and is defined as the ratio of inertial forces to viscous forces:

$$Re_{net} = \frac{\rho u_{net} D}{\mu} \quad (2.1)$$

The oscillatory Reynolds number describes the intensity of mixing in the reactor. In Re_o , the characteristic velocity is the maximum oscillatory velocity:

$$Re_o = \frac{2\pi f x_o \rho D}{\mu} \quad (2.2)$$

Stonestreet and Van Der Veeke (1999) identified three different flow regimes: for $Re_o < 250$ the flow is essentially 2-dimensional and axi-symmetric with low mixing intensity; for $Re_o > 250$ the flow becomes 3-dimensional and mixing is more intense; finally, when $Re_o > 2000$, the flow is fully turbulent.

The Strouhal describes oscillating flow behaviour and is often defined as $St = f_s D / u$. However Brunold et al. (1989) adapted the equation to a baffled tube, following the flow patterns

numerically modelled and observed by Sobey (1980):

$$St = \frac{D}{4\pi x_o} \quad (2.3)$$

This equation is the most used in OBR characterizations. The Strouhal number measures the effective eddy propagation with relation to the tube diameter. Higher values of St promote the propagation of the eddies into the next baffle (Ahmed et al., 2017). The most common range of the Strouhal numbers used in the literature is $0.15 < St < 4$ (Abbott et al., 2013).

It should be pointed out that surprisingly the baffle spacing, l_b , which influences the shape and length of eddies within each baffle cavity, is absent in the definition of St , despite being strongly related. Indeed, there is no dimensionless relationship between l_b and the St in the literature.

The velocity ratio, ψ , describes the relationship between the oscillatory and net flow values. It is typically recommended to operate at a velocity ratio greater than 1 to ensure that the oscillatory flow dominates the superimposed net flow (Stonestreet and Van Der Veecken, 1999). However, the recommended range of ψ to ensure plug flow operation (such that radial flow dominates and limits axial dispersion) is between 2 and 4 (Stonestreet and Van Der Veecken, 1999).

$$\psi = \frac{Re_o}{Re_{net}} \quad (2.4)$$

Nonetheless, the recommended velocity ratio range is not always used in practice and it is often adjusted depending on the application and process objective, and the baffle design. Examples of this are discussed in sections 2.I.3.1, 2.I.3.2, 2.I.3.6.3, and particularly in section 2.I.6.

Table 2.3: Summary of main dimensionless groups in oscillatory baffled reactor design.

Parameter	Symbol	Recommended operating ranges	References
Net flow Reynolds number	Re_{net}	<ul style="list-style-type: none"> • To achieve convection: $Re_{net} > 50$ • No advantage of oscillation flow: $Re_{net} > 250$ 	(Stonestreet and Harvey, 2002; Stonestreet and Van Der Veecken, 1999)
Oscillatory Reynolds number	Re_o	<ul style="list-style-type: none"> • Flow 2D, axi-symmetric: $Re_o < 250$ • Flow 3D, no axi-symmetric: $Re_o > 250$ • Fully turbulent: $Re_o > 2000$ 	(Stonestreet and Van Der Veecken, 1999)
Strouhal number	St	$0.15 < St < 0.4$	(Abbott et al., 2013)
Velocity ratio	ψ	<ul style="list-style-type: none"> • Oscillatory flow dominates the superimposed net flow: $\psi > 1$ • To ensure plug flow: $2 < \psi < 4$ 	(Stonestreet and Van Der Veecken, 1999)

2.I.3. Process enhancements using OBR

2.I.3.1. Macromixing

Mixing in OBRs has been characterised using different measures such as flow patterns, velocity profiles, axial to radial velocity ratio (R_V), plug behaviour (via the residence time distribution (RTD)), the axial dispersion coefficient (D_{ax}), or the Péclet number), mixing time, radial and axial fluid stretching, shear strain rate history, swirl and radial numbers, amongst others.

Velocity profiles and flow patterns, which have been determined by Particle Image Velocimetry (PIV) or Computational Fluids Dynamics (CFD) (Amokrane et al., 2014; González-Juárez et al., 2017; Mazubert et al., 2016a; McDonough et al., 2017; Ni et al., 2003a), are used to understand how the geometrical parameters and dimensionless groups affect the hydrodynamics of the continuous oscillatory flow. Zheng et al. (2007) studied the development of asymmetric flow patterns in the OBR, using numerical methods and the PIV technique. They identified two flow mechanisms depending on the Strouhal number. At small values ($St < 0.1$), the flow moves through the centre of the reactor, where it wobbles and rotates at large Reynolds numbers, due to a shear Kelvin-Helmholtz instability. At higher Strouhal numbers ($St > 0.5$), the flow consists of toroidal eddies that cross one baffle toward the middle of the cavity, striking with eddies generated in the opposite baffle during the backward phase. The collision of eddies has shown to break the flow symmetry if the oscillatory Reynolds number is higher than 225.

The axial to radial velocity ratio, R_V , is determined using the velocity components from the flow and velocity patterns:

$$R_V(t) = \frac{\sum_{j=1}^J \sum_{i=1}^I |u_{y(i,j)}| / J \cdot I}{\sum_{j=1}^J \sum_{i=1}^I |u_{x(i,j)}| / J \cdot I} \quad (2.5)$$

$$R_V(t) = \frac{\sum_i |u_{i,axial}| V_i}{\sum_i |u_{i,transverse}| V_i} \quad (2.6)$$

$$\text{where } u_{i,transverse} = \sqrt{u_y^2 + u_z^2}$$

Equation (2.5) is used in 2D surface-averaged velocity fields (Fitch et al., 2005), and equation (2.6) in 3D volume-averaged (Manninen et al., 2013), with smaller values of R_V indicating better radial or transverse mixing. Fitch et al. (2005) studied the axial to radial velocity ratio through particle image velocimetry (PIV) and CFD in a single orifice baffle geometry; they observed a decrease in the R_V as the Re_o increased, decreasing from a value of eight at very low Re_o , to two at $Re_o = 500$. From their results, they defined a criterion of $R_V < 3.5$ to achieve effective mixing. Other works achieved similar trends as illustrated in Figure 2.5 and values with the same baffle design (Jian and Ni, 2005; Manninen et al., 2013; Ni et al., 2003a). Mazubert et al. (2016a) found that the disc-and-doughnut and helical blade

baffle geometries provide more effective radial mixing at low oscillatory Reynolds number than the single orifice plate geometry.

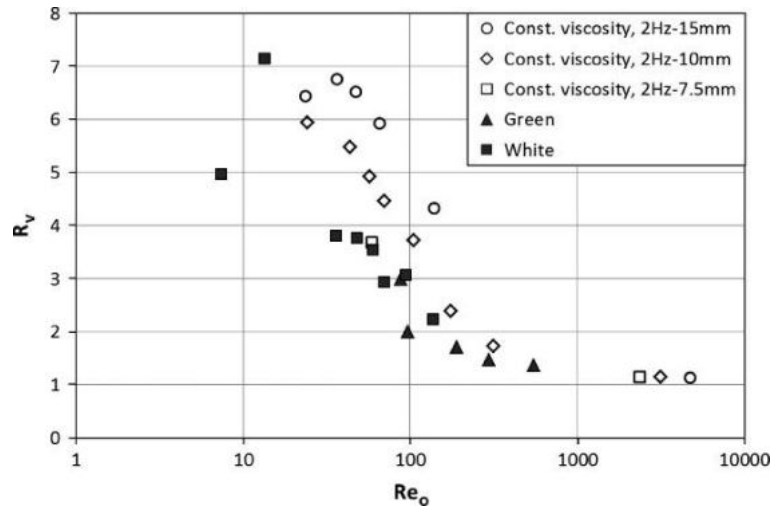


Figure 2.5: Axial to radial velocity ratio (R_V) as function of oscillatory Reynolds number for different fluids (green and white legend in the plot refer to low and high viscosity non-Newtonian fluids, respectively) (Manninen et al., 2013).

In continuous operations, the main objectives of previous works presented in the literature are to evaluate the plug flow behaviour via the residence time distribution (RTD) and to determine the operating conditions required to achieve the narrowest RTD (Abbott et al., 2014a; Dickens et al., 1989; Kacker et al., 2017; Mackley and Ni, 1991; Reis et al., 2004). Most of these studies are experimental and have analysed the dispersion of a pulse injection of homogeneous tracer in the continuous phase as a function of the oscillatory and net flow conditions, as well as the geometrical parameters of the OBR. From these studies, different recommended ranges of ψ have been proposed to achieve plug flow depending on the size and design of the OBR. Stonestreet and Van Der Veeke (1999) proposed the range $2 < \psi < 4$ using a single orifice baffle 24 mm OBR. Phan and Harvey (2010) found good plug flow in 5 mm meso-OBRs with smooth constriction (integral) and central baffle designs in the ranges of $4 < \psi < 8$ and $5 < \psi < 10$, respectively. Phan and Harvey (2011b) used a 5 mm. meso-OBR helical baffle geometry and defined the recommended range within $5 < \psi < 250$.

The axial dispersion coefficient, D_{ax} , is used to characterize mixing in tubular configurations (Levenspiel, 2012). It is a measure of the degree of deviation of flows from the ideal plug flow, in which case D_{ax} should be equal to zero. The one-dimensional axial dispersion convection-diffusion model is described by:

$$\frac{\partial C}{\partial t} = D_{ax} \frac{\partial^2 C}{\partial x^2} - u \frac{\partial C}{\partial x} \quad (2.7)$$

Three different models have been used in the literature to interpret RTD data in OBRs: the tanks-in-series without interaction (compartmental model), tank-in-series with backflow, and the dispersion model. All these models are used to predict the non-ideal behaviour of the OBR on process performance. Many authors found that plug flow can be achieved with laminar flow (low net Reynolds number) and the RTD can be controlled with the oscillatory conditions independently of the net flow, as it can be observed in Figure 2.6 (Ni, 1995; Phan and Harvey, 2010; Reis et al., 2010; Stonestreet and Van Der Veecken, 1999).

The axial diffusion coefficient can be expressed via the dimensionless Péclet number, defined as:

$$Pe = \frac{\bar{u}L}{D_{ax}} \quad (2.8)$$

The Péclet number represents the ratio of the convective transport to diffusive transport, and is the reciprocal of the dimensionless axial dispersion coefficient term. It is recommended that OBRs be operated such that minimum $D_{ax}/\bar{u}L$ is achieved. According to this definition, reactors with $Pe > 100$ present an ideal plug flow behaviour, while reactors with $Pe < 1$ present an ideal perfect mixing behaviour (Hornung and Mackley, 2009).

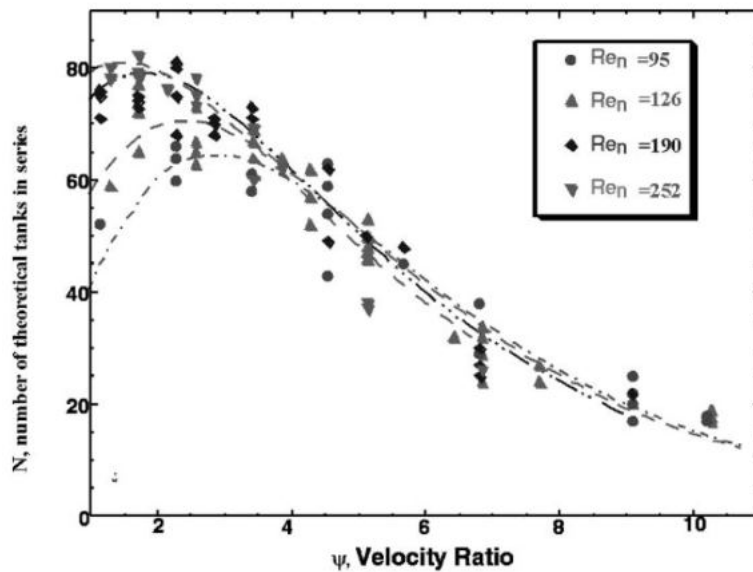


Figure 2.6: The dependency of the tanks-in-series model parameter, N , on the oscillatory Reynolds number for different net Reynolds (Ni et al., 2003b).

Different authors have studied the influence of the oscillatory frequency and amplitude. Palma and Giudici (2003) studied the influence of the pulsating frequency, amplitude and baffle spacing on the axial dispersion coefficient, by measurement of the RTD for a single flow phase in a pulsed sieve plate column. The results show that D_{ax} increases proportionally with an increase in the product of oscillatory

amplitude and frequency. The amplitude has a significant influence on the RTD and axial mixing compared with the frequency, and increasing amplitudes increase D_{ax} (Dickens et al., 1989; Oliva et al., 2018; Slavnić et al., 2017). This is because the amplitude directly controls the length of the eddies generated along the tube (Hamzah et al., 2012).

The multi-orifice baffle geometry has been studied and compared with the performance of single orifice baffle reactors using experimental techniques (Smith and Mackley, 2006) and numerical simulation (González-Juárez et al., 2017). From these works, it has been concluded that an increase of orifices in the baffle geometry leads to a decrease in D_{ax} (and hence an increase in the Pe), thereby resulting in narrow RTD curves and plug flow behaviour.

There have only been a few studies that have addressed mixing performance in OBRs in other ways than evaluating RTD. Ni et al. (1998a) characterized oscillatory baffled columns using the time necessary for a tracer to reach a specific uniform concentration into the column. Mazubert et al., (2016a, 2016b) developed characterisation methods to evaluate radial and axial fluid stretching and shear strain rate history in the OBR. The first method allows spatial mixing to be assessed and to identify the presence of chaotic flow; the second technique is useful for operations that are shear-dependent, e.g. droplet break up. McDonough et al. (2017) characterized mixing in an OBR with helical baffles using PIV and numerical simulation. They used the swirl and radial numbers to identify whether mixing is dominated by swirl or vortex flows. The swirl number describes the ratio of the axial flux of angular momentum to the axial flux of linear momentum:

$$S_n = \frac{\int_Z^v v_z v_\theta r^2 dr}{R \int v_z^2 r dr} \quad (2.9)$$

where v_z and v_θ are the axial and tangential velocity components, r is the radial position, and R the hydraulic radius. The radial number compares the axial flux of radial momentum to the axial flux of axial momentum:

$$r_n = \frac{\int_Z^v v_z v_r r dr}{\int v_z^2 r dr} \quad (2.10)$$

2.1.3.2. Micromixing

Micromixing, i.e. mixing at the molecular scale, is the limiting step in the progress of instantaneous and competitive reactions. Poor micromixing can lead to a loss of conversion and the formation of undesired by-products (Baldyga and Pohorecki, 1995).

Micromixing applications, such fast precipitation and crystallization, in OBRs are a challenging area because this kind of reactor does typically not provide fast micromixing conditions, thereby leading to

local segregation and decreases in selectivity and/or product properties. In a recent study, McDonough et al. (2019b) characterized micromixing in different meso-OBR geometries with the Villermaux-Dushman test reaction. The study showed that central and smooth constriction baffles enabled fast micromixing times when the velocity ratio increased ($\psi > 25$). However, these values of ψ are outside the recommended range for achieving good plug-flow in these geometries ($4 < \psi < 10$) (Phan and Harvey, 2010). On the other hand, the helical design provides fast micromixing times as well as good plug-flow behaviour, thanks to its wide range of velocity ratio at which plug-flow can be achieved ($5 < \psi < 250$) (Phan and Harvey, 2011a). Nevertheless, due to the limited number of studies in this area, the effectiveness of micromixing in OBRs remains is not entirely clear.

2.1.3.3. Shear and strain rate

Knowledge of the shear strain rate generated in OBRs is important for multiphase applications, like emulsions and liquid-liquid dispersion, where high shear rates are needed for efficient droplet breakage, or for bioprocesses containing shear sensitive cells that can be inhibited or damaged by high shear strain rates. Ni et al. (2000) analysed the shear strain rate in an OBR with single baffle orifice using Particle Image Velocity technique and found that lower volume average shear strain rates were obtained compared with those in conventional STRs. Other studies demonstrate that single orifice plate baffle are beneficial for biological applications that require low-shear, like enzymatic saccharification (Abbott et al., 2014b; Ikwebe and Harvey, 2015), fermentations (Gaidhani et al., 2005) and the harvest of microalgae for bioprocesses (Abbott et al., 2015).

Indeed, the geometry of the baffles plays a significant role in the shear strain rate distribution. Mazubert et al. (2016a, 2016b) studied the shear strain rate of five different OBR baffle designs and the results are presented in Figure 2.7. The shear strain rate increases linearly with the increase of the oscillatory Reynolds number, which has a greater influence than the net flow. This suggests that higher oscillatory conditions may be preferred for multiphase applications. However, it should be recalled that as the oscillatory velocity (i.e. $f \cdot x_o$) increases, axial dispersion also increases, which highlights the necessity to find a good compromise depending on the process operation. From Figure 2.7 it can also be seen that the disc-and-doughnut creates the highest shear strain rate, making it suitable for droplet breakup and solid de-agglomerations, whilst the other geometries show lower shear rates. In all cases, a detailed analyse of the flow fields showed that the highest values of the shear strain rate were found close to the baffles, with only a small fraction of the fluid volume being affected. Yang et al. (2015) came up with a similar conclusion in the study of the crystallization of butylparaben: the highest shear rates appear near the baffle, with the nucleation rates reaching their maximum value as the shear rate increases.

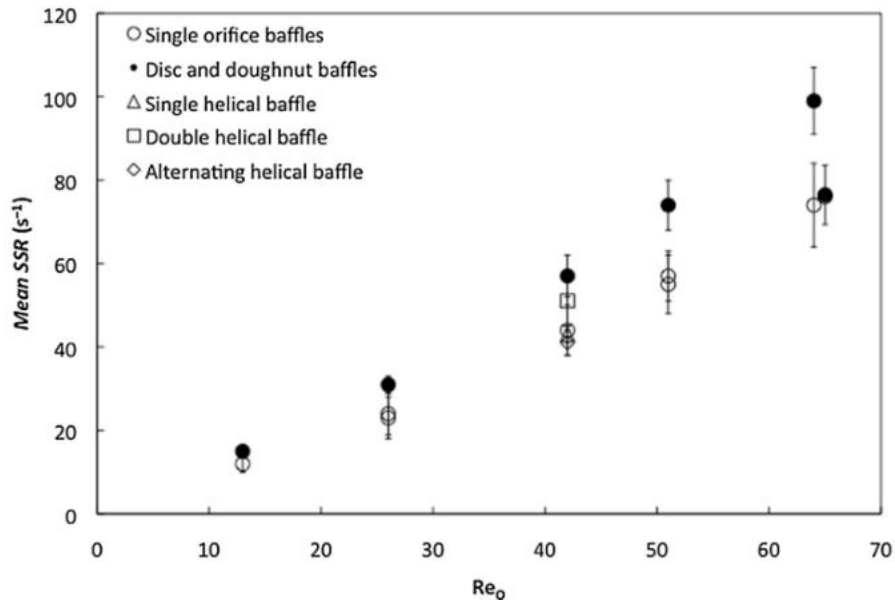


Figure 2.7: Influence of oscillatory conditions and baffle geometry on the mean shear strain rates (Mazubert et al., 2016b).

2.1.3.4. Heat transfer

OBRs have proven to significantly enhance heat transfer in batch and continuous operation when compared with a straight tube (Mackley and Stonestreet, 1995; Stephens and Mackley, 2002). The Nusselt number is often used to characterize heat transfer and to compare the performance between conditions and geometries:

$$Nu = \frac{h_{OBR}D}{k} \quad (2.11)$$

where h_{OBR} is the OBR-side transfer coefficient and k the thermal conductivity of the process fluid.

Mackley and Stonestreet (1995) studied the influence of the ratio of oscillatory Reynolds number to net Reynolds number on heat transfer in a single orifice baffled reactor. A Nusselt number enhancement of up to five-fold was obtained in a baffled tube without oscillations when compared with a smooth tube and up to 30-fold improvement when an oscillatory flow was applied over the net flow, as illustrated in Figure 2.8. As Re_{net} increases, the influence of Re_o becomes less important, collapsing the curves onto the steady-state behaviour, and losing the benefits of the oscillatory flow in the heat transfer. In the laminar flow regime ($Re_{net} < 1000$), the effect of the oscillatory flow on heat transfer becomes significant.

González-Juárez et al. (2018) studied heat transfer for a single orifice baffle reactor using numerical simulations. They reached the same conclusions as Mackley and Stonestreet (1995), and expanded them using two different working fluids. They found a 2-3 fold increment in the Nusselt number when using

a viscous thermal fluid (Duratherm 450 oil) as the working fluid, compared with the same net flow Reynolds number using water. The effect of the amplitude and frequency was also analysed and it was concluded that the amplitude seems to have a negligible influence on the average Nusselt number when compared with the frequency.

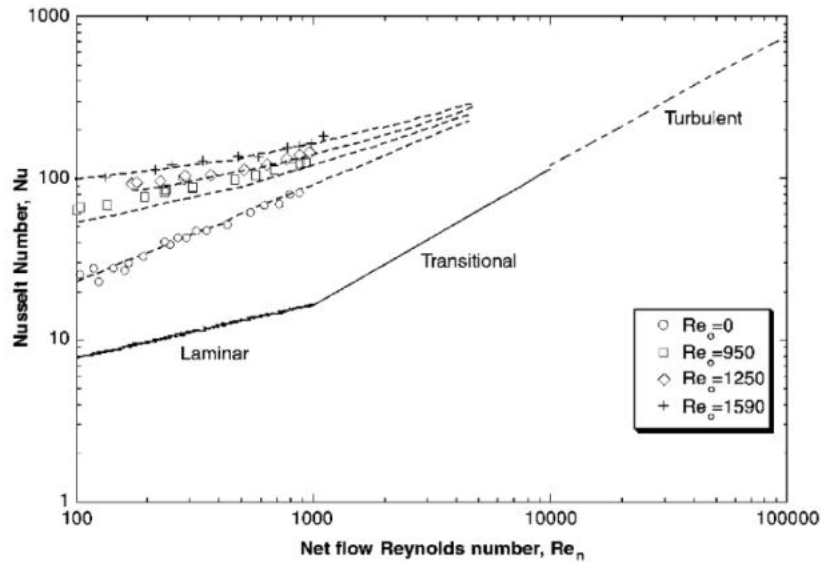


Figure 2.8: Heat transfer enhancement in oscillatory baffled tubes (Ni et al., 2003b).

Solano et al. (2012) carried out numerical simulations of heat transfer in a meso-scale helical baffled reactor. They obtained an enhancement of heat transfer rates of up to four-fold, compared with the steady unbaffled flow. This enhancement was attributed to the chaotic flow structures created by the oscillatory flow interacting with the cold and hot flows, and by obtaining the maximum value of Nu during the formation of the vortex behind the baffle. In more recent studies, experimental studies in other meso-OBR geometries have been performed. Onyemelukwe et al. (2018) investigated the heat transfer performance in a meso- smooth constriction baffled reactor. An increase of 1.7-fold in the heat transfer rate was obtained with the combination of the pulsed flow and the smooth constrictions. Under the chosen conditions ($Re_{net} = 11 - 54$, $Re_o = 0 - 197$), the heat transfer rate was shown to depend more greatly on the net flow rather than the oscillatory flow. It was also shown to be more dependent on the Strouhal number than the frequency, with heat transfer performance decreasing for $St < 0.8$. These results contradict those reported by Mackley and Stonestreet (1995) and González-Juárez et al. (2018) for larger sharp-edged baffled reactors with tube diameters of 12 mm and 25 mm, respectively. Indeed, the effect of the surface to volume ratio plays an important role when comparing heat transfer in different OBR sizes; however, this has not specifically been addressed in these works. Ahmed et al., (2018a) compared the thermal performance of three different meso-OBRs (helical, central and single orifice baffles). In all the geometries, the Nusselt number was increased in the presence of the oscillations. The

helical baffle design showed the highest thermal performance: up to 7-fold when compared with that without oscillations.

Different correlations have been established to predict the Nusselt number in OBRs over recent years. The first and most well-known phenomenological correlation was established by Mackley and Stonestreet (1995) for the range $100 \leq Re_{net} \leq 1200$ and $Re_o \leq 800$:

$$Nu = 0.0035 Re_{net}^{1.3} Pr^{1/3} + 0.3 \left[\frac{Re_o^{2.2}}{(Re_{net} + 800)^{1.25}} \right] \quad (2.12)$$

The first term corresponds to the steady-state flow contribution and was chosen to be similar to the Dittus-Boelter turbulent flow correlation, however the value of the exponent is higher in order to take into account the presence of the baffles. The second term corresponds to the oscillatory flow contribution, assuming that when $Re_o \gg Re_{net}$, the influence of oscillations is superimposed on the steady behaviour by adding the oscillatory term to the steady-state term. In the case when $Re_{net} \gg Re_o$, the oscillatory influence becomes small, and the correlation reduces to that for steady-state behaviour. Nevertheless, the influence of the Prandtl number on the Nusselt was not determined in the study.

Until the end of the 2010s, no other significant correlation was established for the prediction of heat transfer in OBRs. However, over the last years, different research studies have been carried out to obtain more robust Nusselt number correlations. Table 2.4 presents a summary of the correlations found in the literature. The equations are strongly dependent on the geometry, operating conditions and working fluid. González-Juárez et al. (2018) compared their results in a single baffle orifice OBR with the correlations proposed by Mackley and Stonestreet (1995) and by the Polymer Fluid Group from Cambridge University. Both correlations presented a lack of agreement between them and do not represent the behaviour of González-Juárez et al.'s (2018) experimental results. At higher Re_{net} , the values predicted by the correlations from Mackley and Stonestreet (1995) and the Polymer Fluid Group at Cambridge University were in better agreement with those approached with González-Juárez et al.'s (2018) results.

Onyemelukwe et al. (2018) presented their own correlation for a smooth constriction meso-OBR. Their equation follows the same principle of Mackley and Stonestreet's (1995) correlation with the difference that the coefficient of the first term is higher due to the significant influence of the net flow on the heat transfer rate, and the inclusion of the St due to its significant effect, independently of the Re_o .

Ahmed et al. (2018a) proposed general correlations for three meso-OBR designs, following the equations established by Law et al. (2018), which are analogous to the Dittus-Boelter correlation but have an additional term involving Re_o . The coefficient of the correlations depends on the tube diameter and baffle geometry, making the equations more versatile and robust for the prediction of Nusselt

numbers. The correlation shows good agreement with the experimental results for all geometries, as well as with the work of Mackley and Stonestreet (1995) and Law et al. (2018).

2.1.3.5. Energy dissipation

The energy dissipation rate in oscillatory flows can be characterised by the time-averaged power consumption over an oscillation period divided by the volume of the fluid.

There are two models reported in the literature for estimating power density in pulsed batch columns and in oscillatory flow in tubes with no net flow: the quasi-steady flow model, QSM (Jealous and Johnson, 1955) and the eddy enhancement model, EEM (Baird and Stonestreet, 1995). These models, which assume high oscillatory velocities and a turbulent flow regime, are the only ones that have been employed for estimating power dissipation in OBRs.

The quasi-steady flow model (QSM), given in equation (2.13), postulates that the instantaneous pressure drop in an oscillation period is the same as the pressure drop that would be achieved in steady-state flow with the same velocity. The model is based on the standard pressure drop relation across a simple orifice.

$$\frac{P}{V} = \frac{2\rho n(\omega x_o)^3(1/\alpha^2 - 1)}{3\pi C_D^2 L} \quad (2.13)$$

This model has shown to be valid for high oscillation amplitudes x_o (5–30 mm) and low oscillation frequencies f (0.5–2 Hz). In turbulent flow, the orifice discharge coefficient (C_D) varies between 0.6 and 0.7 for simple orifices with sharp edges. However, at low Re, it is known that this coefficient is proportional to \sqrt{Re} and varies with the ratio of reactor diameter to orifice diameter, D/d (Johansen, 1930; Liu et al., 2001). Thus, this limits the application of the model to OBRs with orifice baffles and specific flow conditions. The QSM also assumes that there is no pressure recovery due to the short distance between orifice baffles. This assumption has been studied recently by Jimeno et al. (2018) who claim that some pressure recovery does take place when the baffle spacing is $1.5D$ or greater.

The eddy enhancement model (EEM) is based on acoustic principles and the concept of eddy viscosity (Baird and Stonestreet, 1995). The model was developed considering the acoustic resistance of a single orifice plate, and by replacing the kinematic viscosity with the eddy kinematic viscosity at high Reynolds numbers. This model, given by equation (2.14), has been shown to be valid for low oscillation amplitudes x_o (1–5 mm) and high frequencies f (3–14 Hz) values, which is the opposite to the QSM. It also includes a mixing length (l), which is an adjustable parameter corresponding to the average travel distance of turbulent eddies and is expected to be of the same order as the reactor diameter.

Table 2.4: Correlations for tube-side Nusselt number found the literature.

Geometry	Range of applicability	Correlation	Reference
Single orifice plate baffle $D = 12$ mm $\alpha = 0.35$ $l_b = 1.5D$	$100 \leq Re_{net} \leq 1200$ $Re_o \leq 800$ $Pr = 73$	$Nu = 0.0035 Re_{net}^{1.3} Pr^{1/3} + 0.3 \left[\frac{Re_o^{2.2}}{(Re_{net} + 800)^{1.25}} \right]$	(Mackley and Stonestreet, 1995)
Single orifice plate baffle $D = 24$ mm $\alpha = 0.25$ $l_b = 1.5D$	$Re_{net} \leq 1000$ $Re_o \leq 1590$ $Pr = 73$	$Nu = Pr^{1/3} \left[0.36 Re_{net}^{0.6} + 0.8 \frac{Re_o^{1.7}}{Re_{net} + 10,000} \right]$	(Paste, Particle and Polymer Processing Group (P4G), accessed February 17, 2020)
Smooth constriction baffle $D = 5$ mm $\alpha = 0.16$ $l_b = 2.6D$	$11 \leq Re_{net} \leq 54$ $Re_o \leq 197$ $Pr = 5.37$	$Nu = 0.01616 Re_{net}^{1.16} Pr^{1/3} + 0.0016 \left[Re_o^{0.08} Re_{net}^{1.42} \frac{St}{1.136} \right]$	(Onyemelukwe et al., 2018)
Single orifice plate baffle $D = 26.2$ mm $\alpha = 0.246$ $l_b = 2D$	$200 \leq Re_{net} \leq 1300$ $Re_o \leq 8700$ $4.4 \leq Pr \leq 73$	For $Re_o \leq 1300$ $Nu = 0.022 Re_{net}^{0.7} Pr^{1/3} Re_o^{0.44}$ For $Re_o > 1300$ $Nu = 0.52 Re_{net}^{0.7} Pr^{1/3}$	(Law et al., 2018)
OBRs $D = 5$ mm $l_b = 1.5D$ <u>Helical baffle</u> $\alpha = 0.59$ <u>Central baffle</u> $\alpha = 0.13$ <u>Single orifice plate baffle</u> $\alpha = 0.25$	$61 \leq Re_{net} \leq 2400$ $Re_o \leq 1550$ $Pr = 4.4$	For $Re_o \leq 1300$ $Nu = \lambda Re_{net}^{0.7} Pr^{1/3} Re_o^{0.44}$ For $Re_o > 1300$ $Nu = 23.45\lambda Re_{net}^{0.7} Pr^{1/3}$ Meso-helical baffle: $\lambda = 0.009$ Meso-central baffle: $\lambda = 0.011$ Meso-single orifice baffle: $\lambda = 0.007$	(Ahmed et al., 2018a)

$$\frac{P}{V} = \frac{1.5\rho\omega^3 x_o^2 l}{\alpha l_b} \quad (2.14)$$

In addition to the empirical nature of the mixing length l , which is dependent on reactor geometry, Reis et al. (2004) reported that it is also dependent on oscillation amplitude. This again limits the use of this model.

It is also pointed out that both models were developed for pulsed flow in tubes and columns without a net flow (i.e. equivalent to batch OBRs) and that they have been used to compare performances between traditional stirred-tank reactors and OBR in different applications, such as bioprocesses and crystallization (Abbott et al., 2014b; Ni et al., 2004b). Despite the recommended oscillatory conditions of each model, the QSM model has been the most widely used of the two. Many studies have used the QSM rather than the EEM, and some of them use it outside the originally suggested range of frequency and amplitude (Ahmed et al., 2018b; Callahan and Ni, 2014; Ejim et al., 2017; Siddique et al., 2015; Slavnić et al., 2019; Yang et al., 2015). There are a very limited number of fundamental studies of energy dissipation rate in OBRs, therefore impeding the validation of these models. To date, only two studies have been carried out on this subject. Mackley and Stonestreet (1995) used a correction factor (given by equation (2.15)) in the QSM that takes into account the power density provided by the net flow. However, the physical meaning behind this correction factor remains unclear, making it difficult to use with any degree of confidence.

$$\varphi = \left[1 + 4 \left(\frac{Re_o}{\pi Re_{net}} \right)^3 \right]^{1/3} \quad (2.15)$$

Recently, Jimeno et al. (2018) performed CFD simulations of turbulent flow in a OBR with smooth constrictions and determined the power density via the pressure drop across the reactor for different oscillatory conditions. The results were compared with the values obtained using the QSM and the EEM. They found that the QSM over-estimates power density due to inappropriate values of geometrical parameters, whilst the EEM provides better agreement. Both models were then modified by adjusting the geometrical parameters (e.g. n^x , C_D) and proposing an empirical correlation for mixing length, as given in equations (2.16) and (2.17). The modified models predict similar power densities for a wide range of operating conditions in turbulent flow and are in good agreement with the authors' CFD simulations of continuous flow in the OBR. Nevertheless, these models still include adjustable parameters based on reactor geometry, so it is expected that the values of these parameters would need to be modified again if the reactor geometry – in particular the baffle design – is altered.

$$\frac{P}{\bar{V}} = \frac{2\rho n^{0.7}(\omega x_o)^3 \left(1/\alpha^2 - 1\right)}{3\pi C_D^2(V/A)} \quad (2.16)$$

$$\frac{P}{\bar{V}} = \frac{1.5n^{0.7}\rho\omega^3x_o^2l^*}{\alpha(V/A)} \quad (2.17)$$

$$l^* = 0.002 \left[\alpha^2 \frac{d}{\pi x_o} \right]^{0.57} \quad (2.18)$$

Jimeno (2019) carried out one of the first analyses of the evolution of energy dissipation along the lengths of OBRs using numerical simulation. Indeed, the amount of energy dissipated changes along the reactor due to the decrease in the oscillatory velocity experienced by the liquid phase and by solid particles as they travel downstream in some crystallization processes (Briggs et al., 2015). However, examination of the evolution of power density and pressure drop along the length of the OBR showed no signs of energy losses by the fluid as it moves downstream.

2.1.3.6. Multiphase systems

2.1.3.6.1. Gas-Liquid systems

OBRs have proven to enhance gas-liquid mass transfer due to the oscillatory flow, which decreases the bubble size and increases the gas-liquid contact area. Hewgill et al. (1993) reported an increase in the mass transfer coefficient by up to six-fold for an air-water system when baffles and oscillatory flow were applied and compared with conventional STRs, as shown in Figure 2.9. Many other studies in the literature have compared the mass transfer performance between conventional STRs and OBRs, obtaining higher $k_L a$ values for various combinations of baffle spacing, amplitude and frequency (Ni and Gao, 1996b). The OBR performance has also been compared with that of bubble columns and baffled columns, proving to be more than five and three times more efficient for ozone-water transfer (Al-Abduly et al., 2014).

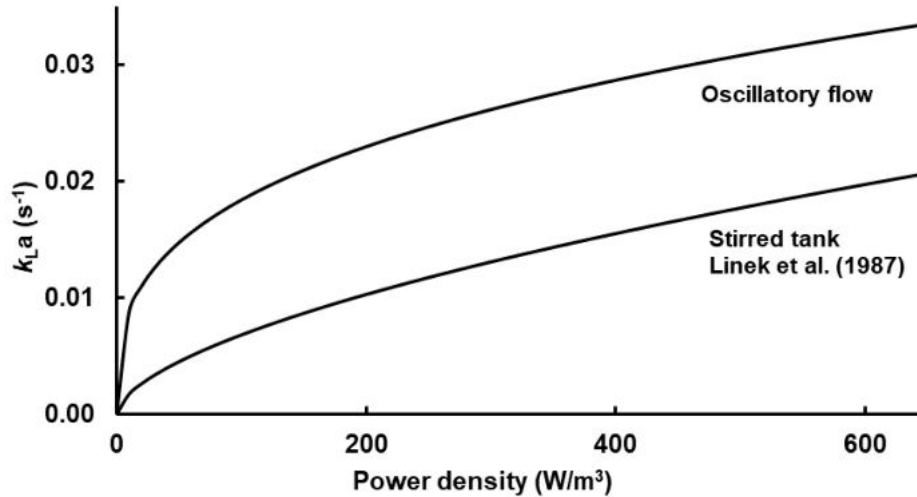


Figure 2.9: $k_L a$ against power density for a single orifice baffle 50 mm OBR and a STR at constant superficial gas velocity (Hewgill et al., 1993).

The reason of this increase in mass transfer coefficients was studied by Oliveira and Ni (2001), who experimentally characterized gas-liquid flow patterns in a single orifice baffle OBR by studying the influence of oscillatory conditions on the gas hold-up and bubble size. They observed how the bubbles interact with the eddies created by the presence of the baffles. As the oscillatory velocity increases, intermediate-scale vortices, formed by the interaction of oscillatory flow and the baffles, are the main cause of continuous bubble breakage. These vortices cause a decrease in the bubble diameter and hence increase surface area. They also retain bubbles for a longer time, increasing the gas-phase residence time and gas hold-up. Later results demonstrated that the gas-liquid hydrodynamics are mostly governed by the oscillatory conditions and are independent of the type of gas sparger. Furthermore, gas hold-up plays a more important role than the bubble size in determining the volumetric transfer rate (Oliveira and Ni, 2004).

Mass transfer has been also studied in meso-OBRs, mainly in the smooth constriction baffle geometry. Reis et al. (2007) found that bubble size is dependent on oscillatory operating conditions, and the bubble size and specific area can be adjusted in the range of oscillatory conditions used in their study ($f = 10 - 15 \text{ s}^{-1}$, $x_o = 0 - 3 \text{ mm}$). The liquid-side mass transfer coefficient, k_L , improved as the oscillatory flow increased, reaching more than two orders of magnitude higher than the values obtained in bubble columns, and twice the value obtained in a 50 mm diameter single orifice baffle OBR, whilst being achieved using much lower superficial gas velocity. An increase in the oscillatory conditions (f and x_o) also has a positive influence on the number of bubbles as it increases the specific interfacial area and enhances the mass transfer. In later work, Reis et al. (2008) found that the enhancement of the mass transfer coefficient was also related to the geometry of the smooth constrictions, which reduced the rise velocity of the bubbles and increase the gas hold-up. The high radial mixing and the detachment mechanism of vortex rings from the walls are the reasons for the increased bubble retention and effective

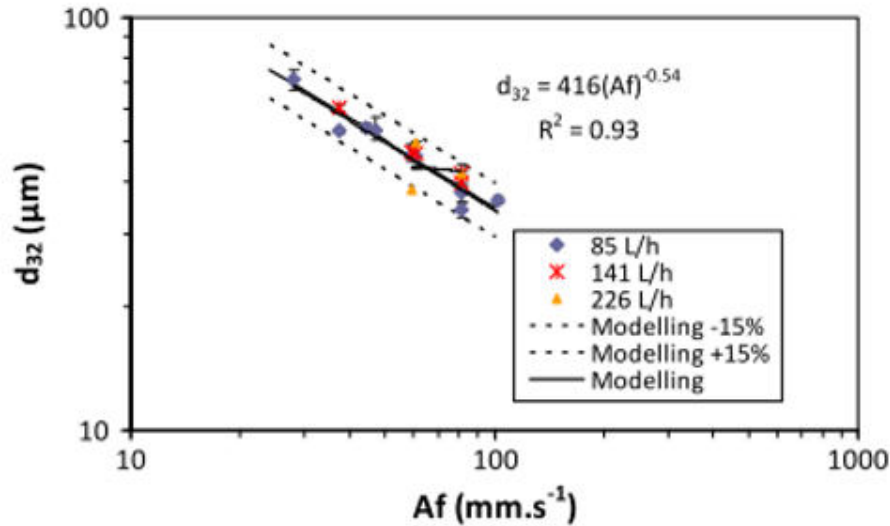
gas-liquid contacting area. The meso-OBR with smooth constriction have been also studied by Ferreira et al. (2015), who conclude that $k_L a$ increases with both superficial gas velocity and oscillatory conditions, the latter having the highest impact on the mass transfer process.

Mass transfer in other geometries, like the multi-orifice and helical baffles, have also been analysed. Pereira et al. (2014) obtained higher mass transfer coefficients with different multi-orifice platforms compared with the single orifice baffle geometry. Ahmed et al. (2018b) found that $k_L a$ increased significantly in the multi-orifice geometry, reaching values up to 7-fold when compared with steady flow in a straight tube. The helical baffle design, on the other hand, did not show any significant improvement in the mass transfer coefficient, making it less recommended in gas-liquid mass transfer applications.

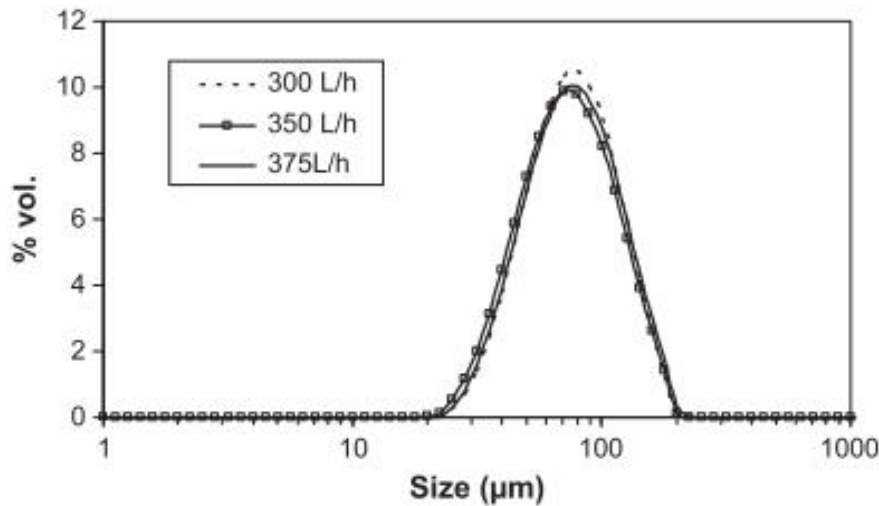
2.I.3.6.2. Liquid–Liquid dispersions

Dispersion of liquid–liquid systems are a key element of many processes, like liquid-liquid reactions and extractions. Good control of the mean droplet size and droplet size distribution defines the quality and properties of the final product or the process performance. Inspired by pulsed extraction column processes (Angelov and Gourdon, 2012; Golding and Lee, 1981; Karr, 1959; Kumar and Hartland, 1988; van Delden et al., 2006), liquid-liquid dispersions have been widely studied in OBRs. Pereira and Ni (2001) studied the influence of the oscillatory velocity over the droplet size distribution and Sauter mean diameter, d_{32} , in a continuous oscillatory baffled reactor. They found that the oscillatory flow plays a more significant role in the control of the mean droplet diameter and size distribution than the net flow. Furthermore, an increase in either the amplitude or the frequency, decreases the droplet size and narrows the distribution. Many other works have also identified the oscillatory flow as the key parameter in the control of the droplet size and distribution (Ni et al., 1999, 1998b; Ni et al., 2001c).

Lobry et al. (2013) confirmed the same results for a disc-and-doughnut baffled reactor, in which an increase in the oscillatory velocity leads to a decrease of the mean droplet size and narrow droplet distribution (Figure 2.10(a)), with no significant effect of the net flow over the size and distribution of droplets (Figure 2.10(b)). The latter means that residence time can be controlled and modified without a loss in the dispersion properties. They also studied the influence of the nature of the material of the baffles and found that the smallest droplet sizes were obtained with baffles made of PTFE.



(a)



(b)

Figure 2.10: (a) mean droplet size as function of oscillatory velocity, with $A = x_o$, (b) droplet size distribution for different net flowrate and same oscillatory conditions ($x_o = 52$ mm and $f = 1.17$ Hz) (Lobry et al., 2013).

Breakage rate has been investigated by Mignard et al. (2006) in a 40 mm diameter OBR. In their work, the breakage of droplets is the dominant mechanism in the system, without any significant influence of the oil properties on the droplet size and distribution. The oscillatory velocity was shown to control the breakage, with the amplitude having a more significant effect than the frequency on the droplet breakage rate, corroborating earlier works (Mignard et al., 2004).

Suspension polymerization of methylmethacrylate (MMA) has also been used to characterise the liquid-liquid dispersion performance in OBRs (Ni et al., 1999, 1998b; Ni et al., 2001c). Ni et al. (1998b) studied the influence of surfactants, showing that higher concentrations of surfactants decrease the droplet size significantly and narrow the distribution. Two different formulations were analysed, one with relatively high amounts of surfactants (MMA (a)), and the other with the same amount of surfactant used in polymerisation tests (MMA (b)). The MMA (a) results in the smallest droplets, due to the

decrease in the interfacial tension with the increased amount of surfactant. For the MMA (a), the mean droplet size was controlled by the breakup and coalescence mechanisms, whilst for the MMA (b) was controlled by the breakup mechanism only. Ni et al. (1999) correlated the Sauter mean diameter (without reaction) with the mean particle size as $d_{v,0.5} = 3.11d_{32}$ (for $x_o = 4 - 8$ mm and $f = 3.5 - 7.5$ Hz), allowing the prediction of final particle sizes of polymer using only the droplet sizes. The frequency was found to have a more significant effect on the mean particle size than the amplitude, but both are equally important for the mean droplet size.

Many correlations for the prediction of mean droplet size can be found in the literature. The mean droplet size is usually presented as a power-law expression in terms of the oscillatory velocity ($x_o f$) or oscillatory Reynolds number and net Reynolds number for continuous operations. However, as the net flow does not have a significant effect on the size and distribution of droplets, d_{32} is usually expressed in terms of the oscillatory conditions only. Table 2.5 presents the correlations for mean droplet size in OBRs. Population balance models together with breakup and coalescence models have also been used to predict the droplet size distribution (Hounslow and Ni, 2004; Mignard et al., 2003). However, most of the correlations do not take into account the influence of fluid properties (interfacial tension, viscosity and density). Lobry et al. (2014, 2013) proposed correlations that used the Weber number, which represents the ratio between the inertial and interfacial forces.

Table 2.5: Mean droplet size correlations for oscillatory baffled reactors.

Geometry	Range of applicability	Correlation	Reference
Single orifice plate baffle $D = 50$ mm $\alpha = 0.19$ $l_b = 1.5D$	$1 \leq x_o \leq 15$ mm $1 \leq f \leq 10$ Hz $0.75 \leq P/V \leq 44$ W kg ⁻¹	$d_{32} = 0.996 \times 10^{-6} (x_o f)^{-1.2}$ (m) $d_{32} = 6.80 \times 10^{-5} (P/V)^{-0.4}$ (m)	(Ni et al., 1998b)
Single orifice plate baffle (pulsed baffles) $D = 50$ mm $\alpha = 0.23$ $l_b = 1.5D$	$10 \leq x_o \leq 50$ mm $1 \leq f \leq 5$ Hz $10 \leq P/V \leq 90$ W kg ⁻¹	$d_{32} = 2.8 \times 10^{-5} (x_o f)^{-0.96}$ (m) $d_{32} = 7.26 \times 10^{-4} (P/V)^{-0.32}$ (m)	(Ni et al., 2001c)
Continuous single orifice plate baffle $D = 40$ mm $\alpha = 0.21$ $l_b = 1.8D$	$0 \leq x_o \leq 60$ mm $0 \leq f \leq 5$ Hz $250 \leq Re_{net} \leq 1000$ $3.18 \leq P/V \leq 25$ W kg ⁻¹	$d_{32} = 1.72 \times 10^{-2} Re_o^{-0.91} Re_{net}^{-0.42}$ (m) $d_{32} = 3.7 \times 10^{-5} (P/V)^{-0.3} (P/V)_n^{-0.14}$ (m)	(Pereira and Ni, 2001)
Continuous disc and doughnut baffle $D = 50$ mm $\alpha = 0.25$ $l_b = 0.48D$	$24 \leq x_o \leq 52$ mm $1.17 \leq f \leq 1.56$ Hz $2600 \leq Re_o \leq 10\,200$ $2190 \leq Re_{net} \leq 2675$	$\frac{d_{32}}{D} = 5 Re_o^{-0.85} We_s^{-0.26}$	(Lobry et al., 2013)
Continuous smooth reduction baffle $D = 15$ mm $\alpha = 0.28$ $l_b = 1.7D$	$10 \leq x_o \leq 70$ mm $0.35 \leq f \leq 1.4$ Hz $800 \leq Re_o \leq 3200$ $180 \leq Re_{net} \leq 300$	$\frac{d_{32}}{D_h} = 2.99 Re_{oh}^{-0.89} We_h^{-0.08}$	(Lobry et al., 2014)

2.I.3.6.3. Liquid–Solid suspensions

Liquid–solid flows are important in crystallization and catalytic reactions, where the size and distribution of particles, as well as the suspension of the solids and kinetic rates are affected directly by the mixing behaviour of the solids in the fluid.

Mackley et al. (1993) used a vertical batch OBR to study the suspension and separation of solids. They demonstrated that the presence of oscillatory flow maintained the suspension of sedimenting particles. As the amplitude and/or frequency increase, a more uniform particle suspension is achieved in the OBR. Additionally, particle mixing was found to be very sensitive to the frequency and amplitude of oscillations, hence allowing good control of the required mixing state by fine-tuning these operating conditions. Particle separation of different sizes can also be carried out in the OBR due to the dependency of the particle distribution on the oscillation velocity, particle density and sedimentation velocity.

Reis et al. (2005) successfully suspended polymer resin particles in a 4.4 mm diameter smooth constriction meso-reactor in both vertical and near-horizontal arrangements. It was found that particles were easier to suspend at higher frequencies and lower amplitudes, with oscillation amplitude/baffle spacing ratios of 0.23. Ejim et al. (2017) studied the effect of baffle geometry and characteristics (d , α , l_b and baffle shape (sharp *versus* smooth edged)) of horizontal continuous baffled reactors ($D = 10$ mm) on the suspension of particles and axial dispersion. The solid flow pattern was characterized by the distribution of cumulative solid concentration and the axial dispersion coefficient. Particle suspension improved as the frequency and/or amplitude increased, and the smooth constriction design required the lowest minimal amplitude for the full suspension of particles, being up to 50% lower than that required with the sharp-edged baffles. This difference in performance could be due to the creation of dead zones around the sharp baffles. They also identified the dimensionless free baffle area, α , as the dominant design parameter in controlling solids backmixing and particle suspension. Small values of α minimised axial dispersion and increased the mean residence time of particles in the reactor. A difference between the experimental mean residence time of particles and the mean residence time of the liquid was observed; longer mean residence times for the solid were observed, implying that particles spent more time in the reactor than the liquid. This is explained by the presence of “dead zones” in the baffle region where particles can be trapped, requiring higher amplitudes values to fully suspend particles. Furthermore, solid dispersion was modelled by fitting a plug flow plus axial dispersion model to the experimental RTD results.

Kacker et al. (2017) investigated the RTD behaviour of heterogeneous (melamine–water) tracer systems in a 15 mm diameter single orifice baffled reactor. They reported that operating at low amplitudes was advantageous for obtaining plug flow behaviour. Optimal operating conditions for the suspension of melamine particles were found at higher frequencies and lower amplitudes, which is in agreement with the results of Reis et al. (2005). The mean residence time of the particles in the heterogeneous tracer system was longer compared with the homogeneous tracer, which is in agreement

with the study of Ejim et al. (2017). Kacker et al. (2017) reported an optimum velocity ratio, ψ , of 5 for the liquid–solid systems that is outside the range of the recommended velocity ratio to ensure plug flow between 2 and 4 (Stonestreet and Van Der Veeke, 1999). Optimal conditions to minimize axial dispersion were different for homogenous and heterogeneous systems, highlighting the importance of not translating results obtained in homogeneous systems to heterogeneous systems.

Solid flow patterns were analysed by Slavnić et al. (2019), who identified four flow regimes of solids: creeping solid flow, dense solid flow, dilute solid flow and solid washout. In the creeping solid flow, particles were moving very slowly, were not effectively suspended and could not be lifted up efficiently. In the dense solid flow, a considerable number of particles are transported in-between the baffles, but particles are still not uniformly dispersed in the tube. For the dilute solid flow regime, higher amounts of solids move from one inter-baffle compartment to the next in a nearly uniform suspension. Finally, in the solid washout flow regime, the oscillatory axial velocity dominates over the particle settling velocity and the solids are washed out of the reactor. An increase in the amplitude and/or frequency leads to a change in solid flow regime, as well as to a decrease in the axial dispersion of solids, the ratio of solids to liquid mean residence time and solids hold-up.

2.I.3.6.4. Gas–Liquid–Solid systems

Very limited studies of gas–liquid–solid systems in OBRs can be found in the literature. Pulsed baffled tube photochemical reactors have been used in three-phase heterogeneous catalysed photo-reactions, due to the good solid handling capacity of these reactors (Fabiya and Skelton, 2000, 1999). Navarro-Fuentes et al. (2019b, 2019a) carried out catalytic hydrogenation of alkynol to alkenol in an OBR and compared the results with a commercial STR. However, these studies focussed on the reaction rate, which makes it difficult to characterize the performance of multiphase systems in more global terms (e.g. mass transfer, particle suspension, etc.).

Ferreira et al. (2017) examined the influence of the solid phase on gas-liquid mass transfer, hold-up, mean bubble size and bubble distribution in a 16 mm diameter smooth constriction baffled reactor. The presence of solids did not have any significant influence on the Sauter mean diameter (d_{32}) or the mass transfer coefficient ($k_L a$) for all operating conditions tested in the study. However, in bubble columns and airlifts, the presence of solids has led to a decrease in $k_L a$ (Mena et al., 2005). Ferreira et al. (2017) tried to explain the lack of influence of the solid phase on $k_L a$ in their work. Indeed, the presence of solids decreases the bubble rise velocity and bubbles then become trapped in each inter baffle compartment, leading to an increase in the gas hold-up and specific interfacial area. This should lead in increased mass transfer. However, the authors postulate that the solids reduce the renewal rate of the liquid film at the bubble interface, thereby decreasing the liquid-side mass transfer coefficient, k_L and counter-balancing the possible increase in $k_L a$ from the increase in specific interfacial area. The

understanding of gas-liquid-solid systems is still challenging, and it is a promising area for different industrial applications, like multiphase bioreactors and catalytic reactions.

2.1.4. Scale-up

The main aim of scaling-up processes is to reproduce mixing and flow conditions, which are achievable at the laboratory scale, at pilot scale and industrial scale. Scaling-up is mainly done by maintaining geometrical or dynamic similarity. Geometrical similarity is achieved in OBRs by keeping the ratios l_b/D and α constant; fluid dynamic similarity is achieved by keeping Re_{net} , Re_o and St constant (Stonestreet and Harvey, 2002). Axial to radial velocity ratios (R_V) (Jian and Ni, 2005), RTD profiles (Ahmed et al., 2017), axial dispersion coefficient (Ni et al., 2001b; Oliva et al., 2018; Smith and Mackley, 2006), mass transfer coefficient (Ahmed et al., 2019; Ni and Gao, 1996a), among others, have been used to assess the impact of scale-up on process performance for different operating conditions.

Ni and Gao (1996a) studied the impact of scale on the mass transfer coefficient in two different vertical single orifice OBRs (50 mm and 100 mm diameter). The scale-up experiments were performed by increasing the column diameter and liquid column height. The gas flow rate was increased in proportion to the cross-sectional area of the reactor, ensuring a constant gas superficial velocity within reactors. The authors observed that, for a given power density, the mass transfer coefficient increased as a function of the increasing scale. This can be attributed to two aspects. Firstly, as both the diameter and the liquid column height were increased in the 100 mm OBR, the residence time of bubbles in the reactor is effectively increased. Secondly, although bubble sizes in the 100 mm diameter reactor were on average bigger than those in the 50 mm OBR, the ratio of the average bubble size to the diameter of the OBR was smaller for the former. This means either more bubbles or more interfacial area per cross-sectional area was created in the 100 mm diameter reactor. Jian and Ni (2005) concluded from their numerical study that the axial to radial velocity ratio (R_V) is independent of the tube diameter, suggesting a linear scale-up behaviour, reaching values of R_V equal to 2–2.5 for the 50 mm, 100 mm and 200 mm OBRs. Smith and Mackley (2006) measured the axial dispersion coefficient, D_{ax} , in three different single orifice OBR with diameters of 24 mm, 54 mm and 150 mm. The axial dispersion coefficient was determined by the imperfect pulse technique of an inert tracer and the dispersion model. The results showed that similar values of D_{ax} are obtained when dynamic parameters (Re_{net} , Re_o and St) are kept constant in the three OBRs sizes.

In recent work, Ahmed et al. (2019) studied the effect of scale-up on the mass transfer coefficient in the multi-orifice baffled reactor for three different diameters: 10 mm, 50 mm and 100 mm. Geometrical parameters (l_b , α , d) were kept constants in all reactors. An increase in the oscillation velocity and aeration rate led to an increase in $k_L a$ for all three reactors, with maximum enhancement increasing from $Re_o = 410$ to 2461 (at 0.1 vvm), up to 5-fold, 4-fold and 3.5-fold for the 100 mm, 50 mm and 10 mm diameter reactors, respectively.

Various scale-up correlations have been established for predicting different performance criteria in OBRs, depending on the system, e.g. mass transfer coefficients in gas-liquid systems and axial diffusion coefficient to assess plug flow. Table 2.6 summarises the correlations, which are in function of geometrical parameters and operating conditions, found in the literature.

Despite the scant existing information about scale-up of OBRs, and that scale-up is a determining step for the success of industrial production, OBRs have proven to intensify processes by reducing the scale of the reactor and maintained equivalent conversion rate of STRs. OBRs also allow continuous production at industrial scale with relatively small reactor volumes (Cruz et al., 2016; Mazubert et al., 2015, 2014; Phan et al., 2012). New trends in OBRs focus on miniaturized reactors that will reduce operating costs and waste production.

Table 2.6: Scale-up correlations forms found the literature.

Reactor / System	Correlation form	Reference
Single baffle orifice OBR / Gas-liquid	$k_L a = f\left(\frac{P}{V}, u_g\right)$	(Ni and Gao, 1996a)
Single baffle orifice OBR / Single phase	$D_{ax} = f(D_h, \varepsilon)$	(Ni et al., 2001b)
Single baffle orifice OBR / Single phase	$D_{ax} = f(Re_{net}, Re_o, St)$	(Smith and Mackley, 2006)
Meso-helical baffle OBR / Single phase	$N = f(Re_{net}, \psi, St)$	(Ahmed et al., 2017)
Single baffle orifice OBR / Gas-liquid	$Sh = f\left(\frac{nd}{D}, Re'_o, Re_G\right)$	(Ahmed et al., 2019)

2.1.5. Applications and industrial processes

As a result of the advantages offered by the OBRs (e.g. controlled mixing, which is independent of the bulk flow and allows effective mixing with longer residence times, as well as enhanced multi-phase mixing, heat and mass transfer), this kind of reactor has been applied in several industrial sectors, including the polymers industry, biofuels production, chemical industry, pharmaceutical industry and bioprocesses. Table 2.7 summarizes some examples available in the literature of reactions and processes carried out in OBRs.

Most of the OBRs used for industrial process are manufactured in borosilicate glass and 316L stainless steel and can handle process conditions between -20 and 200 °C and below 25 bar², with jacket pressures of $0 - 1$ bar. Commercial OBRs have different lengths, typically ranging from 1 m to 20 m long. Stonestreet and Harvey (2002) studied different cases to illustrate the mixing design for OBRs, based on lab-scale studies. For the same production rate (2.3 tonnes/hr), smaller length-to-diameter

² <https://www.nitechsolutions.co.uk/products/> (accessed March 11, 2020)

designs with lower power density requirements are obtained for the OBR compared with a tubular reactor. Figure 2.11 shows the capabilities of the reduced length-to-diameter ratio tube of OBRs.

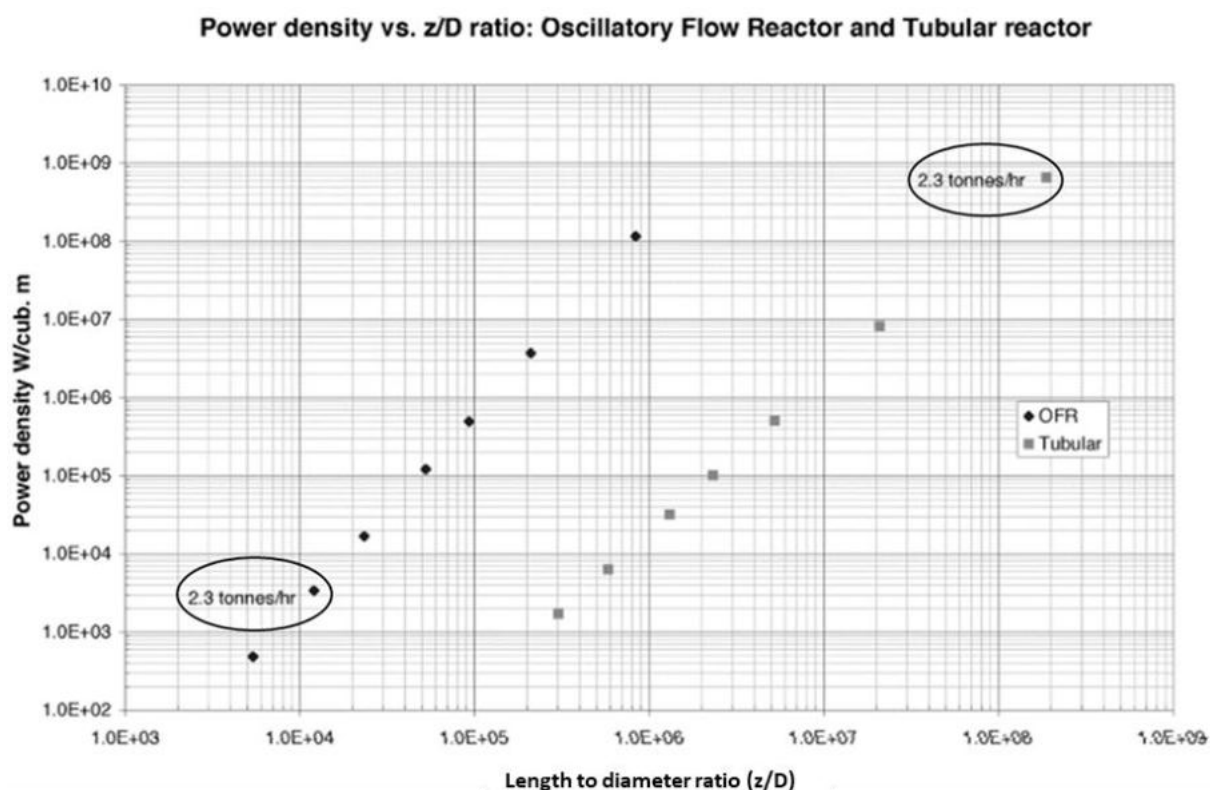


Figure 2.11: Comparison of power density and length to diameter ratio behaviour for OBRs and turbulent flow reactor (Stonestreet and Harvey, 2002).

OBRs have been widely used for crystallization processes, in both batch and continuous modes, particularly for cooling and anti-solvent crystallization, due to the good control of mixing and temperature (Ni and Liao, 2008), and for the intensive mixing between the solvent and antisolvent (Brown and Ni, 2011). The increase of mixing intensity in OBR crystallizers has been demonstrated to lead to high purity crystals (Caldeira and Ni, 2009; McLachlan and Ni, 2016; Zhao et al., 2014), smaller crystals, narrow crystal size distributions (Cruz et al., 2016; Peña et al., 2017; Siddique et al., 2015), and good crystal suspension (Brown et al., 2015) when compared with STRs. In continuous operation, the presence of the net flow decreases the nucleation induction time due to an increase in the average shear rate (Yang et al., 2015). OBR crystallizers are, nevertheless, are less well suited to evaporative and fast reactive crystallizations.

Production of bio-sourced fuels is a field in which interest has been increasing over recent years. Biodiesel, biobutanol and bioethanol have successfully been produced in OBRs (Hamzah et al., 2012; Ikwebe and Harvey, 2011; Masngut and Harvey, 2012; Phan et al., 2012). Biodiesel production is a slow liquid-liquid mass transfer limited reaction and the OBR provides good mass transfer and long residence times in compact geometries, which are adapted to such reactions. These OBRs characteristics are also

advantageous in biobutanol and bioethanol production, which are produced principally by the fermentative action of microorganisms. OBRs offer low-shear, good mixing quality and compact designs to ensure uniform nutrient supplies for the microorganisms and reduced fermentation times. Harvey et al. (2003) demonstrated the feasibility of transesterification of rapeseed oil to biodiesel using a single orifice OBR and achieved shorter residence times than STRs with a suitable conversion rate, which satisfies the German standard for biodiesel (DIN 51606). Phan et al. (2012) used different meso-OBR designs for the transesterification of rapeseed oil. The smooth constriction geometry produced the highest FAME content (82%), compared with the wire wool baffle and the sharp edge helical with central rod baffle (74 – 76%). The smooth constriction baffle reached a steady state in shorter times (1.5 residence times) compared with the other two geometries, which required 2 residence times, thereby allowing stable conversion rates in shorter times and better process performance. Mazubert et al., (2014) reached the reaction equilibrium of the transesterification of waste cooking oil at low temperatures (< 40°C) in a glass OBR without operating under pressure, achieving better performance than the batch reactor, due to the effective mixing generated by flow oscillations. Takriff et al. (2009) studied the feasibility of biobutanol production using a single orifice OBR consisting of a horizontally oriented U-shaped stainless-steel tube of inner diameter of 52.2 mm. The authors demonstrated a biobutanol production increase from 0.84 to 1.59 g/L by increasing the oscillation frequency from 0.45 Hz to 0.75 Hz. Ikwebe and Harvey (2011) also used a single orifice OBR in the simultaneous saccharification and fermentation of cellulose to produce ethanol. They reported an increase of 9% in ethanol production after 48h in a 24 mm diameter OBR compared with 70h in shake flask.

One of the most important problems associated with the operation of OBR is fouling, especially occurring in crystallizations, polymerizations and bioprocesses. Fouling can disrupt mixing quality, hinder heat and mass transfer, lead to excessive pressure drop and even prevent measurements. Fouling depends on the application and the nature of the material of the baffles and internals; metal surfaces are more susceptible to fouling than glass surfaces. Cleaning processes are also difficult and should minimize the cross contamination in reactors that are used for manufacturing different products. Caldeira and Ni (2009) studied a cleaning protocol in a 15 mm diameter OBR with smooth constrictions, in the production of vanilic sodium and aspirin. In this procedure, fresh cleaning solutions are fed continuously to the reactor in three waves (tap water, industrial cleaning solution and USP water, one immediately after the next), and then drained. Under the same oscillatory conditions for both cases ($f = 2$ Hz and $x_o = 40$ mm), the OBR was clean even before the cleaning procedure had been completed, with a total water usage of 11 L (for a 2 L OBR), and maximum residual level of vanilic sodium and aspirin below the industry norms. The time used for each cleaning processes is significantly smaller than the total operation time, with an operation time to cleaning time ratio for vanilic sodium and aspirin of 363 and 531, respectively.

Recently, the biotechnology company Genzyme (now Sanofi) have improved their new API production via a three-phase reaction on the scale of multi-hundred tons using oscillatory baffled

reactors provided by the company NiTech® Solutions, for a process certified by the FDA. The reaction is 40 times faster than the batch process, with higher quality, reduced maintenance and continuous monitor and control throughput, leading to a zero rejection rate for the reaction step³. Whilst information about the physical phenomena and the specific reasons for the improved performance in the NiTech® OBR is not detailed in the report, it is expected that the enhanced performance is due to improved mass transfer in the three-phase system.

In recent years, many companies have started to incorporate the oscillatory baffled reactor technology from NiTech® Solutions in their processes. Corning Incorporated demonstrated continuous flow chemical manufacturing that integrates the Corning® Advanced-Flow™ reactor and the NiTech® continuous crystallizer with Alconbury Weston Limited continuous filtration equipment⁴. Croda Europe, along with NiTech® Solutions, the Centre for Process Innovation (CPI) and the University of Cambridge's Institute for Manufacturing have been working on a collaborative project to develop novel methods for continuous production of surfactants⁵. The goal of this project is to reduce operational and capital costs, increase process sustainability and maintain product quality while delivering new manufacturing processes of existing products. SAS PIVERT, an industrial group specialized in agricultural, chemical, and food & feed sectors, has recently acquired a NiTech® COBR DN15 crystalliser/reactor unit to industrialise chemical products and energy from oilseed biomass⁶.

The Centre of Excellence for Anaerobic Digestion at the University of South Wales (USW) has been evaluating the feasibility and efficiency of C1 gas bio-conversion (methane) for energy production and storage using a Nitech® OBR DN60 crystalliser/reactor and comparing it with CSTRs and Liquid Recirculation Reactors (LRR). Methane is synthesised using a patented microbe culture from waste carbon dioxide reacted with hydrogen. Under standardised conditions, the OBR achieved the highest conversion efficiency with 75%, the CSTR 66% and the LLR was ruled out due to insufficient gas flow⁷. The hydrogenation capabilities of the OBR can also be applied in the food industry, especially for processing vegetable oils, where hydrogen changes liquid vegetable oil to a semi-solid or solid fat, and stabilises the oil, thereby preventing its oxidation. In summary, all these practical cases demonstrate that OBR technology is industry-ready.

³ <https://www.nitecholutions.co.uk/wp-content/uploads/2014/03/HW-case-study-Nov13.pdf> (accessed February 17, 2020)

⁴ <https://www.nitecholutions.co.uk/wp-content/uploads/2015/07/Corning-press-release-Jun15-final.pdf> (accessed March 11, 2020)

⁵ <https://www.nitecholutions.co.uk/wp-content/uploads/2016/02/Newsletter-Feb16.pdf> (accessed March 11, 2020)

⁶ <https://www.nitecholutions.co.uk/nitech-units-to-be-used-in-biotech-research> (accessed March 11, 2020)

⁷ <https://www.nitecholutions.co.uk/market-sectors/biotechnology/university-of-south-wales-case-study/> (accessed March 11, 2020)

Table 2.7: Examples of OBR applications

Reaction / Process	References
Acetylation	(Zheng et al., 2018)
Protein refolding	(Lee et al., 2002, 2001)
Hydrogenation	(Navarro-Fuentes et al., 2019a, 2019b)
Fermentation	(Yussof et al., 2018)
Flocculation	(Gao et al., 1998; Ni et al., 2001a)
Enzymatic reactions	(Abbott et al., 2014b; Ikwebe and Harvey, 2015)
Polymerisation	(Lobry et al., 2014; Ni et al., 1999; Ni et al., 2001c)
Transesterification	(Al-Saadi et al., 2019; Koh et al., 2014; Mazubert et al., 2014, 2013; Soufi et al., 2017)
Solid acid catalysed esterification	(Eze et al., 2017, 2013)
Microalgae culture	(Abbott et al., 2015)
Flotation	(Anderson et al., 2009)
Hydrate formation	(Brown and Ni, 2010)
Synthesis of metal-organic frameworks	(Laybourn et al., 2019)
Photo-oxidation	(Fabiya and Skelton, 1999; Gao et al., 2003)
Ozonation	(Lucas et al., 2016)
Mitigation and wax deposition	(Ismail et al., 2006)
Saponification	(Harvey et al., 2001)
Biofuel production	(Harvey et al., 2003; Kefas et al., 2019; Masngut et al., 2010)
Oil droplet breakage	(Mignard et al., 2006, 2004)
Crystallization / Precipitation	(Briggs et al., 2015; Brown et al., 2015; Castro et al., 2013; Kacker et al., 2017; McLachlan and Ni, 2016; Siddique et al., 2015)
Cross flow filtration	(Horie et al., 2018)

2.I.6. Limitations of recommended operating conditions

The oscillatory baffled reactor, in batch and continuous operation, has already proven to enhance mixing (in single and multiphase systems), mass and heat transfer, as well as use less energy than conventional reactors, like STRs. They have been applied in many different industrial applications, due to the control of mixing intensity being independent of net flow, allowing good mixing quality and long residence times in continuous operation. In the literature, a number of ‘optimal’ operating conditions have been proposed, most of them based on the mixing performance and the plug flow behaviour of the reactor. However, most of these guidelines have been established via qualitative visual experiments in single-phase systems (water or similar), which present some problems and limitations when they are extrapolated to industrial applications, particularly in multiphase systems. Industrial processes have many more variables other than the oscillatory conditions to be adjusted, each one having a different influence over the reaction yield and/or the quality of the final product.

For single orifice OBRs, Stonestreet and Harvey (2002) recommended a minimum net Reynolds number of 50 to achieve convection and obtain ‘optimal’ mixing conditions. Further, Stonestreet and Van Der Veeken (1999) showed that for systems where $Re_{net} > 250$, the influence of the oscillatory flow becomes disadvantageous in single orifice OBRs. The characteristic flow pattern created by

oscillations is overridden thereby decreasing the mixing efficiency, and as the net flow increases, shorter residence times are obtained, which will translate into longer reactors to achieve sufficient reaction conversion. However, in some cases, these limits may not be practical for all applications. For low viscosity liquids (like water), low net flows will be needed to achieve $Re_{net} = 50$. Nevertheless, higher liquid viscosity, which is very common in industrial practice, will require higher net flows, probably reaching excessive flow rates and pressure drops for industrial installations. Processes where the viscosity increases as the reaction progress (like some polymerisations) may not be so limited by these guidelines, however, this may be one of the most challenging situations since different flow and reactor designs may be required during the process. Hence, depending on the fluids used, the application and the process objectives, the recommended values of Re_{net} may vary. An adjustment in the reactor diameter can be a solution to get the right Re_{net} when working with viscous fluids and an increase in the flow rate is not practical; however, in some cases, this kind of modifications cannot always be made and could require an additional reactor. An analysis between operating and capital expenses therefore has to be done to choose the most adapted solution. Howes et al. (1991) defined that the flow separation (when the boundary layer of the fluid flow detaches from the wall and forms eddies and vortices) takes place in OBRs when $Re_o > 50$, and it has been recommended to work above this value since then. However, flow separation has been shown to take place at even lower values of net Reynolds number in a 5 mm diameter OBR with smooth constrictions (Reis et al., 2005), and different 15 mm diameter OBR designs (Mazubert et al., 2016a).

The most common range of the Strouhal number used in the literature is $0.15 < St < 4$ (Abbott et al., 2013), as higher values of St promote the propagation of the eddies into the next baffle (Ahmed et al., 2017). However, this common range may not necessarily be the best operating range for all processes, e.g. Mazubert et al. (2014) observed a decrease in the conversion of waste cooking oil into methyl esters for $St > 0.1$.

The recommended range of the oscillatory to net velocity ratio, ψ , to ensure plug flow operation is between 2 and 4 (Stonestreet and Van Der Veeken, 1999). However, these recommendations are not always used in practice. For example, many continuous crystallization processes in oscillatory baffled reactors have been operated with velocity ratios near the upper limit of the recommended range, or even at much higher values ($\psi = 82$ is the maximum value found in the literature), to ensure solid suspension and uniform particle size and distribution, but non perfect plug flow (Agnew et al., 2017; Briggs et al., 2015; Jiang and Ni, 2019; Peña et al., 2017; Zhao et al., 2014). Kacker et al. (2017) studied the RTD of liquid-liquid and liquid-solid systems and reported an optimum velocity ratio outside the range of 2–4 reported in the literature. This shows that the use of a recommended value of ψ alone cannot guarantee effective mixing or process performance.

Biodiesel production has also been carried out with higher ψ ($\psi = 519$ is the maximum value found in the literature), to ensure good liquid-liquid dispersion (Al-Saadi et al., 2019; Mazubert et al., 2015; Phan et al., 2012). Indeed, in liquid-liquid dispersions and reactions, the operating conditions may be

chosen to ensure small droplets sizes, good droplet size distribution and long residence time, rather than to favour plug flow. Lobry et al. (2014) obtained smaller droplet sizes in the vinyl acetate suspension polymerization when operating with ψ values of 12 and 16, which are significantly greater than the recommended velocity ratio range. In some cases, the operating conditions do not follow the recommended range due to size restrictions of the reactor (Harvey et al., 2003), as often occurs in industry.

Recent studies on heat transfer and power dissipation have also been carried out with values of Re_{net} and ψ outside the suggested ranges. Even if it may not be of interest to all applications, it allows a global analysis over a range of flow regimes, than can be used for reactor design (Ahmed et al., 2018a; Law et al., 2018; McDonough et al., 2016).

From the above, it appears that the recommended and ‘optimal’ operating conditions may depend on the process objective and the relevant parameters used to characterize the process performance. In some cases, when operating conditions present opposing effects on the reactor performance, a compromise may need to be established in order to obtain the best solution possible, based on the limiting phenomenon or the product-controlling phenomenon in the process. Some examples of conflicting operating conditions can be found in the literature. Fabiyi and Skelton (1999) performed a photocatalysed mineralization of methylene blue in a pulsed baffled tube. The mass transfer (adsorption) enhanced with the increase of the mixing intensity (i.e. increase in the oscillatory conditions). However, the reaction rate did not improve with this increase in mass transfer. This was due to the fact that an increase in the oscillatory Reynolds number increased the apparent scattering centres (particles that absorb light energy and re-emit it in different directions with different intensities) within the reactor since the uniformity of particle concentration was modified. An increase in the particle concentration at constant concentration of the absorbing species produces an increase in the optical thickness and an increase in the scattering albedo (ratio of scattering efficiency to total extinction efficiency), thereby leading to a decrease in the average reaction rate with respect to the case with no scattering.

Slavnić et al. (2019) demonstrated that the operating conditions could have opposite effects in the desired goal of liquid-solid suspensions. They found that solids holdup increased with increasing solids concentration in the inlet suspension. Therefore, for high solids hold-up, the solid concentration of the inlet should be high too. However, when the concentration of solids in the inlet suspension are higher, the solids moved more rapidly through the reactor, decreasing the residence time of solids. With increasing inlet solids concentration, hindered settling becomes more pronounced, resulting in a decrease of the settling velocity and in faster movement of the particles along the reactor. If longer residence time of the solid is needed, lower frequency and/or amplitude should be applied, but this may not ensure a good particle suspension and increase the dispersion of the solids. Higher amplitudes suspends particles more effectively, and higher frequencies ensure that they stay suspended. On the other hand, lower amplitudes do not carry enough energy for effective suspension, and lower frequencies allow particles more time to settle. Therefore, using higher frequencies and amplitudes leads to lower

solid axial dispersion. A compromise should be found depending on the specific objectives of the application.

2.I.7. Summary and conclusions

This state of art presents an update and review of the oscillatory baffled reactor technology, for both, batch and continuous operations. The key geometrical parameters and dimensionless groups in the design of the reactor, and the most commonly used ranges of operating parameters in the literature were presented, along with the different geometries used. These geometries are easily adopted for different applications by only adjusting the operating conditions depending on the final process objective.

Performance studies carried out to characterize OBRs depending on the application and the process type were highlighted. OBR technology has proven to enhance mixing, heat and mass transfer, as well as gas-liquid and liquid-liquid dispersion and solid suspensions. Due to this, OBRs have been used in many single phase and multiphase applications, like polymers, biofuels, chemical reactions, pharmaceutical and bioprocesses. More recent studies have demonstrated that OBRs can achieve good gas-liquid mass transfer with the presence of a solid catalyst, extending the industrial applications where oscillatory baffled reactor can be implemented, like multiphase bioreactors and catalytic reactions. Despite all this, the implementation of OBRs is still challenging for some applications, such as fast reactive crystallization, processes employing highly viscous fluids and solid suspension with high particle concentration. This is due to some geometrical restrictions of the reactor, as well as the lack of studies and understanding of the associated phenomena within the OBR.

An important aspect of the recommended and optimal operating conditions widely used in the literature was discussed. Many characterization studies limit their operating conditions to achieve and keep plug flow along the reactor. However, parameters other than plug flow behaviour (like conversion rate, dispersion, macromixing, micromixing, particle size and distribution, etc.) may be a priority depending on the process objectives. The choice of the most convenient method to characterize OBR performance, along with the optimal operating parameters, will indeed depend on the nature and final goal of the process.

Part II: Context and general objectives

Whilst it has been shown in the literature that RTD measurements are a good means to characterize mixing in OBRs for operations that require long residence times (e.g. crystallisation and polymerisation), plug flow and RTD may not necessarily be the only performance characteristics that should be taken into consideration when operating conditions are chosen for this type of reactor. Indeed, depending on the process objective, other characteristics may be important for quantifying mixing, such as the spatial homogeneity of a minor species or a second phase (e.g. solid suspension), or even micromixing and how fast the fluids are mixed (Kukukova et al., 2009). Applications with fast reactions or precipitations, begin as soon as two (or more) reagents are in contact; consequently, the conversion of the chemical reaction and/or the quality of the product is greatly influenced by how fast the reagents are put into contact and mixed. Effects of parameters like the inlet position, inlet velocity, injection time, reagent flow rate, etc. are hence important parameters in the design of efficient reactors for fast/instantaneous reactions.

Batch and semi-batch reactors are widely used for applications with fast chemical reactions and have been studied in detail for a long time (Assirelli et al., 2005; Baldyga and Bourne, 1990, 1989; Duan et al., 2016; Guichardon et al., 2000; Villermaux and Falk, 1994). Fast chemical reactions and precipitations are also performed in continuous flow equipment and a number of different equipment types for this purpose have been studied in the literature. These continuous flow equipment include mixing in pipelines (Bałdyga and Orciuch, 2001), static mixers (Baldyga et al., 1997; Bourne and Maire, 1991; Taylor et al., 2005), centrifugal pumps (Bolzern and Bourne, 1985), rotor-stator mixers (Bourne and Garcia-Rosas, 1986), impinging thin liquid sheets (Demyanovich and Bourne, 1989), reaction injection moulding (RIM) (Lee et al., 1980; Santos et al., 2009), confined impinging jets (Johnson and Prud'homme, 2003), T-jet mixers (Krupa et al., 2014), rotating packed beds (Wenzel and Górak, 2018), and micromixers (Commenge and Falk, 2011; Falk and Commenge, 2010; Su et al., 2011).

Generally, the fastest and most immediate mixing of feeds with the bulk fluid occurs when the feed is introduced into the region where turbulence intensity is highest and/or where local mixing time (or micromixing time) constants are short (Paul et al., 2004a). In laminar flows, fast micromixing can be achieved by a very rapid decrease in the characteristic length scales for diffusion, for example in micromixers (Falk and Commenge, 2010). However, this rapid decrease in length scales is not always easy in larger equipment and mixing performance strongly depends on the position of the feed. In laminar flow pipeline reactors operating with high viscosity liquids, the reagents have to be injected in such a way that they are prevented from flowing along the pipe wall where little or no mixing with the bulk stream occurs (Forney et al., 1996). The influence of the injection position in static mixers in laminar flow has been studied by Hobbs and Muzzio (1997) who showed that the feed injection position strongly influences the quality of mixing. Depending on the mixer type, the feed injection position can

impact mixing lengths by several equivalent tube diameters. In laminar flow static mixers, a coaxial centreline injection at the edge of a mixer element is usually recommended (Hobbs and Muzzio, 1997; Paul et al., 2004b; Zalc et al., 2003). The injection at the tube centreline splits the injected stream equally by the first mixer blades in the upper and lower halves, allowing good quality mixing to be obtained after few mixer elements. An off-centre injection has been shown to exhibit channelling behaviour and significant mixing only begins further downstream (Zalc et al., 2002, 2003).

General objective

Considering the current information on mixing in OBRs available in the literature, there is little knowledge on the effect of operating parameters on spatial mixing quality and micromixing, as well as how a secondary feed should be injected into the OBR to achieve good mixing performance. Indeed, improved mixing performance would typically lead to enhanced process performance, however it could also lead to more compact reactor designs and provide opportunities for new applications (other than reactions with slow kinetics), e.g. precipitation/crystallization processes that require long residence times to allow particle or crystal growth, but also fast mixing in the first stage of the reactor to induced crystal nucleation. OBRs are most often used in applications where the kinetics are slow.

The focus of this thesis is to study the macro and micromixing performance of COBRs of a secondary component in the bulk flow and how it should be introduced into the OBR, with an ultimate goal of providing guidelines and OBR designs that can be employed for a wider range of applications involving varied characteristic process times. In order to achieve this, the effect of the position of secondary feeds, the influence of the oscillatory conditions and power dissipation over the macro and micromixing performance is studied, using numerical simulations and experiments carried out in a commercial Nitech® OBR with smooth constrictions.

Thesis structure

The remainder of this thesis is structured as follows:

In Chapter 3, the governing equations and the description of the numerical modelling approaches (schemes and algorithms) used are presented, including the solvers and discretization methods for the two different Computational Dynamics Fluids (CFD) software packages used in this work, ANSYS CFX 18.2 and ANSYS Fluent 2019R3.

Chapter 4 presents the results of the CFD simulations carried out to evaluate the power density in a COBR with single orifice baffles for different operating conditions in laminar flow. The power dissipation is calculated using two different approaches – via viscous energy dissipation and using a mechanical energy balance.

In Chapter 5, a passive non-reactive tracer released in the COBR at three theoretical source locations is simulated using CFD. The impact of the source positions and the impact of different net and oscillatory flows conditions on the mixing quality is evaluated by analysing the spatial uniformity using the areal distribution method.

Chapter 6 centres on the characterization of micro and macromixing in the COBR with experimental techniques. Micromixing is studied using the Villermaux-Dushman iodide-iodate test reactions and the estimation of micromixing times through the incorporation model. The influence of the oscillation flow and the volumetric flow rate ratio on the micromixing quality are investigated. Macromixing performance is explored via a visual analysis of a passive tracer.

Finally, Chapter 7 presents the conclusion and summary of the results arising from this study, and some recommendations for future work are given.

References

- Abbott, M.S.R., Brain, C.M., Harvey, A.P., Morrison, M.I., Valente Perez, G., 2015. Liquid culture of microalgae in a photobioreactor (PBR) based on oscillatory baffled reactor (OBR) technology – A feasibility study. *Chem. Eng. Sci.* 138, 315–323. <https://doi.org/10.1016/j.ces.2015.07.045>
- Abbott, M.S.R., Harvey, A.P., Morrison, M.I., 2014a. Rapid determination of the Residence time distribution (RTD) function in an oscillatory baffled reactor (OBR) using a design of experiments (DoE) approach. *Int. J. Chem. React. Eng.* 12, 575–586. <https://doi.org/10.1515/ijcre-2014-0040>
- Abbott, M.S.R., Harvey, A.P., Valente Perez, G., Theodorou, M.K., 2013. Biological processing in oscillatory baffled reactors: Operation, advantages and potential. *Interface Focus*. <https://doi.org/10.1098/rsfs.2012.0036>
- Abbott, M.S.R., Valente Perez, G., Harvey, A.P., Theodorou, M.K., 2014b. Reduced power consumption compared to a traditional stirred tank reactor (STR) for enzymatic saccharification of alpha-cellulose using oscillatory baffled reactor (OBR) technology. *Chem. Eng. Res. Des.* 92, 1969–1975. <https://doi.org/10.1016/j.cherd.2014.01.020>
- Agnew, L.R., McGlone, T., Wheatcroft, H.P., Robertson, A., Parsons, A.R., Wilson, C.C., 2017. Continuous crystallization of paracetamol (acetaminophen) form II: selective access to a metastable solid form. *Cryst. Growth Des.* 17, 2418–2427. <https://doi.org/10.1021/acs.cgd.6b01831>
- Ahmed, S.M.R., Law, R., Phan, A.N., Harvey, A.P., 2018a. Thermal performance of meso-scale oscillatory baffled reactors. *Chem. Eng. Process. - Process Intensif.* 132, 25–33. <https://doi.org/10.1016/j.cep.2018.08.009>
- Ahmed, S.M.R., Phan, A.N., Harvey, A.P., 2019. Scale-Up of Gas-Liquid Mass Transfer in Oscillatory Multiorifice Baffled Reactors (OMBRs). *Ind. Eng. Chem. Res.* 58, 5929–5935. <https://doi.org/10.1021/acs.iecr.8b04883>
- Ahmed, S.M.R., Phan, A.N., Harvey, A.P., 2018b. Mass transfer enhancement as a function of oscillatory baffled reactor design. *Chem. Eng. Process. - Process Intensif.* 130, 229–239. <https://doi.org/10.1016/j.cep.2018.06.016>
- Ahmed, S.M.R., Phan, A.N., Harvey, A.P., 2017. Scale-up of oscillatory helical baffled reactors based on residence time distribution. *Chem. Eng. Technol.* 40, 907–914. <https://doi.org/10.1002/ceat.201600480>
- Akmal, M., Rahim, A., Harvey, A.P., 2020. Intensification of epoxidation of vegetable oils using a continuous mesoscale oscillatory baffled reactor. *J. Adv. Manuf. Process.* 1–12. <https://doi.org/10.1002/amp2.10041>
- Al-Abduly, A., Christensen, P., Harvey, A., Zahng, K., 2014. Characterization and optimization of an oscillatory baffled reactor (OBR) for ozone-water mass transfer. *Chem. Eng. Process. Process Intensif.* 84, 82–89. <https://doi.org/10.1016/j.cep.2014.03.015>

- Al-Saadi, L.S., Alegría, A., Eze, V.C., Harvey, A.P., 2019. Rapid Screening of an Acid-Catalyzed Triglyceride Transesterification in a Mesoscale Reactor. *Chem. Eng. Technol.* 539–548. <https://doi.org/10.1002/ceat.201800203>
- Al Khani, S.D., Gourdon, C., Casamatta, G., 1988. Simulation of hydrodynamics and mass transfer of a disks and rings pulsed column. *Ind. Eng. Chem. Res.* 27, 329–333. <https://doi.org/10.1021/ie00074a020>
- Amokrane, A., Charton, S., Lamadie, F., Paisant, J.F., Puel, F., 2014. Single-phase flow in a pulsed column: particle image velocimetry validation of a CFD based model. *Chem. Eng. Sci.* 114, 40–50. <https://doi.org/10.1016/j.ces.2014.04.003>
- Anderson, C.J., Harris, M.C., Deglon, D.A., 2009. Flotation in a novel oscillatory baffled column. *Miner. Eng.* 22, 1079–1087. <https://doi.org/10.1016/j.mineng.2009.04.007>
- Angelov, G., Gourdon, C., 2012. Pressure drop in pulsed extraction columns with internals of discs and doughnuts. *Chem. Eng. Res. Des.* 90, 877–883. <https://doi.org/10.1016/j.cherd.2011.10.011>
- Angelov, G., Journe, E., Line, A., Gourdon, C., 1990. Simulation of the flow patterns in a disc and doughnut column. *Chem. Eng. J.* 45, 87–97. [https://doi.org/10.1016/0300-9467\(90\)80031-7](https://doi.org/10.1016/0300-9467(90)80031-7)
- Assirelli, M., Bujalski, W., Eaglesham, A., Nienow, A.W., 2005. Intensifying micromixing in a semi-batch reactor using a Rushton turbine. *Chem. Eng. Sci.* 60, 2333–2339. <https://doi.org/10.1016/j.ces.2004.10.041>
- Baird, M.H.I., Garstang, J.H., 1972. Gas absorption in a pulsed bubble column. *Chem. Eng. Sci.* 27, 823–833. [https://doi.org/10.1016/0009-2509\(72\)85016-4](https://doi.org/10.1016/0009-2509(72)85016-4)
- Baird, M.H.I., Stonestreet, P., 1995. Energy dissipation in oscillatory flow within a baffled tube. *Trans IChemE* 73(A), 503–511.
- Baldyga, J., Bourne, J.R., 1990. The effect of micromixing on parallel reactions. *Chem. Eng. Sci.* 45, 907–916. [https://doi.org/10.1016/0009-2509\(90\)85013-4](https://doi.org/10.1016/0009-2509(90)85013-4)
- Baldyga, J., Bourne, J.R., 1989. Simplification of Micromixing Calculations. I. Derivation and Application of New Model. *Chem. Eng. J.* 42, 83–92.
- Baldyga, J., Bourne, J.R., Hearn, S.J., 1997. Interaction between chemical reactions and mixing on various scales. *Chem. Eng. Sci.* 52, 457–466. [https://doi.org/10.1016/S0009-2509\(96\)00430-7](https://doi.org/10.1016/S0009-2509(96)00430-7)
- Baldyga, J., Orciuch, W., 2001. Barium sulphate precipitation in a pipe - An experimental study and CFD modelling. *Chem. Eng. Sci.* 56, 2435–2444. [https://doi.org/10.1016/S0009-2509\(00\)00449-8](https://doi.org/10.1016/S0009-2509(00)00449-8)
- Baldyga, J., Pohorecki, R., 1995. Turbulent micromixing in Chemical Reactors - a Review. *Chem. Eng. J.* 58, 183–195. [https://doi.org/10.1016/0923-0467\(95\)02982-6](https://doi.org/10.1016/0923-0467(95)02982-6)
- Bolzern, O., Bourne, J.R., 1985. Rapid chemical reactions in a centrifugal pump. *Chem. Eng. Res. Des.* 63, 275–282.
- Bourne, J.R., Garcia-Rosas, J., 1986. Rotor–stator mixers for rapid micromixing. *Chem. Eng. Res. Des.* 64, 11–17.

- Bourne, J.R., Maire, H., 1991. Micromixing and fast chemical reactions in static mixers. *Chem. Eng. Process.* 30, 23–30. [https://doi.org/10.1016/0255-2701\(91\)80005-A](https://doi.org/10.1016/0255-2701(91)80005-A)
- Briggs, N.E.B., Schacht, U., Raval, V., McGlone, T., Sefcik, J., Florence, A.J., 2015. Seeded crystallization of β -L-glutamic acid in a continuous oscillatory baffled crystallizer. *Org. Process Res. Dev.* 19, 1903–1911. <https://doi.org/10.1021/acs.oprd.5b00206>
- Brown, C.J., Adelakun, J.A., Ni, X., 2015. Characterization and modelling of antisolvent crystallization of salicylic acid in a continuous oscillatory baffled crystallizer. *Chem. Eng. Process. Process Intensif.* 97, 180–186. <https://doi.org/10.1016/j.cep.2015.04.012>
- Brown, C.J., Ni, X., 2011. Evaluation of growth kinetics of antisolvent crystallization of paracetamol in an oscillatory baffled crystallizer utilizing video imaging. *Cryst. Growth Des.* 11, 3994–4000. <https://doi.org/10.1021/cg200560b>
- Brown, C.J., Ni, X., 2010. Evaluation of rate of cyclopentane hydrate formation in an oscillatory baffled column using laser induced fluorescence and energy balance. *Chem. Eng. J.* 157, 131–139. <https://doi.org/10.1016/j.cej.2009.11.019>
- Brunold, C.R., Hunns, J.C.B., Mackley, M.R., Thompson, J.W., 1989. Experimental observations on flow patterns and energy losses for oscillatory flow in ducts containing sharp edges. *Chem. Eng. Sci.* 44, 1227–1244. [https://doi.org/10.1016/0009-2509\(89\)87022-8](https://doi.org/10.1016/0009-2509(89)87022-8)
- Burkhart, L.E., Fahien, R.W., 1958. Pulse column design, United States Atomic Energy Commission.
- Caldeira, R., Ni, X., 2009. Evaluation and establishment of a cleaning protocol for the production of vanilal sodium and aspirin using a continuous oscillatory baffled reactor. *Org. Process Res. Dev.* 13, 1080–1087. <https://doi.org/10.1021/op900120h>
- Callahan, C.J., Ni, X., 2014. An investigation into the effect of mixing on the secondary nucleation of sodium chlorate in a stirred tank and an oscillatory baffled crystallizer. *CrystEngComm* 16, 690–697. <https://doi.org/10.1039/C3CE41467A>
- Castro, F., Ferreira, A., Rocha, F., Vicente, A., Teixeira, J.A., 2013. Continuous-flow precipitation of hydroxyapatite at 37 °c in a meso oscillatory flow reactor. *Ind. Eng. Chem. Res.* 52, 9816–9821. <https://doi.org/10.1021/ie400710b>
- Commenge, J.M., Falk, L., 2011. Villermaux-Dushman protocol for experimental characterization of micromixers. *Chem. Eng. Process. Process Intensif.* 50, 979–990. <https://doi.org/10.1016/j.cep.2011.06.006>
- Cruz, P., Rocha, F., Ferreira, A., 2016. Effect of operating conditions on batch and continuous paracetamol crystallization in an oscillatory flow mesoreactor. *CrystEngComm* 18, 9113–9121.
- Demyanovich, R.J., Bourne, J.R., 1989. Rapid micromixing by the impingement of thin liquid sheets. 2. Mixing study. *Am. Chem. Soc.* 28, 830–839. <https://doi.org/10.1021/ie00090a027>
- Dickens, A.W., Mackley, M.R., Williams, H.R., 1989. Experimental residence time distribution measurements for unsteady flow in baffled tubes. *Chem. Eng. Sci.* 44, 1471–1479. [https://doi.org/10.1016/0009-2509\(89\)80023-5](https://doi.org/10.1016/0009-2509(89)80023-5)

- Duan, X., Feng, X., Yang, C., Mao, Z., 2016. Numerical simulation of micro-mixing in stirred reactors using the engulfment model coupled with CFD. *Chem. Eng. Sci.* 140, 179–188.
<https://doi.org/10.1016/j.ces.2015.10.017>
- Ejimi, L.N., Yerdelen, S., Mcglone, T., Onyemelukwe, I., Johnston, B., Florence, A.J., Reis, N., 2017. A factorial approach to understanding the effect of inner geometry of baffled meso-scale tubes on solids suspension and axial dispersion in continuous, oscillatory liquid-solid plug flows. *Chem. Eng. J.* 308, 669–682. <https://doi.org/10.1016/j.cej.2016.09.013>
- Eze, V.C., Fisher, J.C., Phan, A.N., Harvey, A.P., 2017. Intensification of carboxylic acid esterification using a solid catalyst in a mesoscale oscillatory baffled reactor platform. *Chem. Eng. J.* 322, 205–214. <https://doi.org/10.1016/j.cej.2017.04.038>
- Eze, V.C., Phan, A.N., Pirez, C., Harvey, A.P., Lee, A.F., Wilson, K., 2013. Heterogeneous catalysis in an oscillatory baffled flow reactor. *Catal. Sci. Technol.* 3, 2373.
<https://doi.org/10.1039/c3cy00282a>
- Fabiya, M.E., Skelton, R.L., 2000. Photocatalytic mineralisation of methylene blue using buoyant TiO₂-coated polystyrene beads. *J. Photochem. Photobiol. A Chem.* 132, 121–128.
[https://doi.org/10.1016/S1010-6030\(99\)00250-6](https://doi.org/10.1016/S1010-6030(99)00250-6)
- Fabiya, M.E., Skelton, R.L., 1999. The application of oscillatory flow mixing to photocatalytic wet oxidation. *J. Photochem. Photobiol. A Chem.* 129, 17–24. [https://doi.org/10.1016/S1010-6030\(99\)00177-X](https://doi.org/10.1016/S1010-6030(99)00177-X)
- Falk, L., Commenge, J.M., 2010. Performance comparison of micromixers. *Chem. Eng. Sci.* 65, 405–411. <https://doi.org/10.1016/j.ces.2009.05.045>
- Ferreira, A., Adesite, P.O., Teixeira, J.A., Rocha, F., 2017. Effect of solids on O₂ mass transfer in an oscillatory flow reactor provided with smooth periodic constrictions. *Chem. Eng. Sci.* 170, 400–409. <https://doi.org/10.1016/j.ces.2016.12.067>
- Ferreira, A., Teixeira, J.A., Rocha, F., 2015. O₂ mass transfer in an oscillatory flow reactor provided with smooth periodic constrictions. Individual characterization of k_L and a . *Chem. Eng. J.* 262, 499–508. <https://doi.org/10.1016/j.cej.2014.09.125>
- Fitch, A.W., Jian, H., Ni, X., 2005. An investigation of the effect of viscosity on mixing in an oscillatory baffled column using digital particle image velocimetry and computational fluid dynamics simulation. *Chem. Eng. J.* 112, 197–210. <https://doi.org/10.1016/j.cej.2005.07.013>
- Forney, L.J., Nafia, N., Vo, H.X., 1996. Optimum jet mixing in a tubular reactor. *AIChE J.* 42, 3113.
- Gaidhani, H.K., McNeil, B., Ni, X., 2005. Fermentation of pullulan using an oscillatory baffled fermenter. *Chem. Eng. Res. Des.* 83, 640–645. <https://doi.org/10.1025/cherd.04355>
- Gao, P., Han Ching, W., Herrmann, M., Kwong Chan, C., Yue, P.L., 2003. Photooxidation of a model pollutant in an oscillatory flow reactor with baffles. *Chem. Eng. Sci.* 58, 1013–1020.
[https://doi.org/10.1016/S0009-2509\(02\)00642-5](https://doi.org/10.1016/S0009-2509(02)00642-5)
- Gao, S., Ni, X., Cumming, R.H., Greated, C.A., Norman, P., 1998. Experimental Investigation of

- Bentonite Flocculation in a Batch Oscillatory Baffled Column. *Sep. Sci. Technol.* 33, 2143–2157.
- Golding, J.A., Lee, J., 1981. Recovery and Separation of Cobalt and Nickel in a Pulsed Sieve-Plate Extraction Column. *Ind. Eng. Chem. Process Des. Dev.* 20, 256–261.
<https://doi.org/10.1021/i200013a013>
- González-Juárez, D., Herrero-Martín, R., Solano, J.P., 2018. Enhanced heat transfer and power dissipation in oscillatory-flow tubes with circular-orifice baffles: a numerical study. *Appl. Therm. Eng.* 141, 494–502. <https://doi.org/10.1016/j.applthermaleng.2018.05.115>
- González-Juárez, D., Solano, J.P., Herrero-Martín, R., Harvey, A.P., 2017. Residence time distribution in multiorifice baffled tubes: A numerical study. *Chem. Eng. Res. Des.* 118, 259–269.
<https://doi.org/10.1016/j.cherd.2016.12.008>
- Gough, P., Ni, X., Symes, K.C., 1997. Experimental flow visualisation in a modified pulsed baffled reactor. *J. Chem. Technol. Biotechnol.* 69, 321–328. [https://doi.org/10.1002/\(SICI\)1097-4660\(199707\)69](https://doi.org/10.1002/(SICI)1097-4660(199707)69)
- Guichardon, P., Falk, L., Villermaux, J., 2000. Characterisation of micromixing efficiency by the iodide-iodate reaction system. Part I: experimental procedure. *Chem. Eng. Sci.* 55, 4233–4243.
[https://doi.org/10.1016/S0009-2509\(00\)00069-5](https://doi.org/10.1016/S0009-2509(00)00069-5)
- Hamzah, A.A., Hasan, N., Takriff, M.S., Kamarudin, S.K., Abdullah, J., Tan, I.M., Sern, W.K., 2012. Effect of oscillation amplitude on velocity distributions in an oscillatory baffled column (OBC). *Chem. Eng. Res. Des.* 90, 1038–1044. <https://doi.org/10.1016/j.cherd.2011.11.003>
- Hartman, R.L., McMullen, J.P., Jensen, K.F., 2011. Deciding whether to go with the flow: Evaluating the merits of flow reactors for synthesis. *Angew. Chemie - Int. Ed.* 50, 7502–7519.
<https://doi.org/10.1002/anie.201004637>
- Harvey, A.P., Mackley, M.R., Seliger, T., 2003. Process intensification of biodiesel production using a continuous oscillatory flow reactor, in: *Journal of Chemical Technology and Biotechnology*. pp. 338–341. <https://doi.org/10.1002/jctb.782>
- Harvey, A.P., Mackley, M.R., Stonestreet, P., 2001. Operation and optimization of an oscillatory flow continuous reactor, in: *Industrial and Engineering Chemistry Research*. pp. 5371–5377.
<https://doi.org/10.1021/ie0011223>
- Hewgill, M.R., Mackley, M.R., Pandit, A.B., Pannu, S.S., 1993. Enhancement of gas-liquid mass transfer using oscillatory flow in a baffled tube. *Chem. Eng. Sci.* 48, 799–809.
[https://doi.org/10.1016/0009-2509\(93\)80145-G](https://doi.org/10.1016/0009-2509(93)80145-G)
- Hobbs, D.M., Muzzio, F.J., 1997. Effects of injection location, flow ratio and geometry on kenics mixer performance. *Fluid Mech. Transp. Phenom.* 43, 3121–3132.
<https://doi.org/10.1002/aic.690431202>
- Horie, T., Shiota, S., Akagi, T., Ohmura, N., Wang, S., Eze, V., Harvey, A., Hirata, Y., 2018. Intensification of hollow fiber membrane cross-flow filtration by the combination of helical

- baffle and oscillatory flow. *J. Memb. Sci.* 554, 134–139.
<https://doi.org/10.1016/j.memsci.2018.01.058>
- Hornung, C.H., Mackley, M.R., 2009. The measurement and characterisation of residence time distributions for laminar liquid flow in plastic microcapillary arrays. *Chem. Eng. Sci.* 64, 3889–3902. <https://doi.org/10.1016/j.ces.2009.05.033>
- Hounslow, M.J., Ni, X., 2004. Population balance modelling of droplet coalescence and break-up in an oscillatory baffled reactor. *Chem. Eng. Sci.* 59, 819–828.
<https://doi.org/10.1016/j.ces.2003.11.009>
- Howes, T., 1988. On the dispersion of unsteady flow in baffled tubes. PhD thesis. Department of Chemical Engineering. Cambridge University.
- Howes, T., Mackley, M.R., Roberts, E.P.L., 1991. The Simulation of Chaotic Mixing and Dispersion for Periodic Flows in Baffled Channels. *Chem. Eng. Sci.* 46, 1669–1677.
- Ikwebe, J., Harvey, A.P., 2015. Enzymatic saccharification of cellulose: A study of mixing and agitation in an oscillatory baffled reactor and a stirred tank reactor. *Biofuels* 6, 203–208.
<https://doi.org/10.1080/17597269.2015.1078560>
- Ikwebe, J., Harvey, A.P., 2011. Intensification of bioethanol production by simultaneous saccharification and fermentation (SSF) in an oscillatory baffled reactor (OBR), in: *World Renewable Energy Congress*. Linköping, Sweden, pp. 381–388.
<https://doi.org/10.3384/ecp11057381>
- Ismail, L., Westacott, R.E., Ni, X., 2006. On the characterisation of wax deposition in an oscillatory baffled device. *J. Chem. Technol. Biotechnol.* 81, 1905–1914.
<https://doi.org/https://doi.org/10.1002/jctb.1623>
- Jealous, A.C., Johnson, H.F., 1955. Power requirements for pulse generation in pulse columns. *Ind. Eng. Chem.* 47, 1159–1166. <https://doi.org/10.1021/ie50546a021>
- Jian, H., Ni, X., 2005. A Numerical Study on the Scale-Up Behaviour in Oscillatory Baffled Columns. *Chem. Eng. Res. Des.* 83, 1163–1170. <https://doi.org/10.1205/cherd.03312>
- Jiang, M., Ni, X., 2019. Reactive Crystallization of Paracetamol in a Continuous Oscillatory Baffled Reactor. *Org. Process Res. Dev.* 23, 882–890. <https://doi.org/10.1021/acs.oprd.8b00446>
- Jimeno, G., 2019. Characterisation of solid-liquid flow in a continuous oscillatory baffled reactor using computational fluid dynamics. Heriot Watt University.
- Jimeno, G., Lee, Y.C., Ni, X., 2018. On the evaluation of power density models for oscillatory baffled reactors using CFD. *Chem. Eng. Process. - Process Intensif.* 134, 153–162.
<https://doi.org/10.1016/J.CEP.2018.11.002>
- Johansen, F.C., 1930. Flow through pipe orifices at low reynolds numbers. *Proc. R. Soc. A Math. Phys. Eng. Sci.* 126, 231–245. <https://doi.org/10.1098/rspa.1930.0004>
- Johnson, B.K., Prud'homme, R.K., 2003. Chemical processing and micromixing in confined impinging jets. *AIChE J.* 49, 2264–2282. <https://doi.org/10.1002/aic.690490905>

- Kacker, R., Regensburg, S.I., Kramer, H.J.M., 2017. Residence time distribution of dispersed liquid and solid phase in a continuous oscillatory flow baffled crystallizer. *Chem. Eng. J.* 317, 413–423. <https://doi.org/10.1016/j.cej.2017.02.007>
- Karr, A.E., 1959. Performance of a reciprocating-plate extraction column. *AIChE J.* 5, 446–452. <https://doi.org/10.1002/aic.690050410>
- Kefas, H.M., Yunus, R., Rashid, U., Taufiq-Yap, Y.H., 2019. Enhanced biodiesel synthesis from palm fatty acid distillate and modified sulfonated glucose catalyst via an oscillation flow reactor system. *J. Environ. Chem. Eng.* 7, 102993. <https://doi.org/10.1016/j.jece.2019.102993>
- Knott, G.F., Mackley, M.R., 1980. On eddy motions near plates and ducts, induced by water waves and periodic flows. *Philos. Trans. R. Soc. London. Ser. A Math. Phys. Sci.* 294, 599–623. <https://doi.org/10.1098/rsta.1980.0070>
- Koh, M.Y., Idaty, T., Ghazi, M., Idris, A., Tinia, T.I., Idris, A., 2014. Synthesis of palm based biolubricant in an oscillatory flow reactor (OFR). *Ind. Crops Prod.* 52, 567–574. <https://doi.org/10.1016/j.indcrop.2013.10.042>
- Krupa, K., Nunes, M.I., Santos, R.J., Bourne, J.R., 2014. Characterization of micromixing in T-jet mixers. *Chem. Eng. Sci.* 111, 48–55. <https://doi.org/10.1016/j.ces.2014.02.018>
- Kukukova, A., Aubin, J., Kresta, S.M., 2009. A new definition of mixing and segregation: three dimensions of a key process variable. *Chem. Eng. Res. Des.* 87, 633–647. <https://doi.org/10.1016/j.cherd.2009.01.001>
- Kumar, A., Hartland, S., 1988. Prediction of dispersed phase hold-up in pulsed perforated-plate extraction columns. *Chem. Eng. Process.* 23, 41–59. [https://doi.org/10.1016/0255-2701\(88\)87013-2](https://doi.org/10.1016/0255-2701(88)87013-2)
- Laulan, A., 1980. Hydrodynamics and drop splitting in a pulsed disc and ring column. INP-Toulouse.
- Law, R., Ahmed, S., Tang, N., Phan, A., Harvey, A., 2018. Development of a more robust correlation for predicting heat transfer performance in oscillatory baffled reactors. *Chem. Eng. Process. - Process Intensif.* 125, 133–138. <https://doi.org/10.1016/j.cep.2018.01.016>
- Laybourn, A., López-Fernández, A.M., Thomas-Hillman, I., Katrib, J., Lewis, W., Dodds, C., Harvey, A.P., Kingman, S.W., 2019. Combining continuous flow oscillatory baffled reactors and microwave heating: Process intensification and accelerated synthesis of metal-organic frameworks. *Chem. Eng. J.* 356, 170–177. <https://doi.org/10.1016/j.cej.2018.09.011>
- Lee, C.T., Buswell, A.M., Middelberg, A.P.J., 2002. The influence of mixing on lysozyme renaturation during refolding in an oscillatory flow and a stirred-tank reactor. *Chem. Eng. Sci.* 57, 1679–1684. [https://doi.org/10.1016/S0009-2509\(02\)00066-0](https://doi.org/10.1016/S0009-2509(02)00066-0)
- Lee, C.T., Mackley, M.R., Stonestreet, P., Middelberg, A.P.J., 2001. Protein refolding in an oscillatory flow reactor. *Biotechnol. Lett.* 23, 1899–1901. <https://doi.org/10.1023/A:1012734214751>
- Lee, L.J., Ottino, J.M., Ranz, W.E., Macosko, C.W., 1980. Impingement mixing in reaction injection molding. *Polym. Eng. Sci.* 20, 868–874. <https://doi.org/10.1002/pen.760201306>

- Leroy, P., 1991. Study on the pressure drop in pulsed disc and doughnut columns. INP Lorraine.
- Levenspiel, O., 2012. Tracer Technology: Modeling the Flow of Fluids. Springer, New York.
<https://doi.org/10.1007/978-1-4419-8074-8>
- Liu, S., Afacan, A., Masliyah, J.H., 2001. A new pressure drop model for flow-through orifice plates. *Can. J. Chem. Eng.* 79, 100–106. <https://doi.org/10.1002/cjce.5450790115>
- Lobry, E., Gourdon, C., Xuereb, C., Lasuye, T., 2013. Liquid-liquid dispersion in co-current disc and doughnut pulsed column effect of the operating conditions, physical properties and materials parameters. *Chem. Eng. J.* 233, 24–38. <https://doi.org/10.1016/j.cej.2013.08.020>
- Lobry, E., Lasuye, T., Gourdon, C., Xuereb, C., 2014. Liquid-liquid dispersion in a continuous oscillatory baffled reactor - application to suspension polymerization. *Chem. Eng. J.* 259, 505–518. <https://doi.org/10.1016/j.cej.2014.08.014>
- Lucas, M.S., Reis, N.M., Puma, G.L., 2016. Intensification of ozonation processes in a novel, compact, multi-orifice oscillatory baffled column. *Chem. Eng. J.* 296, 335–339.
<https://doi.org/10.1016/j.cej.2016.03.050>
- Mackley, M.R., Ni, X., 1991. Mixing and dispersion in a baffled tube for steady laminar and pulsatile flow. *Chem. Eng. Sci.* 46, 3139–3151. [https://doi.org/10.1016/0009-2509\(91\)85017-R](https://doi.org/10.1016/0009-2509(91)85017-R)
- Mackley, M.R., Smith, K.B., Wise, N.P., 1993. The Mixing and Separation of Particle Suspensions using Oscillatory Flow in Baffled Tubes. *Trans IChemE* 71, 649–656.
- Mackley, M.R., Stonestreet, P., 1995. Heat Transfer and Associated Energy Dissipation for Oscillatory Flow in Baffled Tubes. *Chem. Eng. Sci.* 50, 2211–2224.
- Mackley, M.R., Tweddle, G.M., Wyatt, I.D., 1990. Experimental heat transfer measurements for pulsatile flow in baffled tubes. *Chem. Eng. Sci.* 45, 1237–1242. [https://doi.org/10.1016/0009-2509\(90\)87116-A](https://doi.org/10.1016/0009-2509(90)87116-A)
- Manninen, M., Gorshkova, E., Immonen, K., Ni, X., 2013. Evaluation of axial dispersion and mixing performance in oscillatory baffled reactors using CFD. *J. Chem. Technol. Biotechnol.* 88, 553–562. <https://doi.org/10.1002/jctb.3979>
- Martin, G., 1987. Extraction from viscous polymer solutions. *Chem. Eng. Prog.* 83, 54–55.
- Masngut, N., Harvey, A.P., 2012. Intensification of biobutanol production in batch oscillatory baffled bioreactor, in: *Procedia Engineering*. pp. 1079–1087.
<https://doi.org/10.1016/j.proeng.2012.07.499>
- Masngut, N., Harvey, A.P., Ikwebe, J., 2010. Potential uses of oscillatory baffled reactors for biofuel production. *Biofuels*. <https://doi.org/10.4155/bfs.10.38>
- Mazubert, A., Aubin, J., Elgue, S., Poux, M., 2014. Intensification of waste cooking oil transformation by transesterification and esterification reactions in oscillatory baffled and microstructured reactors for biodiesel production. *Green Process. Synth.* 3, 419–429. <https://doi.org/10.1515/gps-2014-0057>
- Mazubert, A., Crockatt, M., Poux, M., Aubin, J., Roelands, M., 2015. Reactor comparison for the

- esterification of fatty acids from waste cooking oil. *Chem. Eng. Technol.* 38, 2161–2169.
<https://doi.org/10.1002/ceat.201500138>
- Mazubert, A., Fletcher, D.F., Poux, M., Aubin, J., 2016a. Hydrodynamics and mixing in continuous oscillatory flow reactors—Part I: Effect of baffle geometry. *Chem. Eng. Process. Process Intensif.* 108, 78–92.
- Mazubert, A., Fletcher, D.F., Poux, M., Aubin, J., 2016b. Hydrodynamics and mixing in continuous oscillatory flow reactors—Part II: Characterisation methods. *Chem. Eng. Process. Process Intensif.* 102, 102–116.
- Mazubert, A., Poux, M., Aubin, J., 2013. Intensified processes for FAME production from waste cooking oil: A technological review. *Chem. Eng. J.* 233, 201–223.
<https://doi.org/10.1016/j.cej.2013.07.063>
- McDonough, J.R., Ahmed, S.M.R., Phan, A.N., Harvey, A.P., 2019a. The development of helical vortex pairs in oscillatory flows – A numerical and experimental study. *Chem. Eng. Process. - Process Intensif.* 143, 107588. <https://doi.org/10.1016/j.cep.2019.107588>
- McDonough, J.R., Ahmed, S.M.R., Phan, A.N., Harvey, A.P., 2017. A study of the flow structures generated by oscillating flows in a helical baffled tube. *Chem. Eng. Sci. J.* 171, 160–178.
<https://doi.org/10.1016/j.ces.2017.05.032>
- McDonough, J.R., Oates, M.F., Law, R., Harvey, A.P., 2019b. Micromixing in oscillatory baffled flows. *Chem. Eng. J.* 361, 508–518. <https://doi.org/10.1016/j.cej.2018.12.088>
- McDonough, J.R., Phan, A.N., Harvey, A.P., 2018. The mesoscale oscillatory baffled reactor facilitates intensified kinetics screening when the solvent is removed. *Chem. Eng. Process. Process Intensif.* 129, 51–62. <https://doi.org/10.1016/j.cep.2018.05.003>
- McDonough, J.R., Phan, A.N., Harvey, A.P., 2015. Rapid process development using oscillatory baffled mesoreactors - A state-of-the-art review. *Chem. Eng. J.*
<https://doi.org/10.1016/j.cej.2014.10.113>
- McDonough, J.R., Phan, A.N., Reay, D.A., Harvey, A.P., 2016. Passive isothermalisation of an exothermic reaction in flow using a novel “Heat Pipe Oscillatory Baffled Reactor (HPOBR).” *Chem. Eng. Process. Process Intensif.* 110, 201–213. <https://doi.org/10.1016/j.cep.2016.10.017>
- McLachlan, H., Ni, X., 2016. On the effect of added impurity on crystal purity of urea in an oscillatory baffled crystallizer and a stirred tank crystallizer. *J. Cryst. Growth* 442, 81–88.
<https://doi.org/10.1016/j.jcrysgro.2016.03.001>
- Mena, P.C., Pons, M.N., Teixeira, J.A., Rocha, F.A., 2005. Using image analysis in the study of multiphase gas absorption. *Chem. Eng. Sci.* 60, 5144–5150.
<https://doi.org/10.1016/j.ces.2005.04.049>
- Mignard, D., Amin, L., Ni, X., 2004. Modelling of droplet breakage probabilities in an oscillatory baffled reactor. *Chem. Eng. Sci.* 59, 2189–2200. <https://doi.org/10.1016/j.ces.2004.02.012>
- Mignard, D., Amin, L., Ni, X., 2003. Population balance modelling of droplets in an oscillatory

- baffled reactor - Using direct measurements of breakage rate constants. *J. Chem. Technol. Biotechnol.* 78, 364–369. <https://doi.org/10.1002/jctb.787>
- Mignard, D., Amin, L.P., Ni, X., 2006. Determination of breakage rates of oil droplets in a continuous oscillatory baffled tube. *Chem. Eng. Sci.* 61, 6902–6917. <https://doi.org/10.1016/j.ces.2006.07.025>
- Navarro-Fuentes, F., Keane, M., Ni, X.W., 2019a. A Comparative Evaluation of Hydrogenation of 3-Butyn-2-ol over Pd/Al₂O₃ in an Oscillatory Baffled Reactor and a Commercial Parr Reactor. *Org. Process Res. Dev.* 23, 38–44. <https://doi.org/10.1021/acs.oprd.8b00324>
- Navarro-Fuentes, F., Keane, M., Ni, X.W., 2019b. The effects of modes of hydrogen input and reactor configuration on reaction rate and H₂ efficiency in the catalytic hydrogenation of alkynol to alkenol. *Can. J. Chem. Eng.* 1–8. <https://doi.org/10.1002/cjce.23615>
- Ni, X., 1995. A study of fluid dispersion in oscillatory flow through a baffled tube. *J. Chem. Technol. Biotechnol.* 64, 165–174. <https://doi.org/10.1002/jctb.280640209>
- Ni, X., Brogan, G., Struthers, A., Bennett, D.C., Wilson, S.F., 1998a. A systematic study of the effect of geometrical parameters on mixing time in oscillatory baffled columns. *Chem. Eng. Res. Des.* 76, 635–642. <https://doi.org/10.1205/026387698525162>
- Ni, X., Cosgrove, J.A., Arnott, A.D., Greated, C.A., Cumming, R.H., 2000. On the measurement of strain rate in an oscillatory baffled column using particle image velocimetry. *Chem. Eng. Sci.* 55, 3195–3208. [https://doi.org/10.1016/S0009-2509\(99\)00577-1](https://doi.org/10.1016/S0009-2509(99)00577-1)
- Ni, X., Cosgrove, J.A., Cumming, R.H., Greated, C.A., Murray, K.R., Norman, P., 2001a. Experimental study of flocculation of bentonite and *alcaligenes eutrophus* in a batch oscillatory baffled flocculator. *Chem. Eng. Res. Des.* 79, 33–40. <https://doi.org/10.1205/026387601528507>
- Ni, X., Fitch, A.W., Jian, H., 2004a. Numerical and Experimental Investigations into The Effect of Gap Between Baffle and Wall on Mixing in an Oscillatory Baffled Column. *Int. J. Chem. React. Eng.* 2, 1–16. <https://doi.org/https://doi.org/10.2202/1542-6580.1147>.
- Ni, X., Gao, S., 1996a. Scale-up correlation for mass transfer coefficients in pulsed baffled reactors. *Chem. Eng. J. Biochem. Eng. J.* 63, 157–166. [https://doi.org/10.1016/S0923-0467\(96\)03120-X](https://doi.org/10.1016/S0923-0467(96)03120-X)
- Ni, X., Gao, S., 1996b. Mass transfer characteristics of a pilot pulsed baffled reactor. *J. Chem. Technol. Biotechnol.* 65, 65–71. [https://doi.org/10.1002/\(SICI\)1097-4660\(199601\)65:1<65::AID-JCTB352>3.0.CO;2-1](https://doi.org/10.1002/(SICI)1097-4660(199601)65:1<65::AID-JCTB352>3.0.CO;2-1)
- Ni, X., Gelicourt, Y.S., Baird, M.H.I., Rao, N.V.R., 2001b. Scale-up of single phase axial dispersion coefficients in batch and continuous oscillatory baffled tubes. *Can. J. Chem. Eng.* 79, 444–448.
- Ni, X., Jian, H., Fitch, A., 2003a. Evaluation of turbulent integral length scale in an oscillatory baffled column using large eddy simulation and digital particle image velocimetry. *Chem. Eng. Res. Des.* 81, 842–853. <https://doi.org/10.1205/026387603322482086>
- Ni, X., Jian, H., Fitch, A.W., 2002. Computational fluid dynamic modelling of flow patterns in an oscillatory baffled column. *Chem. Eng. Sci.* 57, 2849–2862. <https://doi.org/10.1016/S0009->

2509(02)00081-7

- Ni, X., Johnstone, J.C., Symes, K.C., Grey, B.D., Bennett, D.C., 2001c. Suspension polymerization of acrylamide in an oscillatory baffled reactor: from drops to particles. *AIChE J.* 47, 1746–1757. <https://doi.org/10.1002/aic.690470807>
- Ni, X., Liao, A., 2008. Effects of cooling rate and solution concentration on solution crystallization of L-glutamic acid in an oscillatory baffled crystallizer. *Cryst. Growth Des.* 8, 2875–2881. <https://doi.org/10.1021/cg7012039>
- Ni, X., Mackley, M.R., Harvey, A.P., Stonestreet, P., Baird, M.H.I., Rao, N.V.R., 2003b. Mixing through oscillations and pulsations—A guide to achieving process enhancements in the chemical and process industries. *Trans IChemE* 81. <https://doi.org/10.1205/02638760360596928>
- Ni, X., Valentine, A., Liao, A., Sermage, S.B.C., Thomson, G.B., Roberts, K.J., 2004b. On the crystal polymorphic forms of L-glutamic acid following temperature programmed crystallization in a batch oscillatory baffled crystallizer. *Cryst. Growth Des.* 4, 1129–1135. <https://doi.org/10.1021/cg0498271>
- Ni, X., Zhang, Y., Mustafa, I., 1999. Correlation of polymer particle size with droplet size in suspension polymerisation of methylmethacrylate in a batch oscillatory-baffled reactor. *Chem. Eng. Sci.* 54, 841–850. [https://doi.org/10.1016/S0009-2509\(98\)00279-6](https://doi.org/10.1016/S0009-2509(98)00279-6)
- Ni, X., Zhang, Y., Mustafa, I., 1998b. An investigation of droplet size and size distribution in methylmethacrylate suspensions in a batch oscillatory-baffled reactor. *Chem. Eng. Sci.* 53, 2903–2919.
- Oliva, J.A., Pal, K., Barton, A., Firth, P., Nagy, Z.K., 2018. Experimental investigation of the effect of scale-up on mixing efficiency in oscillatory flow baffled reactors (OFBR) using principal component based image analysis as a novel noninvasive residence time distribution measurement approach. *Chem. Eng. J.* 351, 498–505. <https://doi.org/10.1016/j.cej.2018.06.029>
- Oliveira, M.S.N., Ni, X., 2004. Effect of hydrodynamics on mass transfer in a gas-liquid oscillatory baffled column. *Chem. Eng. J.* 99, 59–68. <https://doi.org/10.1016/j.cej.2004.01.002>
- Oliveira, M.S.N., Ni, X., 2001. Gas hold-up and bubble diameters in a gassed oscillatory baffled column. *Chem. Eng. Sci.* 56, 6143–6148. [https://doi.org/10.1016/S0009-2509\(01\)00257-3](https://doi.org/10.1016/S0009-2509(01)00257-3)
- Onyemelukwe, I.I., Benyahia, B., Reis, N.M., Nagy, Z.K., Rielly, C.D., 2018. The heat transfer characteristics of a mesoscale continuous oscillatory flow crystalliser with smooth periodic constrictions. *Int. J. Heat Mass Transf.* 123, 1109–1119. <https://doi.org/10.1016/j.ijheatmasstransfer.2018.03.015>
- Paste, Particle and Polymer Processing Group (P4G), Oscillatory Fluid Mixing. OFM: Enhancement of heat transfer rates, < <https://www.ceb.cam.ac.uk/research/groups/rg-p4g/archive-folder/pfg/ofm-folder/ofm-avantages-enhancement-mass-transfer> > (Online; accessed February 17, 2020).
- Palma, M., Giudici, R., 2003. Analysis of axial dispersion in an oscillatory-flow continuous reactor.

- Chem. Eng. J. 94, 189–198. [https://doi.org/10.1016/S1385-8947\(03\)00057-3](https://doi.org/10.1016/S1385-8947(03)00057-3)
- Paul, E.L., Atiemo-Obeng, V.A., Kresta, S.M., 2004a. Mixing and Chemical Reactions, in: Handbook of Industrial Mixing; Science and Practice. John Wiley & Sons, Inc., New Jersey, USA, pp. 755–868. <https://doi.org/10.1002/0471451452>
- Paul, E.L., Atiemo-Obeng, V.A., Kresta, S.M., 2004b. Mixing in Pipelines, in: Handbook of Industrial Mixing; Science and Practice. John Wiley & Sons, Inc., New Jersey, USA, pp. 371–478. <https://doi.org/10.1002/0471451452>
- Peña, R., Oliva, J.A., Burcham, C.L., Jarmer, D.J., Nagy, Z.K., 2017. Process intensification through continuous spherical crystallization using an oscillatory flow baffled crystallizer. Cryst. Growth Des. 17, 4776–4784. <https://doi.org/10.1021/acs.cgd.7b00731>
- Pereira, F.M., Sousa, D.Z., Alves, M.M., Mackley, M.R., Reis, N.M., 2014. CO₂ dissolution and design aspects of a multiorifice oscillatory baffled column. Ind. Eng. Chem. Res. 53, 17303–17316. <https://doi.org/10.1021/ie403348g>
- Pereira, N.E., Ni, X., 2001. Droplet size distribution in a continuous oscillatory baffled reactor. Chem. Eng. Sci. 56, 735–739. [https://doi.org/https://doi.org/10.1016/S0009-2509\(00\)00283-9](https://doi.org/10.1016/S0009-2509(00)00283-9)
- Phan, A.N., Harvey, A.P., 2011a. Characterisation of mesoscale oscillatory helical baffled reactor - experimental approach. Chem. Eng. J. 180, 229–236. <https://doi.org/10.1016/j.cej.2011.11.018>
- Phan, A.N., Harvey, A.P., 2011b. Effect of geometrical parameters on fluid mixing in novel mesoscale oscillatory helical baffled designs. Chem. Eng. J. 169, 339–347. <https://doi.org/10.1016/j.cej.2011.03.026>
- Phan, A.N., Harvey, A.P., 2010. Development and evaluation of novel designs of continuous mesoscale oscillatory baffled reactors. Chem. Eng. J. 159, 212–219. <https://doi.org/10.1016/j.cej.2010.02.059>
- Phan, A.N., Harvey, A.P., Eze, V., 2012. Rapid Production of Biodiesel in Mesoscale Oscillatory Baffled Reactors. Chem. Eng. Technol. 35, 1214–1220. <https://doi.org/10.1002/ceat.201200031>
- Phan, A.N., Harvey, A.P., Lavender, J., 2011a. Characterisation of fluid mixing in novel designs of mesoscale oscillatory baffled reactors operating at low flow rates (0.3-0.6ml/min). Chem. Eng. Process. Process Intensif. 50, 254–263. <https://doi.org/10.1016/j.cep.2011.02.004>
- Phan, A.N., Harvey, A.P., Rawcliffe, M., 2011b. Continuous screening of base-catalysed biodiesel production using New designs of mesoscale oscillatory baffled reactors. Fuel Process. Technol. 92, 1560–1567. <https://doi.org/10.1016/j.fuproc.2011.03.022>
- Rasdi, F.R.M., Phan, A.N., Harvey, A.P., 2013. Rapid determination of reaction order and rate constants of an imine synthesis reaction using a mesoscale oscillatory baffled reactor. Chem. Eng. J. 222, 282–291. <https://doi.org/10.1016/j.cej.2013.02.080>
- Raval, V., Siddique, H., Brown, C.J., Florence, A.J., 2020. Development and characterisation of a cascade of moving baffle oscillatory crystallisers (CMBOC). CrystEngComm. <https://doi.org/10.1039/d0ce00069h>

- Reis, N., Gonçalves, C.N., Aguedo, M., Gomes, N., Teixeira, J.A., Vicente, A.A., 2006a. Application of a novel oscillatory flow micro-bioreactor to the production of γ -decalactone in a two immiscible liquid phase medium. *Biotechnol. Lett.* 28, 485–490. <https://doi.org/10.1007/s10529-006-0003-x>
- Reis, N., Gonçalves, C.N., Vicente, A.A., Teixeira, J.A., 2006b. Proof-of-concept of a novel micro-bioreactor for fast development of industrial bioprocesses. *Biotechnol. Bioeng.* 95, 744–753. <https://doi.org/10.1002/bit.21035>
- Reis, N., Harvey, A.P., Mackley, M.R., Vincente, A.A., Teixeira, J.A., 2005. Fluid Mechanics and Design Aspects of a novel oscillatory flow screening mesoreactor. *Chem. Eng. Res. Des.* 83(A4), 357–371. <https://doi.org/10.1205/cherd.03401>
- Reis, N., Mena, P.C., Vicente, A.A., Teixeira, J.A., Rocha, F.A., 2007. The intensification of gas-liquid flows with a periodic, constricted oscillatory-meso tube. *Chem. Eng. Sci.* 62, 7454–7462. <https://doi.org/10.1016/j.ces.2007.09.018>
- Reis, N., Pereira, R.N., Vicente, A.A., Teixeira, J.A., 2008. Enhanced gas-liquid mass transfer of an oscillatory constricted-tubular reactor. *Ind. Eng. Chem. Res.* 47, 7190–7201. <https://doi.org/10.1021/ie8001588>
- Reis, N., Vicente, A.A., Teixeira, J.A., 2010. Liquid backmixing in oscillatory flow through a periodically constricted meso-tube. *Chem. Eng. Process. Process Intensif.* 49, 792–802. <https://doi.org/10.1016/j.cep.2010.01.014>
- Reis, N., Vicente, A.A., Teixeira, J.A., Mackley, M.R., 2004. Residence times and mixing of a novel continuous oscillatory flow screening reactor. *Chem. Eng. Sci.* 59, 4967–4974. <https://doi.org/10.1016/j.ces.2004.09.013>
- Santos, R.J., Erkoç, E., Dias, M.M., Lopes, J.C., 2009. Dynamic Behavior of the Flow Field in a RIM Machine Mixing Chamber. *AIChE J.* 55, 1338–1351. <https://doi.org/10.1002/aic>
- Schaber, S.D., Gerogiorgis, D.I., Ramachandran, R., Evans, J.M.B., Barton, P.I., Trout, B.L., 2011. Economic analysis of integrated continuous and batch pharmaceutical manufacturing: A case study. *Ind. Eng. Chem. Res.* <https://doi.org/10.1021/ie2006752>
- Siddique, H., Brown, C.J., Houson, I., Florence, A.J., 2015. Establishment of a continuous sonocrystallization process for lactose in an oscillatory baffled crystallizer. *Org. Process Res. Dev.* 19, 1871–1881. <https://doi.org/10.1021/acs.oprd.5b00127>
- Singh, B., Rizvi, S.S.H., 1994. Design and Economic Analysis for Continuous Countercurrent Processing of Milk Fat with Supercritical Carbon Dioxide. *J. Dairy Sci.* 77, 1731–1745. [https://doi.org/10.3168/jds.S0022-0302\(94\)77114-9](https://doi.org/10.3168/jds.S0022-0302(94)77114-9)
- Slavnić, D., Bugarski, B., Nikačević, N., 2019. Solids flow pattern in continuous oscillatory baffled reactor. *Chem. Eng. Process. - Process Intensif.* 135, 108–119. <https://doi.org/10.1016/j.cep.2018.11.017>
- Slavnić, D.S., Živković, L. V., Bjelić, A. V., Bugarski, B.M., Nikačević, N.M., 2017. Residence time

- distribution and Peclet number correlation for continuous oscillatory flow reactors. *J. Chem. Technol. Biotechnol.* 92, 2178–2188. <https://doi.org/10.1002/jctb.5242>
- Smith, K.B., Mackley, M.R., 2006. An Experimental Investigation into the Scale-up of Oscillatory Flow Mixing in Baffled Tubes. *Chem. Eng. Res. Des.* 84, 1001–1011. <https://doi.org/10.1205/cherd.05054>
- Sobey, I.J., 1980. On flow through furrowed channels. Part 1. Calculated flow patterns. *J. Fluid Mech.* 96, 1. <https://doi.org/10.1017/S002211208000198X>
- Solano, J.P., Herrero, R., Espin, S., Phan, A.N., Harvey, A.P., 2012. Numerical study of the flow pattern and heat transfer enhancement in oscillatory baffled reactors with helical coil inserts. *Chem. Eng. Res. Des.* 90, 732–742. <https://doi.org/10.1016/j.cherd.2012.03.017>
- Soufi, M.D., Ghobadian, B., Najafi, G., Mousavi, S.M., Aubin, J., 2017. Optimization of methyl ester production from waste cooking oil in a batch tri-orifice oscillatory baffled reactor. *Fuel Process. Technol.* 167, 641–647. <https://doi.org/10.1016/j.fuproc.2017.07.030>
- Stephens, G.G., Mackley, M.R., 2002. Heat transfer performance for batch oscillatory flow mixing. *Exp. Therm. Fluid Sci.* 25, 583–594. [https://doi.org/10.1016/S0894-1777\(01\)00098-X](https://doi.org/10.1016/S0894-1777(01)00098-X)
- Stonestreet, P., Harvey, A.P., 2002. A mixing-based design methodology for continuous oscillatory flow reactors. *Chem. Eng. Res. Des.* 80, 31–44. <https://doi.org/10.1205/026387602753393204>
- Stonestreet, P., Van Der Veecken, P.M.J., 1999. The effects of oscillatory flow and bulk flow components on residence time distribution in baffled tube reactors. *Chem. Eng. Res. Des.* 77, 671–684. <https://doi.org/10.1205/026387699526809>
- Su, Y., Chen, G., Yuan, Q., 2011. Ideal micromixing performance in packed microchannels. *Chem. Eng. Sci.* 66, 2912–2919. <https://doi.org/10.1016/j.ces.2011.03.024>
- Takriff, M.S., Masngut, N., Kadhum, A.A.H., Kalil, M.S., Mohammad, A.W., 2009. Solvent fermentation from palm oil mill effluent using *Clostridium acetobutylicum* in oscillatory flow bioreactor. *Sains Malaysiana* 38, 191–196.
- Taylor, R.A., Penney, W.R., Vo, H.X., 2005. Scale-up methods for fast competitive chemical reactions in pipeline mixers. *Ind. Eng. Chem. Res.* 44, 6095–6102. <https://doi.org/10.1021/ie040237u>
- van Delden, M.L., Vos, G.S., Kuipers, N.J.M., de Haan, A.B., 2006. Extraction of caprolactam with toluene in a pulsed disc and doughnut column - Part II: Experimental evaluation of the hydraulic characteristics. *Solvent Extr. Ion Exch.* 24, 519–538. <https://doi.org/10.1080/07366290600760649>
- Van Dijk, W.J.D., 1935. Process and apparatus for intimately contacting fluids. Pat. US 2,011,186.
- Villermaux, J., Falk, L., 1994. A generalized mixing model for initial contacting of reactive fluids. *Chem. Eng. Sci.* 49, 5127–5140. [https://doi.org/10.1016/0009-2509\(94\)00303-3](https://doi.org/10.1016/0009-2509(94)00303-3)
- Wenzel, D., Górak, A., 2018. Review and analysis of micromixing in rotating packed beds. *Chem. Eng. J.* 345, 492–506. <https://doi.org/10.1016/j.cej.2018.03.109>
- Yang, H., Yu, X., Raval, V., Makkawi, Y., Florence, A., 2015. Effect of Oscillatory Flow on

- Nucleation Kinetics of Butyl Paraben. *Cryst. Growth Des.* 16, 875–886.
<https://doi.org/10.1021/acs.cgd.5b01437>
- Yoshida, J.I., Kim, H., Nagaki, A., 2011. Green and sustainable chemical synthesis using flow microreactors. *ChemSusChem* 4, 331–340. <https://doi.org/10.1002/cssc.201000271>
- Yu, Z., Lv, Y., Yu, C., 2012. A continuous kilogram-scale process for the manufacture of o-difluorobenzene. *Org. Process Res. Dev.* 16, 1669–1672. <https://doi.org/10.1021/op300127x>
- Yussof, H.W., Bahri, S.S., Mazlan, N.A., 2018. Evaluation of power density on the bioethanol production using mesoscale oscillatory baffled reactor and stirred tank reactor, in: *IOP Conference Series: Materials Science and Engineering*. <https://doi.org/10.1088/1757-899X/334/1/012070>
- Zalc, J.M., Szalai, E.S., Muzzio, F.J., 2003. Mixing dynamics in the SMX static mixer as a function of injection location and flow ratio. *Polym. Eng. Sci.* 43, 875–890.
<https://doi.org/10.1002/pen.10072>
- Zalc, J.M., Szalai, E.S., Muzzio, F.J., Jaffer, S., 2002. Characterization of flow and mixing in an SMX static mixer. *Fluid Mech. Transp. Phenom.* 48, 427–436. <https://doi.org/10.1002/aic.690480303>
- Zhao, L., Raval, V., Briggs, N.E.B., Bhardwaj, R.M., McGlone, T., Oswald, I.D.H., Florence, A.J., 2014. From discovery to scale-up: α -lipoic acid: nicotinamide co-crystals in a continuous oscillatory baffled crystalliser. *CrystEngComm* 16, 5769–5780.
<https://doi.org/10.1039/c4ce00154k>
- Zheng, H., Yan, Z., Chu, S., Chen, J., 2018. Continuous synthesis of isobornyl acetate catalyzed by a strong acid cation exchange resin in an oscillatory flow reactor. *Chem. Eng. Process. - Process Intensif.* 134, 1–8. <https://doi.org/10.1016/j.cep.2018.10.005>
- Zheng, M., Li, J., Mackley, M.R., Tao, J., 2007. The development of asymmetry for oscillatory flow within a tube containing sharp edge periodic baffles. *Phys. Fluids* 19.
<https://doi.org/10.1063/1.2799553>

Chapter 3: Description of the numerical modelling approaches used

3.1. Introduction

In this chapter, a brief description of the numerical modelling approaches (schemes and algorithms) used in this work is presented. Two different Computational Dynamics Fluids (CFD) software packages are used in this work, ANSYS CFX 18.2 and ANSYS Fluent 2019R3. ANSYS CFX was chosen initially to perform the numerical simulations because of its ease of use, familiarity and CEL (CFX Expression Language) present in its CFD-Post processor. CEL makes it easier to define algebraic equations and monitor them during runs. However, due to the need of longer transient runs, simulation work was moved to ANSYS Fluent, which allows the use of true 2D meshes and a non-iterative time-advancement (NITA) algorithm, significantly speeding up transient simulations. Information about the Navier-Stokes equations, as well the solver algorithms and discretization schemes for both software packages (ANSYS CFX and ANSYS Fluent) is given in this Chapter.

3.2. The Navier-Stokes equations

Fluid flow is described by the concept of conservation of mass and momentum (Bird et al., 2002). The equation for mass conservation is also known as the continuity equation, while the momentum conservation equation is an expression of the generalized Newton law, defining the equation of motion of a fluid. When applied to a viscous fluid, this set of equations are known as the Navier-Stokes equations (Hirsch, 2007). These equations are used to describe the behaviour of transient and steady flow.

The conservation of mass equation, or continuity equation, is derived from the mass balance over a volume element $\Delta x \Delta y \Delta z$ through which a fluid is flowing and gives

$$\frac{\partial \rho}{\partial t} = - \left(\frac{\partial}{\partial x} \rho u_x + \frac{\partial}{\partial y} \rho u_y + \frac{\partial}{\partial z} \rho u_z \right) \quad (3.1)$$

The equation of continuity describes the rate of change of the fluid density at a fixed point in space, and can be expressed using vector representation as:

$$\frac{\partial \rho}{\partial t} = -(\nabla \cdot \rho \mathbf{u}) \quad (3.2)$$

where $\frac{\partial \rho}{\partial t}$ is the rate of change of the density, the vector $\rho \mathbf{u}$ is the mass flux, and its divergence represents the rate of mass flux in and out of the control volume. For an incompressible fluid, where the density is constant, the continuity equation can be simplified to:

$$(\nabla \cdot \mathbf{u}) = 0 \quad (3.3)$$

The motion equation is obtained from the momentum balance over a volume element $\Delta x \Delta y \Delta z$. Momentum enters and leaves the volume $\Delta x \Delta y \Delta z$ by two mechanisms: convective transport and molecular transport. There is also the external force (typically the gravitational force) acting on the fluid in the volume element. The sum of the rate of momentum in and out, and the external force on the fluid for the three spatial components gives the set of equations below:

$$\frac{\partial(\rho u_x)}{\partial t} = -\left(\frac{\partial}{\partial x}\phi_{xx} + \frac{\partial}{\partial y}\phi_{yx} + \frac{\partial}{\partial z}\phi_{zx}\right) + \rho g_x \quad (3.4)$$

$$\frac{\partial(\rho u_y)}{\partial t} = -\left(\frac{\partial}{\partial x}\phi_{xy} + \frac{\partial}{\partial y}\phi_{yy} + \frac{\partial}{\partial z}\phi_{zy}\right) + \rho g_y \quad (3.5)$$

$$\frac{\partial(\rho u_z)}{\partial t} = -\left(\frac{\partial}{\partial x}\phi_{xz} + \frac{\partial}{\partial y}\phi_{yz} + \frac{\partial}{\partial z}\phi_{zz}\right) + \rho g_z \quad (3.6)$$

These equations can be represented in vector-tensor notation as:

$$\frac{\partial(\rho u)_i}{\partial t} = -(\nabla \cdot \boldsymbol{\phi})_i + \rho g_i \quad i = x, y, z \quad (3.7)$$

where ρu_i are the Cartesian components of the vector $\rho \mathbf{u}$, which is the momentum at a point in the fluid, ρg_i are the components of the vector $\rho \mathbf{g}$, which is the external force, and $-(\nabla \cdot \boldsymbol{\phi})_i$ is the i^{th} component of the vector $-(\nabla \cdot \boldsymbol{\phi})$. Multiplying the i^{th} component by the unit vector in the i^{th} direction and adding the components vectorially, Equation (3.8) is obtained:

$$\frac{\partial(\rho \mathbf{u})}{\partial t} = -(\nabla \cdot \boldsymbol{\phi}) + \rho \mathbf{g} \quad (3.8)$$

The flux tensor $\boldsymbol{\phi}$ is the sum of the convective momentum flux tensor $\rho \mathbf{u} \otimes \mathbf{u}$ and the molecular momentum flux tensor $\boldsymbol{\sigma}$. The latter can be written as the sum of $p\boldsymbol{\delta}$ and $\boldsymbol{\tau}$, which are the normal pressure force applied to a specific surface (pressure multiplied by the unit tensor $\boldsymbol{\delta}$) and the stress tensor (or viscous momentum flux tensor), respectively. Adding $\boldsymbol{\phi} = \rho \mathbf{u} \otimes \mathbf{u} + p\boldsymbol{\delta} - \boldsymbol{\tau}$ into equation (3.8), the follow equation of motion is obtained:

$$\frac{\partial(\rho \mathbf{u})}{\partial t} = -\nabla \cdot (\rho \mathbf{u} \otimes \mathbf{u}) - \nabla p + \nabla \cdot \boldsymbol{\tau} + \rho \mathbf{g} \quad (3.9)$$

$\frac{\partial(\rho\mathbf{u})}{\partial t}$ represents the rate of increase of momentum, $(\rho\mathbf{u} \otimes \mathbf{u})$ the rate of momentum addition by convection, $-\nabla p + \nabla \cdot \boldsymbol{\tau}$ is the rate of momentum addition by molecular transport and $\rho\mathbf{g}$ the gravitational force. The stress tensor $\boldsymbol{\tau}$ is a time independent function of the fluid deformation and for Newtonian fluids it can be related to the rate of shear strain by the constitutive equation:

$$\boldsymbol{\tau} = -\mu(\nabla\mathbf{u} + (\nabla\mathbf{u})^T) + \left(\frac{2}{3}\mu - \kappa\right)(\nabla \cdot \mathbf{u})\boldsymbol{\delta} \quad (3.10)$$

where $\nabla\mathbf{u}$ is the velocity gradient tensor, $(\nabla\mathbf{u})^T$ is the transpose of the velocity gradient tensor, μ is the fluid viscosity and κ is the dilatational viscosity. If the fluid is incompressible with a constant Newtonian viscosity and the effect of gravity can be neglected, the momentum equation is simplified to:

$$\rho \frac{D\mathbf{u}}{Dt} = -\nabla p + \mu \nabla^2 \mathbf{u} \quad (3.11)$$

3.3. Solvers

Two different commercial CFD software are used in this work, ANSYS CFX 18.2 and ANSYS Fluent 2019R3. Both software packages are general purpose CFD solvers used widely in industry and academia. In this work, the Navier-Stokes equations are solved numerically without any turbulence model, as all flows studied are laminar. ANSYS CFX and ANSYS Fluent have been used in many numerical simulations of oscillatory baffled reactors in the literature (Fitch et al., 2005; González-Juárez et al., 2017; Jimeno et al., 2018; Mazubert et al., 2016a, 2016b; Reis et al., 2005).

The pressure-based solver uses an algorithm from a general class of methods known as projection methods (Chorin, 1968). In this method, the mass conservation (continuity) constraint of the velocity is achieved by solving a pressure correction equation. The pressure equation is derived from the continuity and the momentum equations in such a way that the velocity field, corrected by the pressure, satisfies the continuity equation. As the governing equations are non-linear and coupled; the solver iterates and solves the entire set of equations until convergence is achieved. The pressure field is obtained from the pressure correction equation. Segregated and coupled algorithms can be found in ANSYS Fluent, while ANSYS CFX only has the coupled algorithm (ANSYS Inc., 2019, 2017). In this work, the segregated pressure-based solver is used in ANSYS Fluent and the coupled pressure-solver is used in ANSYS CFX. The sections below present the algorithms used in this study. For additional information about other discretization schemes the reader is referred to ANSYS Inc. (2019, 2017).

ANSYS Fluent

Pressure-based segregated algorithm

The pressure-based segregated algorithm solves the governing equations sequentially (segregated from one other). Individual governing equations for the solution variable (u_x, u_y, u_z, p , etc.) are solved one after each other. Since the discretized equations need to be stored one at a time in memory, the algorithm is very memory-efficient. Nevertheless, solution convergence is relatively slow, as the equations are solved in a decoupled way. Each iterative step is illustrated in Figure 3.1(a).

ANSYS CFX

Pressure-based coupled algorithm

The pressure-based coupled algorithm solves the governing equations as a single system (for u_x, u_y, u_z, p). This solution approach uses a fully implicit discretization of the equations at any given time step. When solving fields in the ANSYS CFX, the outer (or time step) iteration is controlled by a pseudo or real time step for steady and transient analyses, respectively. Only one inner (linearization) iteration is performed per outer iteration in steady state analyses, whereas multiple inner iterations are performed per time step in transient analyses (ANSYS Inc., 2017). Due to the simultaneous solution of the continuity and momentum equations, the solution convergence is faster compared with the segregated algorithm. However, the memory requirement is increased as the velocity and pressure fields must be stored in memory. The iterative process is presented in Figure 3.1(b).

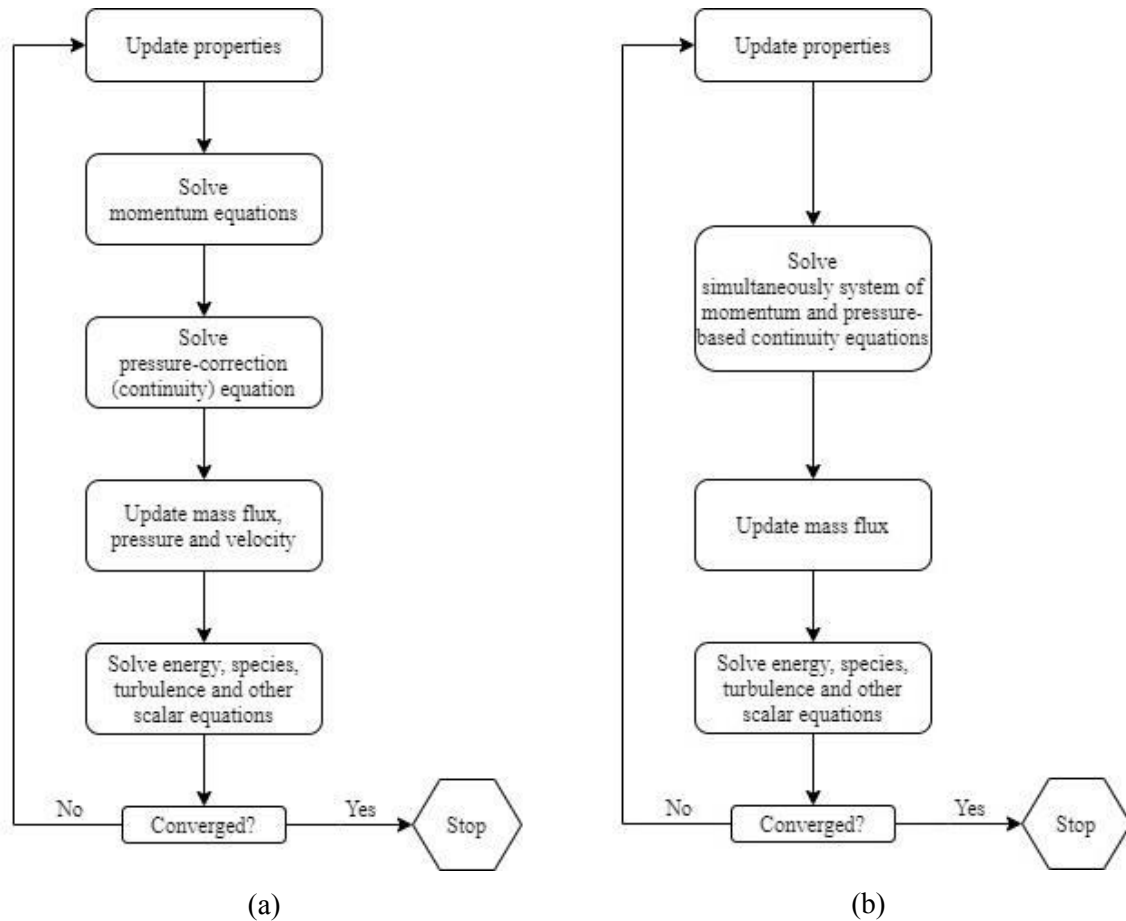


Figure 3.1: Overview of the Pressure-Based Solution Methods (a) Segregated algorithm (b) Coupled algorithm (ANSYS Inc., 2019).

3.3.1. Pressure-velocity coupling

ANSYS Fluent

Due to the coupled nature of the Navier-Stokes equations, solving these governing equations is a complex task as all the equations are dependent on the pressure. For incompressible flow, the pressure does not appear explicitly in the continuity equation. However, the continuity equation can be used as an equation for pressure by using a pressure-velocity coupling algorithm that is implemented into the continuity equation. A pressure field can be constructed to ensure that the velocities satisfy the continuity condition, allowing consistent velocity and pressure fields to be derived. ANSYS Fluent provides five pressure-velocity coupling algorithms: SIMPLE, SIMPLEC, PISO, Coupled, and Fractional Step (FSM). Except for the Coupled scheme, the other pressure-velocity coupling schemes are based on the predictor-corrector approach. The Fractional Step Method is the scheme chosen in the present work.

Fractional time-step method

In the Fractional-step method (FSM) the momentum equations are decoupled from the continuity equation using a mathematical technique called operator-splitting or approximate factorization. The formalism used in the approximate factorization allows control of the order of splitting error. The FSM is adopted in ANSYS Fluent as a velocity-coupling scheme in the non-iterative time-advancement (NITA) algorithm, presented in Figure 3.2. The NITA scheme does not need outer iterations, performing only a single outer iteration per timestep, which significantly speeds up transient simulations (ANSYS Inc., 2019).

ANSYS CFX

The coupled algorithm solves the momentum and pressure-based continuity equations together. The linear set of equations that arise by applying the finite volume method to all elements in the domain are discrete conservation equations. The system of equations can be written in the form:

$$\sum_{nb_i} a_i^{nb} \phi_i^{nb} = b_i \quad (3.12)$$

where ϕ is the solution, b the righthand side, a the coefficients of the equation, i is the identifying number of the control volume or node in question, and nb means “neighbour”, but also includes the central coefficient multiplying the solution at the i -th location. The node may have any number of neighbours which means that the method is equally applicable to both structured and unstructured meshes. The set of these, for all control volumes constitutes the complete linear equation system. For a scalar equation, a_i^{nb} , ϕ_i^{nb} and b_i are each single numbers (ANSYS Inc., 2017). For the coupled 3D mass-momentum equation set, they are a (4×4) matrix or a (4×1) vector, which can be expressed as:

$$a_i^{nb} = \begin{bmatrix} a_{u_x u_x} & a_{u_x u_y} & a_{u_x u_z} & a_{u_x p} \\ a_{u_y u_x} & a_{u_y u_y} & a_{u_y u_z} & a_{u_y p} \\ a_{u_z u_x} & a_{u_z u_y} & a_{u_z u_z} & a_{u_z p} \\ a_{p u_x} & a_{p u_y} & a_{p u_z} & a_{p p} \end{bmatrix}_i^{nb} \quad (3.13)$$

$$\phi_i^{nb} = \begin{bmatrix} u_x \\ u_y \\ u_z \\ p \end{bmatrix}_i^{nb} \quad (3.14)$$

$$b_i = \begin{bmatrix} b_{u_x} \\ b_{u_y} \\ b_{u_z} \\ b_p \end{bmatrix}_i \quad (3.15)$$

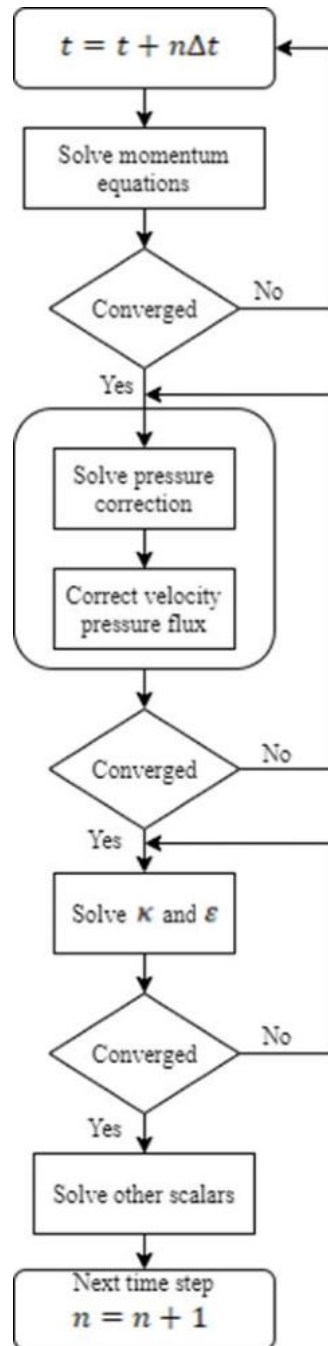


Figure 3.2: Non-Iterative Time Advancement Solution algorithm (ANSYS Inc., 2019).

3.4. Discretization methods

3.4.1. Discretization of governing equations

Discretization of governing equations can be illustrated by the unsteady conservation equation for a scalar quantity variable ϕ :

$$\frac{\partial(\rho\phi)}{\partial t} + \nabla \cdot (\rho\mathbf{u}\phi - \Gamma\nabla\phi) = \dot{S}_c \quad (3.16)$$

where Γ is the relevant effective diffusivity coefficient for the variable ϕ and \dot{S}_c is the source term.

Equation (3.16) is integrated over each control volume and Gauss's theorem is applied, which converts volume integrals involving divergence and gradient operators to surface integrals, so that the equation becomes:

$$\int_V \frac{\partial(\rho\phi)}{\partial t} dV + \int_S \rho\mathbf{u}\phi \cdot \mathbf{n} dS - \int_S \Gamma\nabla\phi \cdot \mathbf{n} dS = \int_V \dot{S}_c dV \quad (3.17)$$

Therefore, the continuity and Navier-Stokes equations, equations (3.3) and (3.11), can take the form:

$$\int_S \mathbf{u} \cdot \mathbf{n} dS = 0 \quad (3.18)$$

$$\int_V \rho \frac{\partial \mathbf{u}}{\partial t} dV + \int_S \rho \mathbf{u} (\mathbf{u} \cdot \mathbf{n}) dS = - \int_S \nabla p \cdot \mathbf{n} dS + \int_S \mu \nabla^2 \mathbf{u} \cdot \mathbf{n} dS \quad (3.19)$$

ANSYS Fluent and ANSYS CFX use a finite volume-based method to convert these equations to algebraic equations that can be solved numerically, which involves the discretization of the spatial domain using a mesh. The variables in the mass, momentum and scalar equations are stored on the finite control volumes in the created meshes. ANSYS Fluent and ANSYS CFX differ about how the discretization of the finite volume is done. ANSYS Fluent uses the cell-centred method, while ANSYS CFX uses the vertex-centred method, both illustrated in Figure 3.3. The main difference between the methods is the location where variables to be solved are stored. The cell-centred method uses the cells themselves as control volumes, with the flow variables being stored at the cell centres and linking them with its surrounding neighbours. This means the number of control volumes is equal to the number of cells. In the vertex-centred method, control volumes are constructed around each mesh node, where each element is divided into sub volumes, as shown in Figure 3.3(b). The control volume is defined by joining the centres of the edges and cell centres surrounding the node. Variable values and fluid properties are stored at the nodes (i.e mesh vertices). ANSYS Fluent (cell-centred method) is capable of handling polyhedral and cut-cell meshes, while ANSYS CFX (vertex-centred) only allows the use of traditional

tetrahedral and hexahedral mesh topologies, but ANSYS CFX works with a polyhedral mesh internally (Figure 3.3(b)).

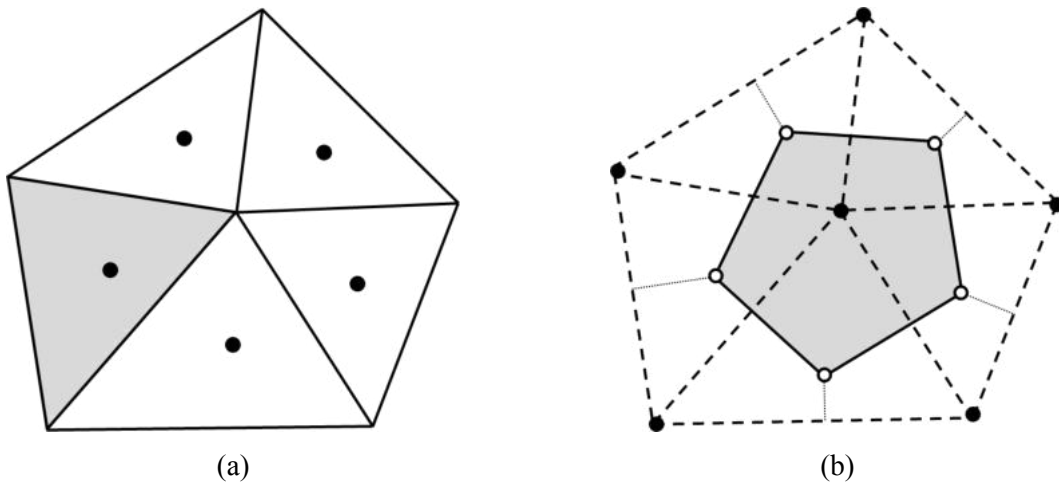


Figure 3.3: Control volume definition (a) cell-centred formulation, (b) vertex-centred formulation (Acharya, 2016).

3.4.2. Discretization schemes

Different spatial and temporal discretization schemes are available in ANSYS Fluent and ANSYS CFX. These schemes include amongst others: first order upwind differencing, second order central differencing, high-resolution scheme, as well as first and second order Backward Euler for ANSYS CFX; first order and second order upwind differencing, second order central differencing, power law, QUICK, explicit and implicit time integrations, etc. for ANSYS Fluent. This section presents the schemes used in this work. For additional information about other discretization schemes, the reader is referred to ANSYS Inc. (2019).

3.4.2.1. Spatial discretization

ANSYS Fluent

ANSYS Fluent stores values of the scalar ϕ at the cell centres (c_0 and c_1 in Figure 3.4) and at the centre of every face of each control volume, f . The value of the scalar at the face ϕ_f are obtained by interpolating the cell centre values using an upwind scheme. This means that the value at the face is derived from values in the upstream cells, or “upwind”, relative to the direction of the normal velocity.

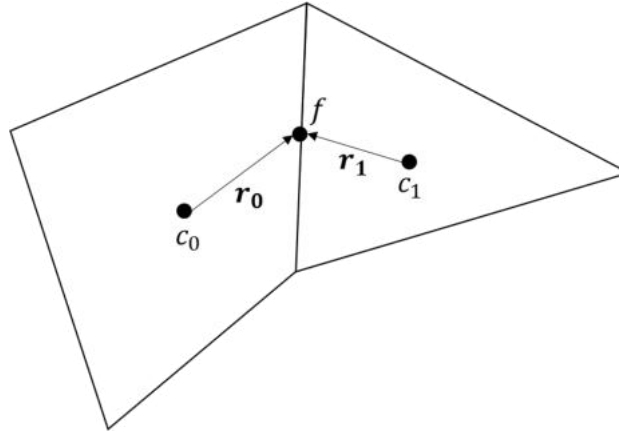


Figure 3.4: Illustration of spatial discretization of the control volume defined by Fluent ANSYS (ANSYS Inc., 2019).

Quadratic Upwind Differencing (QUICK) scheme

The QUICK scheme is a third order accurate upwind differencing scheme that takes into account three points (two upstream points and one downstream) using weighted quadratic interpolation for the cell face values. Figure 3.5 presents a one-dimensional control volume in order to illustrate the QUICK discretization scheme. The variable value at the face e , and for the case where the flow is from left to right, is given by:

$$\phi_e = \frac{3}{8}\phi_E + \frac{3}{4}\phi_P - \frac{1}{8}\phi_W \tag{3.20}$$

This scheme is more accurate on structured meshes that are aligned with the flow direction. For unstructured or hybrid meshes, the second-order upwind discretization scheme is used at the faces of non-hexahedral (or non-quadrilateral, in 2D) cells. The QUICK scheme is used in this work to solve the momentum equations.

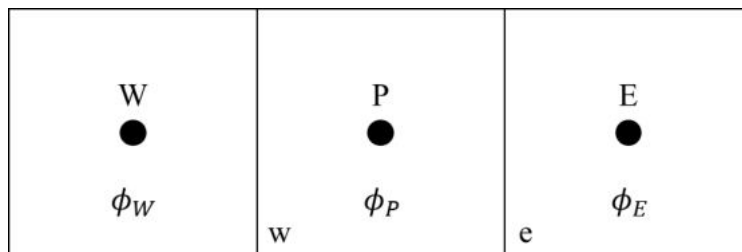


Figure 3.5: One-dimensional control volumes showing cell locations used in the QUICK scheme (ANSYS Inc., 2019).

Third order MUSCL scheme

The third order convection scheme was developed from the original MUSCL (Monotone Upstream Centred Schemes for Conservation Laws) by blending a central differencing scheme and second order upwind scheme as:

$$\phi_f = \theta \left(\frac{1}{2}(\phi_{c_0} + \phi_{c_1}) + \frac{1}{2}(\nabla\phi_{c_0} \cdot \mathbf{r}_0 + \nabla\phi_{c_1} \cdot \mathbf{r}_1) \right) + (1 - \theta)(\phi_{c_0} + \nabla\phi_{c_0} \cdot \mathbf{r}_0) \quad (3.21)$$

The first term on the right-hand side equation correspond to the central differencing scheme and the second term to the second order upwind scheme. The implementation in ANSYS Fluent uses a variable, which is a solution-dependent value of θ , chosen to avoid introducing any new solution extrema. Unlike the QUICK scheme, which is best used on structured hexahedral meshes, the MUSCL scheme is applicable to arbitrary meshes. Compared with the second order upwind scheme, the third order MUSCL has a potential to improve spatial accuracy for all types of meshes by reducing numerical diffusion, most significantly for three dimensional flows, and it is available for all transport equations. In this work, the mass fraction equations were solved using this scheme.

Second order scheme

The second order scheme is used in the present work for the pressure calculation. This scheme reconstructs the face pressure using a central differencing scheme. The pressure values at the face are given by:

$$P_f = \frac{1}{2}(P_{c_0} + P_{c_1}) + \frac{1}{2}(\nabla P_{c_0} \cdot \mathbf{r}_0 + \nabla P_{c_1} \cdot \mathbf{r}_1) \quad (3.22)$$

ANSYS CFX

Volume integrals are discretized within each element sector and accumulated to the control volume to which the sector belongs. The control volume defined in ANSYS CFX is shown in Figure 3.6. Surface integrals are discretized at the integration points (ip_n) located at the centre of each surface segment within an element and then distributed to the adjacent control volumes. As the surface integrals are equal and opposite for control volumes adjacent to the integration points, the surface integrals are guaranteed to be locally conservative (ANSYS Inc., 2017).

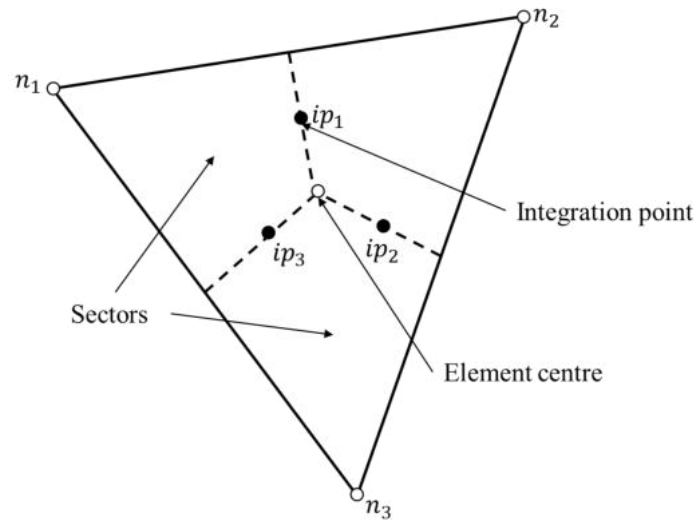


Figure 3.6: Illustration of spatial discretization of the control volume defined In ANSYS CFX (ANSYS Inc., 2017).

High-resolution scheme (second order bounded scheme)

The advection term needs the values of ϕ at the integration points to be approximated in terms of the values of ϕ at the nodes. Advection schemes in ANSYS CFX can be expressed in the form:

$$\phi_{ip} = \phi_{up} + \beta \nabla \phi \cdot \Delta \mathbf{r} \quad (3.23)$$

where ϕ_{up} is the value at the upwind node, and \mathbf{r} is the vector from the upwind node to the ip (integration point). The high-resolution scheme uses a special nonlinear gradient limiter β at each node, computed to be as close to 1 as possible without introducing new extrema. The advective flux is then evaluated using the values of β and $\nabla \phi$ from the upwind node. The methodology for calculating β is based on the boundedness principles used by Barth and Jespersen (1989). This method firstly consists in the computation of ϕ_{min} and ϕ_{max} at each node using a stencil involving adjacent nodes (including the node itself). Following this, for each integration point around the node, equation (3.23) is solved for β to ensure that it does not undershoot ϕ_{min} or overpass ϕ_{max} . The nodal value for β is taken to be the minimum value for all integration points surrounding the node. The value of β is also not permitted to exceed one.

3.4.2.2. Temporal discretization

To account for transient effects, the governing equations must be discretized in time. Transient effects are usually dealt with by using a time stepping procedure, with an initial condition provided. Temporal discretization is the process of integration of every term in the differential equations over a time step Δt .

Both solvers, ANSYS CFX and ANSYS Fluent, use the bounded second order implicit integration scheme (or second order backward Euler scheme). Implicit methods calculate the state at a current time by solving equations that include the current time state and the previous values:

$$\frac{\phi^{n+1} - \phi^n}{\Delta t} = F(\phi^{n+1}) \quad (3.24)$$

Any independent variable can be discretized in time as:

$$\frac{\partial \phi}{\partial t} = \frac{\phi_{n+1/2} - \phi_{n-1/2}}{\Delta t} \quad (3.25)$$

The start and end of time step values are approximated as:

$$\phi_{n-1/2} = \phi_{n-1} + \frac{1}{2}\beta_{n-1/2}(\phi_{n-1} - \phi_{n-2}) \quad (3.26)$$

$$\phi_{n+1/2} = \phi_n + \frac{1}{2}\beta_{n+1/2}(\phi_n - \phi_{n-1}) \quad (3.27)$$

where n , $n - 1$, $n - 2$, $n + 1/2$, $n - 1/2$ are different time levels. $\beta_{n+1/2}$ and $\beta_{n-1/2}$ are bounding factors for each variable at the $n + 1/2$ and $n - 1/2$ time level. This scheme is robust, implicit, conservative in time, and does not have a time step limitation for stability but the timestep must be sufficiently small for accuracy.

3.4.2.3. Gradients and derivatives

Gradients are needed for constructing values of a scalar, for computing secondary diffusion terms and velocity derivatives. The gradient $\nabla\phi$ of a given variable ϕ is used to discretize the convection and diffusion terms in the flow conservative equations. ANSYS Fluent offers the Green-Gauss method (cell-based and node-based methods) and the least square cell-based method to compute gradients, and ANSYS CFX uses only the Green-Gauss method:

$$\nabla\phi_{c_0} = \frac{1}{V} \sum_f \bar{\phi}_f \mathbf{S}_f \quad (3.28)$$

In the present work, the Green-Gauss node-based gradient evaluation for ANSYS Fluent is chosen. In this methodology, ϕ_f is calculated by the arithmetic average of the nodal value on the face:

$$\bar{\phi}_f = \frac{1}{N_f} \sum_n^{N_f} \bar{\phi}_n \quad (3.29)$$

where N_f is the number of nodes on the face. This scheme reconstructs exact values of a linear function at a node from surrounding cell-centred values on arbitrary unstructured meshes by solving a constrained minimization problem, preserving a second order spatial accuracy (ANSYS Inc., 2019).

3.5. Conclusion

In this chapter, the numerical solvers and discretization schemes available in ANSYS Fluent and ANSYS CFX used in the present work for the numerical simulations in a continuous oscillatory baffled reactor have been presented and discussed.

3.6. References

- Acharya, R., 2016. Investigation of differences in Ansys solvers CFX and Fluent.
- ANSYS Inc., 2019. ANSYS Fluent Theory Guide, Release 2019R3.
- ANSYS Inc., 2017. ANSYS CFX-Solver Theory, Release 18.2.
- Barth, T.J., Jespersen, D., 1989. The design and application of upwind schemes on unstructured meshes., in: AIAA 27th Aerospace Sciences Meeting.
- Bird, R.B., Stewart, W.E., Lightfoot, E.N., 2002. Transport Phenomena, Second. ed. John Wiley & Sons, Inc.
- Chorin, A.J., 1968. Numerical Solution of the Navier-Stokes Equations. *Math. Comput.* 22, 745–762.
- Fitch, A.W., Jian, H., Ni, X., 2005. An investigation of the effect of viscosity on mixing in an oscillatory baffled column using digital particle image velocimetry and computational fluid dynamics simulation. *Chem. Eng. J.* 112, 197–210. <https://doi.org/10.1016/j.cej.2005.07.013>
- González-Juárez, D., Solano, J.P., Herrero-Martín, R., Harvey, A.P., 2017. Residence time distribution in multiorifice baffled tubes: A numerical study. *Chem. Eng. Res. Des.* 118, 259–269. <https://doi.org/10.1016/j.cherd.2016.12.008>
- Hirsch, C., 2007. Numerical Computation of Internal and External Flows - Volume 1 Fundamentals of Computational Dynamics, Second. ed. John Wiley & Sons, Ltd.
- Jimeno, G., Lee, Y.C., Ni, X., 2018. On the evaluation of power density models for oscillatory baffled reactors using CFD. *Chem. Eng. Process. - Process Intensif.* 134, 153–162. <https://doi.org/10.1016/J.CEP.2018.11.002>
- Mazubert, A., Fletcher, D.F., Poux, M., Aubin, J., 2016a. Hydrodynamics and mixing in continuous oscillatory flow reactors—Part I: Effect of baffle geometry. *Chem. Eng. Process. Process Intensif.* 108, 78–92.
- Mazubert, A., Fletcher, D.F., Poux, M., Aubin, J., 2016b. Hydrodynamics and mixing in continuous oscillatory flow reactors—Part II: Characterisation methods. *Chem. Eng. Process. Process Intensif.* 102, 102–116.
- Reis, N., Harvey, A.P., Mackley, M.R., Vicente, A.A., Teixeira, J.A., 2005. Fluid Mechanics and Design Aspects of a novel oscillatory flow screening mesoreactor. *Chem. Eng. Res. Des.* 83(A4), 357–371. <https://doi.org/10.1205/cherd.03401>

Chapter 4: Predicting power consumption in continuous oscillatory baffled reactors

4.1. Introduction

In industrial processes, one important parameter to be considered is the energy dissipation rate or power density, since it influences mixing performance, mass and heat transfer, and scale-up guidelines. The energy dissipation rate in oscillatory flows can be characterised by the time-averaged power consumption over an oscillation period divided by the volume of the fluid. Experimentally, power density is determined by pressure drop measurements. In practice, pressure transducers are most often installed in the pipes upstream and downstream of the COBR, thereby encompassing fittings, bends and valves and hence making it difficult to determine the energy dissipation rate in the COBR alone. As a result, most of the studies on power dissipation in COBRs available in the literature employ empirical models, and only more recently CFD simulation. CFD is an attractive tool for this type of analysis since it allows the impact of the exact geometry on power consumption to be assessed without relying on any adjustable parameters, as is the case in empirical models. However, there are different ways to calculate power dissipation using CFD, including the volume integral of viscous dissipation (in laminar flow) or turbulence energy dissipation rate (in turbulent flow) and mechanical energy balances, and the computational ease and accuracy of each method may differ.

This study uses CFD simulation to compute power consumption in a NiTech® COBR with smooth constrictions for a range of net flow and oscillatory Reynolds numbers ($Re_{net} = 6 - 27 / Re_o = 24 - 96$). In particular, it explores two different ways to calculate power consumption – via viscous energy dissipation and using a mechanical energy balance, which are generic and therefore independent of COBR geometry – and evaluates them in terms of computational ease and accuracy. The range of operating conditions covered in the study complements the data recently obtained by Jimeno et al. (2018) and allows the validity of the QSM revised by these authors to be assessed. The work presented in this chapter has been published in Chemical Engineering Science, volume 212 (Avila et al., 2020).

4.2. Power dissipation characterization

Power dissipation is a key parameter for comparing the performance of different COBR geometries and operating conditions. In the laminar flow regime, the power dissipation can be calculated by the volume integral of the viscous dissipation:

$$P_{VD} = \iiint \Phi_v dV \quad (4.1)$$

where Φ_v is the viscous dissipation function, which represents the energy loss per unit time and volume due to the viscosity (internal friction). In Cartesian form, this is given by:

$$\Phi_v = 2\mu \left[\left(\frac{\partial u_x}{\partial x} \right)^2 + \left(\frac{\partial u_y}{\partial y} \right)^2 + \left(\frac{\partial u_z}{\partial z} \right)^2 \right] + \left(\left(\frac{\partial u_y}{\partial x} \right) + \left(\frac{\partial u_x}{\partial y} \right) \right)^2 + \left(\left(\frac{\partial u_z}{\partial y} \right) + \left(\frac{\partial u_y}{\partial z} \right) \right)^2 + \left(\left(\frac{\partial u_x}{\partial z} \right) + \left(\frac{\partial u_z}{\partial x} \right) \right)^2 \quad (4.2)$$

Alternately, viscous dissipation can be evaluated using a mechanical energy balance. Starting from the differential form of the conservation of momentum equation and taking the dot product with the velocity vector \mathbf{u} gives an equation for conservation of mechanical energy:

$$\mathbf{u} \cdot \left(\frac{\partial(\rho\mathbf{u})}{\partial t} + \nabla \cdot (\rho\mathbf{u} \otimes \mathbf{u}) = -\nabla p + \nabla \cdot \boldsymbol{\tau} \right) \quad (4.3)$$

This can then be simplified to

$$\frac{\partial}{\partial t} \left(\frac{1}{2} \rho u^2 \right) + \nabla \cdot \left(\rho \mathbf{u} \frac{1}{2} u^2 \right) = -\mathbf{u} \cdot \nabla p + \mathbf{u} \cdot \nabla \cdot \boldsymbol{\tau} \quad (4.4)$$

By manipulating the pressure and stress terms, equations (4.3) and (4.4) are obtained.

$$\mathbf{u} \cdot \nabla p = \nabla \cdot (p\mathbf{u}) - p\nabla \cdot \mathbf{u} \quad (4.5)$$

$$\mathbf{u} \cdot \nabla \cdot \boldsymbol{\tau} = \nabla \cdot (\boldsymbol{\tau}\mathbf{u}) - \boldsymbol{\tau} : \nabla \mathbf{u} \quad (4.6)$$

By defining

$$\Phi_v = \boldsymbol{\tau} : \nabla \mathbf{u} \quad (4.7)$$

and using equations (4.5) to (4.7), the mechanical energy balance can be written as:

$$\frac{\partial}{\partial t} \left(\frac{1}{2} \rho u^2 \right) + \nabla \cdot \left(\rho \mathbf{u} \frac{1}{2} u^2 \right) = -(\nabla \cdot (p\mathbf{u}) - p\nabla \cdot \mathbf{u}) + \nabla \cdot (\boldsymbol{\tau}\mathbf{u}) - \Phi_v \quad (4.8)$$

Integration of the mechanical energy conservation equation over the fluid volume and assuming incompressible flow then gives:

$$\frac{d}{dt} \int_V \frac{1}{2} \rho u^2 dV + \int_V \nabla \cdot \left(\rho \mathbf{u} \frac{1}{2} u^2 \right) dV = - \int_V \nabla \cdot (p \mathbf{u}) dV + \int_V \nabla \cdot (\boldsymbol{\tau} \mathbf{u}) dV - \int_V \Phi_v dV \quad (4.9)$$

Applying Gauss's theorem, equation (4.9) becomes:

$$\frac{d}{dt} \int_V \frac{1}{2} \rho u^2 dV + \int_S \frac{1}{2} \rho u^2 (\mathbf{u} \cdot \mathbf{n}) dS = \int_S (-p \mathbf{n}) \cdot \mathbf{u} dS + \int_S (\boldsymbol{\tau} \cdot \mathbf{n}) \cdot \mathbf{u} dS - \int_V \Phi_v dV \quad (4.10)$$

Normal viscous stresses ($\boldsymbol{\tau} \cdot \mathbf{n}$) are often negligible with respect to the pressure stresses, which are purely normal. Assuming zero velocity at the wall $\mathbf{u} = \mathbf{0}$, the above equation reduces to:

$$P_{ME} = - \left(\underbrace{\frac{d}{dt} \int_V \frac{1}{2} \rho u^2 dV}_{\text{Term 1}} + \underbrace{\int_S (p \mathbf{n} \cdot \mathbf{u}) dS}_{\text{Term 2}} + \underbrace{\int_S \frac{1}{2} \rho u^2 (\mathbf{u} \cdot \mathbf{n}) dS}_{\text{Term 3}} \right) = \int_V \Phi_v dV \quad (4.11)$$

where P_{ME} refers to the power dissipation obtained via the mechanical energy equation, Term 1 is the rate of increase of kinetic energy in the system, Term 2 is the work done by pressure on the fluid and Term 3 is the rate of addition of kinetic energy by convection into the system. In periodic motion, Term 1 is equal to zero over a flow cycle. Term 3 is equal to zero when the flow domain is unchanging with time and has an inlet (S_1) and outlet (S_2) with the same area, S .

The average power dissipation in the COBR has been calculated by taking the time average of equations (4.1) and (4.11) over an oscillation cycle, T .

$$P_{VD \text{ Total}} = \frac{1}{T} \int_0^T P_{VD} dt \quad (4.12)$$

$$P_{ME \text{ Total}} = \frac{1}{T} \int_0^T P_{ME} dt \quad (4.13)$$

4.3. Numerical method

4.3.1. Geometry and operating conditions

The geometry studied is the NiTech[®] COBR, which is a single orifice baffled reactor with smooth constrictions, as shown in Figure 4.1(a). The COBR tube has a diameter (D) of 15 mm with 7.5 mm diameter orifices (d); the distance between orifices (or inter-baffle distance), l_b , is 16.9 mm. The model test section comprised a tube of length (L) 144.5 mm and five orifices. A smooth reduction at the orifices was modelled to best represent the real geometry of the NiTech[®] glass COBR, as shown in Figure 4.1(b).

The fluid considered in these simulations is a single-phase fluid with density $\rho = 997 \text{ kg/m}^3$ and dynamic viscosity $\mu = 2 \times 10^{-2} \text{ Pa.s}$. Isothermal conditions were assumed. Table 4.1 lists the conditions used to study the interaction between the oscillatory conditions (frequency and amplitude) and net flow,

and their influence on the power dissipation. The oscillatory frequency was set at between 1 Hz and 2 Hz and the oscillatory amplitude was either 5 mm or 10 mm (i.e. $0.3l_b$ – $0.6l_b$). These values of amplitude fall in the optimal operational range of amplitudes described in previous studies (Brunold et al., 1989; Gough et al., 1997; Soufi et al., 2017). The net flow and oscillatory Reynolds numbers corresponding to these conditions were in the ranges 6–27 and 24–96, respectively, ensuring axisymmetrical laminar flow since it is well below the transition to chaotic flow, i.e. for oscillatory Reynolds numbers less than 250 (Stonestreet and Van Der Veecken, 1999; Zheng et al., 2007). These flow conditions have enabled the COBR to be modelled as a thin wedge with symmetry boundary conditions on the front and back faces, which computational times to be reduced drastically. A no-slip boundary condition was applied to the inner walls of the reactor and the area-averaged gauge pressure was set to 0 Pa at the outlet.

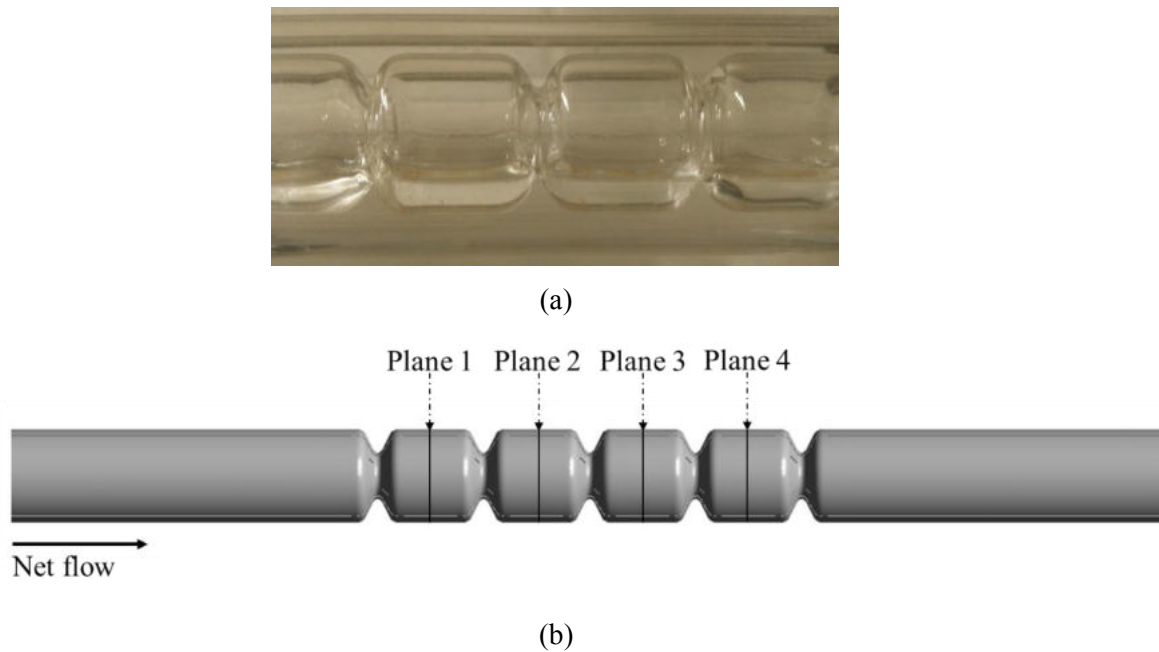


Figure 4.1: (a) Photograph of the NiTech® COBR and (b) the geometry of the COBR simulated by CFD.

The numerical simulations of the flow in the COBR have been performed using the commercial package ANSYS CFX 18.2, which applies a finite volume discretization based on a coupled solver to solve the Navier-Stokes equations.

For incompressible, laminar, Newtonian flow, the transient Navier-Stokes equations for mass and momentum conservation are:

$$\nabla \cdot \mathbf{u} = 0 \tag{4.14}$$

$$\frac{\partial(\rho\mathbf{u})}{\partial t} + \nabla \cdot (\rho\mathbf{u} \otimes \mathbf{u}) = -\nabla p + \nabla \cdot \boldsymbol{\tau} \tag{4.15}$$

The boundary condition at the inlet of the COBR was described by a time-dependent velocity profile:

$$u_{in} = 2\bar{u} \left(1 - \left(\frac{r}{R} \right)^2 \right) \quad (4.16)$$

where r is the radial position, $r = (y^2 + z^2)^{1/2}$, and R is the radius of the reactor and the mean velocity, \bar{u} , is the sum of the velocity of the net flow and the oscillatory flow given by:

$$\bar{u} = u_{net} + 2\pi f x_0 \sin(2\pi f t) \quad (4.17)$$

The convective terms were discretized using a second order bounded scheme and the second order backward Euler transient scheme was applied. Time steps were chosen to ensure the Courant-Friedrichs-Levy condition $Co < 1$ and such that the results were time-step independent, as detailed in Section 4.3.2. Simulations were considered to be converged when the normalized residuals fell below 10^{-6} .

Table 4.1: Simulation conditions proposed.

Case	Q (l h ⁻¹)	f (Hz)	x_o (mm)	Re_{net}	Re_o	Ψ
1	22.8	1	5	27	24	0.9
2	22.8	1.5	5	27	36	1.3
3	22.8	2	5	27	48	1.8
4	22.8	1	10	27	48	1.8
5	22.8	1.5	10	27	72	2.7
6	22.8	1.75	10	27	84	3.1
7	22.8	2	10	27	96	3.6
8	5.1	1	5	6	24	4.0
9	5.1	1.5	5	6	36	6.0
10	5.1	2	5	6	48	8.0
11	5.1	1	10	6	48	8.0
12	5.1	1.5	10	6	72	12.0
13	5.1	1.75	10	6	84	14.0
14	5.1	2	10	6	96	16.0

4.3.2. Meshing

A tetrahedral mesh with inflation layers was used in all cases. The body size of the mesh and the number of inflation layers were chosen such that the results were independent of these parameters. An example image of the mesh is presented in Figure 4.2.

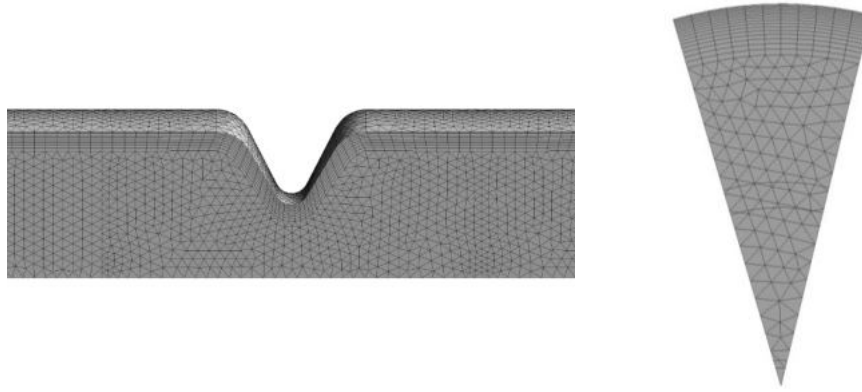


Figure 4.2: Example of tetrahedral mesh and inflation layers employed.

To ensure the numerical results are independent of the mesh density and time step, a detailed sensitivity analysis was carried out by studying the effect of different mesh sizes, inflation layer parameters and time steps on the results. The axial velocity, pressure and power dissipation were calculated and compared at the monitor points and lines shown in Figure 4.3, as well as the total power dissipation in one unit cell. $Re_o = 96$ and $Re_{net} = 27$ were used for all mesh density and time step studies, giving high axial velocity and a fast change of flow direction, which typically require a finer mesh. Details of all studied meshes and time steps are summarized in Table 4.2.

The simulations were run for several oscillation periods until the difference between the axial velocities and pressure values at different monitor points and lines from one oscillatory cycle to the next were small enough to be considered negligible. Once this was achieved, it was considered that a pseudo-steady state was reached and the performance characterization of the COBR was then conducted.

To minimize the effect of flow upstream and downstream of the baffles, the power dissipation was calculated using equations (14) and (15) in a single unit of the COBR delimited by lines L1 and L2 in Figure 4.3.

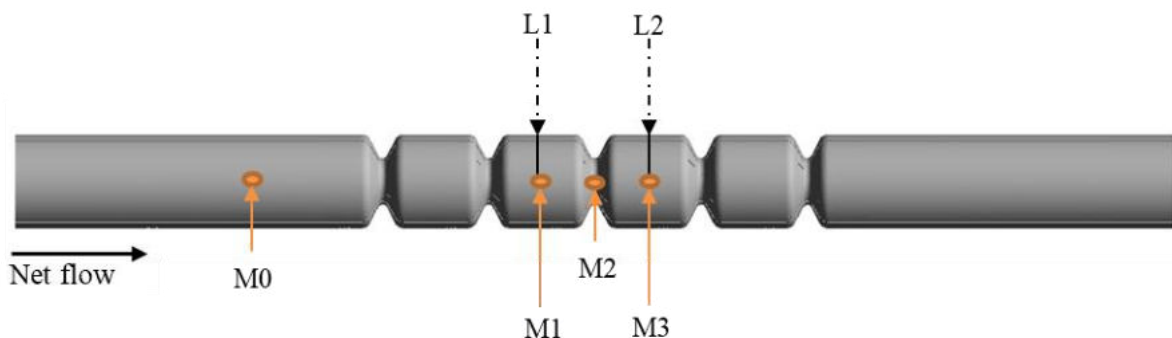


Figure 4.3: Locations of the monitor points and lines. M0: tube centreline, 8.45 mm upstream of the first orifice. M1 & L1: tube centreline, 8.45 mm upstream of the third orifice. M2: tube centreline, in the third orifice of the geometry. M3 & L2: tube centreline, at 8.45 mm downstream of the third orifice.

In order to evaluate mesh independency, the relative differences between data were calculated using the mean absolute deviation percent (MADP):

$$\text{MADP} = \frac{\sum_{t=1}^N |A_t - F_t|}{\sum_{t=1}^N |F_t|} \times 100 \quad (4.18)$$

where A_t is the actual value and F_t is the forecast value, both at time t . The results obtained with the finer mesh or smaller time step were used as F_t in the determination of relative error and values obtained with the coarser mesh were used for A_t . This method prevents having extremely large relative differences if F_t is close to or equal to zero, which occurs with other methods, such as the mean percentage error (MPE) or mean absolute percentage error (MAPE).

To study the effect of body mesh size, number of inflation layers and time step on the numerical results, five different meshes and three different time steps were chosen as described in Table 4.2. Examples of the studied meshes are shown in Figure 4.4.

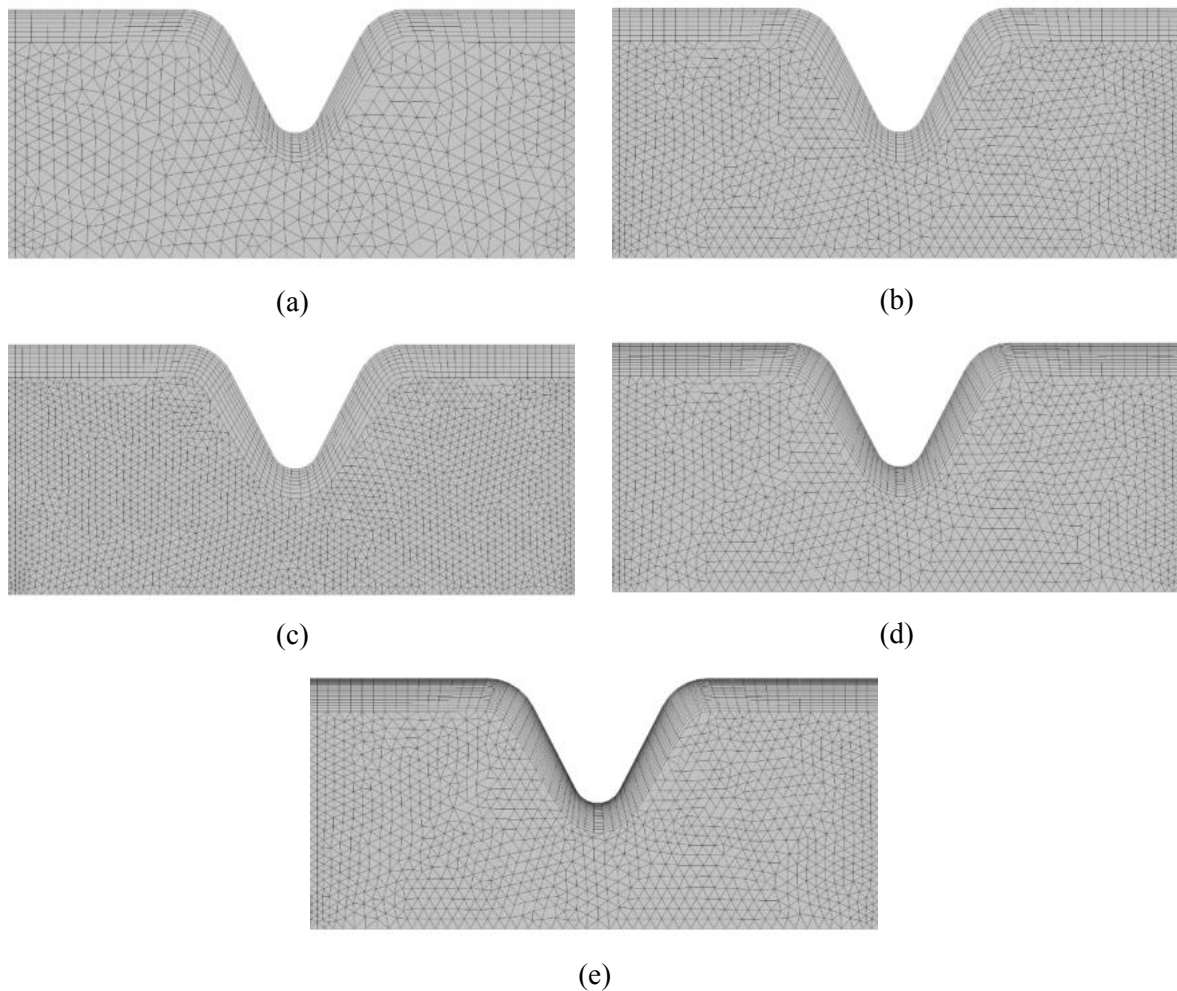


Figure 4.4: Images of the meshes used for the mesh and time step independency study: (a) Mesh 1, (b) Mesh 2, (c) Mesh 3, (d) Mesh 4, (e) Mesh 5.

Table 4.2: Characteristics of different meshes used for the mesh and time step independency study.

Mesh Time-step	1 1 ms	2 1 ms	3 1 ms	4 1 ms	5 1 ms	4 2 ms	4 0.5 ms
Max. face size (mm)	0.5	0.35	0.25	0.35	0.35	0.35	0.35
Max. thickness of inflation layers (mm)	1						
No. inflation layers	8	8	8	16	24	16	15
Growth rate	1.1						
Total no. elements	150 165	337 873	719 957	433 986	528 703	433 986	433 986
Δt (s)	0.001	0.001	0.001	0.001	0.001	0.002	0.0005
x_o (mm)	10						
f (hz)	2						
T (s)	0.5						
$\lambda = T/\Delta t$	500	500	500	500	500	250	1000
u_{net} (m/s)	3.59×10^{-2}						
u_{max} (m/s)	1.63×10^{-1}						
ψ	3.6						

Table 4.3 presents the effect of the body mesh size, inflation layers and time step on the axial velocity and pressure values using the MADP. The axial velocity and pressure tracked at the monitor points show excellent mesh independency for the Mesh 2 (330 000 elements) with MADP values close to 1% with respect to the solution using Mesh 3 (720 000 elements). Between Mesh 2, 4 and 5, the MADP values (below 1%) show that the axial velocity and pressure are already independent of the number of inflation layers with Mesh 2 (8 inflation layers).

Table 4.3: Quantification of the effect of body mesh, inflation layers and time step on the axial velocity and pressure at different monitor points (M0-M3) with the MADP.

	A_t : Mesh 1, 1 ms F_t : Mesh 3, 1 ms	A_t : Mesh 2, 1 ms F_t : Mesh 3, 1 ms	A_t : Mesh 2, 1 ms F_t : Mesh 5, 1 ms	A_t : Mesh 4, 1 ms F_t : Mesh 5, 1 ms	Mesh 4 A_t : 2 ms F_t : 0.5 ms	Mesh 4 A_t : 1 ms F_t : 0.5 ms
MADP values (%) – Axial velocity						
M0	0.71	0.23	0.18	0.09	0.16	0.03
M1	1.02	0.38	0.27	0.16	0.14	0.03
M2	1.78	0.82	0.13	0.09	0.14	0.03
M3	0.98	0.36	0.23	0.13	0.18	0.04
MADP values (%) – Pressure						
M0	1.04	0.34	0.21	0.14	0.23	0.07
M1	1.24	0.41	0.23	0.12	0.30	0.09
M2	1.12	1.07	0.21	0.13	0.32	0.09
M3	1.15	0.39	0.22	0.11	0.29	0.09

The values of power dissipation calculated using equations (4.12) and (4.13), and the MADP values are presented in Table 4.4. Figure 4.5 compares the power dissipation calculated by both methods, P_{VD} and P_{ME} for all three mesh sizes. Both P_{VD} and P_{ME} were normalized with the highest value obtained over the period using the finest mesh. An increase in body mesh density from Mesh 1 to Mesh 2 and Mesh 3 decreases the MADP of power dissipation calculated by both methods to less than 1% for P_{VD} and P_{ME} , and therefore shows mesh independency with Mesh 2. However, it is important to point out that the difference in power dissipation calculated by both methods P_{VD} and P_{ME} is still significant, being approximately 6% for the finest mesh (Mesh 3). This suggests that the resolution of the flow close to the wall is important for an accurate prediction of power dissipation.

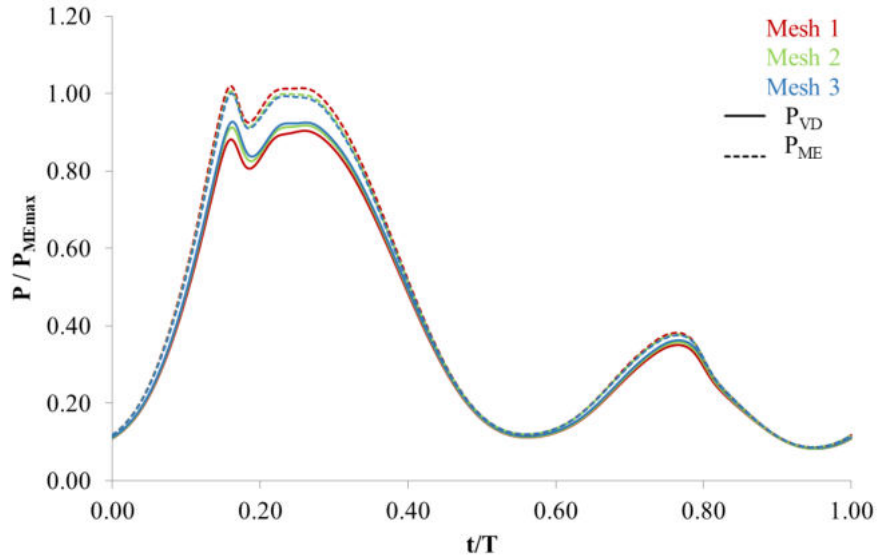


Figure 4.5: Comparison between power dissipation calculation methods for the three different mesh sizes.

The influence of the near-wall resolution (via the number of inflation layers) on the power dissipation can be seen in Table 4.4 and Figure 4.6 by comparing results for Meshes 2, 4 and 5. It can be seen that P_{VD} is sensitive to the number of inflation layers and that there are significant differences between the values obtained with Mesh 2 and those with Meshes 4 and 5. The difference in P_{VD} obtained with 16 and 24 inflation layers is very small, therefore demonstrating mesh independency for P_{VD} with 16 inflation layers (Mesh 4). The values of P_{ME} on the other hand show that P_{ME} is already mesh independent with just 8 inflation layers (Mesh 2). The values of P_{ME} are higher than those of P_{VD} and the latter increases towards the former when the number of inflation layers increases. This suggests that P_{VD} may be under predicted and it would be expected that the value of P_{VD} should reach the value calculated by the mechanical energy balance if the mesh is further refined near the walls. However, only a slight increase in P_{VD} is observed when the number of inflation layers is increased from 16 to 24. This means that an extremely large number of inflation layers would be required to reach the value of P_{ME} , thereby increasing the simulation times and computational costs prohibitively.

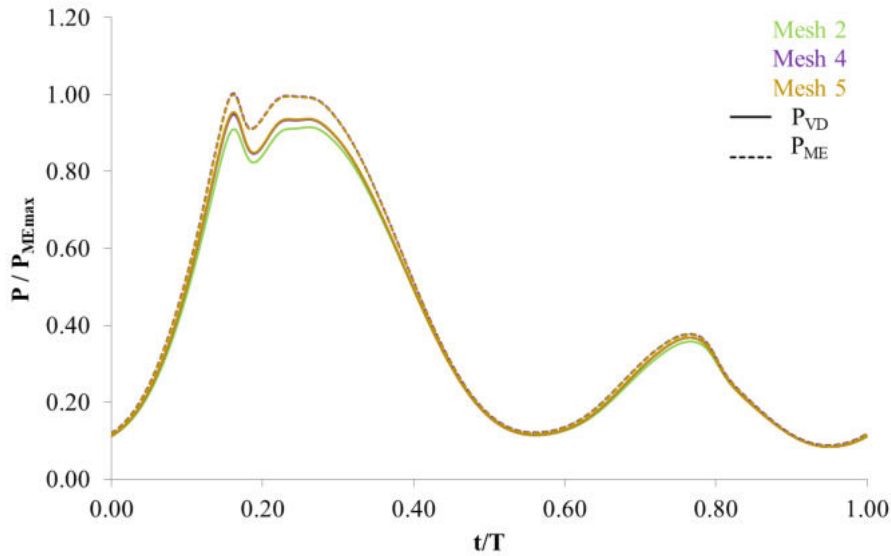


Figure 4.6: Comparison between power dissipation calculation methods for different numbers of inflation layers.

Figure 4.7 presents the normalised profiles of power dissipation calculated from the viscous dissipation at $t/T = 0.5$ at L2. It is clearly observed that most of the viscous dissipation takes place near the edges of the reactor and it increases as it approaches the wall, thereby explaining its strong dependency on the mesh resolution at the wall. Therefore, it is extremely important that computational meshes are highly refined at the wall in order to avoid poor prediction of power dissipation when calculated via the integration of viscous dissipation.

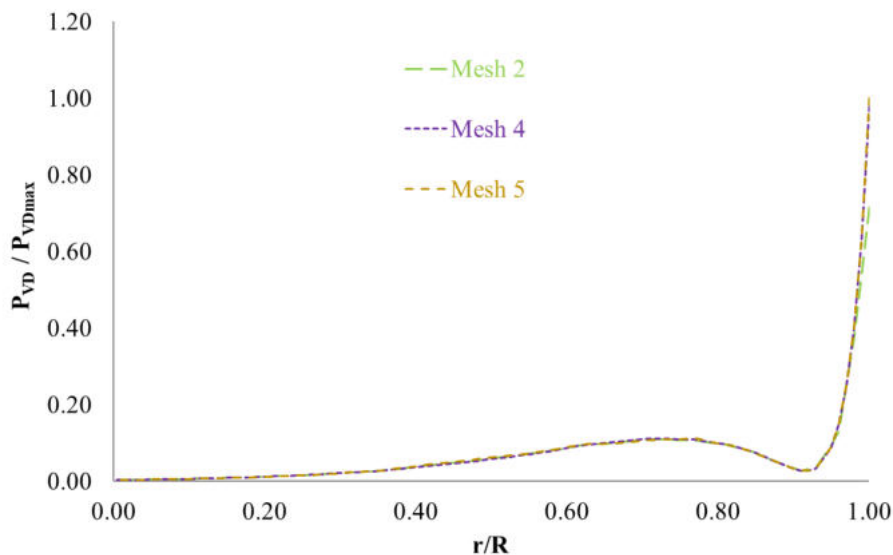


Figure 4.7: Power dissipation profiles determined via the integral of viscous dissipation at L2 as a function of the radius for three different numbers of inflation layers at $t/T = 0.60$.

Table 4.4: Influence of the body mesh, inflation layers, time step and power calculation method on power dissipation and MADP values.

	Mesh 1, 1 ms	Mesh 2, 1 ms	Mesh 3, 1 ms	MADP values (%)	
				A_t : Mesh 1, 1 ms F_t : Mesh 3, 1ms	A_t : Mesh 2, 1 ms F_t : Mesh 3, 1 ms
$P_{VD\ Total}$ (W)	3.51×10^{-5}	3.58×10^{-5}	3.61×10^{-5}	2.77	0.83
$P_{ME\ Total}$ (W)	3.90×10^{-5}	3.85×10^{-5}	3.83×10^{-5}	1.83	0.52
	Mesh 2, 1 ms	Mesh 4, 1 ms	Mesh 5, 1ms	A_t : Mesh 2, 1 ms F_t : Mesh 5, 1 ms	A_t : Mesh 4, 1 ms F_t : Mesh 5, 1 ms
$P_{VD\ Total}$ (W)	3.58×10^{-5}	3.66×10^{-5}	3.68×10^{-5}	2.71	0.54
$P_{ME\ Total}$ (W)	3.85×10^{-5}	3.86×10^{-5}	3.85×10^{-5}	0.00	0.26
	Mesh 4, 2 ms	Mesh 4, 1 ms	Mesh 4, 0.5 ms	A_t : Mesh 4, 2 ms F_t : Mesh 4, 0.5 ms	A_t : Mesh 4, 1 ms F_t : Mesh 4, 0.5 ms
$P_{VD\ Total}$ (W)	3.66×10^{-5}	3.66×10^{-5}	3.67×10^{-5}	0.27	0.27
$P_{ME\ Total}$ (W)	3.78×10^{-5}	3.86×10^{-5}	3.89×10^{-5}	2.83	0.77

Mesh 4 (0.35 mm body mesh size and 16 inflation layers) was used to study the influence of the time step, since it showed mesh independency for power dissipation. Three values of time steps – 0.5 ms, 1 ms and 2 ms – were used to evaluate mesh independency. Table 4.3 shows that both the axial velocity and pressure are independent of time step for a value of 2 ms, with MADP values lower than 1%. In Table 4.4 and Figure 4.8, it can be noticed that P_{VD} is already time step independent at 2 ms (with differences less than 1% over the entire cycle), whilst P_{ME} only becomes time step independent at 1 ms. A time step of 1 ms is therefore considered as the minimum time step required for solution independency.

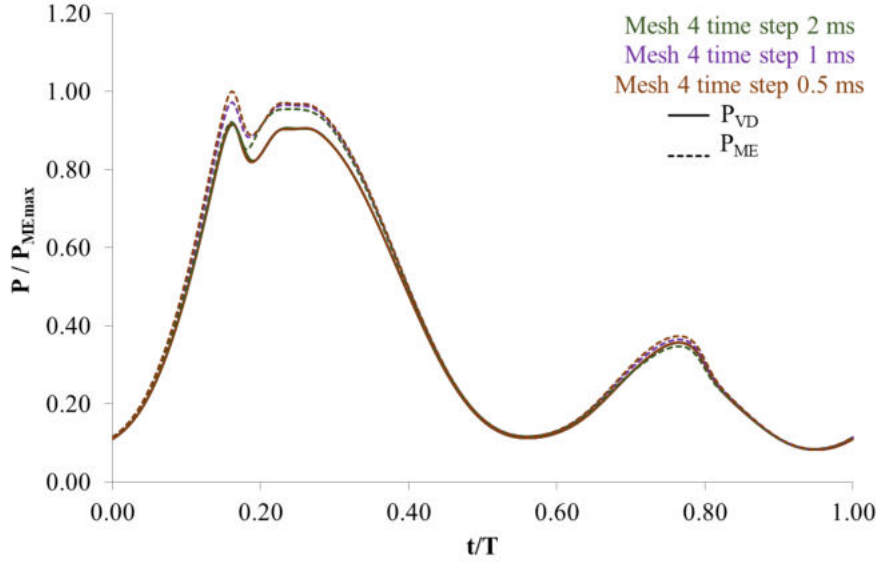


Figure 4.8: Comparison between power dissipation calculation methods for different time steps.

4.3.3. Implications for the calculation of P_{ME}

Table 4.5 presents the time-averaged value of P_{ME} over one oscillation cycle, as well as the time-averaged values of each term given in equation (4.11). Term 1 is shown to be sensitive to the time step, while Term 3 is sensitive to the mesh size. Term 1 decreases as the time step decreases, whilst Term 3 decreases as the mesh size is reduced. The influence of the number of inflation layer does not show any remarkable influence over the value of any of the three terms of the P_{ME} equation. Despite these reductions, it can be seen that the values of Terms 1 and 3 are ten times smaller than that of Term 2; however, they do not reach a zero-value due to finite errors arising from discretisation of the equations. Terms 1 and 3 represent between 1-4% and 4-5% of the total power dissipation, respectively. As explained in Section 4.2, Terms 1 and 3 should be zero in the current case such that the power dissipation is only dependent on the work done by pressure on the fluid. Hence, to avoid this numerical error, P_{ME} is calculated using only the value of Term 2 in the rest of the study.

Table 4.5: Contribution of the individual terms of equation (4.11) on power dissipation P_{ME} .

	Mesh 1 1 ms	Mesh 2 1 ms	Mesh 3 1 ms	Mesh 4 1 ms	Mesh 5 1 ms	Mesh 4 2 ms	Mesh 4 0.5 ms
Term 1 (W)	-7.38×10^{-7}	-7.66×10^{-7}	-7.93×10^{-7}	-7.71×10^{-7}	-7.57×10^{-7}	-1.49×10^{-6}	-3.94×10^{-7}
Term 2 (W)	4.19×10^{-5}	4.12×10^{-5}	4.10×10^{-5}	4.13×10^{-5}	4.12×10^{-5}	4.13×10^{-5}	4.13×10^{-5}
Term 3 (W)	-2.12×10^{-6}	-1.93×10^{-6}	-1.88×10^{-6}	-1.95×10^{-6}	-1.95×10^{-6}	-1.95×10^{-6}	-1.95×10^{-6}
P_{ME} (W)	3.90×10^{-5}	3.85×10^{-5}	3.83×10^{-5}	3.86×10^{-5}	3.85×10^{-5}	3.79×10^{-5}	3.90×10^{-5}
Term 1/Term 2 (%)	1.76	1.86	1.93	1.87	1.84	3.61	0.95
Term 3/Term 2 (%)	5.06	4.68	4.58	4.72	4.73	4.72	4.72

4.4. Results and discussion

Figure 4.9 shows the time-averaged power density as a function of oscillatory Reynolds number for all operating conditions given in Table 4.1. As expected, the power density increases with an increase in the oscillatory intensity, i.e. $f \cdot x_o$. The effects of frequency and amplitude at constant oscillatory intensity ($Re_o = 48$) but different net Reynolds numbers are examined by comparing Cases 3 & 4 ($Re_{net} = 27$, $\psi = 1.8$) and Cases 10 & 11 ($Re_{net} = 6$, $\psi = 8$). For both Re_{net} , slightly higher values of power density were obtained when a higher frequency and a lower amplitude are combined. This may be explained by the fact that the average power dissipation in oscillatory systems is determined by pressure drop, which includes the contribution of both inertial and frictional forces (Jealous and Johnson, 1955). The inertial term involves acceleration, which in oscillatory flow is equal to $x_o(2\pi f)^2 \sin(2\pi ft)$. Since frequency is squared in this relationship, higher values of average power density are obtained when higher frequencies are used for a constant oscillatory Reynolds number.

The influence of net flow can also be studied in Figure 4.9 and it can be seen that for a given Re_o , as the net flow increases (i.e. the oscillatory to net velocity ratio ψ decreases), power density also increases. For high values of ψ , the contribution of the net flow becomes insignificant, because the intensity of the oscillatory flow greatly exceeds the contribution of the net flow. This trend can be observed explicitly in Figure 4.10. Whilst at $Re_o = 24$, an increase in the velocity ratio from 1 to 4 (by decreasing the net flow), reduces the power density by 71%. At $Re_o = 96$, increasing the velocity ratio from 4 to 16 only results in a reduction of power density by 12%. This result is of interest when operating COBRs in the recommended range of velocity ratios to ensure plug flow operation, i.e. $2 < \psi < 4$ (Stonestreet and Van Der Veecken, 1999); in such cases, it clearly appears to be important to take into account the effect of the net flow in the average power dissipation.

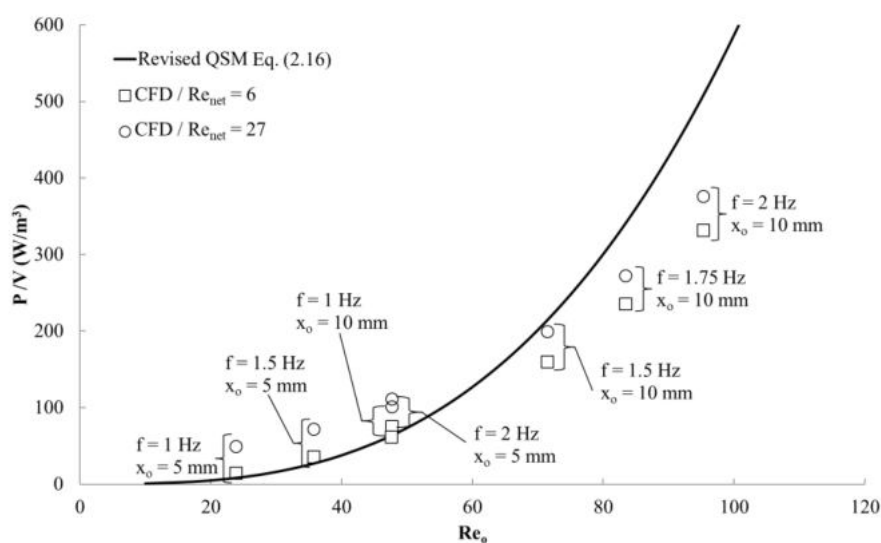


Figure 4.9: Power density as function of Re_o .

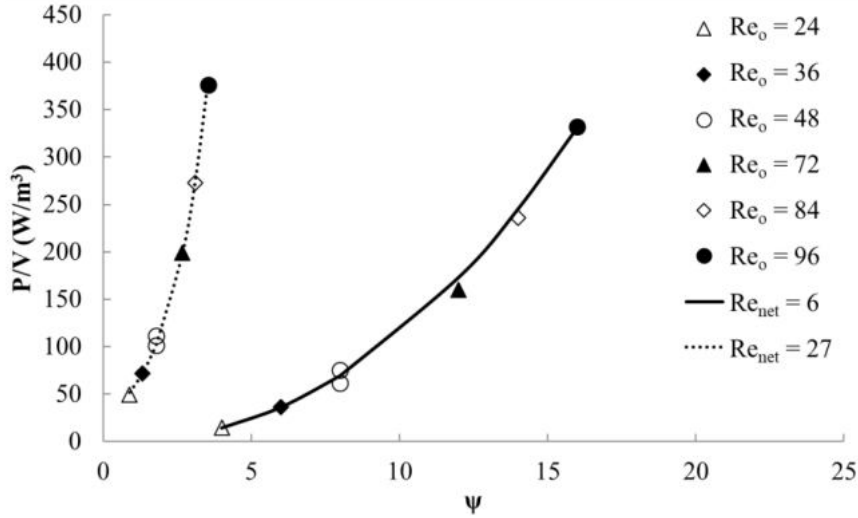


Figure 4.10: Power density as a function of velocity ratio (ψ).

The power density determined by equation (4.11) was initially compared with the power density calculated using the quasi-steady flow model given by equation (2.13), since the latter is recommended for high amplitudes ($5 < x_o < 0.3$ mm) and low frequencies ($0.5 < f < 2$ Hz). To include the contribution of the net flow in the power density, the correction coefficient from equation (2.15) was also used. For all cases, the power density was overestimated when equations (2.13) and (2.15) were used, with extremely high MADP values of 165% for $C_D = 0.7$, and 261% for $C_D = 0.6$. A similar result has been recently reported by Jimeno et al. (2018) for the same NiTech[®] COBR geometry used here and was explained by the power law dependency on the number of baffles cells, as well as the use of an inappropriate value of the discharge coefficient C_D for the smooth geometry of the orifice baffles. Jimeno et al. (2018) hence proposed the revised QSM (equation (2.16)) to better estimate the power density. Figure 4.9 also compares the power density obtained with the values calculated using the revised quasi-steady flow model (equation (2.16)). The differences between the current results with the revised QSM predictions present a MADP of 35.7%, with a better agreement at lower Re_{net} and Re_o but still poor agreement at higher Re_o . It can also be seen that the influence of net flow is not taken into account in the original model.

Figure 4.11 compares the power density of the revised quasi-steady flow model (equation (2.16)) with the current simulation results as a function of Re_T as defined by Jimeno et al. (2018). This total Reynolds number takes into account the effect of the net flow and the geometry of the COBR and is defined as:

$$Re_T = \frac{(2\pi f x_o + u_{net})\rho D}{\mu} \sqrt{\frac{\beta}{\alpha}} \quad (4.19)$$

$$\beta = \frac{l_b^{opt}}{l_b} \quad (4.20)$$

l_b^{opt} is defined as $1.5D$, and was proposed by Brunold et al. (1989) based on a qualitatively visual analysis of flow patterns. Even though this baffle spacing of $1.5D$ was considered ‘optimal’ and is now the most commonly used value in the literature, recent studies have demonstrated that the optimal baffle length depends on the process objective of interest (Soufi et al., 2017), making a single optimal value difficult to define for all applications and processes. For each set of data different curves can now be observed because the net flow is being taken into account in Re_T and this is more consistent with the current results of the simulated power density. It appears that the model fits the simulated data slightly better at $Re_{net} = 6$ than at $Re_{net} = 27$, and this can be related to the velocity ratio ranges of each curve. The highest net Reynolds number curve ($Re_{net} = 27$) presented the lowest values of ψ ($1 < \psi < 3.6$), which means a more significant influence of the net flow, however this is not taken into account in the determination of power density with the revised quasi-steady flow model. Power density as a function of Re_T as predicted by the QSM is presented in Figure 4.11 and compared with the data of Jimeno et al. (2018) and this work. Their COBR geometry is also a NiTech® single orifice baffled reactor with smooth constrictions, with a tube diameter of 15 mm, 7 mm diameter orifices and a distance between orifices of 23.5 mm. The shift between red and blue curves is due the nature of the fluid used: power density is higher at the same Re_T when working with more viscous fluids. Since Re_T is inversely proportional to the viscosity, the characteristic velocity needs to be increased in order to obtain the same Re_T when working with more viscous fluids. The power density is directly proportional to the pressure drop of the system, which increases with increasing flow velocities and viscosity due to increased friction. This observation is in agreement with the work by González-Juárez et al., (2018). Figure 4.11 shows that for the same fluid and system, power density – as predicted by the model – is independent of Re_{net} only for relatively high Re_T . For a specific fluid type and corresponding relatively low Re_T , plotting QSM as a function of Re_T results in the prediction of different power densities depending on Re_{net} . Jimeno et al. (2018) state that their revised quasi-steady flow model is valid in both OBRs (batch) and COBRs, claiming that the contribution of the net flow to the power dissipation is negligible when operating with velocity ratios between 6 and 150. However, the current results do not always corroborate this. Figure 4.10 shows the effect of the velocity ratio and the oscillatory Reynolds number on the power density. Whilst the data are scant, it appears that as the oscillatory Reynolds number increases, the impact of the velocity ratio on power density decreases. Indeed, for $Re_o = 96$ power density decreases by 12% when the velocity ratio increases from 4 to 16, whilst for $Re_o = 24$ it decreases by 71% when the velocity ratio increases from 1 to 4. However, it is also easily seen at a fixed velocity ratio, e.g. $\psi = 4$, the higher oscillatory Reynolds number results in significantly higher power density. Identifying a velocity ratio whereby the contribution of net flow to power dissipation is negligible does therefore not seem to be straightforward since it also depends on the oscillatory flow. As a result, the limits of validity of the revised QSM (where the contribution of the net flow to power density can be assumed negligible) remain unclear.

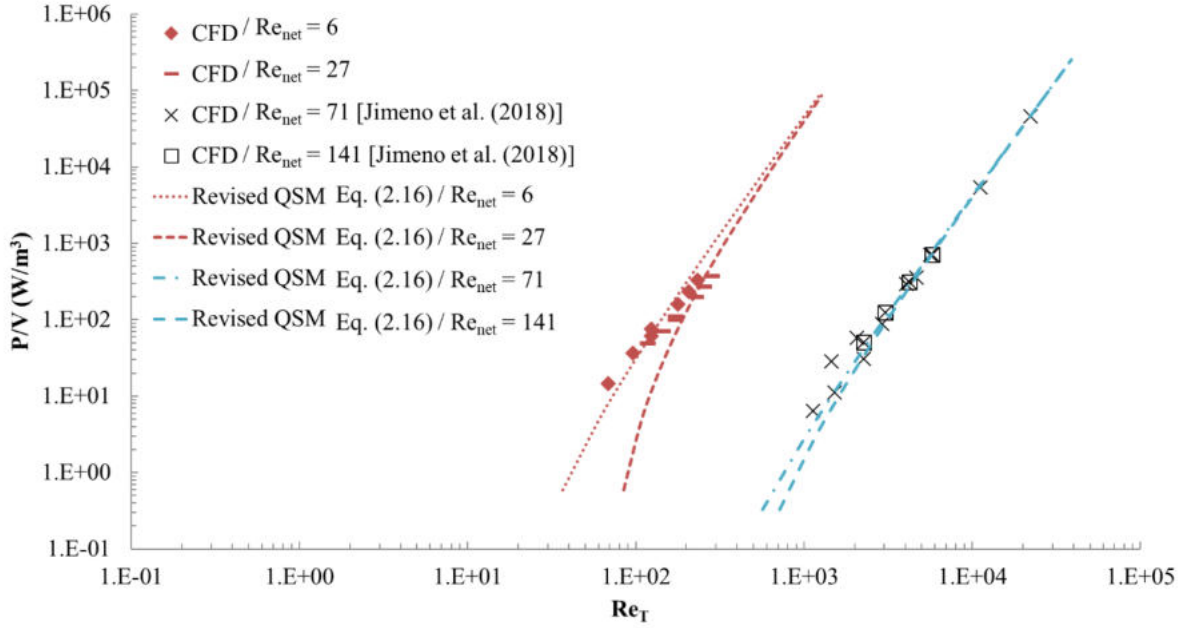


Figure 4.11: Power density as function of Re_T .

Although previous studies in the literature have tried to correlated power density with the oscillatory Reynolds number (e.g. González-Juárez et al., 2018; Jimeno et al., 2018), for chemical engineering design, it is more useful to plot a dimensionless form of the dissipated mechanical energy as a function of Reynolds number such that the effect of fluid properties are eliminated; the resulting plot depends on system geometry only. Some common examples are the friction factor for the flow in pipes or the power number in stirred tanks. One common feature of these charts is that for a specific geometry, the dimensionless number representing energy dissipation is constant in fully-developed turbulent flow, whilst it is inversely proportional to Reynolds number in laminar flow. In a similar manner, one can define a dimensionless power density $(P/V)^*$ as:

$$\left(\frac{P}{V}\right)^* = \frac{(P/V)D}{\rho(2\pi f x_o + u_{net})^3} \quad (4.21)$$

Figure 4.12 presents the dimensionless power density for the NiTech® COBR from the current simulations and those conducted by Jimeno et al. (2018). The data are compared with dimensionless power density that has been predicted from the revised QSM. It can be seen that for $Re_T < 300$, $(P/V)^*$ from the simulations is proportional to $(Re_T)^{-1}$ and for $Re_T > 1000$, $(P/V)^*$ is constant, as would be expected. From these data, the power density constants for the NiTech® geometry in laminar flow and in turbulent flow are found to be:

$$(P/V)^* = 330/Re_T \quad \text{for laminar flow } (\alpha = 0.25 / l_b = 1.1D) \quad (4.22)$$

$$(P/V)^* = 1.92 \quad \text{for turbulent flow } (\alpha = 0.22 / l_b = 1.6D) \quad (4.23)$$

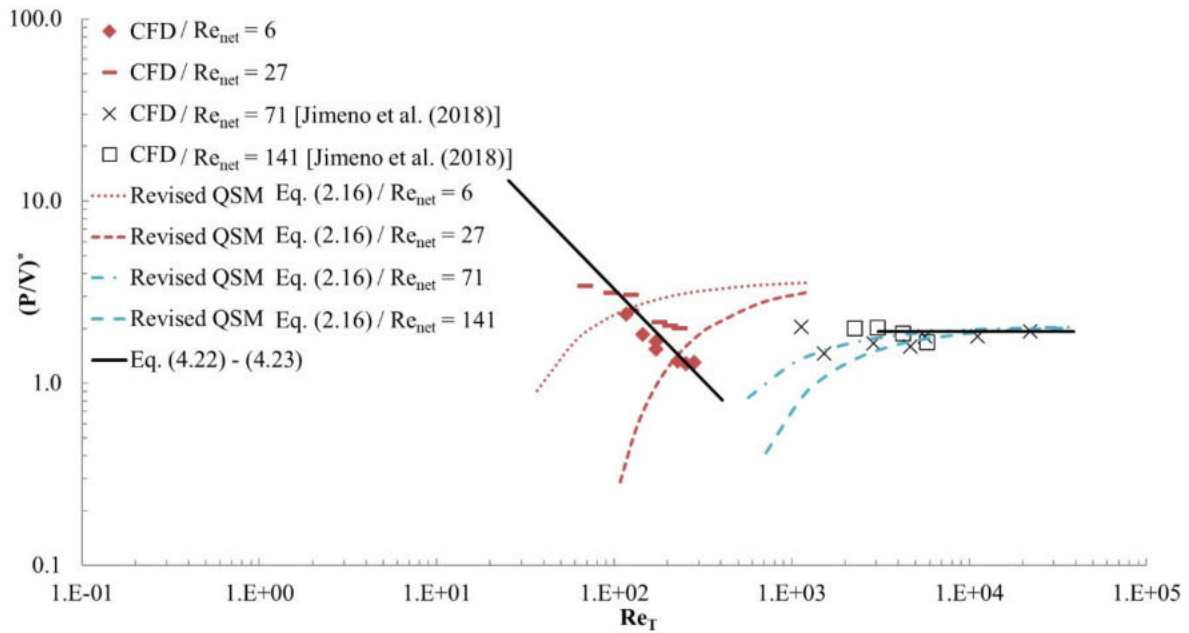


Figure 4.12: Dimensionless power density as a function of Re_T .

It can also be seen that whilst the revised QSM correctly predicts the constant value of $(P/V)^*$ in fully turbulent flow, it provides an unphysical representation of power density in the transitional and laminar flow regimes. The QSM is hence only useful for predicting power density in fully developed turbulent flow. However, it should be kept in mind that it may be difficult to reach turbulent flow in many applications either because the fluid viscosity is relatively high (e.g. liquid-liquid flows) or the net flow rates are lowered to increase residence times, therefore resulting in lower oscillatory velocities such that the velocity ratio is kept in a reasonable range. The power curve shown in Figure 4.12 is therefore a useful design tool for predicting power density and pressure drop in the NiTech® COBR over a range of flow regimes. It is obvious that the development of similar curves for other COBR and baffle geometries would also be of significant use.

4.5. Conclusions

CFD simulations have been carried out to evaluate power density in a COBR with single orifice baffles for different operating conditions.

The calculation of power dissipation using the simplified mechanical energy balance equation is preferred over the viscous dissipation equation, since when using the latter method it is difficult to resolve without using extremely fine mesh near the walls and consequently very high computational resources. Determination of power dissipation via the mechanical energy balance enables an exact value to be obtained, providing that mesh independence is demonstrated, which is the case here.

Comparison of computed power dissipation with that predicted by empirical quasi-steady flow models found in the literature shows that these models are still not able to correctly predict the values for all operating conditions and in particular when the flow is not fully turbulent. Indeed, when the flow is not fully turbulent, the QSM provides an unphysical representation of power density. The operating conditions used to define the limits of validity of the QSM therefore appear to be more complex than merely high/low frequencies and amplitudes, and the velocity ratio. Re_o and Re_{net} and the resulting flow regime play a very important role. By plotting dimensionless power density as a function of Reynolds number based on the sum of both the oscillatory and net flow velocities, Re_T , it has been demonstrated that dimensionless power dissipation is inversely proportional to Re_T in laminar flow and constant in turbulent flow, as is the case for flow in pipes and stirred tanks.

4.6. References

- Avila, M., Fletcher, D.F., Poux, M., Xuereb, C., Aubin, J., 2020. Predicting power consumption in continuous oscillatory baffled reactors. *Chem. Eng. Sci.* 212. <https://doi.org/10.1016/j.ces.2019.115310>
- Brunold, C.R., Hunns, J.C.B., Mackley, M.R., Thompson, J.W., 1989. Experimental observations on flow patterns and energy losses for oscillatory flow in ducts containing sharp edges. *Chem. Eng. Sci.* 44, 1227–1244. [https://doi.org/10.1016/0009-2509\(89\)87022-8](https://doi.org/10.1016/0009-2509(89)87022-8)
- González-Juárez, D., Herrero-Martín, R., Solano, J.P., 2018. Enhanced heat transfer and power dissipation in oscillatory-flow tubes with circular-orifice baffles: a numerical study. *Appl. Therm. Eng.* 141, 494–502. <https://doi.org/10.1016/j.applthermaleng.2018.05.115>
- Gough, P., Ni, X., Symes, K.C., 1997. Experimental flow visualisation in a modified pulsed baffled reactor. *J. Chem. Technol. Biotechnol.* 69, 321–328. [https://doi.org/10.1002/\(SICI\)1097-4660\(199707\)69](https://doi.org/10.1002/(SICI)1097-4660(199707)69)
- Jealous, A.C., Johnson, H.F., 1955. Power requirements for pulse generation in pulse columns. *Ind. Eng. Chem.* 47, 1159–1166. <https://doi.org/10.1021/ie50546a021>
- Jimeno, G., Lee, Y.C., Ni, X., 2018. On the evaluation of power density models for oscillatory baffled reactors using CFD. *Chem. Eng. Process. - Process Intensif.* 134, 153–162. <https://doi.org/10.1016/J.CEP.2018.11.002>
- Soufi, M.D., Ghobadian, B., Najafi, G., Mousavi, S.M., Aubin, J., 2017. Optimization of methyl ester production from waste cooking oil in a batch tri-orifice oscillatory baffled reactor. *Fuel Process. Technol.* 167, 641–647. <https://doi.org/10.1016/j.fuproc.2017.07.030>
- Stonestreet, P., Van Der Veecken, P.M.J., 1999. The effects of oscillatory flow and bulk flow components on residence time distribution in baffled tube reactors. *Chem. Eng. Res. Des.* 77, 671–684. <https://doi.org/10.1205/026387699526809>
- Zheng, M., Li, J., Mackley, M.R., Tao, J., 2007. The development of asymmetry for oscillatory flow within a tube containing sharp edge periodic baffles. *Phys. Fluids* 19. <https://doi.org/10.1063/1.2799553>

Chapter 5: Mixing performance in continuous oscillatory baffled reactors

5.1. Introduction

Determination of spatial mixing quality in COBRs requires knowledge of concentration fields of a tracer in cross-sections along the length of the reactor. Whilst information of this type can be obtained experimentally using Planar Laser Induced Fluorescence (PLIF), its application to COBRs (in which mixing relies on the interaction of oscillatory flow with the reactor baffles upstream of the measurement plane) is technically not feasible. CFD simulations are therefore an attractive solution to evaluate three-dimensional spatial mixing quality in COBRs. Nevertheless, such simulations are not without major challenges, including the need for a highly refined mesh on a sufficiently long reactor model and the consequent computational resources to correctly resolve the time-dependent concentration gradients.

In the current literature, there is limited information on the influence of operating parameters on spatial mixing quality and how a secondary feed should be introduced into continuous oscillatory baffled reactors (COBR) to achieve good mixing quality. The objective of this Chapter is to begin to explore the impact of the position where a secondary feed enters the COBR on the spatial mixing quality. To do this, transient laminar flow CFD simulations are performed for a passive non-reactive tracer, which is released in the COBR in three theoretical ways in a NiTech® COBR with smooth constrictions. The simulations enable access to time-resolved concentration fields throughout the volume of the reactor and the influence of operating conditions on macromixing performance is evaluated by analysing the spatial uniformity of the tracer using the areal distribution method developed by Alberini et al. (2014a). The work presented in this chapter has been published in *Chemical Engineering Science*, volume 219 (Avila et al., 2020).

5.2. Characterization of mixing performance

5.2.1. Statistical analysis of concentration distribution

Mixing performance was evaluated by studying the tracer concentration over the reactor length. The uniformity of tracer concentration is assessed at different cross-sections in the COBR, each located midway between baffles. The dimensionless tracer concentration in each computational cell, C_i^* , is:

$$C_i^* = \frac{C_i}{\bar{C}} \quad (5.1)$$

where C_i is the instantaneous tracer concentration and \bar{C} corresponds to the fully mixed concentration assuming perfect blending of the tracer:

$$\bar{C} = C_0 \left(\frac{q}{Q + q} \right) \quad (5.2)$$

where C_0 is the concentration of tracer in the injected fluid, q is the mass flow of tracer and Q is the net flow rate.

The plane-averaged concentration, C^* , of the non-reactive tracer over cross-sections at each time step of the transient solution and different times of the oscillatory cycle, t/T , was then calculated. If $C^* > \bar{C}$, it is referred to in this study as overly concentrated.

5.2.2. Areal distribution of mixing intensity

The areal distribution method enables mixing intensity in laminar flow to be analysed by considering areas in a cross-section that have the same level of mixing (Alberini et al., 2014a). The results of the areal distribution of mixing intensity represent a record of how tracer is mixed over time, taking into account both the intensity of segregation (or uniformity of concentration) and the scale of segregation. This methodology enables identification of poorly mixed areas (both over-concentrated and under-concentrated regions), unlike the coefficient of variance or maximum striation thickness, which can lead to misleading interpretation of mixing performance when used separately (Alberini et al., 2014a; Kukukova et al., 2009, 2011).

In practice, the areal distribution method analyses the distribution of concentration at different cross-sections in the flow that have been obtained by either experimental (e.g. PLIF) or numerical techniques. Based on the perfectly mixed concentration criterion \bar{C} , the limits for a certain level of mixing, $X\%$, can be defined. For example, to determine the amount of the cross-sectional area that is in a state of 90% mixing or greater, two limits are firstly defined: $C_{X-} = 0.9\bar{C}$ and $C_{X+} = 1.1\bar{C}$. The total area whereby the concentration satisfies $C_{X-} < C_i < C_{X+}$ is then determined and this corresponds to the amount of fluid in the cross-section, which is 90% mixed or greater.

5.3. Numerical method

5.3.1. Geometry and operating conditions

The geometry studied is the NiTech[®] COBR described in Chapter 4 section 4.3.1. The model test section comprises a tube of length 144.5 mm and five orifices. A smooth reduction at the orifices is modelled to best represent the real geometry of the NiTech[®] glass COBR, as shown in Figure 5.1.

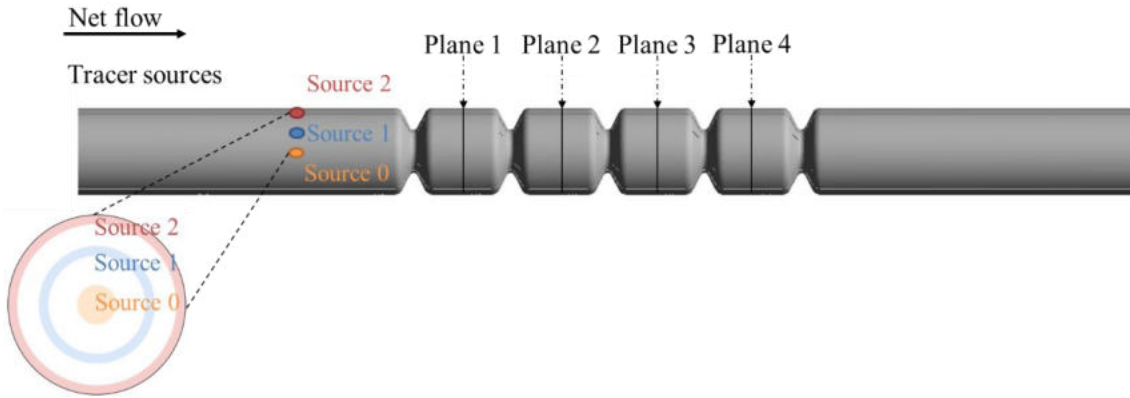


Figure 5.1: Geometry of the COBR simulated by CFD with the location of tracer sources and monitoring planes.

The fluid considered in these simulations is a single-phase fluid with density $\rho = 997 \text{ kg/m}^3$ and dynamic viscosity $\mu = 2 \times 10^{-2} \text{ Pa}\cdot\text{s}$. Isothermal conditions are assumed. A Schmidt number (Sc) of 1000 is chosen, as this is characteristic of liquid systems.

A 2^k factorial design is chosen to study the interaction between oscillatory conditions (frequency and amplitude) and net flow, and their influence on the mixing performance. Two different levels are studied for each of the three variables and Table 5.1 lists the conditions used. The oscillatory frequency was set at between 1 Hz and 2 Hz and the oscillatory amplitude was either 5 mm or 10 mm (i.e. $0.3l_b$ – $0.6l_b$). These values of amplitude fall in the optimal operational range of amplitudes described in previous studies (Brunold et al., 1989; Gough et al., 1997; Soufi et al., 2017). The net flow and oscillatory Reynolds numbers corresponding to these conditions are in the ranges 6–27 and 24–96, respectively, ensuring axi-symmetrical laminar flow since it is well below the chaotic flow transition, i.e. for oscillatory Reynolds numbers less than 250 (Stonestreet and Van Der Veecken, 1999; Zheng et al., 2007). These flow conditions enable the COBR to be modelled in 2D, allowing computational times to be reduced drastically. A no-slip boundary condition is applied to the inner walls of the reactor and the area-averaged gauge pressure was set to 0 Pa at the outlet. To obtain a wider vision of the influence of operating conditions on mixing quality in the first sections of the reactor, the simulations cover values of the velocity ratio ψ outside the range for plug flow as recommended by Stonestreet and Van Der Veecken (1999).

Table 5.1: Experimental conditions proposed by 2^k factorial design.

Case	Q (l h ⁻¹)	f (Hz)	x_o (mm)	Re_{net}	Re_o	Ψ
1	22.8	1	5	27	24	0.9
2	22.8	2	5	27	48	1.8
3	22.8	1	10	27	48	1.8
4	22.8	2	10	27	96	3.6
5	5.1	1	5	6	24	4.0
6	5.1	1	10	6	48	8.0
7	5.1	2	5	6	48	8.0
8	5.1	2	10	6	96	16.0

In order to analyse mixing performance, a passive inert tracer is introduced into the reactor. The presence of this tracer has a minimal effect on the hydrodynamic flow of the fluid since the flow rate ratio $\left(\frac{q}{Q+q}\right)$ is set to 3×10^{-4} . It should be noted that the final results do not depend on this value since the concentration data are presented relative to the well-mixed state. The tracer is introduced continuously at three different theoretical locations in the COBR. Source 0 is located at the centreline of the COBR, Source 1 is upstream of the edge of the first baffle, and Source 2 is at the wall of the reactor. Source 0 represents a coaxial source, and Sources 1 and 2 are annular sources, as shown in Figure 5.1. Whilst the latter two are not practical possibilities for feed streams, the differences in the three locations enable the impact of the inlet location on mixing to be evaluated. Due to the oscillatory flow, the tracer can flow out of the inlet and outlet boundaries. However, when the flow re-enters the reactor it does not contain any tracer. This can result in erroneous concentration fields. Therefore, in order to guarantee that tracer is not lost via the inlet boundary condition, and that any the tracer that leaves and returns as new fluid (without tracer) via the outlet does not reach the baffled zone, 30 mm portions of straight pipe have been added before and after the baffled zone. Tracer concentration and mixing performance are analysed as described in Section 5.2 on four cross-sectional planes located between the baffles, which are depicted in Figure 5.1.

The numerical simulations of the flow in the COBR have been performed using the commercial package ANSYS Fluent 2019R3, which applies a finite volume discretization to solve the Navier-Stokes equations.

For incompressible, laminar, Newtonian flow, the transient Navier-Stokes equations for mass and momentum conservation are:

$$\nabla \cdot \mathbf{u} = \sum_{i=1}^3 \dot{S}_{Ci} \quad (5.3)$$

$$\frac{\partial(\rho \mathbf{u})}{\partial t} + \nabla \cdot (\rho \mathbf{u} \otimes \mathbf{u}) = -\nabla p + \nabla \cdot \boldsymbol{\tau} \quad (5.4)$$

The boundary condition at the inlet of the COBR is described by a time-dependent velocity profile:

$$u_{in} = 2\bar{u} \left(1 - \left(\frac{r}{R} \right)^2 \right) \quad (5.5)$$

where r is the radial position R is the radius of the reactor and the mean velocity, \bar{u} , is the sum of the velocity of the net flow and the oscillatory flow given by:

$$\bar{u} = u_{net} + 2\pi f x_0 \sin(2\pi f t) \quad (5.6)$$

The gauge pressure was set to zero at the outlet, the tube wall was set to have no slip.

The transport of the tracer is described by the scalar transport equation without chemical reaction for incompressible flow:

$$\frac{\partial C_i}{\partial t} + \nabla \cdot (C_i \mathbf{u}) - \nabla \cdot (D_f \nabla C_i) = \dot{S}_{C_i} \quad (5.7)$$

where \dot{S}_{C_i} is a source term that is used to inject tracer into various zones in the domain, as described above. The diffusion coefficient D_f was set to give a Schmidt number of 1000. The concentration value was set to zero at the inlet and at the start of the simulation.

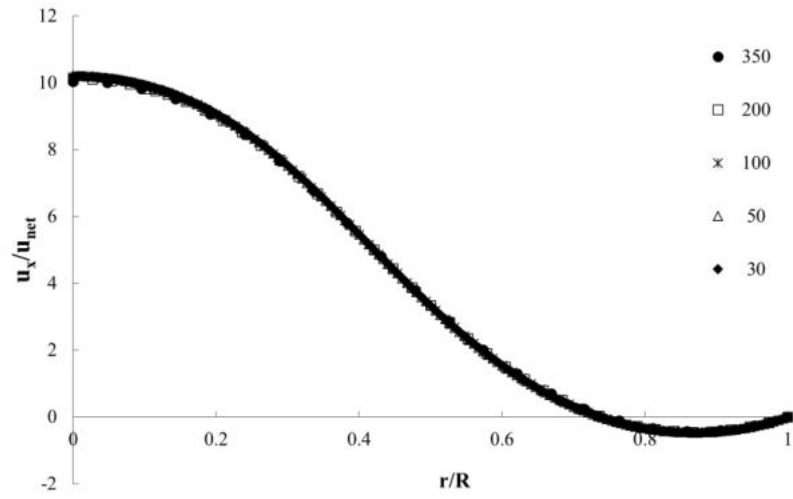
As will be evident in the next section, extremely fine meshes are needed to avoid numerical diffusion of the high Schmidt number scalars. Our previous simulations to study the power dissipation (Chapter 4) used ANSYS CFX, simulating a wedge of the true geometry. However, for the study of mass transfer it soon became evident that massively finer meshes are needed and that there would be significant benefits in using ANSYS Fluent for these simulations. This is because ANSYS Fluent allows the use of a true 2D axisymmetric solver, thereby reducing the mesh requirement and reducing the number of equations to be solved. It also contains non-iterative solvers that provide very fast transient simulations. Here the fractional timestep method was employed to couple pressure and velocity. Finally, ANSYS Fluent has high order differencing schemes, which are not present in ANSYS CFX. Here gradients were calculated by the Green-Gauss nodal scheme, pressure via a second order method, momentum using the third order QUICK scheme, mass fractions using the third order bounded MUSCL scheme and the bounded second order scheme was applied to the time derivatives. A non-dimensional local residual convergence target of 10^{-5} . A timestep that resulted in 500 steps per period was found to give timestep independent results.

5.3.2. Meshing and solution independence

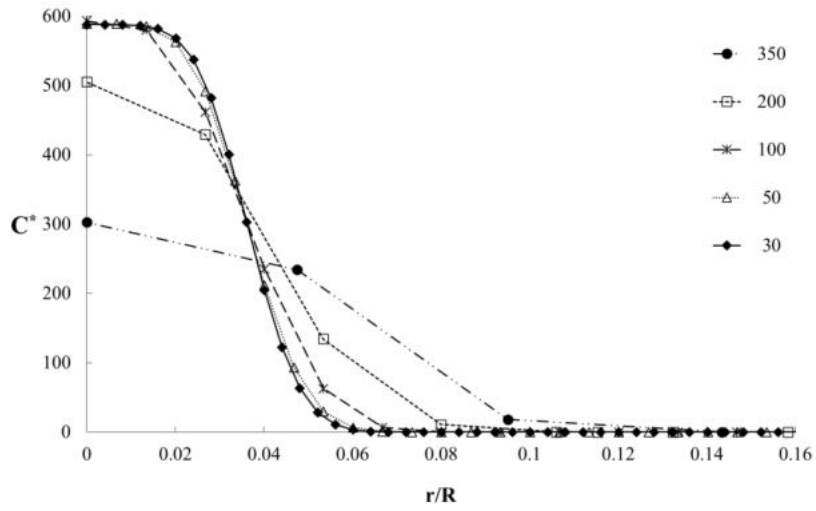
Simulations were performed to determine the mesh requirement to obtain effectively mesh independent solutions. The 2D mesh was constructed in ANSYS Meshing using a paving algorithm, which used mostly quadrilateral cells whilst occasionally introducing triangular cells to fit geometric constraints. The starting point was a mesh size of 350 microns that was shown to give mesh independent simulations for the hydrodynamics (Chapter 4, section 4.3.2); this mesh was then progressively refined with the smallest cell size used being 30 microns.

Several cases with different oscillating and net flow operating conditions were studied, and the worst-case scenario for mixing is presented. This occurs when there is high net flow causing high Péclet numbers. Figure 5.2 contains the mesh dependency of the axial velocity and the tracer concentration when released from the axis and mid-baffle sources. Data are presented in non-dimensional form. It is evident from Figure 5.2(a) that the velocity field is mesh independent using a 350 micron mesh, which consistent with the observation made in our earlier results using ANSYS CFX (Chapter 4, section 4.3.2). However, when using this mesh size, the concentrations are highly diffused. For the axial injection (Source 0) the results are almost mesh independent for a 100 micron mesh and are definitely independent for a 50 micron mesh. For Source 1 it is apparent that the very thin striation is not yet fully mesh independent for the 30 micron mesh but the shape of the profile is not too different to that for the 50 micron mesh.

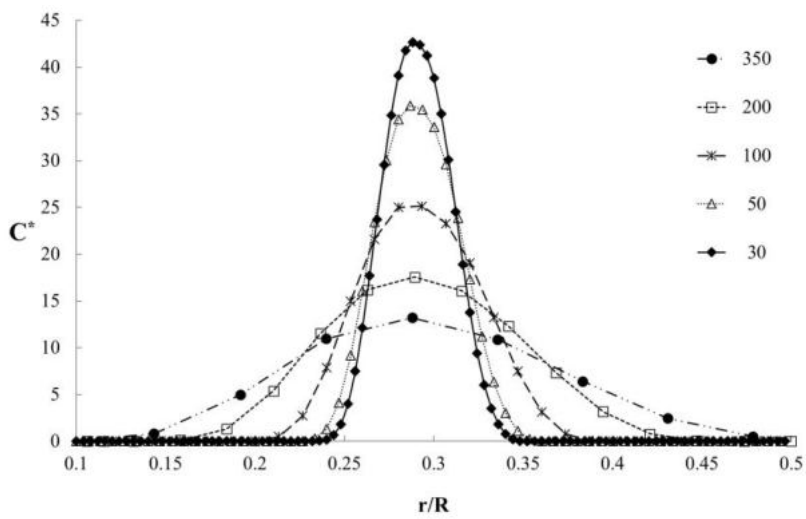
Based on the above results and the analysis of other cases, it was decided to use a 50 micron mesh as a good compromise between accuracy and computing time. This mesh size gave a cell count of 1.46 million for the computational domain. Additionally, timestep independence was tested and observed to be achieved with 500 steps per period. The use of second order time differencing proved to be important in achieving independence with this timestep size.



(a)



(b)



(c)

Figure 5.2: Radial variation of (a) axial velocity and scalars released (b) at the axis (Source 0) and (c) mid-baffle (Source 1) at one quarter of the time through the first period for Case 1. The legend gives the mesh size in microns.

5.4. Results and discussion

To study the effect of oscillatory conditions and tracer source position (as shown in Figure 5.1) on the mixing performance in the COBR, the dispersion of an inert tracer was simulated. Mixing performance was assessed after the average tracer concentration values at the different monitoring planes had reached a pseudo steady state (i.e. data do not present differences between consecutive oscillatory periods).

5.4.1. Flow and tracer patterns

Figure 5.3 shows the velocity vectors over an oscillatory cycle for Case 5 ($Re_{net} = 6$, $Re_o = 24$, $\psi = 4$). In this figure, the process of flow separation, generation, propagation and detachment of vortices can be observed at different stages of flow acceleration and deceleration during the oscillatory period. During the start of acceleration (for both the forward and backward phases, Figure 5.3(a) and Figure 5.3(d)), flow separation begins and small eddy structures, which are not longer than the baffle width, are generated in front or behind the baffle constrictions, depending of the direction of the flow. As the cycle progresses, the toroidal vortex propagates towards the next baffle, until the flow speed reaches its maximum value (Figure 5.3(b) and Figure 5.3(e)). Once the flow reversal phase starts, the vortex grows to fill most of the space between the baffles until the flow begins to be completely reversed (Figure 5.3(c) and Figure 5.3(f)). With the decrease of the velocity during the flow reversal, the vortex acts as an obstacle. This makes the flow move along the reactor wall, detaching the toroidal vortex from the wall and engulfing it into the centre of the reactor at the start of flow acceleration and the cycle starts again (Figure 5.3(a)). The generation and presence of vortices in the baffle area and their displacement from the wall to the centre of the reactor ensures radial mixing, unlike laminar flow in a straight tube. These flow patterns have already been identified in both OBR and COBR in the literature (Brunold et al., 1989; Gough et al., 1997; Mazubert et al., 2016; Ni et al., 2002). Velocity vectors over one oscillation period for all cases are presented in Appendix 1.

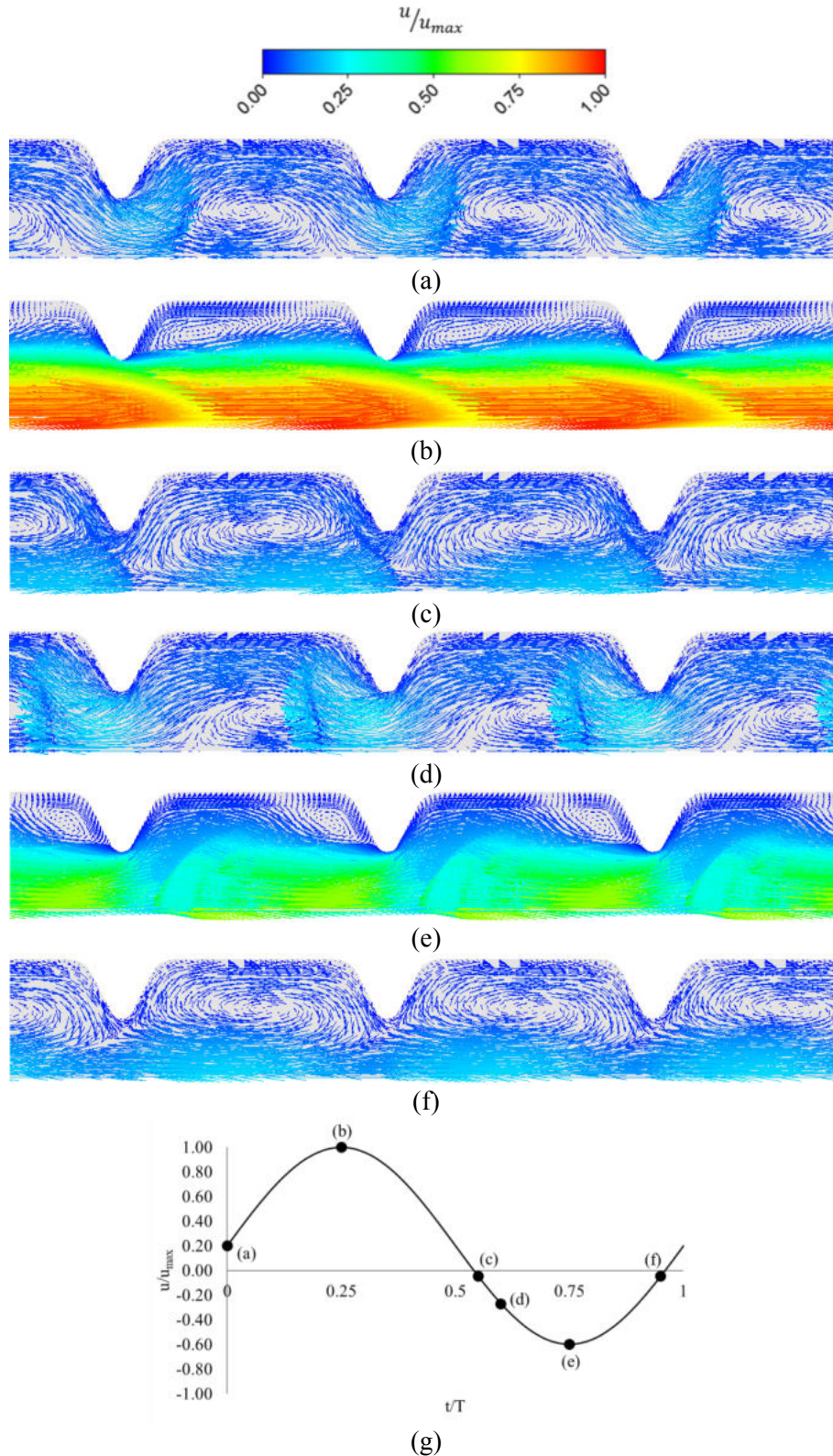


Figure 5.3: Velocity vectors during the oscillatory flow for Case 5 ($Re_{net} = 6$, $f = 1$ Hz, $x_o = 5$ mm): (a) $t/T = 0.00$, (b) $t/T = 0.25$, (c) $t/T = 0.55$, (d) $t/T = 0.6$, (e) $t/T = 0.75$, (f) $t/T = 0.95$, (g) normalized inlet velocity over an oscillatory period for Case 5 with the representation of the positions of the different times t/T during the period.

The tracer patterns are strongly influenced by the synergy of the source position, and the net and oscillatory flows. To better understand this interaction, Figure 5.4 shows the evolution of the tracer distribution over one oscillatory cycle for the different source locations using Case 1 as an example. Case 1 has a net Reynolds number of 27 and a velocity ratio equal to 0.9. Figure 5.4(a) shows that when the tracer is introduced at the centre of the tube, it is transported down the central axis of the reactor, creating a region of highly concentrated tracer along the axial axis. The eddies created by the interaction of the oscillatory flow with the baffles do not enable effective radial mixing of the tracer. On the other hand, when the tracer is introduced from Source 1, which is in-line with the baffle edge midway between the centre and the wall of the tube as shown in Figure 5.4(b), it can be seen that there is an improvement in radial mixing of the tracer along the reactor, resulting in an increase in the homogeneity and reaching values of C^* between 25 and 75% in the length of reactor simulated. A region of highly concentrated tracer is still present; however, it is disrupted by the baffle edge and then moves down the reactor over the oscillation cycle. This pattern allows shorter mixing lengths to be obtained compared with Source 0. Figure 5.4(c) shows the concentration fields when the tracer is introduced at the wall at Source 2. In this case, the tracer moves slowly along the wall (where the axial velocity is close to zero), until it reaches the first orifice baffle. Due to the interaction of the oscillatory flow with the baffles and the subsequent eddies that are created, the tracer is then distributed radially. However, unlike with Source 1, a jet of fluid without tracer dominates the centreline of the reactor that is slowly mixed with the tracer by diffusion as the flow moves down the reactor.

5.4.2. Mixing performance

The mixing quality in the COBR can be quantified by analysing the tracer concentrations at different cross-sections using the areal-based distribution of mixing method. Figure 5.5 gives an example of concentration fields on Plane 4 for Case 1 when the tracer is introduced at the wall (Source 2). This figure highlights the inhomogeneity of tracer concentration across the cross-section. The data are used to determine distributions of mixing quality. Figure 5.6 and Figure 5.7 present the distributions of mixing quality (averaged over one oscillation period) at Plane 4 for the different cases studied and two different source positions, Source 1 and Source 2. These distributions enable the impact of operating conditions on mixing quality to be clearly seen and will be discussed in detail in the following paragraphs. Charts of the areal distribution of mixing intensity averaged over one oscillation period for all planes and sources positions are presented in Appendix 2.

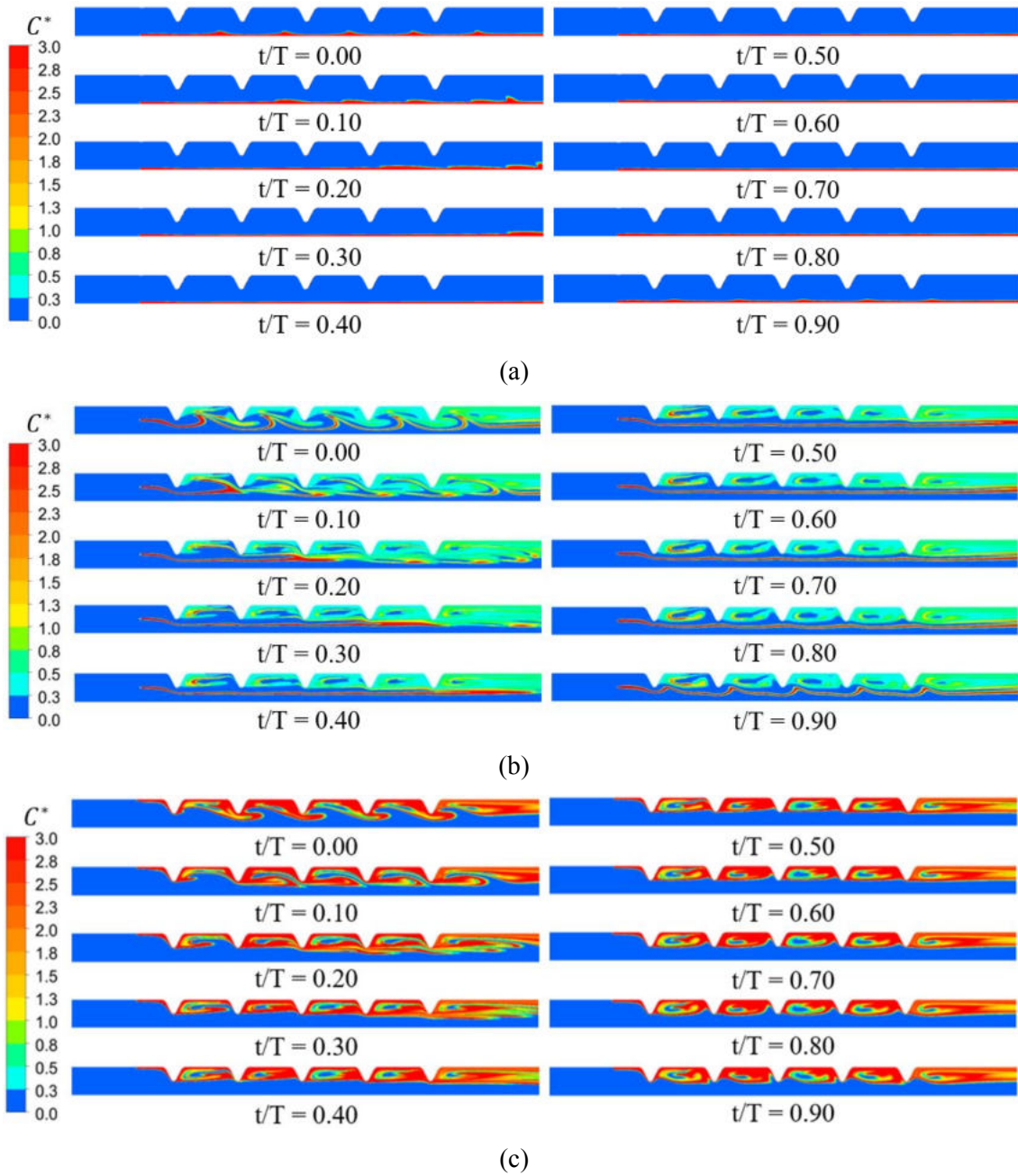


Figure 5.4: Effect of source position on tracer patterns over a flow period (T) for Case 1 ($Re_{net} = 27$, $f = 1$ Hz, $x_o = 5$ mm): (a) Source 0, (b) Source 1, (c) Source 2.

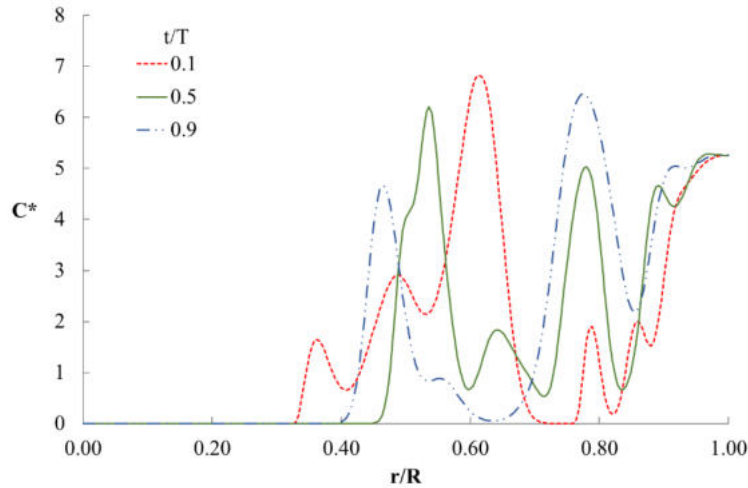


Figure 5.5: Tracer profiles from Source 2 over a flow period (T) at Plane 4 for Case 1 ($Re_{net} = 27$, $f = 1$ Hz, $x_o = 5$ mm).

5.4.2.1. Influence of the frequency

The influence of the oscillatory frequency on the mixing performance can be studied by comparing Cases 1 & 2, Cases 3 & 4, Cases 5 & 7 and Cases 6 & 8 in Figure 5.6 and Figure 5.7 for Source 1 and Source 2, respectively. For both source positions and for almost all cases, an increase in oscillation frequency (from 1 to 2 Hz) improves the mixing quality. An exception to this is at high oscillation amplitude ($x_o/l_b = 0.6$) and a low net Reynolds number ($Re_{net} = 6$), i.e. Cases 6 and 8, whereby the increased oscillation frequency in Case 8 does not improve mixing performance. An explanation for this is discussed in section 5.4.2.5.

5.4.2.2. Influence of the amplitude

The effect of the oscillation amplitude on mixing can be assessed by comparing Cases 1 & 3, Cases 2 & 4, Cases 5 & 6 and Cases 7 & 8. In all cases, the amplitude is increased from 5 to 10 mm at different net Reynolds numbers. An analysis of these results shows that there is no clear trend of the effect of oscillation amplitude on mixing quality, neither for high nor low net Reynolds numbers. This is different than what is observed for mixing in batch OBRs, whereby higher oscillatory conditions typically lead to improved mixing (Mackley and Neves Saraiva, 1999; Ni et al., 1998). Indeed, isolating the effect of oscillatory flow on mixing COBRs without taking into account the influence of the net flow is extremely complicated since it is the interaction between the pulsed flow, the net flow and the baffles that generates complex flow patterns that are responsible for mixing (Mazubert et al., 2016).

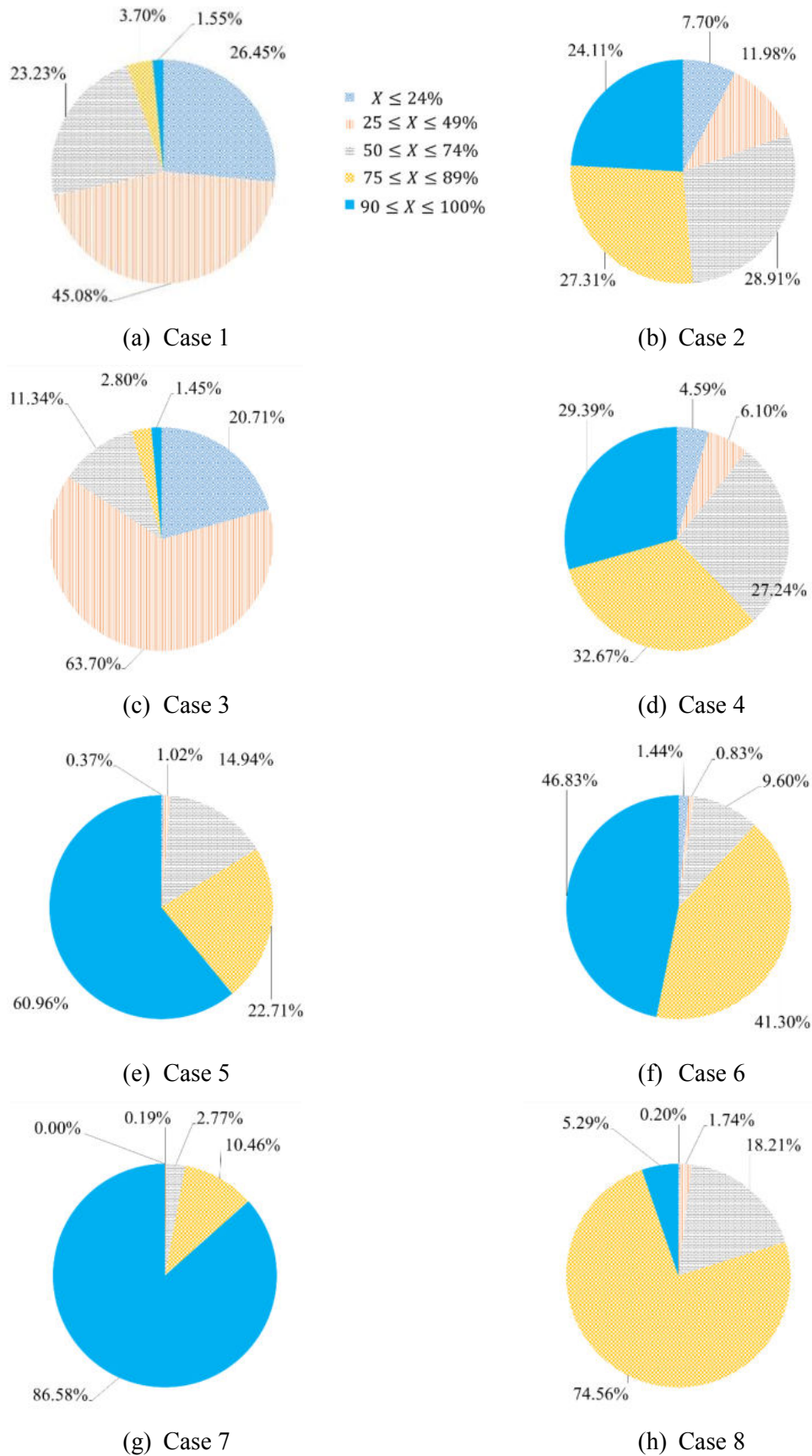


Figure 5.6: Areal distribution of mixing intensity averaged over one oscillation period at Plane 4 for Source 1: (a) Case 1, (b) Case 2, (c) Case 3, (d) Case 4, (e) Case 5, (f) Case 6, (g) Case 7, (h) Case 8.

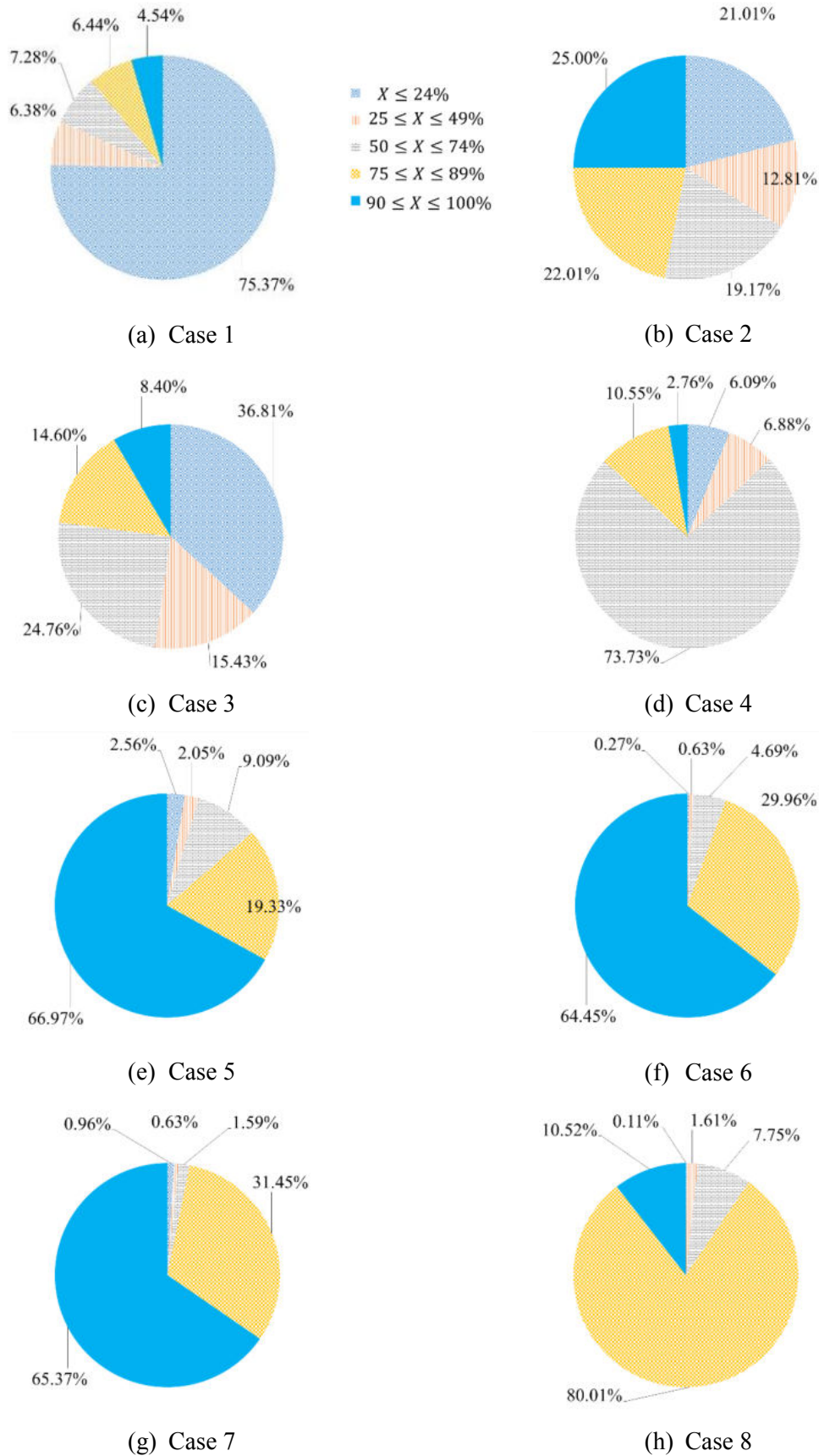


Figure 5.7: Areal distribution of mixing intensity averaged over one oscillation period at Plane 4 for Source 2: (a) Case 1, (b) Case 2, (c) Case 3, (d) Case 4, (e) Case 5, (f) Case 6, (g) Case 7, (h) Case 8.

5.4.2.3. Synergy of the oscillatory frequency and amplitude

Comparison of Cases 2 & 3 ($Re_{net} = 27$, $Re_o = 48$, $\psi = 1.8$) and Cases 6 & 7 ($Re_{net} = 6$, $Re_o = 48$, $\psi = 8$) enables the impact of oscillatory conditions and net Reynolds number on mixing to be assessed. At the same oscillatory Reynolds number and velocity ratio, working with high frequencies and small amplitudes results in better mixing quality than with low frequencies and high amplitudes. For cases with $\psi = 1.8$ (Cases 2 & 3) and $\psi = 8$ (Cases 6 & 7) and Source 1, the interaction of the tracer with the baffle due to the pulsed flow is similar to that shown in Figure 5.4(b) for Case 1. However, at higher amplitudes the tracer is transported further with each oscillation and it does not have the possibility to mix sufficiently in short distances. On the other hand, a smaller amplitude allows better interaction of the tracer with the flow and faster mixing. Cases with $\psi = 8$ demonstrate better mixing quality than cases with $\psi = 1.8$ due to the higher velocity ratio. Indeed, the lower net flow rate allows the tracer to spend more time in the cell between two baffles, where it is recirculated and mixed due to the generated eddies before being transported along the reactor to the next cell.

5.4.2.4. Influence of the source position

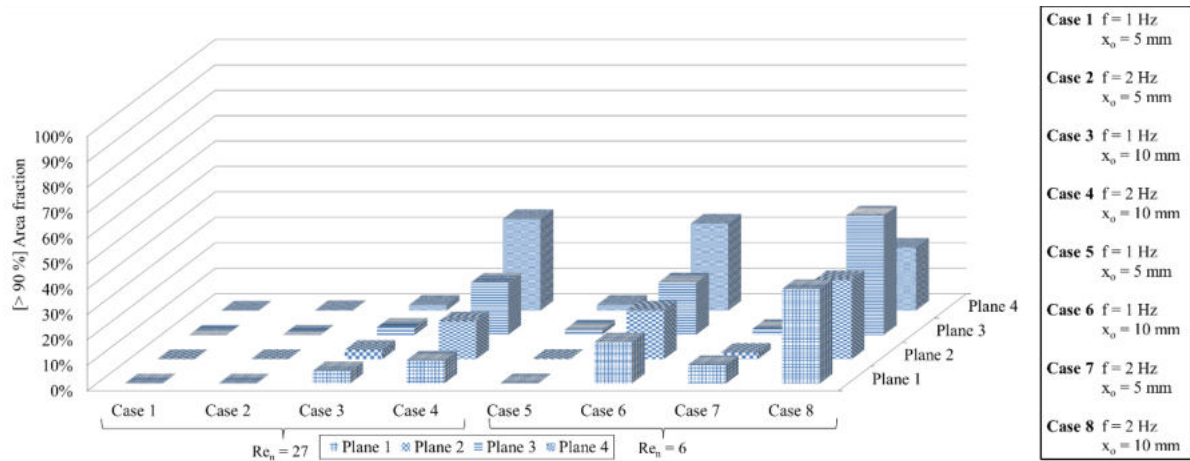
Figure 5.8 presents a summary of the mixing quality at different axial positions along the COBR for all of the different operating conditions and tracer source positions. The graph shows the area fraction of each plane that is well-mixed, i.e. that corresponds to $> 90\%$ of the perfectly mixed state. The effect of the source position can be clearly observed by comparing Figure 5.8 (a), (b) and (c). In a general manner, as is expected, all source positions show that mixing performance improves along the reactor. Source 2 from Case 8 is an exception to this and is discussed later. When the tracer is introduced at the centre of the tube (Source 0), poor mixing performance is observed for most operating conditions since the tracer is transported down the centreline of the reactor without interacting with the recirculating eddies. This source position results in significant axial dispersion and radial mixing is limited, reaching values up to 30% of the perfectly mixed state in the best cases. There is a clear improvement in mixing quality when the tracer source is close to the reactor wall (Source 2). It is interesting to point out that this is a different result than that found by Alberini et al. (2014b) for mixing in a Kenics static mixer. They found poorest mixing performance with a wall source, whilst the central source provided good mixing. Indeed, a static mixer element spans the entire cross-section of the tube so high axial dispersion along the centreline of the tube is not possible, unlike in the single orifice baffle geometry studied here. It is expected that mixing would be greatly improved in the COBR with a centreline source if other baffle geometries, e.g. multiple orifice plates or even static mixer elements, are used.

5.4.2.5. Influence of the velocity ratio

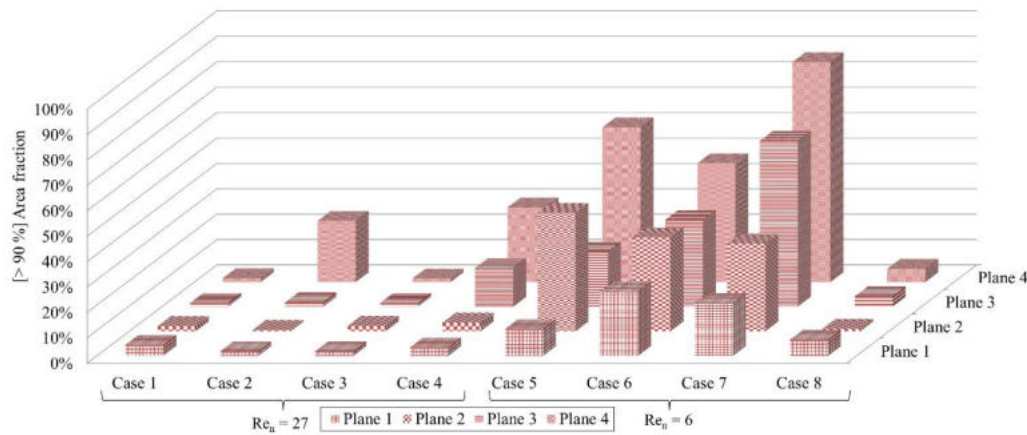
In a general manner, it can be seen from Figure 5.8 that the net Reynolds number also plays an important role in mixing. In laminar flow, a lower net Reynolds number provides improved mixing quality and

shorter mixing lengths since the residence time is longer and the tracer has more time to recirculate and mix by diffusion. However, the ratio of the oscillatory flow to the net flow, or velocity ratio, is also important and the impact of this is shown by comparing Cases 1 & 5, Cases 3 & 6, Cases 4 & 8, and Cases 2 & 7, in which case the oscillatory conditions are kept constant and the velocity ratio is increased by decreasing the net Reynolds number. In general, an increase in the velocity ratio results in an improved mixing performance. To understand this better, the tracer concentration fields for Case 7 ($\psi = 8$) and all three source locations are shown in Figure 5.9. When operating with a higher velocity ratio, i.e. the oscillatory flow dominates, the net flow does not transport the tracer too far along the reactor, allowing it to mix and diffuse in the cells between baffles due to the recirculating flow. Nevertheless, it appears that if the velocity ratio is too high, mixing performance is hindered and this is illustrated with the results of Case 8, where $\psi = 16$, as shown in Figure 5.10. Under this condition, the net flow has a small influence on the oscillatory flow and the COBR starts to operate more like a batch OBR. In this case, a large portion of the tracer gets pushed backwards, upstream of the source position, such that the tracer starts to mix before reaching the baffled zone. However, mixing here is slow since there are no recirculating eddies to enhance the transport process. Mixing quality would be expected to improve for the same operating conditions if the source location is situated within the baffled zone. In this position, the dye that is pushed upstream will still be within the baffle zone, profiting from eddies and recirculation flow (similar to those for Case 7), and enhancing mixing performance. When the tracer source is close to the wall where the axial velocity is close to zero, the tracer spends more time in the vicinity of the source before being pushed down the reactor, explaining the better mixing performance at early planes seen in Figure 5.8(c).

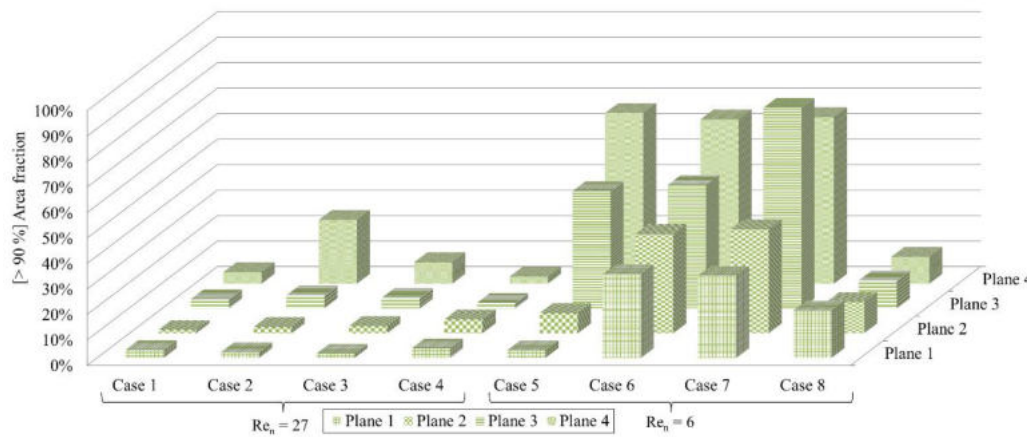
The velocity ratio has an important influence in the reversed flow phase of the oscillatory cycle. When $\psi = 0.9$ (Case 1), the net flow dominates over the oscillatory flow, causing the reverse flow portion of the cycle to be small. The absence of fully reversing flow causes a deceleration of the net flow. This condition does not allow the eddies created between consecutive baffles to move to the centre of the reactor due to the difference between the velocity magnitudes at the centreline and the baffle zone, which increases axial mixing and decreases radial mixing. As ψ increases, the time fraction over which reverse flow occurs during the oscillatory cycle increases and the vortices start to interact with the net flow, enhancing radial mixing and decreasing axial mixing. For $\psi = 1.8$ (Cases 2 & 3) reverse flow occurs for $\Delta t/T = 0.3$ of the overall flow cycle, at $\psi = 8$ (Cases 6 & 7) it is for $\Delta t/T = 0.46$ and at $\psi = 16$ (Case 8) it is for $\Delta t/T = 0.48$. As ψ increases, the COBR behaves more like a batch OBR, having reverse flow for close to $\Delta t/T = 0.5$. For some value of the velocity ratio between $\psi = 8$ and $\psi = 16$, the influence of the reverse flow over the net flow becomes preponderant and the oscillatory conditions become detrimental to the mixing performance due the backward flux of tracer. This explains the reduction of mixing performance when increasing the frequency from 1 Hz in Case 6, to 2 Hz in Case 8.



(a)



(b)



(c)

Figure 5.8: Area fraction of Planes 1, 2, 3, and 4 (averaged over one oscillation period) where > 90% mixing is achieved for Cases 1 to 8. (a) Source 0; (b) Source 1; (c) Source 2.

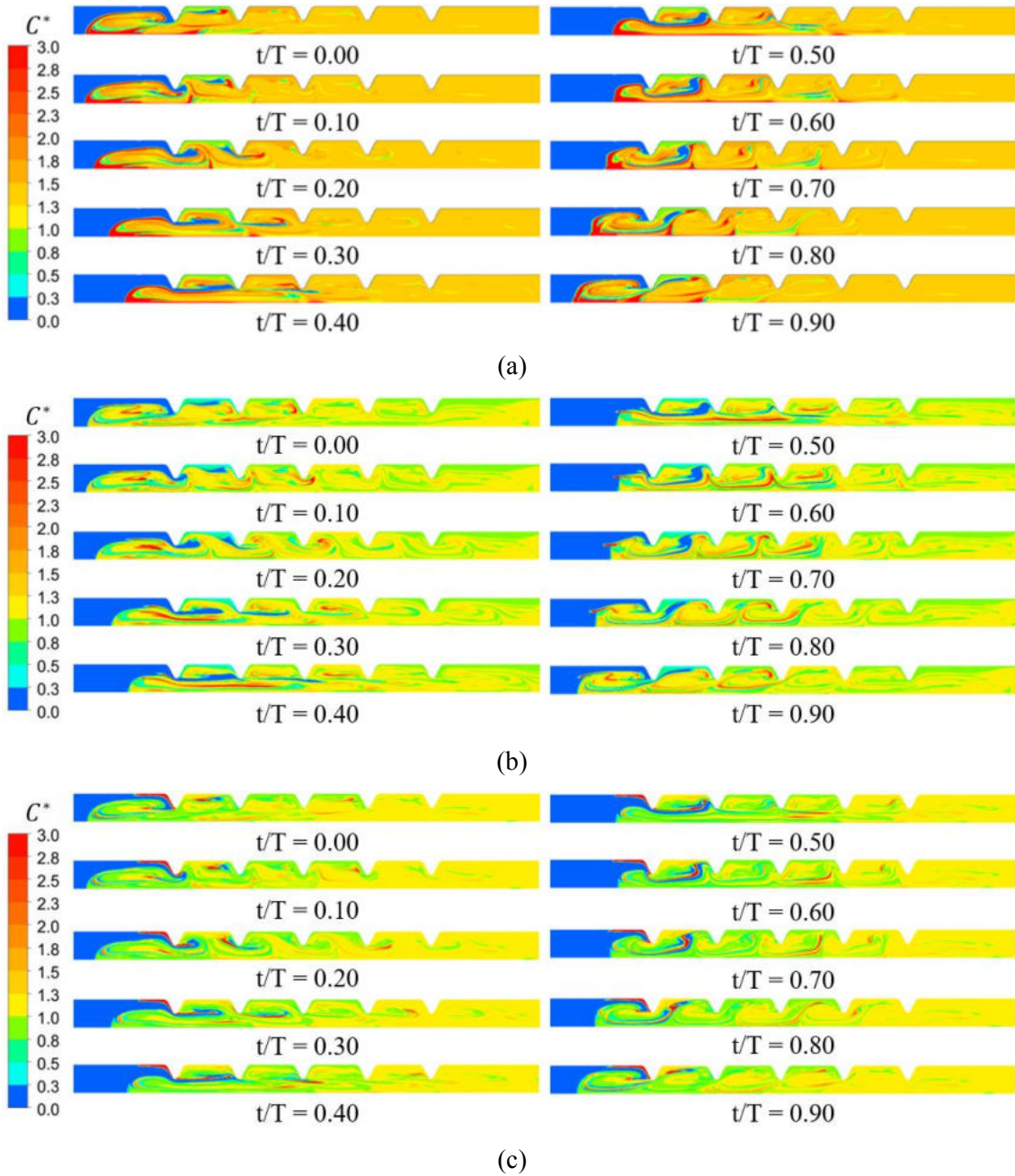


Figure 5.9: Tracer patterns over a flow period (T) for Case 7 ($Re_{net} = 6$, $f = 2$ Hz, $x_o = 5$ mm): (a) Source 0, (b) Source 1, (c) Source 2.

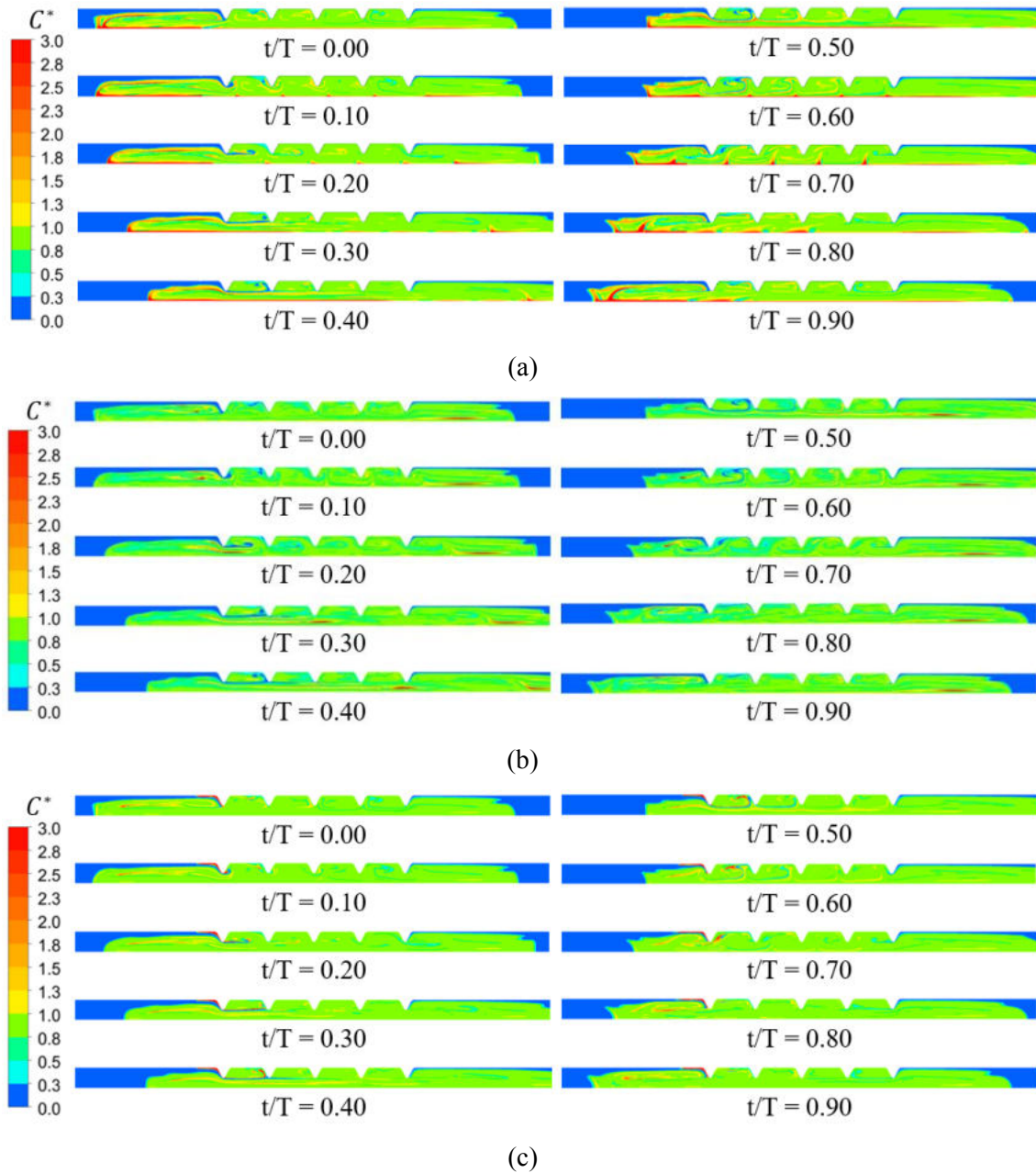
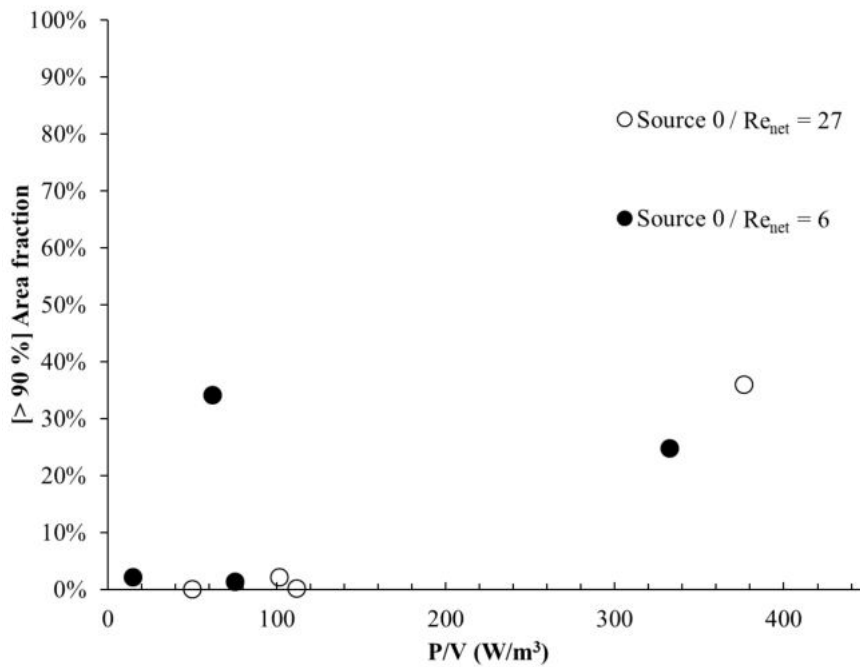


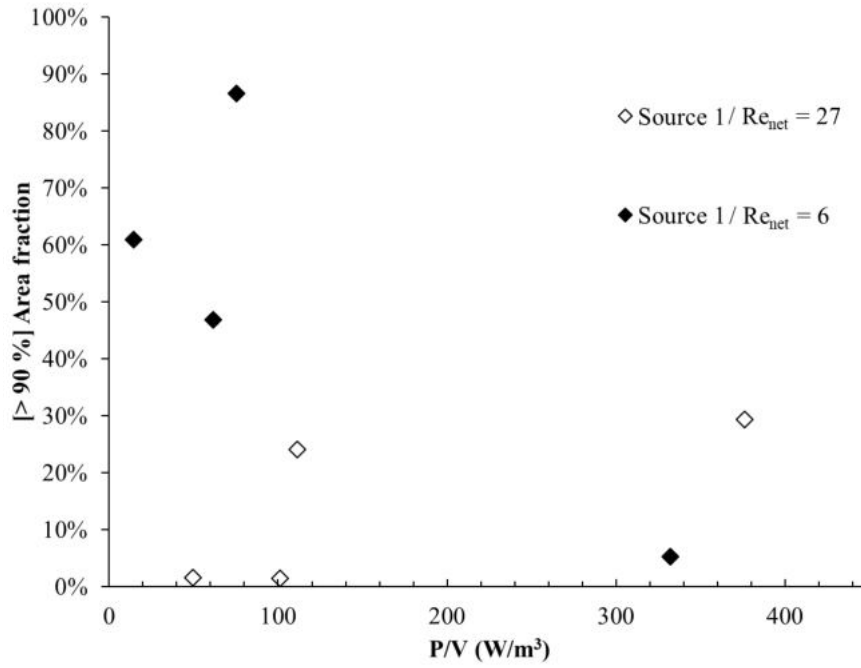
Figure 5.10: Tracer patterns over a flow period (T) for Case 8 ($Re_{net} = 6$, $f = 2$ Hz, $x_o = 10$ mm): (a) Source 0, (b) Source 1, (c) Source 2.

5.4.3. Power dissipation

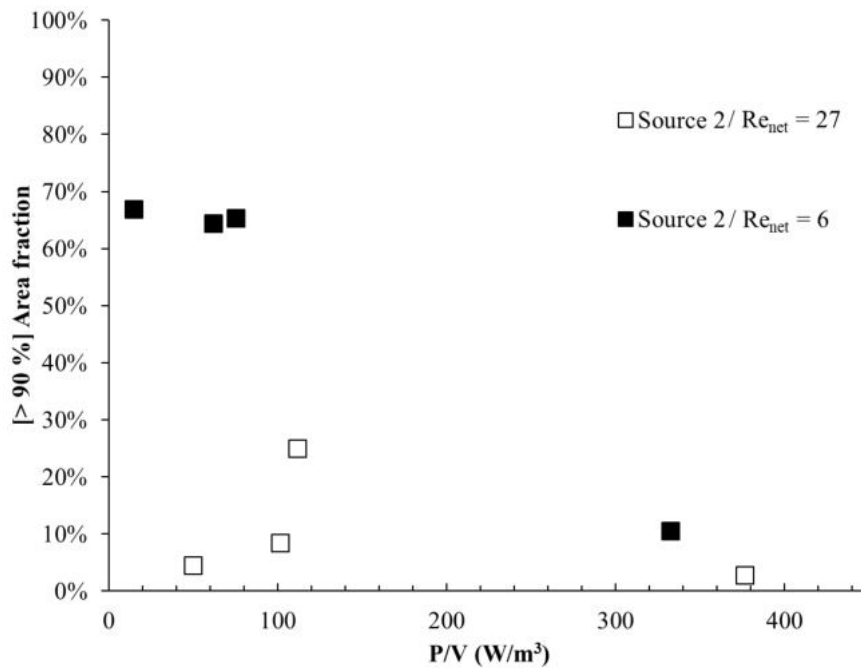
The influence of energy dissipation on mixing performance can be observed in Figure 5.11. For all cases and all sources positions, a clear trend cannot be identified. In some cases, better mixing performance is achieved at low power dissipation values, as can be seen in Figure 5.11(b) for $Re_{net} = 6$ and Figure 5.11(c) for both Re_{net} . Whilst in other cases, an increase in the power density leads to an enhancement in the mixing quality, as observed in Figure 5.11(a) and Figure 5.11(b) for $Re_{net} = 27$. In the same way as with oscillation amplitude, it is extremely difficult to isolate the effect of the power density on the spatial mixing uniformity without explicitly taking into account the position of the source and its interaction with the flow (oscillatory and net) in the baffled reactor that generates complex recirculation eddies.



(a)



(b)



(c)

Figure 5.11: Area fraction of Planes 4 (averaged over one oscillation period) where $> 90\%$ mixing is achieved as a function of the power dissipation. (a) Source 0; (b) Source 1; (c) Source 2.

5.5. Conclusions

The impact of oscillatory and flow parameters (frequency, amplitude and velocity ratio) and tracer source position on mixing quality in a COBR were studied through CFD simulations. Introduction of the tracer at the reactor wall or approximately midway between the wall and the centre of the tube (in front of the first orifice baffle) results in significantly better mixing performance than when it is introduced at the tube centreline. The latter results in high axial dispersion with limited radial mixing; this is primarily due to the orifice baffle geometry. Introduction of the tracer away from the tube centreline enables improved radial mixing due to the recirculation eddies created by the interaction of the baffles and the pulsed flow. A simple change in the source position can increase this to values of 87% of the perfectly mixed state (where $> 90\%$ of mixing is achieved).

An increase in the frequency usually leads to an improvement in mixing quality, contrary to an increase in the amplitude, where no clear trend was found. The interaction between the oscillatory flow, the net flow and the baffles make it difficult to characterise mixing by taking only into account the oscillatory conditions (i.e. f and x_o). For a fixed oscillatory Reynolds number, higher oscillation frequencies with amplitudes close to $0.3l_b$ (which is close to the value recommended by Gough et al. 1997, i.e. 25% of baffle spacing from a simple experimental observation of flow patterns in a pulsed baffled reactor) provide better mixing than low frequencies and high amplitudes. Mixing quality typically increases with an increase in the velocity ratio, provided that an adequate position of the source is chosen, enabling the tracer to be convected by the recirculation eddies created by the interaction of the pulsed flow with the baffles. The increase of velocity ratio enhances mixing quality from poorly mixed conditions (less than 4% of the perfect mixed state) up to 87% of the perfectly mixing state. From previous studies, the recommended velocity ratio to obtain plug flow in a COBR is $\psi = 2 - 4$ (Stonestreet and Van Der Veeken, 1999). However, this work shows that higher velocity ratios are preferred to obtain uniform spatial mixing rapidly, which highlights that different operating conditions may be required depending on the process objective (Kacker et al., 2017; Soufi et al., 2017). The magnitude of the net flow is also important. If the net flow is too low, mixing may be hindered because the secondary stream (tracer) is pushed upstream of the baffles, where it does not benefit from flow recirculation. In such a case, it is expected that introduction of the secondary stream in the baffled region, rather than upstream, would greatly improve mixing. These results provide a first estimate of where the plume of an injection jet needs to be positioned for future studies.

5.6. References

- Alberini, F., Simmons, M.J.H., Ingram, A., Stitt, E.H., 2014a. Use of an areal distribution of mixing intensity to describe blending of non-newtonian fluids in a Kenics KM static mixer using PLIF. *AIChE J.* 60, 332–342. <https://doi.org/10.1016/j.ces.2014.03.022>
- Alberini, F., Simmons, M.J.H., Ingram, A., Stitt, E.H., 2014b. Assessment of different methods of analysis to characterise the mixing of shear-thinning fluids in a Kenics KM static mixer using PLIF. *Chem. Eng. Sci.* 112, 152–169. <https://doi.org/10.1016/j.ces.2014.03.022>
- Avila, M., Fletcher, D.F., Poux, M., Xuereb, C., Aubin, J., 2020. Mixing performance in continuous oscillatory baffled reactors. *Chem. Eng. Sci.* 219. <https://doi.org/10.1016/j.ces.2020.115600>
- Brunold, C.R., Hunns, J.C.B., Mackley, M.R., Thompson, J.W., 1989. Experimental observations on flow patterns and energy losses for oscillatory flow in ducts containing sharp edges. *Chem. Eng. Sci.* 44, 1227–1244. [https://doi.org/10.1016/0009-2509\(89\)87022-8](https://doi.org/10.1016/0009-2509(89)87022-8)
- Gough, P., Ni, X., Symes, K.C., 1997. Experimental flow visualisation in a modified pulsed baffled reactor. *J. Chem. Technol. Biotechnol.* 69, 321–328. [https://doi.org/10.1002/\(SICI\)1097-4660\(199707\)69](https://doi.org/10.1002/(SICI)1097-4660(199707)69)
- Kacker, R., Regensburg, S.I., Kramer, H.J.M., 2017. Residence time distribution of dispersed liquid and solid phase in a continuous oscillatory flow baffled crystallizer. *Chem. Eng. J.* 317, 413–423. <https://doi.org/10.1016/j.cej.2017.02.007>
- Kukukova, A., Aubin, J., Kresta, S.M., 2011. Measuring the scale of segregation in mixing data. *Can. J. Chem. Eng.* 89, 1122–1138. <https://doi.org/10.1002/cjce.20532>
- Kukukova, A., Aubin, J., Kresta, S.M., 2009. A new definition of mixing and segregation: three dimensions of a key process variable. *Chem. Eng. Res. Des.* 87, 633–647. <https://doi.org/10.1016/j.cherd.2009.01.001>
- Mackley, M.R., Neves Saraiva, R.M.C., 1999. The quantitative description of fluid mixing using Lagrangian- and concentration-based numerical approaches. *Chem. Eng. Sci.* 54, 159–170. [https://doi.org/10.1016/S0009-2509\(98\)00169-9](https://doi.org/10.1016/S0009-2509(98)00169-9)
- Mazubert, A., Fletcher, D.F., Poux, M., Aubin, J., 2016. Hydrodynamics and mixing in continuous oscillatory flow reactors—Part I: Effect of baffle geometry. *Chem. Eng. Process. Process Intensif.* 108, 78–92.
- Ni, X., Brogan, G., Struthers, A., Bennett, D.C., Wilson, S.F., 1998. A systematic study of the effect of geometrical parameters on mixing time in oscillatory baffled columns. *Chem. Eng. Res. Des.* 76, 635–642. <https://doi.org/10.1205/026387698525162>
- Ni, X., Jian, H., Fitch, A.W., 2002. Computational fluid dynamic modelling of flow patterns in an oscillatory baffled column. *Chem. Eng. Sci.* 57, 2849–2862. [https://doi.org/10.1016/S0009-2509\(02\)00081-7](https://doi.org/10.1016/S0009-2509(02)00081-7)
- Soufi, M.D., Ghobadian, B., Najafi, G., Mousavi, S.M., Aubin, J., 2017. Optimization of methyl ester production from waste cooking oil in a batch tri-orifice oscillatory baffled reactor. *Fuel Process.*

Technol. 167, 641–647. <https://doi.org/10.1016/j.fuproc.2017.07.030>

Stonestreet, P., Van Der Veecken, P.M.J., 1999. The effects of oscillatory flow and bulk flow components on residence time distribution in baffled tube reactors. *Chem. Eng. Res. Des.* 77, 671–684. <https://doi.org/10.1205/026387699526809>

Zheng, M., Li, J., Mackley, M.R., Tao, J., 2007. The development of asymmetry for oscillatory flow within a tube containing sharp edge periodic baffles. *Phys. Fluids* 19. <https://doi.org/10.1063/1.2799553>

Chapter 6. Experimental characterization of mixing

This chapter focuses on the characterization of mixing in the COBR with experimental techniques. The chapter is divided into two parts. Part I aims at characterizing micromixing performance, which is the key parameter in the progress of instantaneous and competitive reactions, using a competitive parallel reaction system. Part II intends to explore macromixing performance via a visual analysis of a passive tracer.

Part I: Micromixing characterization in a continuous oscillatory baffled reactor

6.I.1. Introduction

Most of the previous works on mixing quality in continuous OBRs (COBRs) have focused on evaluating plug flow behaviour via the residence time distribution (RTD) and on determining the operating conditions required to achieve the narrowest RTD (Abbott et al., 2014a; Dickens et al., 1989; Kacker et al., 2017; Mackley and Ni, 1991; Reis et al., 2004). However, Levenspiel (1999) demonstrated that the RTD of an inert tracer does not provide enough information for the prediction of conversion or selectivity of a set of chemical reactions. In fact, it is only possible to predict the conversion of a chemical reaction with the RTD in one of the following cases: (a) for a reaction with first order kinetics, or (b) when the residence time is the same for all molecules in the reactor. In the latter, the molecules have the same history of mixing and will therefore all be transformed in the same proportion. This is the case for the plug flow tubular reactor with premixed reagents (Xuereb et al., 2006).

Micromixing, i.e. mixing at the molecular scale, is the limiting step in the progress of instantaneous and competitive reactions. The conversion of fast/instantaneous chemical reactions depends on how the molecules are initially contacted. Poor micromixing can lead to local segregation and hence decreases in selectivity and conversion, altered product properties and the formation of undesired by-products (Baldyga and Pohorecki, 1995), thereby requiring high purification costs.

Micromixing in COBRs is challenging because this kind of reactor typically does not provide fast micromixing conditions. However, micromixing performance in the COBRs is of interest for applications with initial fast reactions or precipitations that also require long residence time (e.g. for consecutive reactions and crystal/precipitate growth). Precipitation and crystallization processes often exhibit rapid nucleation kinetics and the quality of the product is greatly influenced by the manner in which the reagents are put into contact and mixed (Xuereb et al., 2006). The effects of parameters like the inlet position, inlet velocity, injection time, reagent flow rate, etc. are hence important for the design of efficient reactors for fast/instantaneous reactions.

To date, there has only been one study on micromixing in COBRs presented in the literature. McDonough et al. (2019b) characterized the micromixing performance of different meso-OBR

geometries (5 mm diameter) with the Villermaux-Dushman test reaction across a broad range of oscillatory and net Reynolds numbers ($50 \leq Re_o \leq 1000$ and $5 \leq Re_{net} \leq 40$). The reactants were injected directly into the baffled zone of the reactor at the equal flow rates. The results showed that the helical design provides fast micromixing times as well as good plug-flow behaviour, because of the wide range of velocity ratio at which plug-flow can be achieved ($5 < \psi < 250$) (Phan and Harvey, 2011). The authors developed empirical equations for the estimation of micromixing times for the different baffle geometries that correlate micromixing quality and plug flow behaviour as a function of the oscillatory to net flow velocity ratio (ψ). For the COBR with smooth constrictions, they proposed the following equation:

$$t_m/\tau = 0.124\psi^{-1.29} \quad (6.1)$$

where t_m is the micromixing time and τ the mean residence time. However, this equation was established using the same inlet flow rates. Commenge and Falk (2011), authors of the correlation used by McDonough et al. (2019) for the estimation of the micromixing time, established that their equation should not be exploited for other flow ratio values different from 1. The impact of different operating conditions of reactant injection, as well as how this interacts with the oscillatory flow and influences the micromixing performance in the OBRs was therefore not explored in this study.

The objective of this work is to explore the effect of the oscillatory conditions and the secondary flow rate on the micromixing quality in a Nitech® COBR in the laminar flow regime ($Re_o < 2000$). Micromixing performance is evaluated using the Villermaux-Dushman iodide-iodate test reactions (Fournier et al., 1996a) where the reactants are injected just upstream of the baffled zone in the COBR. Micromixing times for different oscillatory velocities and volumetric flow rate ratios (between the main stream and the injection flow) are then estimated using the incorporation micromixing model developed by Fournier et al. (1996b).

6.I.2. Materials and methods

6.I.2.1. Experimental rig

Micromixing experiments have been carried out in a commercial NiTech® glass COBR⁸, which is a single orifice baffled reactor with smooth constrictions, as shown in Figure 6.1. The COBR length is 700 mm, equipped with 22 orifice baffle-cells. The COBR tube has a diameter (D) of 15 mm with 7.5 mm diameter orifices (d); the distance between orifices (or inter-baffle distance), l_b , is 16.9 mm.

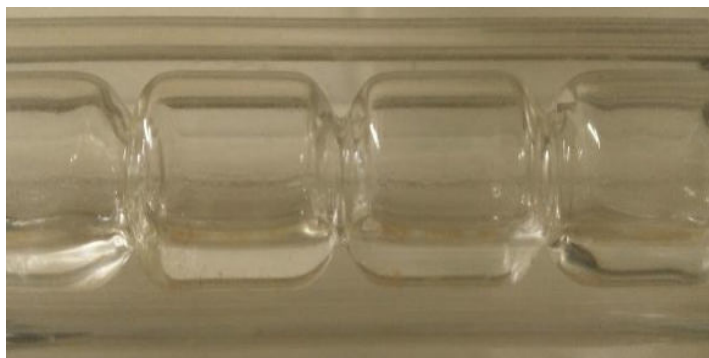


Figure 6.1: Photograph of the baffles in the NiTech® COBR

Figure 6.2(a) shows a simplified process flow diagram of the experimental system. Pumps P-01 and P-02 circulate the fluids into the COBR from feed vessels FV-01 and FV-02, respectively, while Pump P-03 provides the oscillatory flow. Pump P-01 feeds the bulk flow of the experimental rig, while Pump P-02 feeds the side injection through a perpendicular T-junction (4 mm diameter), which is located 75 mm before the first orifice baffle, as is shown in Figure 6.2(b).

⁸ <https://www.nitechsolutions.co.uk/products/lab-scale-dn15-range/>

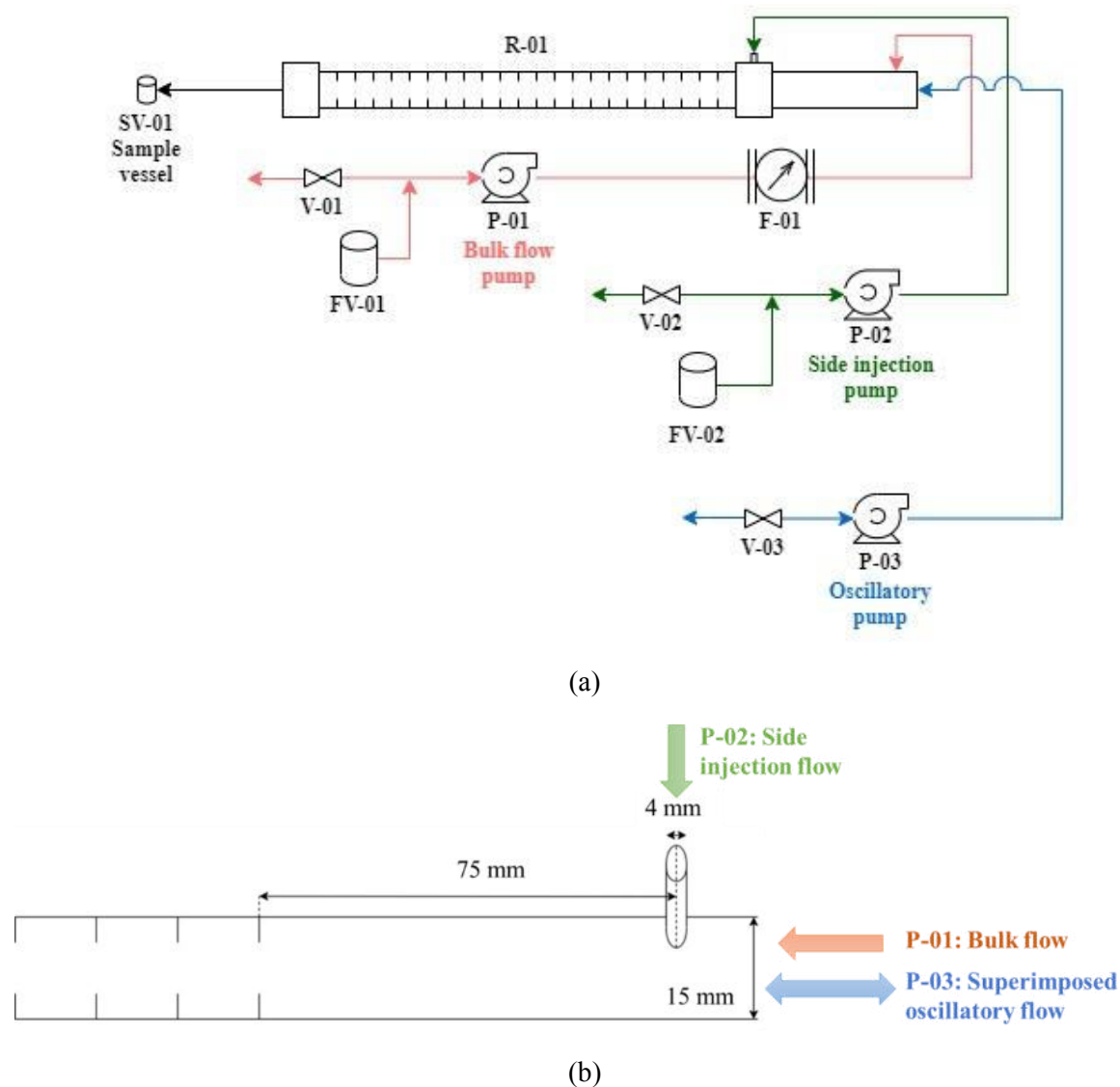


Figure 6.2: (a) Schematic diagram of the experimental setup containing the Nitech® reactor R-01. V-01 to V-03 are valves, FV-01 and FV-02 are feed vessels, P-01 to P-03 are gear pumps, F-01 is the flowmeter and SV-01 is the sample vessel. (b) Schematic diagram of the entries from P-01 (bulk flow), P-02 (side injection flow) and P-03 (oscillatory flow) to the Nitech® reactor.

6.1.2.2. Test reactions and quantification of micromixing

The chemical method used to characterize micromixing is a competitive parallel reactive system known as the Villiermaux-Dushman or iodide/iodate reaction, which was first used by Fournier et al. (1996) to study micromixing in a stirred tank. Its use was then extended to the study of micromixing performance in continuous flow microreactors (Falk and Commenge, 2010). Details of the experimental method are given in Guichardon et al. (2000a) and a detailed study of the reaction kinetics is given in Guichardon et al. (2000b).

The reaction system is composed of three reactions: a neutralisation reaction (R1), a redox reaction (R2) and (R3). Reaction (R1) is almost instantaneous whilst Reaction (R2) is very fast and of the same order of magnitude as the micromixing process.



It is the competition between these two reactions that allows the degree of micromixing to be determined. In addition to the above reactions, the iodine formed in reaction (R2) can react with iodide ions as follows:



where reaction (R3) is very fast compared with reaction (R2) and can be considered to be in equilibrium.

The rate of reaction (R1) is given by:

$$r_1 = k_1[\text{H}^+][\text{H}_2\text{BO}_3^-] \quad (6.2)$$

where

$$k_1 = 10^{11} \text{ L mol}^{-1}\text{s}^{-1} \quad (6.3)$$

The rate of reaction (R2) is given by:

$$r_2 = k_2[\text{H}^+]^2[\text{I}^-]^2[\text{IO}_3^-] \quad (6.4)$$

where Guichardon et al. (2000a) determined:

$$\log_{10}k_2 = 9.28105 - 3.664\sqrt{I} \quad \text{for } I < 0.166 \text{ M} \quad (6.5a)$$

$$\log_{10}k_2 = 8.383 - 1.5112\sqrt{I} + 0.237I \quad \text{for } I > 0.166 \text{ M} \quad (6.5b)$$

where I is the ionic strength of the mixture defined by:

$$I = \frac{1}{2} \sum_{i=1}^n C_i z_i^2 \quad (6.6)$$

where C_i is the molar concentration of ion i and z_i is the charge number of species i , with the sum taken over all ions in the solution (Falk and Commenge, 2010).

For reaction (R3), the equilibrium condition is expressed in terms of the equilibrium constant (K_B), given by Palmer et al. (1984) as:

$$K_B = \frac{k_{3f}}{k_{3b}} = \frac{[I_3^-]}{[I_2][I^-]} \quad (6.7)$$

$$\log_{10} K_B = \frac{555}{T} + 7.355 - 2.575 \log_{10} T \quad (6.8)$$

The value of K_B for a temperature of 25°C is 700 L mol⁻¹. The reaction rates are given by:

$$k_{3f} = 5.9 \times 10^9 \text{ L mol}^{-1} \quad (6.9)$$

and

$$k_{3b} = 7.5 \times 10^6 \text{ s}^{-1} \quad (6.10)$$

The test methodology consists in adding a small quantity of sulphuric acid to a mixture of iodate, iodide and borate ions $H_2BO_3^-/H_3BO_3$. The acid concentration must be set such that it ensures a deficit of H^+ protons with respect to the stoichiometry of borate ions. Under perfect micromixing conditions, the acid is totally consumed by the neutralization reaction (R1), which is infinitely faster than the redox reaction (R2). In this case reaction (R2) cannot proceed due to the stoichiometric deficit of sulphuric acid. Under poor mixing conditions, however, high local concentrations of acid react with the iodide and iodate ions to produce iodine I_2 after complete consumption of the borate ion. The selectivity in I_2 can then be considered as a measure of molecular-scale segregation of the fluid and indicates mixing quality.

These test reactions are used to quantify micromixing via the use of the segregation index, X_S , which is 0 when the flow is perfectly mixed and 1 when it is completely segregated (Fournier et al., 1996a). When micromixing is poor, reaction (R2) is favoured, whereas when micromixing is fast almost all of the H^+ ions are consumed by reaction (R1), so there is no or little I_2 formed. From the reaction (R2), 2 moles of H^+ are required for every mole of I_2 generated. Therefore, for continuous flow mixers, the selectivity of the iodide reaction, Y , is defined via:

$$Y = \frac{2(\dot{n}_{I_2} + \dot{n}_{I_3^-})_{out}}{(\dot{n}_{H^+})_{in}} = 2 \frac{\dot{q}_{out}([I_2] + [I_3^-])_{out}}{\dot{q}_{acid} [H^+]_{in}} \quad (6.11)$$

where \dot{n} denotes the molar flow rate and \dot{q} denotes the volumetric flow rate.

The segregation index is given by

$$X_S = Y/Y_{TS} \quad (6.12)$$

where Y_{TS} is the selectivity of iodide when there is total segregation. In this case, where the mixing time is very long, two reactions (R1) and (R2) can be assumed to be infinitely fast and the selectivity is only controlled by the relative concentrations of $[IO_3^-]_{in}$ and $[H_2BO_3^-]_{in}$ such that:

$$Y_{TS} = \frac{6[IO_3^-]_{in}}{6[IO_3^-]_{in} + [H_2BO_3^-]_{in}} \quad (6.13)$$

$[I_3^-]$ can be easily measured by UV-vis spectrophotometry at 353 nm following the Beer-Lambert law:

$$[I_3^-] = \frac{OD}{\epsilon l} \quad (6.14)$$

where OD is the optical density (or light absorption), ϵ is the molar extinction coefficient of I_3^- ions at 353 nm and l is the optical path length.

$[I_2]$ is determined from a second-order algebraic equation as given by Guichardon et al. (2000a):

$$-\frac{5}{3}[I_2]^2 + \left([I^-]_0 - \frac{8}{3}[I_3^-]\right)[I_2] - \frac{[I_3^-]}{K_B} = 0 \quad (6.15)$$

6.I.2.2.1. Test reactions and quantification of micromixing

The buffer solution (iodide, iodate, borate solution) is prepared according to the procedure in Guichardon et al. (2000a). To prepare 5 L of the buffer solution, 9.7 g of KI and 2.5 g of KIO_3 are dissolved separately in 50 and 500 ml of water respectively, making two different solutions with concentration of $[KI] = 0.0116 \text{ mol L}^{-1}$ and $[KIO_3] = 0.0023 \text{ mol L}^{-1}$. A boric acid solution of $[H_3BO_3] = 0.1818$ is prepared dissolving 56.2 g of H_3BO_3 in 1.5 L of water. 18.2 g of $NaOH$ are dissolved in 500 ml to obtain a concentration of $[NaOH] = 0.0909 \text{ mol L}^{-1}$. Boric acid and sodium hydroxide solutions are mixed together to obtain an equimolar solution. The KI and KIO_3 solutions are then mixed with the $H_3BO_3/NaOH$ solution and 2.45 L of water. The procedure to prepare the buffer solution has to be followed cautiously in order to avoid thermodynamic iodine formation. The acid solution is prepared with commercial concentrated solution of sulphuric acid, H_2SO_4 (18 mol L^{-1}).

6.I.2.2.2. Experimental procedure

The buffer solution (iodide, iodate, borate solution) and the sulphuric acid solution are fed to the reactor from the vessels FV-01 and FV-02, respectively, as depicted in Figure 6.2(a). Samples of 30 ml of the reacted mixture are taken at the reactor outlet, approximately 8 cm after the last baffle of the COBR (represented by SV-01 in Figure 6.2(a)). The concentration of I_3^- ions is measured using an OceanOptics S2000 spectrophotometer with a reflection dip probe (path length = 1 cm) and a UV/VIS light source DH-2000-BAL. Calibration was performed by correlating the measured absorbance of various known concentrations of KI/I_2 solutions in water. The value of the molar extinction coefficient of I_3^- at 353 nm is $26\,344\text{ L mol}^{-1}\text{ cm}^{-1}$, which is in good agreement with the results given in the literature (Awtrey and Connick, 1951; Guichardon et al., 2000a; Kölbl et al., 2013; Wenzel et al., 2018). The fit of the calibration curve and the protocol for the absorbance experiments with the OceanOptics software are described in Appendix 3.

Table 6.1 lists the conditions used to study the influence of the oscillatory conditions (frequency and amplitude) on the micromixing performance. The oscillatory frequency is set at values in the range 0.5–1.5 Hz and the oscillatory amplitude is in the range 3–13 mm (i.e. $0.18\text{--}0.77l_b$). Under these ranges of oscillatory conditions, the oscillatory Reynolds number, Re_o , varies in the range 300 to 1800, thereby ensuring a laminar flow regime ($Re_o < 2000$). The flow rate of the main stream is fixed to 4.7 L/h, corresponding to a net Reynolds number of 125. The flow rate is chosen to such that $Re_{net} < 250$ and that the oscillatory flow dominates the net flow (Stonestreet and Van Der Veecken, 1999). The influence of the injection flow rate is studied using different volumetric flow rate ratios between the bulk and jet stream:

$$R = \frac{Q_{net}}{q_{jet}} \quad (6.16)$$

where Q_{net} and q_{jet} are the volumetric flow rates of the main stream and the side injection, respectively. Values of $R = 7$ and 3.5 are studied by keeping the flow rate of the bulk stream constant at 4.7 L/h and using side injection flow rates of 0.67 and 1.34 L/h. These values correspond to injection Reynolds numbers of 59 and 118, respectively.

Table 6.1: Operating conditions studied.

Case	1	2	3	4	5	6	7
f (Hz)	0	1.5	1	1	0.5	1	1.5
x_o (mm)	0	3	4.5	6.5	13	13	13
x_o/l_b	0	0.18	0.24	0.36	0.77	0.77	0.77
Re_o	0	400	400	600	600	1200	1800

6.I.2.2.3. Determination of acid concentration

As a first approach for the characterization of micromixing in the COBR and following the experimental protocol of Guichardon et al. (2000a), an acid concentration of 1 mol L^{-1} was used for the initial micromixing experiments. The reactant concentrations used are shown in Table 6.2.

Table 6.2: Reactant concentrations.

Reactant	H_3BO_3	$NaOH$	KIO_3	KI
Concentration [mol L^{-1}]	0.1818	0.0909	0.00233	0.0116

Figure 6.3 shows samples taken at the reactor outlet, with oscillatory conditions of $x_o = 13 \text{ mm}$ and $f = 1.5 \text{ Hz}$, in which it is evident that iodine (I_2) has been formed. This is because the acid concentration in the side stream is too high for the concentration of iodide (I^-) and iodate (IO_3^-) ions in the bulk stream. Higher concentrations of H^+ ions released by reaction (R1), are dissipated in the bulk flow, reacting with the iodide and iodate from reaction (R2), creating I_2 , and consuming the iodide necessary for reaction (R3) to take place. It can be seen in Figure 6.4 that the peak of I_3^- at 353 nm is absent in the experimental absorption spectra. Two peaks at 227 and 460 nm are identified, which correspond to the presence of iodine and iodide (Wan and Xu, 2013). The presence of these peaks is supported by the formation of iodine by disproportionation, as described by reaction (R4):



Reaction (R4) takes place when zones with a pH lower than the pH of iodine disproportionation (pH_{I_2}) appear (Guichardon et al., 2000a; Truesdale et al., 2003). pH_{I_2} depends on the total iodine concentration and if the mean working pH is lower than pH_{I_2} , iodine forms naturally. For a buffer solution with a pH of 8.5-9, pH_{I_2} is close to 7 (Guichardon et al., 2000a). Therefore, the amount of acid and its concentration have to be adjusted such that the average pH is close to pH_{I_2} . From the pH curve between sulphuric acid and $H_3BO_3/NaOH$ solution given by Commenge and Falk (2011), an acid concentration of $[H_2SO_4] = 0.03 \text{ mol L}^{-1}$ was selected as the new concentration.



Figure 6.3: Photograph of the presence of iodide (I_2) in the experiments without oscillations, with an acid concentration $[H_2SO_4] = 1 \text{ mol L}^{-1}$.

When an acid concentration of 0.03 mol L^{-1} is used, the segregation index only varies slightly or not at all when different oscillatory conditions are tested and this can be attributed to the sensitivity of the measurement, which is dependent on the amount of H^+ added. Guichardon et al. (2000a) proposed diverse recommendations to adapt the procedure of the Villermaux-Dushman reaction procedure when problems of measurement sensitivity are observed. Typically, they suggest increasing the acid concentration and decreasing the volume of acid injected in order to keep the stoichiometry constant. However, in the current experiments, the acid flow rate is set to a constant value 0.67 L/h to have a value of the volumetric flow rate ratio $R = 7$ and study its influence over the micromixing quality. An increase in the acid concentration would lead to an overconcentration of H^+ ions, thereby increasing the amount of $[I_3^-]$ formed. This then would result in an optical density that is too high to be measured with the spectrophotometer ($OD > 2$), or in the disproportionation of iodine. Therefore, in order to decrease the number of H^+ ions added to the system, a lower acid concentration $[H_2SO_4] = 0.015 \text{ mol L}^{-1}$ obtained from the pH evolution curve of Commenge and Falk (2011) is used in further experiments.

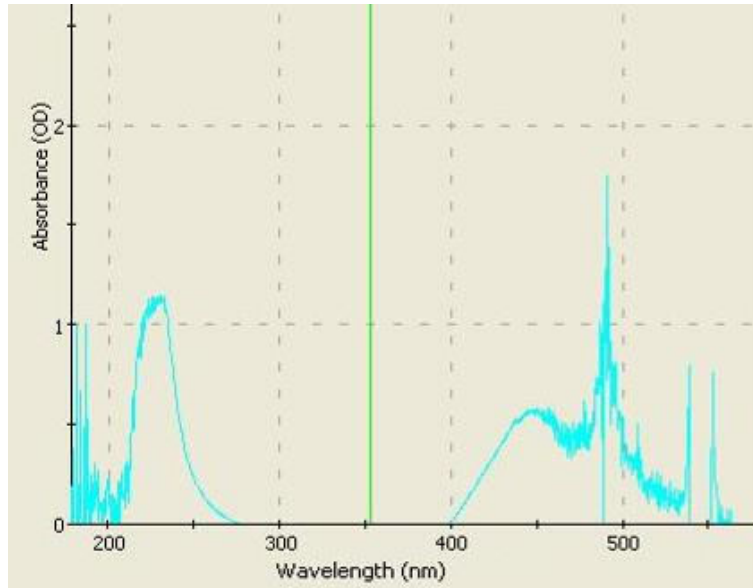


Figure 6.4: Absorption spectra obtained for experiments without oscillations using an acid concentration $[H_2SO_4] = 1 \text{ mol L}^{-1}$.

6.I.2.2.4. Quantitative analysis of micromixing performance

The segregation index has the characteristic of being highly dependent on the concentration of reactants, making it difficult to compare the results obtained when different concentration sets are used. The segregation index is therefore only useful for qualitative studies of micromixing performance. The micromixing time, a parameter independent of the concentration, is commonly used in quantitative micromixing characterisations. In order to calculate the micromixing time, the use of micromixing models has been widely used by researchers. These models are simplified approaches to describe mixing phenomena coupled with the reaction occurring at the microscale. In order to access the order of magnitude of the micromixing time and to study the influence of the volumetric flow rate ratio, the theoretical and calculated micromixing times are estimated using two different models.

Theoretical micromixing time

Baldyga and Bourne (1984) proposed that in laminar flow the total mixing time is influenced simultaneously by the shear stretching characteristic time and the diffusion time. At large segregation scales, stretching is the dominating step, whilst at fine segregation scales, mixing is controlled by diffusion. The theoretical micromixing time model proposed by Baldyga and Bourne (1984) for intertwined lamella in laminar regime, given by the equation (6.17), only considers the phenomena of molecular diffusion and does not take into account a reaction term.

$$t_{m \text{ theo}} = t_{diff+shear} = \frac{\text{arcsinh}\left(\frac{0.76\dot{\gamma}\delta_0^2}{D_f}\right)}{2\dot{\gamma}} \quad (6.17)$$

where $\dot{\gamma}$ is the mean shear rate, δ_0 the initial striation thickness and D_f the diffusion coefficient. This model has been used to estimate the theoretical mixing time in laminar flow micromixers and static mixers (Falk and Commenge, 2010; Ghanem et al., 2014; Zha et al., 2018). In this work, the initial striation thickness, δ_0 , is assumed equal to the diameter of the injection tube (i.e. 4 mm), the value of the self-diffusion coefficient of water at 25°C, $D_f = 2.3 \times 10^{-9} \text{ m}^2 \text{ s}^{-1}$ (Holz et al., 2000), and the mean shear rate in the tube is estimated by the following equation given by Falk and Commenge (2010):

$$\dot{\gamma} = \left(\frac{\varepsilon}{2\nu}\right)^{1/2} = \left(\frac{\varepsilon\rho}{2\mu}\right)^{1/2} \quad (6.18)$$

Calculated micromixing time

Almost all the literature studies on micromixing in continuous devices have been carried out for systems with equal inlet flow rates of the buffer and acid solutions (Commenge and Falk, 2011; McDonough et al., 2019; Panic et al., 2004; Su et al., 2011) and little research has been done on the estimation of calculated micromixing time in continuous devices using different volumetric flow rates. In recent studies, the incorporation model, despite being established initially for turbulent flow, has also been used to calculate micromixing time in laminar flow when different inlet flow rates are used. (Cheng et al., 2019; Lafficher et al., 2018; Li et al., 2019; Wu et al., 2009). The incorporation model was developed by Fournier et al. (Fournier et al., 1996b) as a simplified model to describe micromixing phenomena. The model considers two fluids to be mixed; one of the fluids (fluid 2 in Figure 6.5) is divided into aggregates, which are dispersed in a bulk volume of the second fluid (fluid 1 in Figure 6.5). The aggregates increase in size by incorporating the surrounding fluid. The volume of the aggregates will grow according to the law:

$$V_2 = V_{20} g(t) \quad (6.19)$$

where V_{20} represents the initial value of the aggregate volume and $g(t)$ is the incorporation function. $g(t)$ depends on the incorporation mechanism, which is a linear function when the incorporation flow rate is constant (equation (6.20)), or an exponential relationship when the flow rate is proportional to the aggregate volume (equation (6.21)):

$$g(t) = 1 + \frac{t}{t_{m\text{ cal}}} \quad (6.20)$$

$$g(t) = e^{(t/t_{m\text{ cal}})} \quad (6.21)$$

The calculated micromixing time, $t_{m\text{ cal}}$, is equal to the incorporation time, which is the time for the aggregate of fluid 2 to be completely diffuse in fluid 1.

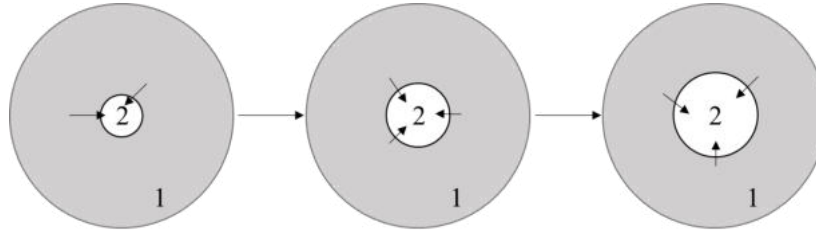


Figure 6.5 : Schematic diagram of the incorporation model.

The concentration of species i , c_i found in fluid 2 is given by:

$$\frac{dc_i}{dt} = (c_{i10} - c_i) \frac{1}{g} \frac{dg}{dt} + R_i \tag{6.22}$$

where c_{i10} is the concentration of the specie i in the surrounding fluid, and R_i the reaction rate from reactions (R1), (R2) and (R3) of species i .

Calculated micromixing times are estimated by assuming total dissociation of the sulphuric acid and using the exponential approach of the incorporation model. The ordinary differential equations from the mass balance of the species in reactions (R1), (R2) and (R3) are solved using Matlab software. The Matlab script code is provided in Appendix 4. The solution of the differential equations is then used to calculate the corresponding segregation index, resulting in a curve relating micromixing time and the segregation index as a function of the initial concentration of each reagent and the flow rate, as shown in Figure 6.6. This graph is then used to determine micromixing time from an experimental value of the segregation index.

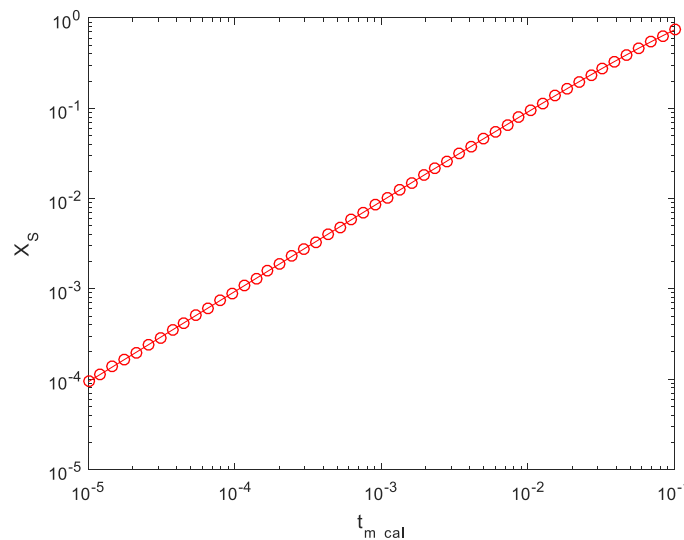


Figure 6.6: Example curve of segregation index as function of the calculated micromixing time for $R = 7$ and $[H_2SO_4] = 0.015 \text{ mol L}^{-1}$.

6.I.3. Results and discussions

6.I.3.1. Influence of oscillatory conditions

Figure 6.7 shows the segregation index X_s as a function of oscillatory Reynolds number, Re_o , for different oscillation conditions and acid concentrations. All experimental points were collected in duplicate, obtaining an experimental error between 2 and 5%. A value of $Re_o = 0$ means that there is no oscillation, only the net flow rate. The net flow rate is 4.7 L/h, which corresponds to a $Re_{net} = 125$. This case is used as a reference and allows the effect of oscillations on the micromixing quality to be identified.

In a global manner, it can be seen that the presence of oscillations leads to a decrease in X_s , indicating an improvement in the micromixing performance. However, it is clear that the segregation index is not correlated solely with Re_o . For constant oscillation frequency f , an increase in the oscillation amplitude decreases X_s . However, at constant oscillation amplitude, an increase in frequency results in an increase in segregation index, which means decreased micromixing performance. At the same oscillatory Reynolds number, working with high amplitudes and small frequencies typically results in better micromixing quality than with lower amplitudes and higher frequencies. This observation is opposite than that presented in Chapter 5 where high amplitudes and small frequencies give poorer macromixing quality along the length of the COBR when compared with lower amplitudes and higher frequencies. The oscillation amplitude has a significant impact on the RTD and axial mixing. Indeed, increasing oscillation amplitude has shown to increase axial dispersion, D_{ax} (Dickens et al., 1989; Oliva et al., 2018; Slavnić et al., 2017). This is because oscillation amplitude directly controls the length of the eddies generated along the tube (Hamzah et al., 2012). From the macromixing results obtained in Chapter 5, it was observed that an increase in oscillation amplitude increased the backmixing upstream of the source position (see section 5.4.2.3 and Figure 5.10). However, if micromixing is improved under these conditions, this suggests that the mixing mechanism obtained with long and slow oscillations provides better contacting of the side and bulk streams at the injection point. Indeed, when there are fast changes of flow direction due to an increase in frequency as shown in Figure 5.9, there is significant non uniformity of the concentration field in the vicinity of the source position which could explain the high X_s and decreased micromixing performance shown in Figure 6.7. Similar behaviour has been observed by McDonough et al. (2019) in the characterization of micromixing in a 5 mm single orifice OBR with smooth constrictions under net flow conditions of Re_{net} of 5 - 40, and oscillatory conditions of $0.13 \leq x_b/l_b \leq 1.1$ and $1 \leq f \leq 10$ Hz, corresponding to Re_o of 0 - 1000. They observed an improvement in micromixing performance with the increase of Re_o . Our experimental results are in agreement with McDonough et al. (2019)'s results, who also found that high oscillation amplitudes increase the backmixing and improve micromixing quality.

From this, it is clear that a compromise between amplitude and frequency is required in order to achieve good mixing quality, shorter mixing lengths and good micromixing efficiency depending on the

specific objective and limiting phenomena of the application. For example, conditions of Case 6 from Chapter 5 ($x_o = 10 \text{ mm}$, $f = 1 \text{ Hz}$, $\psi = 8$) can achieve 64% of the perfectly mixed state (from a maximal of 87% obtained in our simulations) when a wall source is used. These conditions are very similar to those of Case 6 from this chapter ($x_o = 13 \text{ mm}$, $f = 1 \text{ Hz}$, $\psi = 9.5$), at which a good micromixing quality is obtained, as can be seen in Figure 6.7. In fast precipitations, this compromise between the choice of oscillatory conditions that improve both macro- and micromixing would allow acceptable micromixing performance for the nucleation of crystals and adequate homogeneity for short lengths of COBR, allowing controlled crystal growth in compact reactors.

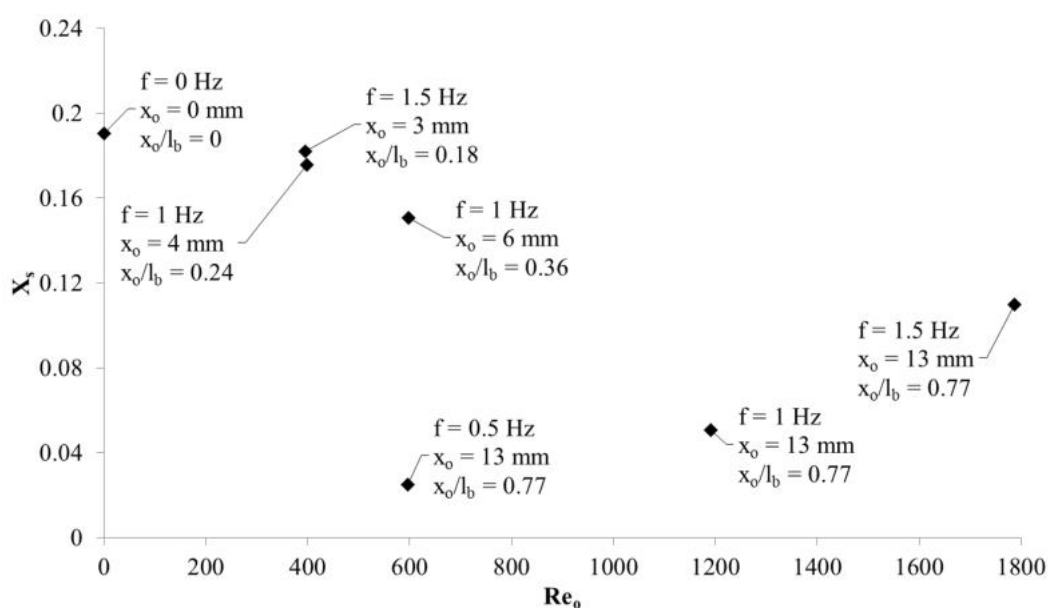


Figure 6.7: Segregation index as function of oscillatory Reynolds number for $[H_2SO_4] = 0.015 \text{ mol L}^{-1}$, $R = 7$ and $Re_{net} = 125$.

6.1.3.2. Influence of feed flow rate

The influence the volumetric flow rate ratio between the bulk and jet stream (R) over the micromixing performance is studied by increasing the flow rate at of the acid solution entering at the side injection. The side stream (acid) flow rate was increased from 0.67 L/h to 1.34 L/h whilst the flow rate of the bulk stream was kept constant at 4.7 L/h. To keep the number of moles introduced into the reactor constant and to avoid too high or too small amounts of iodine formed, the sulphuric acid concentration was adjusted, from 0.015 mol L^{-1} to $0.0075 \text{ mol L}^{-1}$, corresponding to a volumetric flow rate ratio between the main and jet streams equal to $R = 7$ and $R = 3.5$, respectively.

Figure 6.8 summarizes and compares the segregation index obtained with both volumetric flow rate ratios, $R = 7$ and $R = 3.5$ for different oscillatory conditions. The experimental error obtained between duplicates was found to be between 2 and 7%. Comparison of cases at the same oscillatory conditions allows the effect of the volumetric flow rate ratio on the micromixing quality to be studied. It can be

seen that for fixed oscillatory conditions, the segregation index decreases with an increase in the acid flow rate (or decrease the flow rate ratio R). For $R = 7$, a higher initial concentration of H^+ ions is used, which can cause a local excess of acid with respect to borate ions. In this case the excess acid is consumed by reaction (R2), thereby increasing X_S . The improved micromixing quality with the increase in acid flow rate may also be explained by an increase in the specific power density in the contacting zone. Indeed, an increase in the injection flow rate (and hence velocity) leads to an increase in the specific pressure drop and therefore, an increase in the specific power density in the mixing zone (Paul et al., 2004).

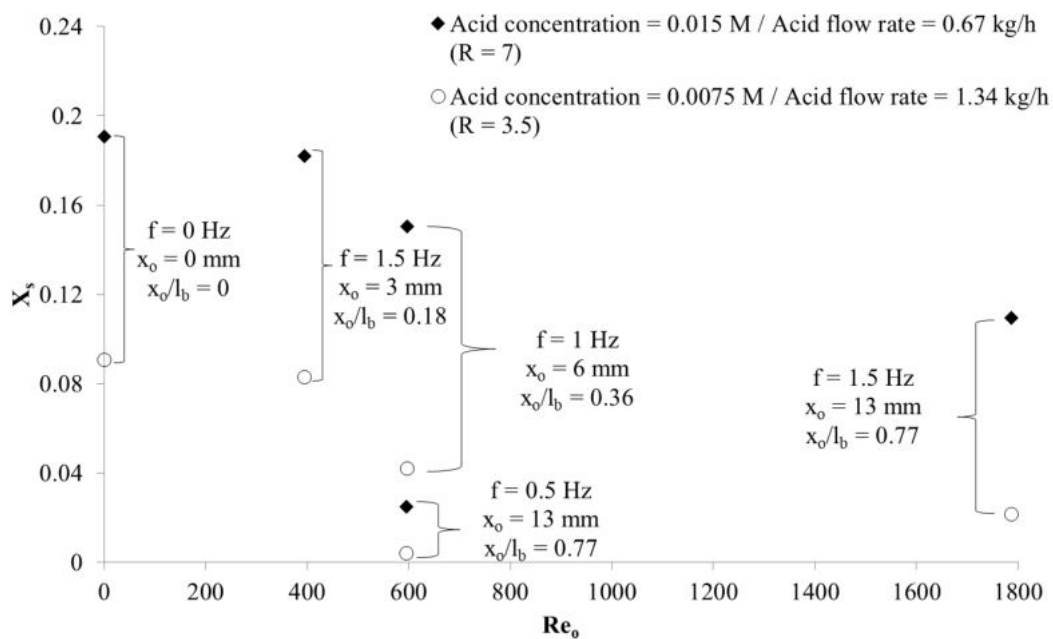


Figure 6.8: Segregation index as function of oscillatory Reynolds number for different acid flow rates.

It appears, hence, of interest to try to correlate the segregation index with specific power density. Since the micromixing is principally occurring in the acid-buffer contacting zone upstream of the baffles, the energy dissipation in this zone appears to be most relevant.

The energy dissipation in the injection zone is calculated using CFD using the mechanical energy balance approach from Chapter 4. The specific power density is evaluated for the volume indicated by the grey zone in Figure 6.9. The specific power density ($W\ kg^{-1}$) is obtained by dividing the energy dissipation per unit volume by the density.

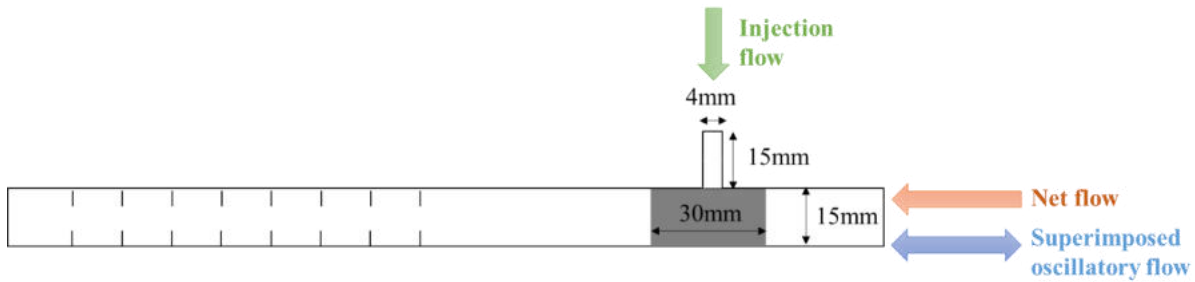


Figure 6.9: Schematic diagram of the acid-buffer contacting zone; the grey zone is the volume used for the calculation of specific power density.

Figure 6.10 presents the segregation index as a function of the specific power density in the injection zone for different acid flow rates. Whilst the data are scant, Figure 6.10 shows that the segregation index as a function of specific power density roughly follows a power law. However, 66% of the experimental points are within $\pm 50\%$ of this trendline. Two of the outliers (represented by the squares), correspond to the best micromixing quality, which were obtained with $x_o = 13 \text{ mm}$ and $f = 0.5 \text{ Hz}$ for both flow rates. These oscillatory conditions give lower specific power density when compared with Case 4, which has the same oscillatory Reynolds number (represented by the diamonds with $x_o = 6.5 \text{ mm}$ and $f = 1 \text{ Hz}$), but leads to improved micromixing quality. This is certainly due to the interaction of the acid plume with the bulk flow, as it was discussed in section 6.I.3.1. Furthermore, in the absence of oscillations (represented by the pentagons in Figure 6.10), an increase in the injection flow rate of acid by a factor of 2, results in a decrease in the segregation index by 50% but has no impact on the energy dissipation in the injection zone.

These results may suggest that the segregation index, and therefore micromixing in this system with oscillating flow does not correlate exclusively with specific power density, which is in agreement with the results on macromixing presented in Chapter 5. A possible explanation of this is that the mixing mechanism, which is dominated by stretching and folding of the acid plume in the bulk, controls the micromixing performance rather the energy dissipation. The increased injection flow rate of the acid, and hence a higher injection velocity, results in increased penetration of the acid jet in the bulk flow and improves the contact and mixing of the reactants.

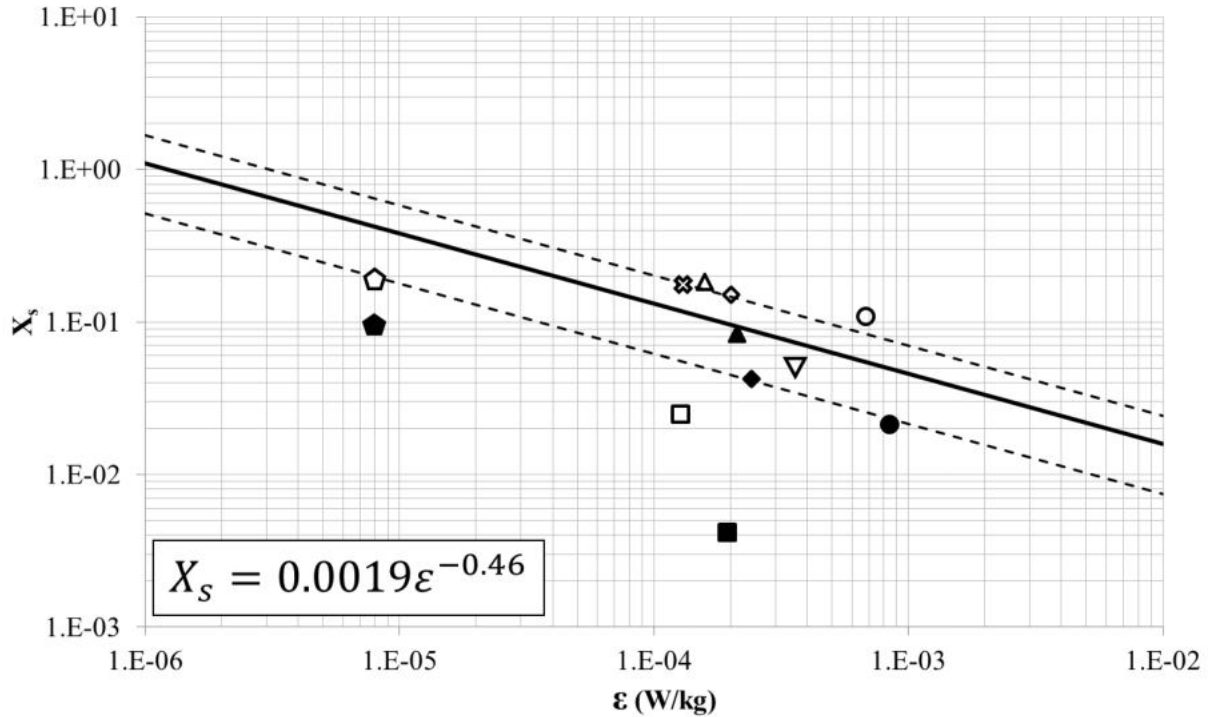


Figure 6.10: Segregation index as function of the specific power density. Dashed lines denote the positive and negative deviation from the trendline (solid line): $\pm 50\%$. Open symbols correspond to acid concentration $[H_2SO_4] = 0.015 \text{ mol L}^{-1}$ and $R = 7$; filled symbols correspond acid concentration $[H_2SO_4] = 0.0075 \text{ mol L}^{-1}$ and $R = 3.5$. Symbol shapes represent the operatory conditions: \diamond \blacklozenge ($x_o = 0 \text{ mm}$, $f = 0 \text{ Hz}$, $Re_o = 0$), \triangle \blacktriangle ($x_o = 3 \text{ mm}$, $f = 1.5 \text{ Hz}$, $Re_o = 400$), \boxtimes ($x_o = 4.5 \text{ mm}$, $f = 1 \text{ Hz}$, $Re_o = 400$), \diamond \blacklozenge ($x_o = 6.5 \text{ mm}$, $f = 1 \text{ Hz}$, $Re_o = 600$), \square \blacksquare ($x_o = 13 \text{ mm}$, $f = 0.5 \text{ Hz}$, $Re_o = 600$), ∇ ($x_o = 13 \text{ mm}$, $f = 1 \text{ Hz}$, $Re_o = 1200$) and \circ \bullet ($x_o = 13 \text{ mm}$, $f = 1.5 \text{ Hz}$, $Re_o = 1800$).

6.1.3.3. Micromixing time

Within the range of specific power density generated in the system (between 1×10^{-5} and 1×10^{-2} W/kg), the theoretical micromixing times from equation (6.17) range between 10^{-1} and 1 seconds. These results follow a power law function with the dissipated power such that $t_{m \text{ theo}} = 12(\nu/\varepsilon)^{1/2}$. The value of the constant is between that for the micromixing time by engulfment $t_m = 17.2(\nu/\varepsilon)^{1/2}$ proposed by Baldyga and Bourne (1989) for turbulent STRs and the micromixing time in static mixers in turbulent flow $t_m = 7.1(\nu/\varepsilon)^{1/2}$ (Fang and Lee, 2001). The values of the constants are significantly lower than for laminar flow micromixers where $t_m = 150(\nu/\varepsilon)^{1/2}$ (Falk and Commenge, 2010). This suggests that in terms of energy dissipation, mixing efficiency in COBRs is similar to stirred tanks and static mixers; however, times are significantly greater than what can be achieved in micromixers.

Figure 6.11 compares the theoretical and calculated micromixing times obtained with the incorporation model as a function of the specific power density for different acid concentrations and volumetric flow rate ratios. According to the experimental values of X_s , it can be seen that $t_{m \text{ cal}}$ is within the range of 1-23 ms, which are 1-2 orders of magnitude lower than the theoretical micromixing times. Similarly, the constant value of the trend equation for the calculated micromixing is 2 order of

magnitude lower than the trend equation of the theoretical micromixing time. Considering the laminar injection of the acid stream and the gentle mixing mechanism in the COBR, this order of magnitude of micromixing time calculated by the incorporation model appears to be too short and non-physical. Indeed, the incorporation model may not correctly represent the physics of the mixing mechanism in the system whereby the acid plume is stretched, folded and transported axially due to the combination of the net and oscillatory flows. This mixing mechanism encountered by the acid plume is different than that encountered in turbulent and laminar flows encountered in STRs and micromixers.

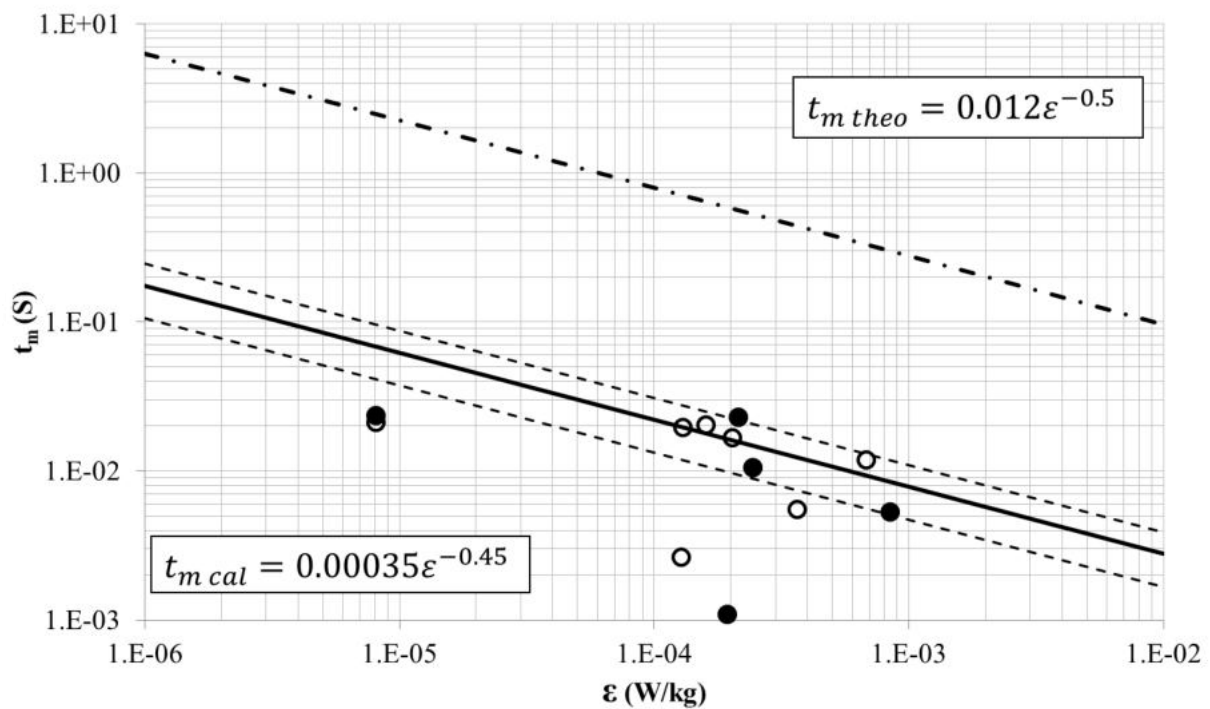


Figure 6.11: Theoretical (dash-dotted line) and calculated (open/filled symbols) micromixing time as function of the specific power density. Dashed lines denote the positive and negative deviation from the trendline (solid line): $\pm 40\%$. Open symbols correspond to acid concentration $[H_2SO_4] = 0.015\ mol\ L^{-1}$ and $R = 7$; filled symbols correspond acid concentration $[H_2SO_4] = 0.0075\ mol\ L^{-1}$ and $R = 3.5$.

6.I.4. Conclusions

The influence of the oscillatory conditions and flow rate of a secondary feed on the micromixing quality using the iodide-iodate or Villermaux-Dushman test reactions has been studied in a COBR with smooth constrictions in the laminar flow regime ($Re_o < 2000$).

Analysis of the segregation index, X_s , as a measure of micromixing quality, has shown that the presence of oscillatory flow improves the micromixing performance in the reactor. The relationship between X_s is not exclusively correlated to Re_o , as differences between segregation index were found when different combinations of amplitude and frequency were used for the same Re_o . Higher amplitudes and lower frequencies are preferred over lower amplitudes and higher frequencies to have a better micromixing performance.

Micromixing times were calculated with the exponential approach of the incorporation model, which are within the range of 1-23 ms. These times are considered to be too fast for the laminar flow studied. This may be attributed to limitations of the micromixing model chosen, which does not take into consideration the particular hydrodynamics of the oscillating reactant flows.

A compromise between amplitude and frequency may be required in order to achieve acceptable macro- and micromixing performances, depending on the specific objective and limiting phenomena of the application considered. In the current setup, oscillation amplitude and frequency can be chosen such that they improve mixing homogeneity, while the micromixing performance can be improved just by increasing the injection flow rate. The mixing mechanism between the injection flow with the main stream and oscillatory flow needs to be studied further.

Part II: Visual analysis of a passive tracer upstream of the baffled zone

6.II.1. Introduction

The present study aims the visualization of macromixing of a passive tracer injected at the axis of the tube upstream of the baffled zone. The initial goal was to compare the experimental results with those obtained with the numerical simulation from Chapter 5. However, the first experiments revealed unexpected mixing behaviour of the system. Due to this, the objective of the study was reoriented to focus on the zone between the tracer injection point and the first baffle of the COBR in order to better understand the observations. The effect of the oscillations, inlet orientations and viscosity on the tracer dispersion in the zone between the tracer injection point and the first baffle of the COBR was therefore explored.

6.II.2. Materials and methods

6.II.2.1. Experimental rig

Visualisation experiments are carried out in the commercial NiTech® glass COBR presented in detail in Chapter 6 Part I. The passive tracer is injected with an elbow pipe (1.5 mm diameter) at the central axis of the reactor and 75 mm before the first orifice baffle, as is shown in Figure 6.12. This is different to the injection configuration used in the micromixing experiments in Chapter 6 Part I. The bulk flow is fed 40 cm from the first orifice baffle. Two different orientations of the inlets (bulk flow and secondary injection) are tested, being both perpendiculars to the reactor axis, named top entry and bottom entry and presented in Figure 6.13(a) and Figure 6.13(b), respectively. The visual analysis of mixing is performed in the first three cells of the COBR.

6.II.2.2. Fluids and operating conditions

Macromixing experiments are performed using fluids of different viscosity: water ($\mu = 1 \times 10^{-3}$ Pa.s) and a solution of 69% wt. of glycerol-water ($\mu = 2 \times 10^{-2}$ Pa.s), which is the same viscosity used in the numerical simulation from Chapter 5. The passive tracer is methylene blue, which was diluted in either water or the glycerol solution at a concentration of 0.7 g/L, and injected into the bulk flow of the same fluid without tracer. The bulk and secondary flow rates are 5 L/h and 6.5×10^{-2} L/h, respectively. The net Reynolds numbers for the water and glycerol solution are 126 and 7, respectively.

The oscillatory frequency is set to values of 1 and 1.75 Hz and the oscillatory amplitude is set to 5, 10 and 20 mm, which correspond to $0.3l_b$, $0.6l_b$ and $1.2l_b$, respectively. The operating conditions are chosen to be similar to the ones used nowadays in crystallization processes in OBRs: high frequencies (above 1 Hz) and amplitudes within the range of $0.3l_b$ – $0.6l_b$ (Brown and Ni, 2011a, 2011b; Callahan et al., 2012; Ni et al., 2004). An amplitude above this range is also tested since there are some

crystallization processes operates under this condition (Briggs et al., 2015). Under these ranges of oscillatory conditions, the oscillatory Reynolds number, Re_o , varies in the range 470 to 1880 for water and from 28 to 190 for the glycerol solution, thereby ensuring a laminar flow regime for water ($Re_o < 2000$), and axi-symmetrical laminar flow for the glycerol-water solution ($Re_o < 250$).

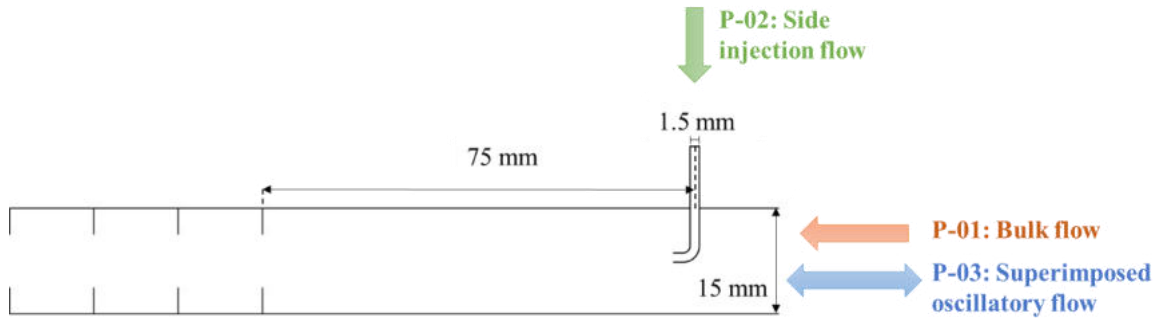


Figure 6.12: Schematic diagram of the entries from P-01 (bulk flow), P-02 (side injection flow) and P-03 (oscillatory flow) to the Nitech® reactor.



(a)



(b)

Figure 6.13: Images for the different inlets orientations: (a) top entry, (b) bottom entry. Blue tube feed the bulk flow, and the red tube feed the secondary injection – the distance between the tubes is 30 cm.

6.II.3. Observations

6.II.3.1. Initial experiments on macromixing

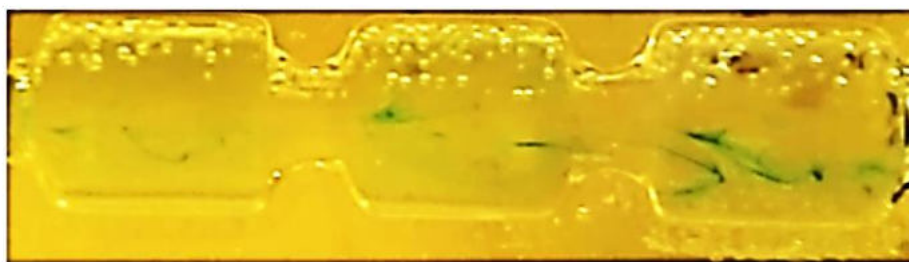
Two different cases were investigated as preliminary tests to ensure the correct operation of experimental rig:

- Case 1: Inlet orientations: top entry, glycerol solution, $f = 1$ Hz and $x_o = 10$ mm.
- Case 2: Inlet orientations: bottom entry, water, $f = 1$ Hz and $x_o = 5$ mm.

The rig is firstly fed with the bulk and secondary flows without oscillations. Once the tracer injection is stable along the axis of the COBR, the oscillations are started and the mixing of the tracer in the first three baffles is observed. Images obtained for Cases 1 and 2 are presented in Figure 6.14. Despite the fact that for both cases the tracer injection was initially stable along the axis of the COBR, the start-up of oscillations causes the tracer to be transported along the top or the bottom of the COBR, depending on the oscillatory conditions and the orientation of the inlets. To better understand the cause of these observations, the subsequent visualisation experiments focused on the zone between the tracer injection point and the first baffle of the COBR, which will be detailed in the following sections.



(a)



(b)

Figure 6.14: Tracer patterns for (a) Case 1 and (b) Case 2.

6.II.3.2. Influence of the frequency and amplitude

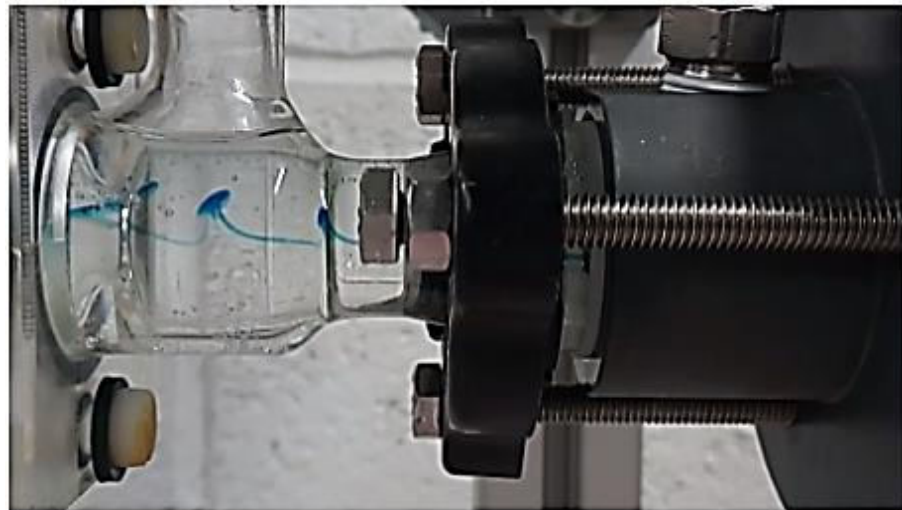
Figure 6.15 shows the tracer flow pattern for the top entry inlet orientation for different oscillatory conditions. The presence of the oscillatory flow deforms and folds the tracer filament, and this differently depending on the oscillation conditions (frequency and amplitude). As the frequency increases from 1 to 1.75 Hz, the number of perturbations or “waves” increases. The number of

perturbations increases from 3 to 4 when the frequency increases from 1 to 1.75 with $x_o = 5$ mm (Figure 6.15(a) and Figure 6.15(b)), and from 2 to 3 with $x_o = 10$ mm (Figure 6.15(c) and Figure 6.15(d)).

An increase in the amplitude leads to a change in the shape of the perturbations and a reduced number of perturbations in the downstream space. For an amplitude of 5 mm, the tracer filament folds due to the oscillations (Figure 6.15(a) and Figure 6.15(b)). With the increase of the amplitude to 10 mm, the shape of tracer changes to a bell-shape with two vortices, one at the top and the other at the bottom of the perturbation (Figure 6.15(c) and Figure 6.15(d)). Despite the different shapes of the perturbations between cases at different amplitudes, it can be seen that the number of perturbations decreases from 3 to 2 when the amplitude increases from 5 to 10 mm with $f = 1$ Hz (Figure 6.15(a) and Figure 6.15(c)), and from 4 to 3 with $f = 1.75$ Hz (Figure 6.15(b) and Figure 6.15(d)).

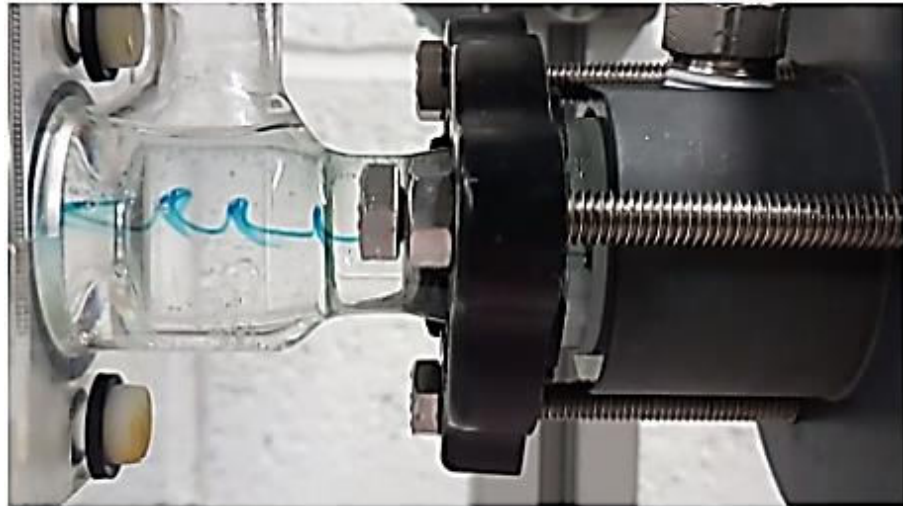
It is interesting to highlight that the tracer starts to migrate slightly towards the top of the reactor in the presence of oscillations, and this effect becomes greater as the oscillatory velocity increases (e.g. Figure 6.15(e) $f = 1$ Hz and $x_o = 20$ mm). This change in the tracer flow direction leads to the apparition of heterogeneous areas in the first baffle cell in the COBR with segregated zones between the upper and lower sections of the baffles, with almost of the tracer in the upper part and none in the lower part (as shown in Figure 6.14(a)). This segregation in the COBR can be detrimental for mixing performance. These phenomena (i.e. the change of the number and shape of the perturbations and the migration of the tracer flow pattern towards the top wall) are still present at lower net flow rates. A possible explanation for this phenomenon is discussed in the following section.

$f = 1$ Hz
 $x_o = 5$ mm
 $Re_o = 470$
 $\psi = 4$



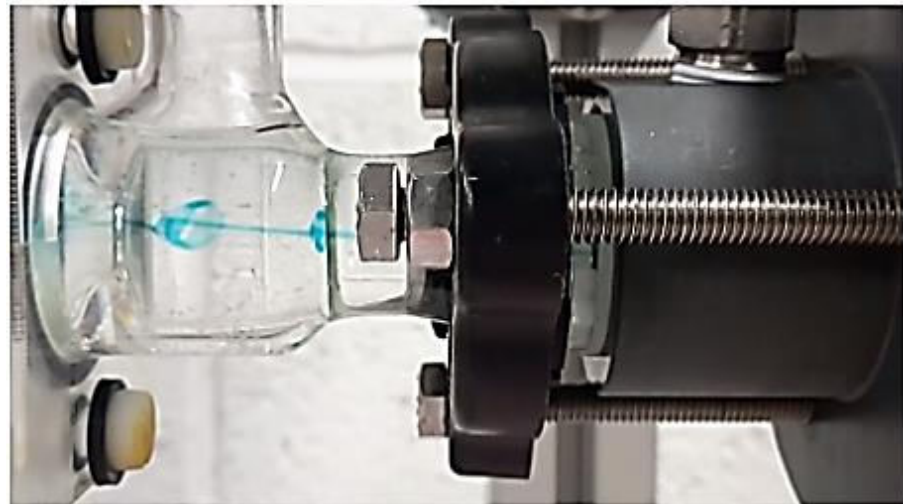
(a)

$f = 1.75 \text{ Hz}$
 $x_o = 5 \text{ mm}$
 $Re_o = 820$
 $\psi = 7$



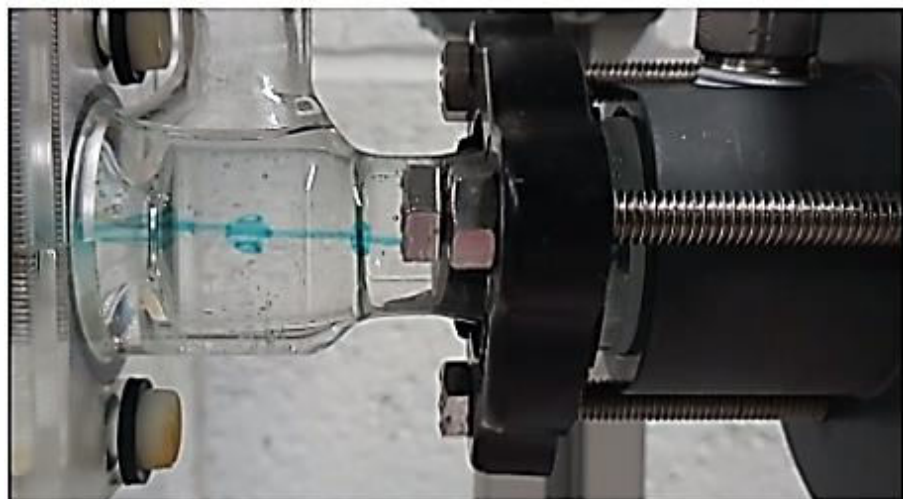
(b)

$f = 1 \text{ Hz}$
 $x_o = 10 \text{ mm}$
 $Re_o = 940$
 $\psi = 7$



(c)

$f = 1.75 \text{ Hz}$
 $x_o = 10 \text{ mm}$
 $Re_o = 1644$
 $\psi = 13$



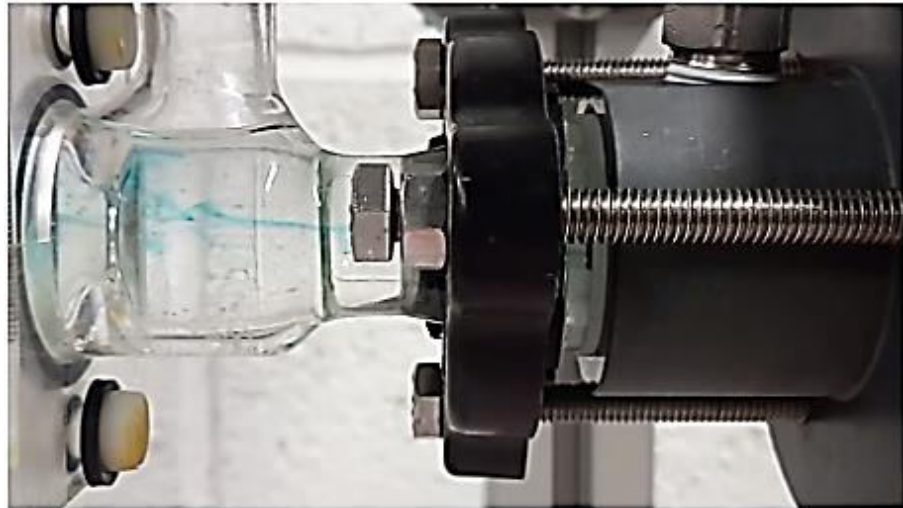
(d)

$$f = 1 \text{ Hz}$$

$$x_o = 20 \text{ mm}$$

$$Re_o = 1880$$

$$\psi = 15$$



(e)

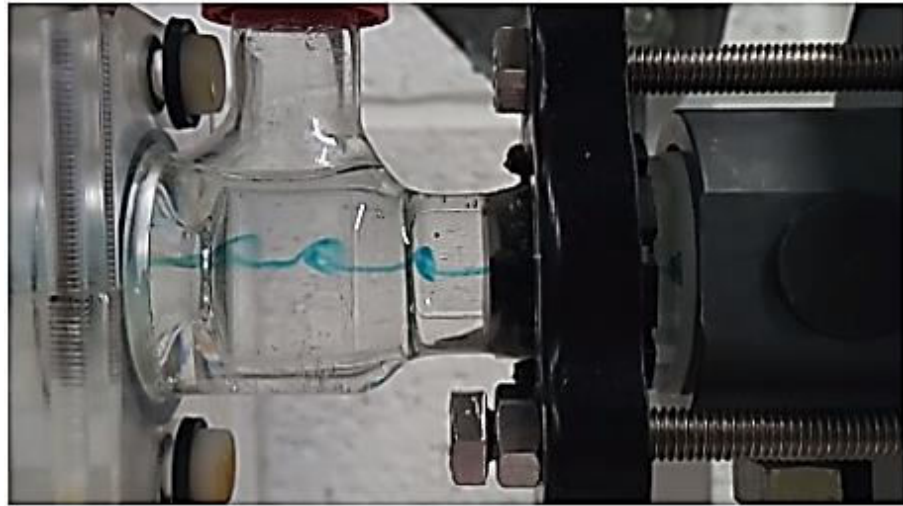
Figure 6.15: Results of the central passive injection for the inlets top entry orientation using water as the working fluid.

6.II.3.3. Influence of the inlet orientation

The effects of the orientation of the inlet flows (i.e. top and bottom entry) on the tracer flow pattern are studied by comparing Figure 6.15 (for top entry orientation) and Figure 6.16 (for bottom entry orientation). When the inlets are orientated at the bottom, it can be seen in Figure 6.16 that the influence of the amplitude and frequency on the tracer flow pattern is the same as that observed for the top entry orientation (i.e. increase in the number of deformations with the increase of the frequency, and decrease in the number of deformations and change in its shape with the increase of the amplitude). The most remarkable difference, however, is that the tracer migrates towards the bottom of the reactor with an increase of the oscillatory velocity (Figure 6.15(d) and Figure 6.15(e)), which is the opposite effect observed with the top entry orientation but also leading to the same problems of the apparitions of heterogeneous areas, like the ones presented in Figure 6.14(b), where the segregated zones are created, being more notable after the first baffle.

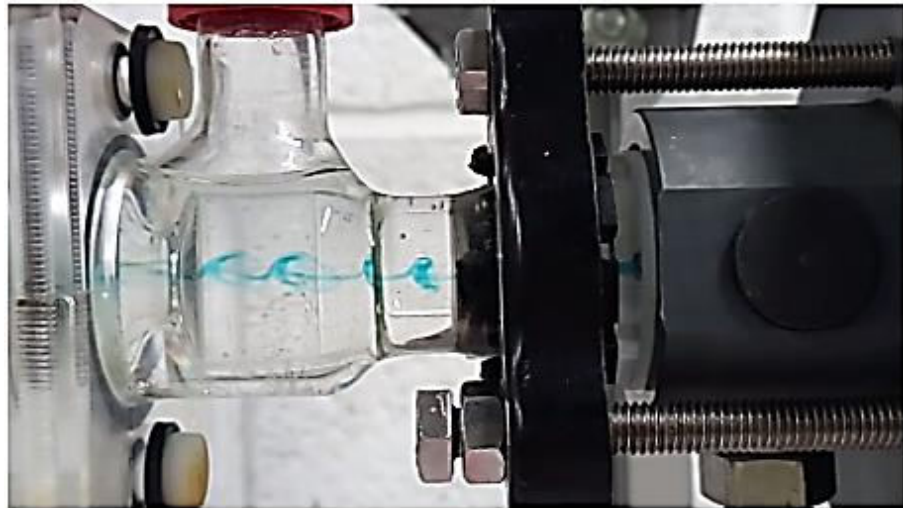
The migration of the tracer towards the top or the bottom of the COBR clearly depends on the orientation. One explanation for this is that the bulk flow that enters the 30 cm feed tube does not have time to achieve a pseudo-stationary profile before convecting the tracer. In order to confirm this hypothesis, further visualisation studies with a longer tube installed before the secondary injection will be required.

$f = 1 \text{ Hz}$
 $x_o = 5 \text{ mm}$
 $Re_o = 470$
 $\psi = 4$



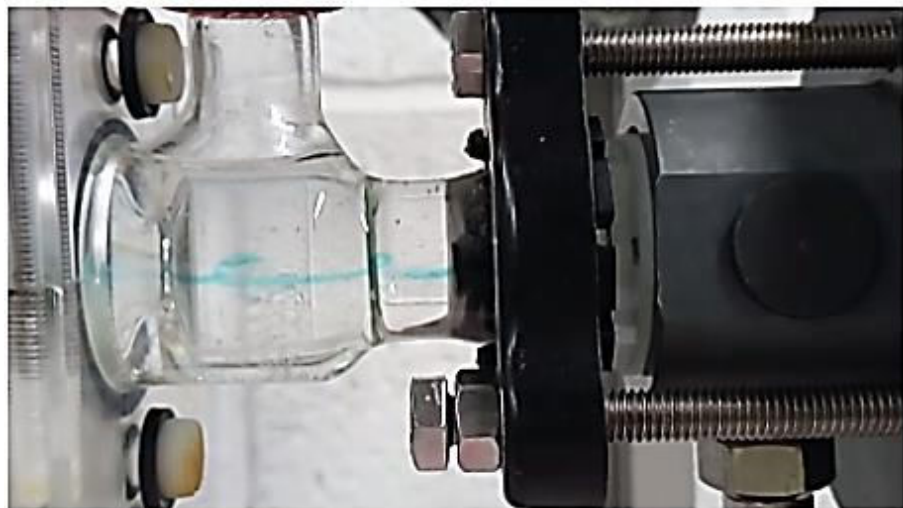
(a)

$f = 1.75 \text{ Hz}$
 $x_o = 5 \text{ mm}$
 $Re_o = 820$
 $\psi = 7$



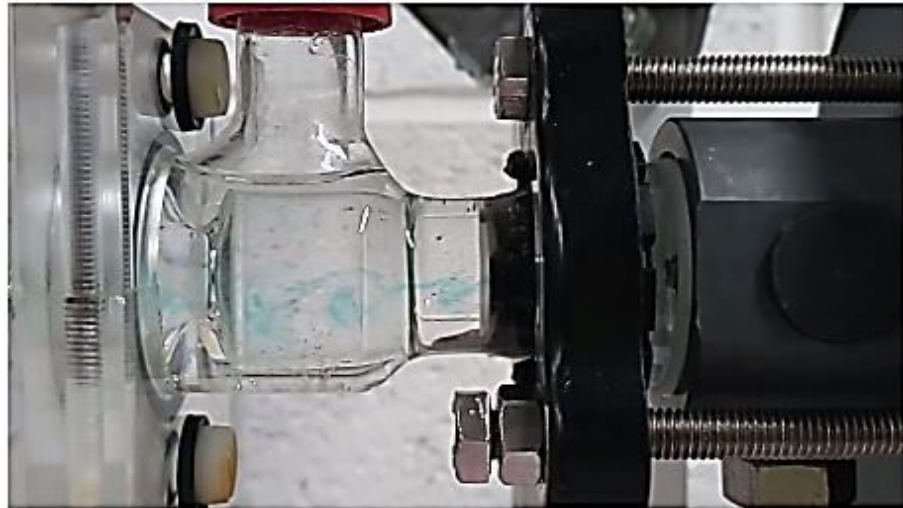
(b)

$f = 1 \text{ Hz}$
 $x_o = 10 \text{ mm}$
 $Re_o = 940$
 $\psi = 7$



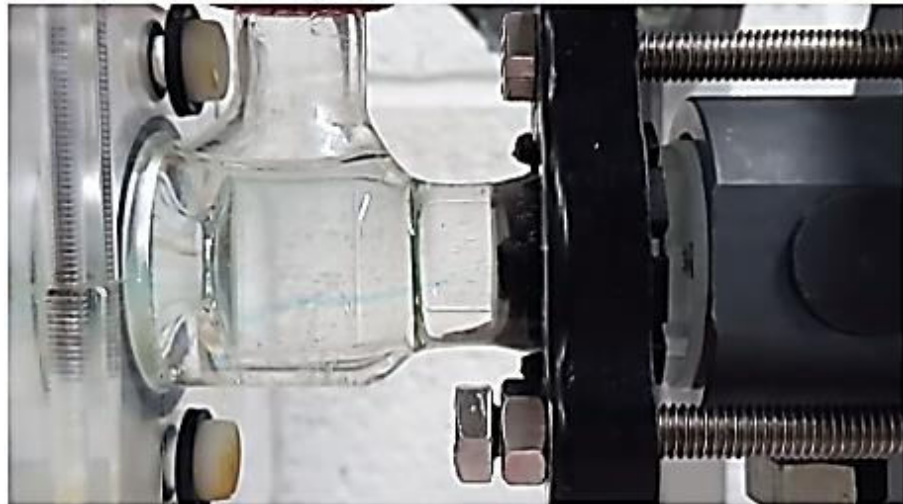
(c)

$f = 1.75 \text{ Hz}$
 $x_o = 10 \text{ mm}$
 $Re_o = 1644$
 $\psi = 13$



(d)

$f = 1 \text{ Hz}$
 $x_o = 20 \text{ mm}$
 $Re_o = 1880$
 $\psi = 15$



(e)

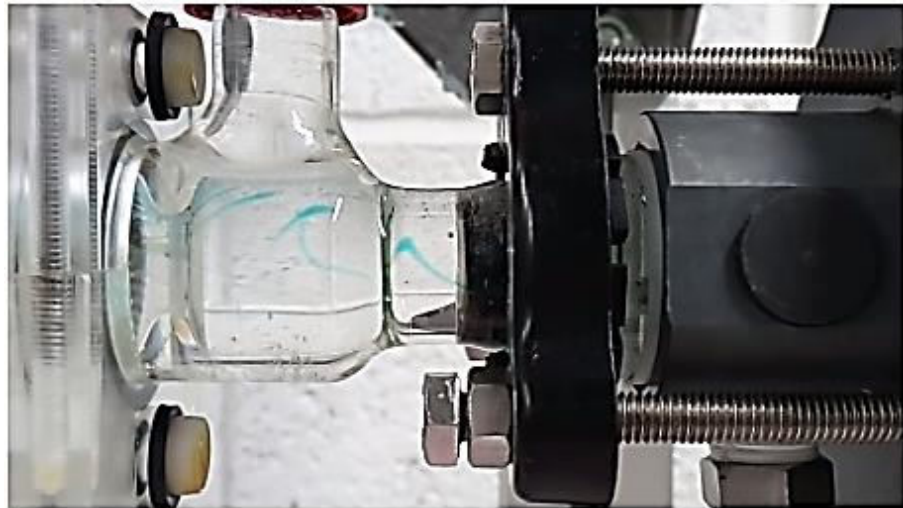
Figure 6.16: Results of the central passive injection for the inlets bottom entry orientation using water as the working fluid.

6.II.3.4. Influence of the viscosity

Figure 6.17 presents the tracer patterns obtained with the glycerol solution for the bottom entry inlet orientation. The tracer appears to be stretched and folded more than when water is used, and no ring patterns are created. Surprisingly, and unlike what is observed in Figure 6.16 for water with the same inlet orientation, the tracer migrates towards the top of the reactor. Since the same net flow rate is used for the cases water and glycerol solution as working fluids, this difference in the migration of the tracer may be due to the difference between the viscosities (or net Reynolds number). The net flow is introduced to the system through a 4 mm diameter pipe connected to a 15 mm T-junction, with a depth of 3 cm (Figure 6.18). The net Reynolds number decreases from 470 to 126 for water, and from 27 to 7 for the glycerol solution when going from the 4 mm diameter tube to the 15 mm diameter tube. This reduction in the net Reynolds number, together with the interaction between the oscillatory flow as the

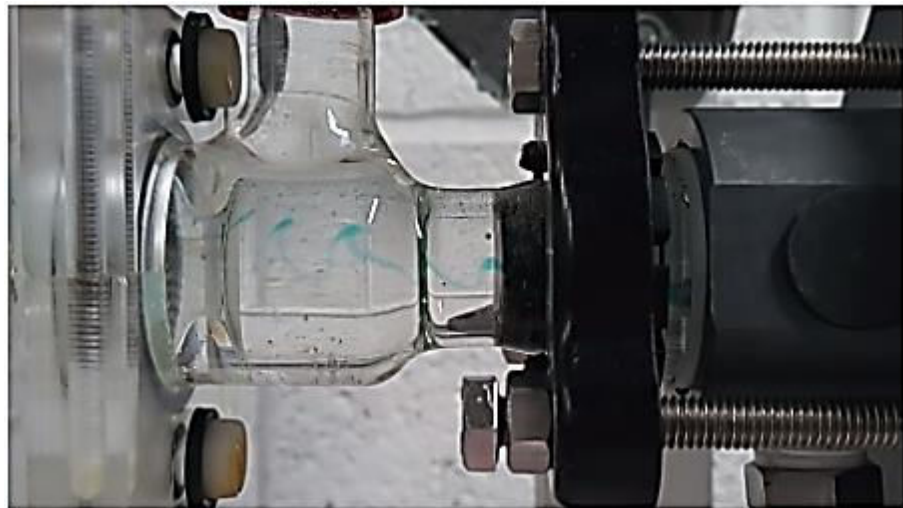
net flow crosses the T-junction depth, could modify the velocity profiles by different degrees depending on the value of the net Reynolds number. Under a laminar flow regime (without the presence of the oscillations), the 30 cm feed tube should be long enough to stabilize a stationary profile, however, there is no study in the literature that establishes the minimum length to achieve a pseudo-stationary profile when a perpendicular flow encounters the oscillatory flow. Nevertheless, these possible explanations need to be corroborated before more conclusive discussions can be made.

$$\begin{aligned}f &= 1 \text{ Hz} \\x_o &= 5 \text{ mm} \\Re_o &= 28 \\ \psi &= 4\end{aligned}$$



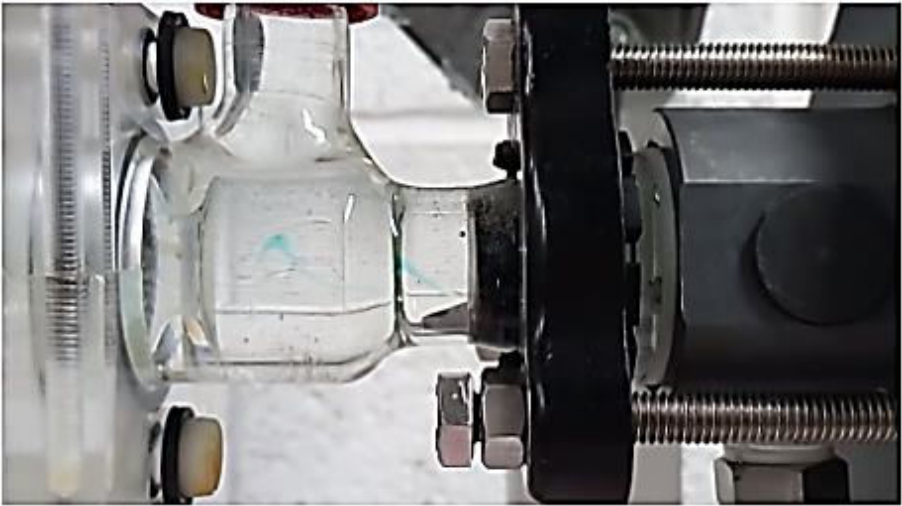
(a)

$$\begin{aligned}f &= 1.75 \text{ Hz} \\x_o &= 5 \text{ mm} \\Re_o &= 49 \\ \psi &= 7\end{aligned}$$



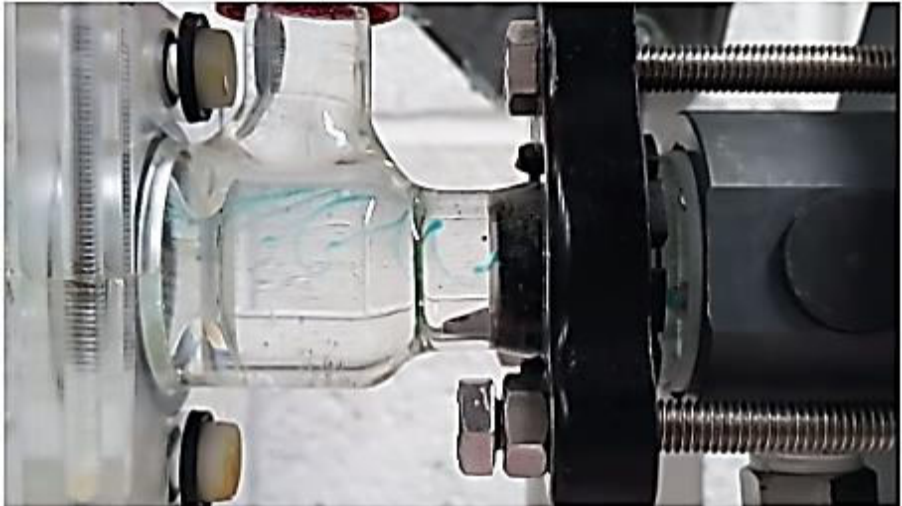
(b)

$f = 1 \text{ Hz}$
 $x_o = 10 \text{ mm}$
 $Re_o = 56$
 $\psi = 8$



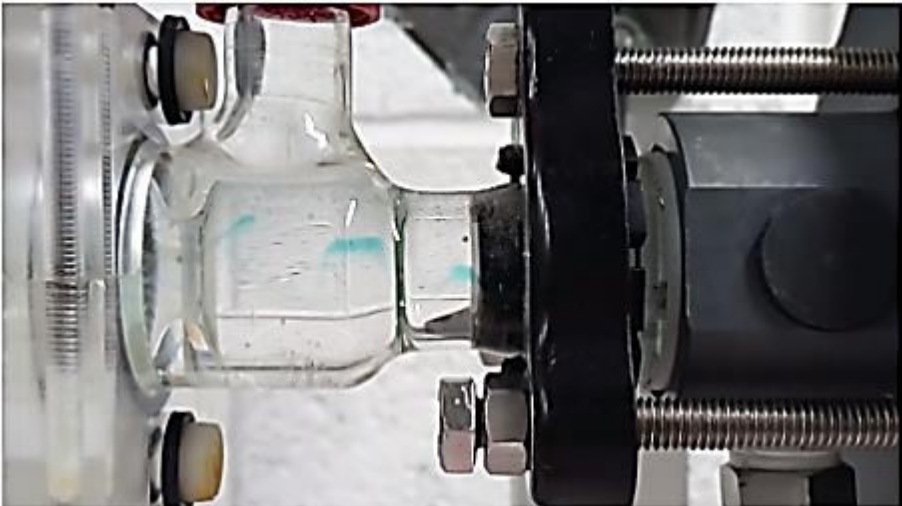
(c)

$f = 1.75 \text{ Hz}$
 $x_o = 10 \text{ mm}$
 $Re_o = 98$
 $\psi = 14$



(d)

$f = 1 \text{ Hz}$
 $x_o = 20 \text{ mm}$
 $Re_o = 108$
 $\psi = 15$



(e)

$f = 1.75 \text{ Hz}$
 $x_o = 20 \text{ mm}$
 $Re_o = 190$
 $\psi = 27$



(f)

Figure 6.17: Results of the central passive injection for the inlets bottom entry orientation using a solution of 69% wt. glycerol/water as the working fluid.

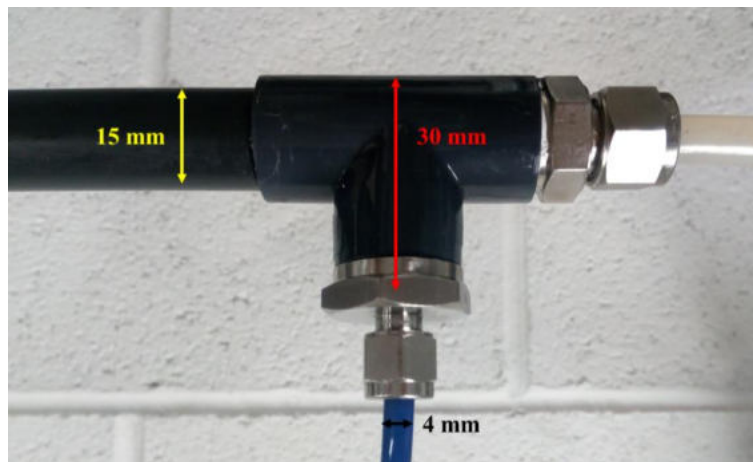


Figure 6.18: Inlet zone between the net flow (blue pipe) and the system, with the oscillations being provided through the white pipe.

6.II.4. Conclusions

The influence of oscillatory conditions, viscosity and inlet orientations on the flow of a passive tracer upstream the COBR has been observed visually. Frequency and amplitude show to modify the flow between the injection point and the first baffles. Furthermore, the flow shows to move up or down from the injection point towards the reactor walls, depending in the inlet orientation and the viscosity. If the secondary injection is poorly distributed in the first cells of the COBR, segregated zones and over- and under-concentrated areas can be formed, which would cause a decrease in mixing quality at early stages of the reactor, which are important for the nucleation of crystals in rapid crystallization and precipitation processes.

The experimental system seems to be very sensitive to the orientation of the net inlet flow and its interaction with the oscillatory flow and the viscosity. This could be related to the minimal length necessary to allow a fully well-developed flow profile of the net flow before it reaches the secondary injection. Due to lack of time, it was very difficult to made well-supported conclusions and it was not possible to go any further in the corroboration of the possible explanations discussed to explain the phenomena observed. Different tracks of research are given for future work, like the study of the flow in the T-junction, or the minimum length to achieve the pseudo-steady state.

General conclusions

In this chapter, micro and macromixing experiments have been carried out in a commercial NiTech[®] glass COBR.

The micromixing performance is shown to be dependent on the oscillatory conditions, and the flow rate of the secondary stream, whilst there is little or no correlation of micromixing with specific power density. This result is in agreement with the results presented in Chapter 5 for the characterization of macromixing.

A preliminary visualisation study of a passive tracer has been carried out to obtain information on macromixing in the COBR. The flow between the injection point and the first baffles show to be sensitive to the orientation of the net inlet flow and its interaction with the oscillatory flow and the viscosity. Despite not having any decisive conclusion due to lack of time, research tracks for future work are given.

The results obtained in this chapter should be taken into account to favour better conditions for micro and macromixing performance at the first stages of a COBR as a first step towards the ultimate goal of the implementation of rapid/instantaneous reaction applications in this kind of reactor.

References

- Abbott, M.S.R., Harvey, A.P., Morrison, M.I., 2014. Rapid determination of the Residence time distribution (RTD) function in an oscillatory baffled reactor (OBR) using a design of experiments (DoE) approach. *Int. J. Chem. React. Eng.* 12, 575–586.
<https://doi.org/10.1515/ijcre-2014-0040>
- Awtrey, A.D., Connick, R.E., 1951. The absorption spectra of I₂, I₃⁻, I⁻, IO₃⁻, S₄O₅⁻ and S₂O₃⁻. Heat of the reaction I₃⁻ = I₂ + I⁻. *J. Am. Chem. Soc.* 73, 1842–1843.
<https://doi.org/10.1021/ja01148a504>
- Baldyga, J., Bourne, J.R., 1989. Simplification of micromixing calculations. I. Derivation and application of new model. *Chem. Eng. J.* 42, 83–92.
- Baldyga, J., Bourne, J.R., 1984. A fluid mechanical approach to turbulent mixing and chemical reaction part iii computational and experimental results for the new micromixing model. *Chem. Eng. Commun.* 28, 259–281. <https://doi.org/10.1080/00986448408940136>
- Baldyga, J., Pohorecki, R., 1995. Turbulent micromixing in Chemical Reactors - a Review. *Chem. Eng. J.* 58, 183–195. [https://doi.org/10.1016/0923-0467\(95\)02982-6](https://doi.org/10.1016/0923-0467(95)02982-6)
- Briggs, N.E.B., Schacht, U., Raval, V., McGlone, T., Sefcik, J., Florence, A.J., 2015. Seeded crystallization of β- L -glutamic acid in a continuous oscillatory baffled crystallizer. *Org. Process Res. Dev.* 19, 1903–1911. <https://doi.org/10.1021/acs.oprd.5b00206>
- Brown, C.J., Ni, X., 2011a. Online evaluation of paracetamol antisolvent crystallization growth rate with video imaging in an oscillatory baffled crystallizer. *Cryst. Growth Des.* 11, 719–725.
<https://doi.org/10.1021/cg1011988>
- Brown, C.J., Ni, X., 2011b. Evaluation of growth kinetics of antisolvent crystallization of paracetamol in an oscillatory baffled crystallizer utilizing video imaging. *Cryst. Growth Des.* 11, 3994–4000.
<https://doi.org/10.1021/cg200560b>
- Callahan, C.J., Ni, W., Ni, X.-W.W., 2012. Probing into Nucleation Mechanisms of Cooling Crystallization of Sodium Chlorate in a Stirred Tank Crystallizer and an Oscillatory Baffled Crystallizer. *Cryst. Growth Des.* 12, 2525–2532. <https://doi.org/10.1021/cg300135w>
- Cheng, K., Liu, C., Guo, T., Wen, L., 2019. CFD and experimental investigations on the micromixing performance of single countercurrent-flow microchannel reactor. *Chinese J. Chem. Eng.* 27, 1079–1088. <https://doi.org/10.1016/j.cjche.2018.11.026>
- Commonge, J.M., Falk, L., 2011. Villermaux-Dushman protocol for experimental characterization of micromixers. *Chem. Eng. Process. Process Intensif.* 50, 979–990.
<https://doi.org/10.1016/j.cep.2011.06.006>
- Dickens, A.W., Mackley, M.R., Williams, H.R., 1989. Experimental residence time distribution measurements for unsteady flow in baffled tubes. *Chem. Eng. Sci.* 44, 1471–1479.
[https://doi.org/10.1016/0009-2509\(89\)80023-5](https://doi.org/10.1016/0009-2509(89)80023-5)
- Falk, L., Commonge, J.M., 2010. Performance comparison of micromixers. *Chem. Eng. Sci.* 65, 405–

411. <https://doi.org/10.1016/j.ces.2009.05.045>
- Fang, J.Z., Lee, D.J., 2001. Micromixing efficiency in static mixer. *Chem. Eng. Sci.* 56, 3797–3802. [https://doi.org/10.1016/S0009-2509\(01\)00098-7](https://doi.org/10.1016/S0009-2509(01)00098-7)
- Fonte, C.P., Fletcher, D.F., Guichardon, P., Aubin, J., 2020. Simulation of micromixing in a T-mixer under laminar flow conditions. *Chem. Eng. Sci.* 222, 115706. <https://doi.org/10.1016/j.ces.2020.115706>
- Fournier, M.C., Falk, L., Villiermaux, J., 1996a. A new parallel competing reaction system for assessing micromixing efficiency - Experimental approach. *Chem. Eng. Sci.* 51, 5053–5064.
- Fournier, M.C., Falk, L., Villiermaux, J., 1996b. A new parallel competing reaction system for assessing micromixing efficiency - Determination of micromixing time by simple mixing model. *Chem. Eng. Sci.* 51, 5187–5192. [https://doi.org/10.1016/0009-2509\(96\)00270-9](https://doi.org/10.1016/0009-2509(96)00270-9)
- Ghanem, A., Lemenand, T., Della Valle, D., Peerhossaini, H., 2014. Static mixers: Mechanisms, applications, and characterization methods - A review. *Chem. Eng. Res. Des.* 92, 205–228. <https://doi.org/10.1016/j.cherd.2013.07.013>
- Guichardon, P., Falk, L., Villiermaux, J., 2000a. Characterisation of micromixing efficiency by the iodide-iodate reaction system. Part I: experimental procedure. *Chem. Eng. Sci.* 55, 4233–4243. [https://doi.org/10.1016/S0009-2509\(00\)00069-5](https://doi.org/10.1016/S0009-2509(00)00069-5)
- Guichardon, P., Falk, L., Villiermaux, J., 2000b. Characterisation of micromixing efficiency by the iodide-iodate reaction system. Part II: kinetic study. *Chem. Eng. Sci.* 55, 4245–4253.
- Hamzah, A.A., Hasan, N., Takriff, M.S., Kamarudin, S.K., Abdullah, J., Tan, I.M., Sern, W.K., 2012. Effect of oscillation amplitude on velocity distributions in an oscillatory baffled column (OBC). *Chem. Eng. Res. Des.* 90, 1038–1044. <https://doi.org/10.1016/j.cherd.2011.11.003>
- Holz, M., Heil, S.R., Sacco, A., 2000. Temperature-dependent self-diffusion coefficients of water and six selected molecular liquids for calibration in accurate ¹H NMR PFG measurements. *Phys. Chem. Chem. Phys.* 2, 4740–4742. <https://doi.org/10.1039/b005319h>
- Kacker, R., Regensburg, S.I., Kramer, H.J.M., 2017. Residence time distribution of dispersed liquid and solid phase in a continuous oscillatory flow baffled crystallizer. *Chem. Eng. J.* 317, 413–423. <https://doi.org/10.1016/j.cej.2017.02.007>
- Kölbl, A., Kraut, M., Dittmeyer, R., 2013. Kinetic investigation of the Dushman reaction at concentrations relevant to mixing studies in stirred tank reactors. *Chem. Eng. Sci.* 101, 454–460. <https://doi.org/10.1016/j.ces.2013.07.008>
- Lafficher, R., Digne, M., Salvatori, F., Boualleg, M., Colson, D., Puel, F., 2018. Influence of micromixing time and shear rate in fast contacting mixers on the precipitation of boehmite and NH₄-dawsonite. *Chem. Eng. Sci.* 175, 343–353. <https://doi.org/10.1016/j.ces.2017.10.011>
- Levenspiel, O., 1999. *Chemical reaction engineering*, 3rd ed. John Wiley & Sons, Inc.
- Li, W., Xia, F., Qin, H., Zhang, M., Li, W., Zhang, J., 2019. Numerical and experimental investigations of micromixing performance and efficiency in a pore-array intensified tube-in-tube

- microchannel reactor. *Chem. Eng. J.* 370, 1350–1365. <https://doi.org/10.1016/j.cej.2019.03.189>
- Mackley, M.R., Ni, X., 1991. Mixing and dispersion in a baffled tube for steady laminar and pulsatile flow. *Chem. Eng. Sci.* 46, 3139–3151. [https://doi.org/10.1016/0009-2509\(91\)85017-R](https://doi.org/10.1016/0009-2509(91)85017-R)
- McDonough, J.R., Oates, M.F., Law, R., Harvey, A.P., 2019. Micromixing in oscillatory baffled flows. *Chem. Eng. J.* 361, 508–518. <https://doi.org/10.1016/j.cej.2018.12.088>
- Ni, X., Valentine, A., Liao, A., Sermage, S.B.C., Thomson, G.B., Roberts, K.J., 2004. On the crystal polymorphic forms of L-glutamic acid following temperature programmed crystallization in a batch oscillatory baffled crystallizer. *Cryst. Growth Des.* 4, 1129–1135. <https://doi.org/10.1021/cg0498271>
- Oliva, J.A., Pal, K., Barton, A., Firth, P., Nagy, Z.K., 2018. Experimental investigation of the effect of scale-up on mixing efficiency in oscillatory flow baffled reactors (OFBR) using principal component based image analysis as a novel noninvasive residence time distribution measurement approach. *Chem. Eng. J.* 351, 498–505. <https://doi.org/10.1016/j.cej.2018.06.029>
- Palmer, D.A., Ramette, R.W., Mesmer, R.E., 1984. Triiodide ion formation equilibrium and activity coefficients in aqueous solution. *J. Solut. Chem.* 13, 673–683.
- Panic, S., Loebbecke, S., Tuercke, T., Antes, J., Bošković, D., 2004. Experimental approaches to a better understanding of mixing performance of microfluidic devices. *Chem. Eng. J.* 101, 409–419. <https://doi.org/10.1016/j.cej.2003.10.026>
- Paul, E.L., Atiemo-Obeng, V.A., Kresta, S.M., 2004. Mixing in Pipelines, in: *Handbook of Industrial Mixing; Science and Practice*. John Wiley & Sons, Inc., New Jersey, USA, pp. 371–478. <https://doi.org/10.1002/0471451452>
- Phan, A.N., Harvey, A.P., 2011. Characterisation of mesoscale oscillatory helical baffled reactor - experimental approach. *Chem. Eng. J.* 180, 229–236. <https://doi.org/10.1016/j.cej.2011.11.018>
- Reis, N., Vicente, A.A., Teixeira, J.A., Mackley, M.R., 2004. Residence times and mixing of a novel continuous oscillatory flow screening reactor. *Chem. Eng. Sci.* 59, 4967–4974. <https://doi.org/10.1016/j.ces.2004.09.013>
- Slavnić, D.S., Živković, L. V., Bjelić, A. V., Bugarski, B.M., Nikačević, N.M., 2017. Residence time distribution and Peclet number correlation for continuous oscillatory flow reactors. *J. Chem. Technol. Biotechnol.* 92, 2178–2188. <https://doi.org/10.1002/jctb.5242>
- Stonestreet, P., Van Der Veecken, P.M.J., 1999. The effects of oscillatory flow and bulk flow components on residence time distribution in baffled tube reactors. *Chem. Eng. Res. Des.* 77, 671–684. <https://doi.org/10.1205/026387699526809>
- Su, Y., Chen, G., Yuan, Q., 2011. Ideal micromixing performance in packed microchannels. *Chem. Eng. Sci.* 66, 2912–2919. <https://doi.org/10.1016/j.ces.2011.03.024>
- Truesdale, V.W., Luther, G.W., Greenwood, J.E., 2003. The kinetics of iodine disproportionation: a system of parallel second-order reactions sustained by a multi-species pre-equilibrium. *Phys. Chem. Chem. Phys.* 5, 3428–3435. <https://doi.org/10.1039/b303351a>

- Wan, L., Xu, Y., 2013. Iodine-sensitized oxidation of ferrous ions under UV and visible light: the influencing factors and reaction mechanism. *Photochem. Photobiol. Sci.* 12, 2084.
<https://doi.org/10.1039/c3pp50245g>
- Wenzel, D., Assirelli, M., Rossen, H., Lopattschenko, M., Górak, A., 2018. On the reactant concentration and the reaction kinetics in the Villermaux-Dushman protocol. *Chem. Eng. Process. - Process Intensif.* 130, 332–341. <https://doi.org/10.1016/j.cep.2018.06.022>
- Wu, Y., Hua, C., Li, W., Li, Q., Gao, H., Liu, H., 2009. Intensification of micromixing efficiency in a ceramic membrane reactor with turbulence promoter. *J. Memb. Sci.* 328, 219–227.
<https://doi.org/10.1016/j.memsci.2008.12.010>
- Xuereb, C., Poux, M., Bertrand, J., 2006. Principes du mélange, in: *Agitation et Mélange. Aspects Fondamentaux et Applications Industrielles*. Dunod, Paris.
- Zha, L., Pu, X., Shang, M., Li, G., Xu, W., Lu, Q., Su, Y., 2018. A study on the micromixing performance in microreactors for polymer solutions. *AIChE J.* 64, 3479–3490.
<https://doi.org/10.1002/aic.16188>

Chapter 7. Conclusion and future work

The objective of this PhD thesis is the study the macro and micromixing performance of COBRs of a secondary component in the bulk flow and how it should be introduced into a COBR. The effect of the position of the secondary feed, the influence of the oscillatory conditions and power dissipation on the macro and micromixing performance were studied in a commercial Nitech® OBR with smooth constrictions using numerical simulations and experiments. In this chapter, a summary of the conclusions reached from the numerical and experimental results obtained on this research are presented, along with suggestions for future work.

Despite the fact that COBRs are already used in many applications, like polymers, biofuels, bioprocess, pharmaceutical and chemical reactions, they typically do not offer favourable conditions to carry out operations with fast kinetics, like fast reactive crystallization. A lack of information on the influence of the operating conditions and energy dissipation on macro and micromixing, as well, as how a secondary feed should be introduced into the COBR to achieve good mixing has been identified.

In this work, power dissipation, one important parameter in mixing performance and scale-up guidelines, was calculated through CFD simulations using two different ways – via viscous energy dissipation and the mechanical energy balance. The mesh requirements to obtain converged pressure and velocity fields are much less stringent than those for mixing. Viscous energy dissipation was found to be difficult to correctly resolve near the walls without the use of extremely refined computational meshes, which increases the simulation times and computational costs excessively. The mechanical energy balance equation was hence preferred for the calculation of energy dissipation as accurate results could be obtained once mesh independence for the velocity field was achieved. The simulated values of power dissipation were compared with those predicted by empirical quasi-steady state models from the literature. However, these models did not properly estimate energy dissipation when flow is not fully-developed and turbulent. Additionally, the net flow is not taken into account in these empirical models; this is only appropriate at high velocity flow ratios, when the influence of the net flow is overshadowed by the oscillatory flow. Following the approach used for the friction factor for flow in pipes and the power number in STRs, a dimensionless power density number was proposed. When this number is plotted as a function of the total Reynolds number based on the sum of both the oscillatory and net flow velocities, the resulting plot depends on the system geometry only. Combining data from this work and from the literature, it is shown that the dimensionless power density number is constant in fully-developed turbulent flow and inversely proportional to the total Reynolds number in laminar flow, being a useful tool in the prediction of power density in COBRs.

The influence of oscillatory and net flows conditions and three theoretical source locations on macro mixing quality in a COBR was studied by the analysis of the spatial uniformity of a non-reactive tracer using CFD simulations. In contrast with the energy dissipation simulations run in ANSYS CFX, mixing

simulations required mesh cells that are extremely small to eliminate numerical diffusion using the same software, leading to a huge increase in the simulation times and computational costs. For example, for a 50 mm diameter reactor, and following the mesh requirements from our reactor geometry for obtaining mesh independency, mesh sizes of 1.17 mm are needed for velocity fields and mechanical energy balance equation (with 8 and 16 inflation layers, respectively), and 167 μm meshes for mixing. Mixing simulations were, therefore, moved to ANSYS Fluent, which allows the use of true 2D meshes and a non-iterative time-advancement (NITA) algorithm. The NITA algorithm performs only a single outer iteration per timestep, which significantly speeds up transient simulations, becoming crucial to reduce simulation times and make calculations feasible when extremely high refined meshes are required. The mixing quality was studied by the analysis of the spatial uniformity of a non-reactive tracer. High frequencies were shown to improve mixing performance, but an increase in the amplitude did not indicate any clear trend. When operating at the same oscillatory Reynolds number, high frequencies with amplitude values close to $0.3l_b$ offers better mixing quality than low frequencies and high amplitudes.

Concerning the source position, the source located at the tube centre line results in high axial dispersion of the tracer and limited radial mixing due to the orifice baffle geometry. Better mixing results were obtained when the tracer was introduced midway between the centre of the tube and the wall. This position improves radial mixing due to the recirculation eddies created by the oscillatory flow interacting with the baffles. The results showed that the change of the position of a source injection could improve mixing quality significantly. The simultaneous influence of the oscillatory and net flow was studied by comparing mixing performance at different velocity ratios. When the source position is chosen correctly, an increase in the velocity ratio improves mixing performance from 2% to 87% of the perfectly mixed state. However, for lower net flow conditions, the influence of the reverse flow of the oscillation over the net flow becomes preponderant, pushing the tracer flow upstream of the baffles, thereby decreasing mixing performance. From RTD studies in the literature, the recommended velocity ratio to obtain plug flow behaviour is $\psi = 2 - 4$. However, our results show that better spatial mixing is obtained at higher velocity ratios ($\psi = 4 - 8$), highlighting that depending on the process goal, different operating conditions could be preferred.

Micromixing quality in a COBR in the laminar flow regime was studied using the competing parallel iodide-iodate, or Villermaux-Dushman test reactions. The presence of oscillations (i.e. frequency and amplitude) was shown to reduce the segregation index, and therefore improve the micromixing performance. However, micromixing is not directly correlated with the oscillatory velocity, or Re_o , since for the same Re_o , higher amplitudes and lower frequencies lead to better micromixing quality than higher frequencies and lower amplitudes. The increase of the injection flow rate has shown to enhance micromixing quality, but this did not depend on the increase of specific power density, which has little or no correlation with micromixing. Instead, the mixing mechanism (stretching and folding of the injected plume in the bulk) seems to control the micromixing quality. Two different models were

used to estimate theoretical and calculated micromixing times. A comparison of the theoretical micromixing time with the literature suggests that in terms of energy dissipation, mixing efficiency in COBRs is similar to stirred tanks and static mixers, but its times are significantly greater than what can be achieved in micromixers. Calculated micromixing times were obtained using the incorporation model with the experimental results. Nevertheless, calculated micromixing times were 2 order of magnitude smaller than theoretical ones. This discrepancy could be attributed to limitations in the incorporation model, which do not take into account the particular hydrodynamics of the oscillation with the reactant flows to describe mixing.

Preliminary visualization studies of a passive tracer upstream the COBR were carried out. The results revealed that oscillatory conditions modify the flow between the injection point and the first baffles (increase in the number of deformations with the increase of the frequency, and decrease in the number of deformations and change in its shape with the increase of the amplitude). Furthermore, the flow shows to move up or down from the injection point towards the reactor walls, depending in the inlet orientation and the viscosity. Due to lack of time, it was very difficult to made well-supported conclusions and it was not possible to go any further in the corroboration of the possible explanations to the phenomena observed.

Future work

The results obtained and presented in this work are a first step into the understanding of how secondary feed influences the macro- and micromixing in COBRs, with the ultimate goal of assessing the possibility of implementing fast reactions in this reactor. However, more studies still need to be performed before successful implementation, which leads to different propositions to future work.

The methodology presented in this work for the estimation of the energy dissipation could be employed to determine the dimensionless power density number for different OBR geometries, like the helical and helical with central rod designs, whose attention have been growing in the last years. This would allow more precise power density estimates to be made, and a better comparison of energy consumption between different geometries could be done. The correct estimation of the energy dissipation is advantageous to better correlate it with the enhancement in macro and micromixing performance, and mass and heat transfer. It is also useful in scale-up guidelines and as a tool for comparing power cost among different operating conditions, geometries and reactors.

The results obtained from the influence of the theoretical sources (despite not representing the exact reality of a feed in real processes) provide a first estimate of where the plume of an injection jet needs to be positioned for future studies. It is expected that the introduction of the secondary stream in the baffled region, rather than upstream of the baffles, would greatly improve mixing. Numerical simulations with a jet injected inside the baffled region should be the next step into the understanding of introducing secondary streams in COBRs.

Concerning micromixing quality, the mixing mechanism between the injection flow with the main stream and oscillatory flow needs to be further studied, since it shows to be a controlling factor in the micromixing performance, rather than the specific power density. Numerical simulations of the side jet injection and its interaction with the bulk and oscillatory flow will offer a better understanding of the mixing mechanism. This mixing mechanism could be used as a starting point to develop and establish a more adapted micromixing model that takes into consideration the effect of the oscillation in the micromixing phenomena.

Different numerical studies of micromixing test reactions in the COBR can be proposed. Conventional CFD simulation of fast reactions in laminar flows can be computationally challenging and require extremely high computational time (even for simple geometries and low Reynolds numbers), due to the fact that extremely fine grids are required in order to correctly resolve the concentration gradients. This can be especially difficult for complex geometries, like COBR geometries, and when the flow is non-axisymmetrical ($Re_o > 250$). Recently Fonte et al. (2020)⁹ proposed the use of a lamellae-based micromixing model, which offers an attractive alternative to the direct simulation of chemical reaction in CFD. In this model, the flow field from the CFD calculations is coupled with a Lagrangian model that is used to perform the chemical reactions indirectly, thereby greatly reducing computational costs compared with conventional CFD approaches. This methodology appears promising for simulating micromixing in COBRs and it would be of interest to test the procedure in future work.

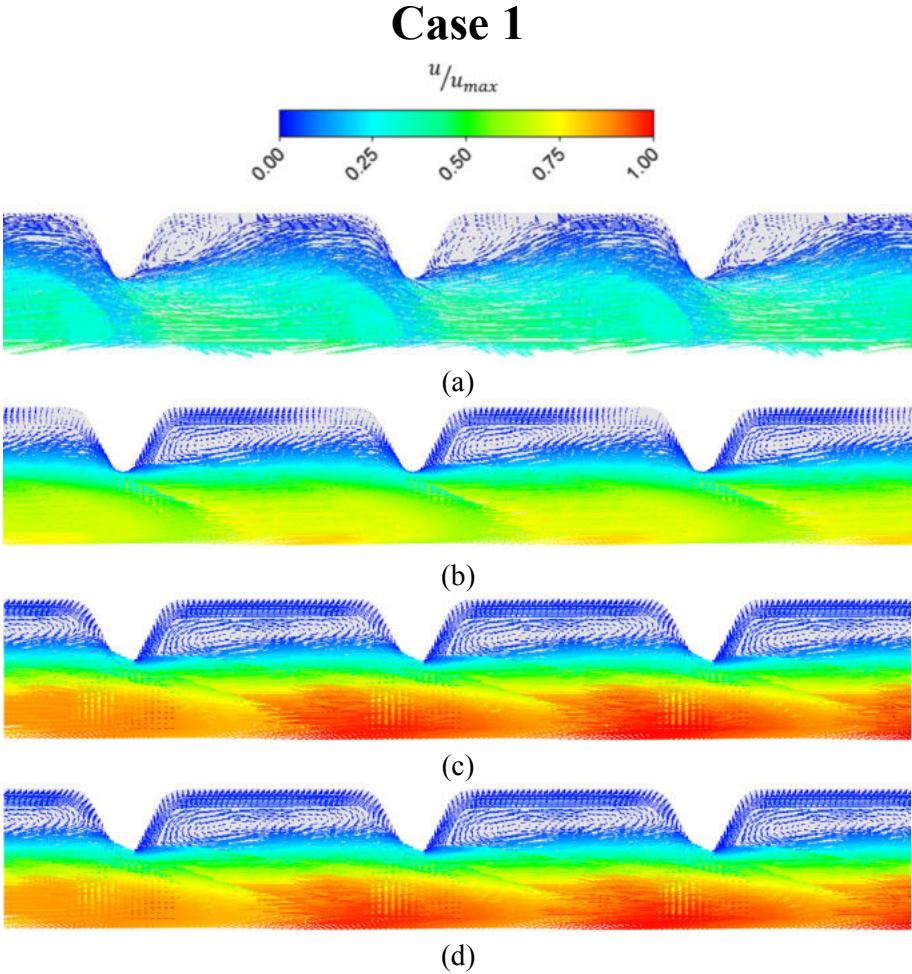
The preliminary results obtained from the visualization of the inert tracer has given tracks for future research that need to be tested to validate the explanations proposed with respect to the specific behaviour of the flow in the zone between the injection and the COBR. Some ideas for future work are the study of the influence of the viscosity in a T-junction where the inlet of the net flow a sudden change in Reynolds number due to the increase in tube diameter and interacts with oscillatory flow, as well as the determination of the minimal length to achieve the pseudo-steady state in laminar flow regime when oscillations are presented.

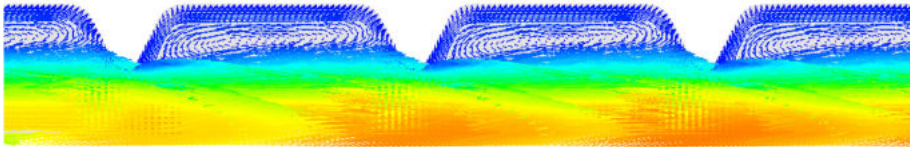
Finally, once the influence of the injection position on the macro- and micromixing performance have been deeply studied, together with the effect of the operating conditions, a feasibility study should be done using a fast chemical reaction in the COBR, like the synthesis of barium sulphate. This reaction has been widely used to evaluate the precipitation process performance, micromixing efficiency, and precipitation models. Once this is achieved, different COBR designs that can be employed for a wider range of applications involving varied characteristic process times can be proposed.

⁹ Fonte, C.P., Fletcher, D.F., Guichardon, P., Aubin, J., 2020. Simulation of micromixing in a T-mixer under laminar flow conditions. *Chem. Eng. Sci.* 222, 115706. <https://doi.org/10.1016/j.ces.2020.115706>

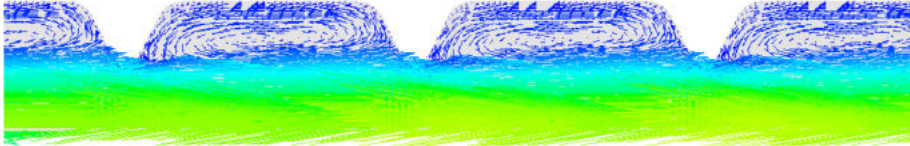
Appendix 1: Velocity vectors over one oscillation period

This appendix presents the velocity vectors over one oscillation period for the different cases studied in Chapter 5, represented in Table 5.1. (a) $t/T = 0.00$, (b) $t/T = 0.25$, (c) $t/T = 0.55$, (d) $t/T = 0.6$, (e) $t/T = 0.75$, (f) $t/T = 0.95$, (g) normalized inlet velocity over an oscillatory period with the representation of the positions of the different times t/T during the period.

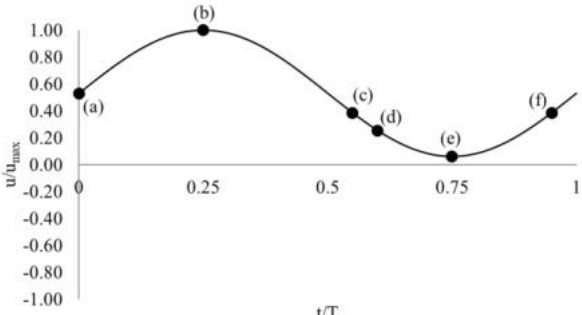




(e)

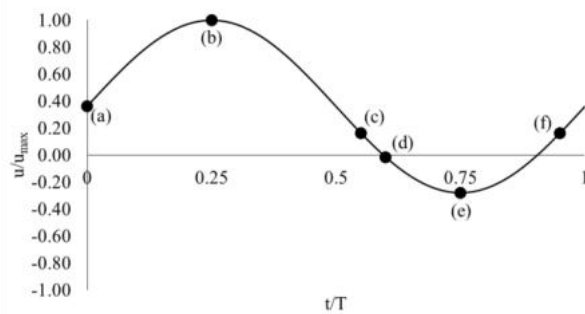
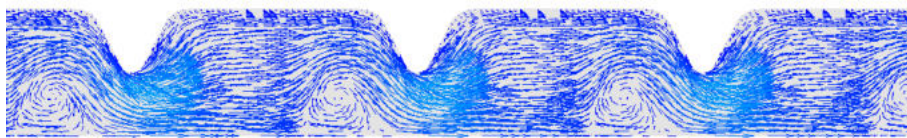
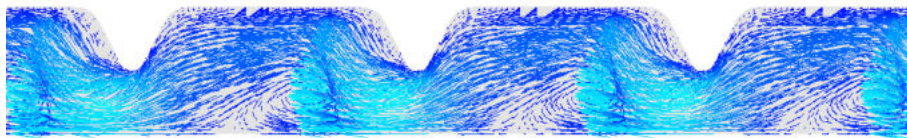
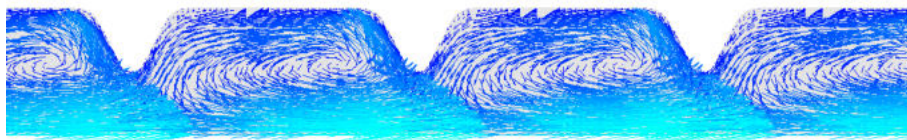
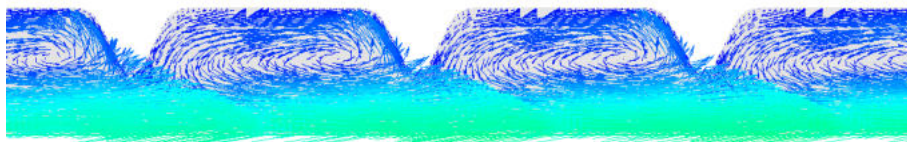
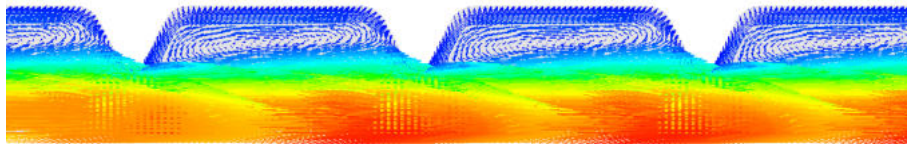
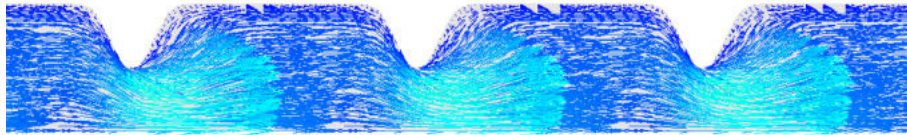
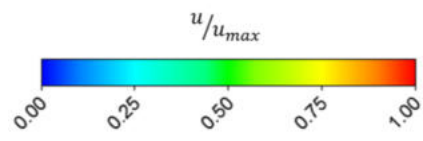


(f)



$u_{max} = 0.41 \text{ m s}^{-1}$
(g)

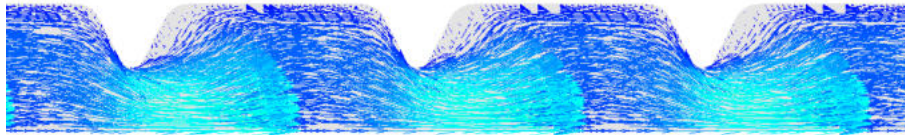
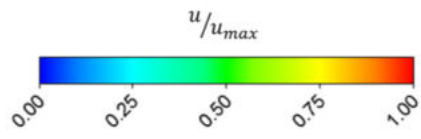
Case 2



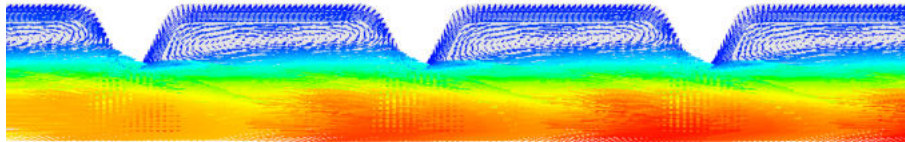
$$u_{max} = 0.59 \text{ m s}^{-1}$$

(g)

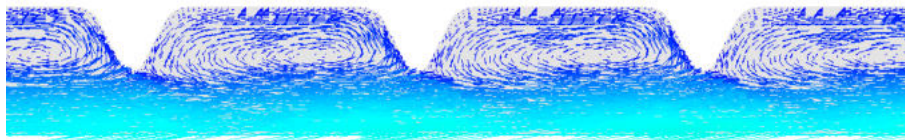
Case 3



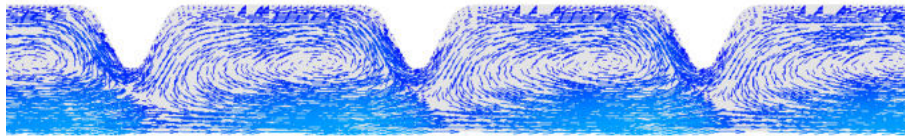
(a)



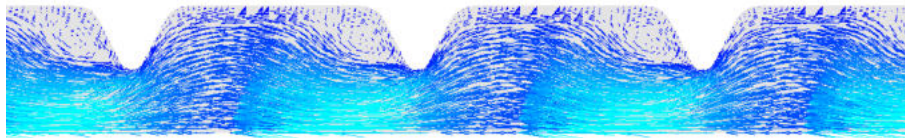
(b)



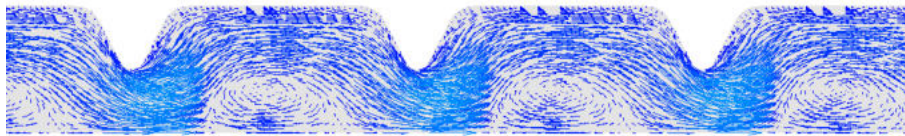
(c)



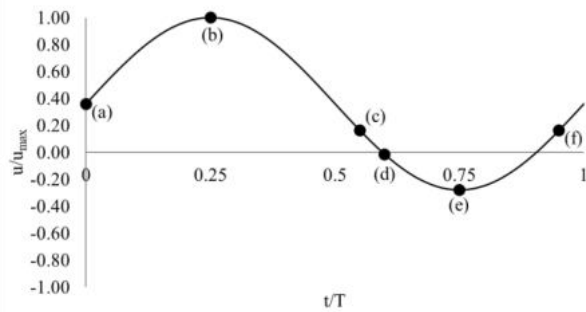
(d)



(e)

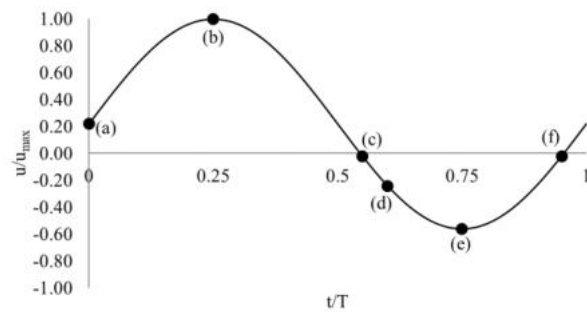
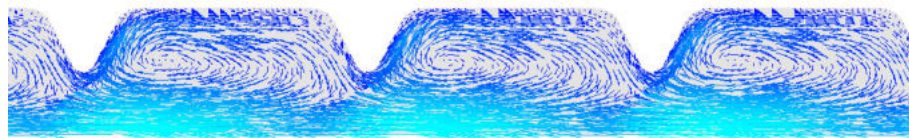
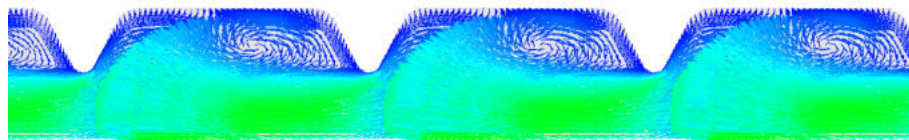
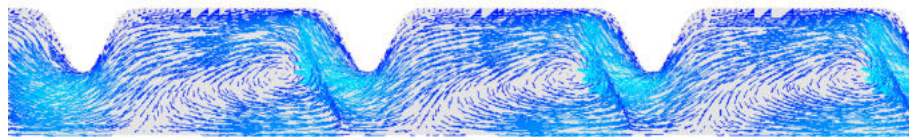
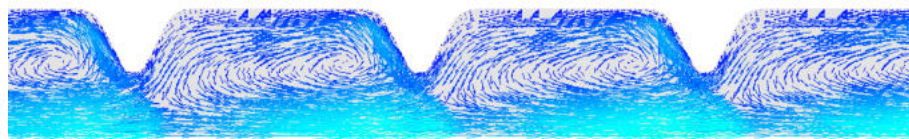
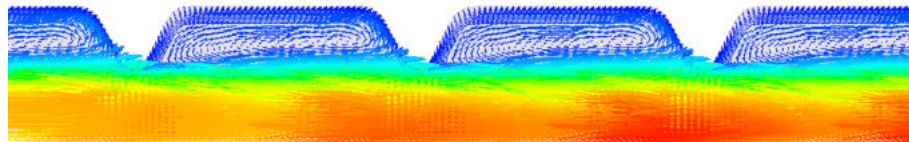
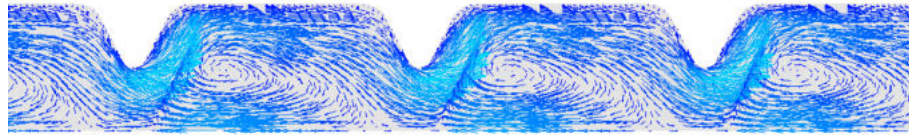
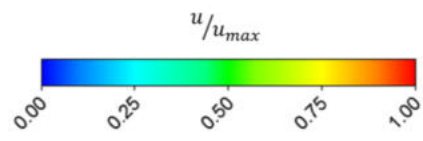


(f)



$u_{max} = 0.62 \text{ m s}^{-1}$
(g)

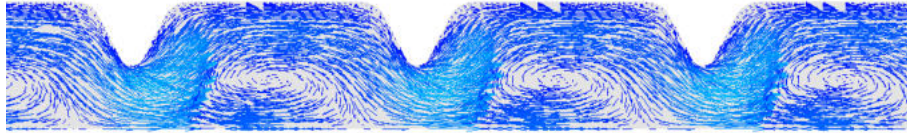
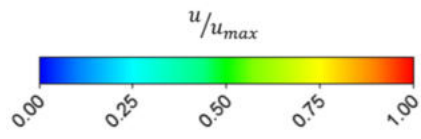
Case 4



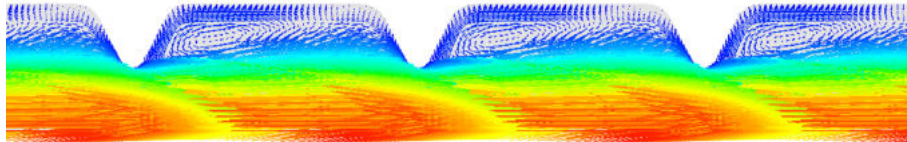
$$u_{max} = 0.98 \text{ m s}^{-1}$$

(g)

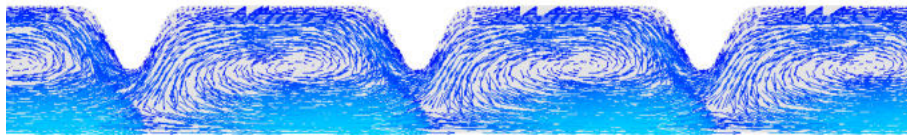
Case 5



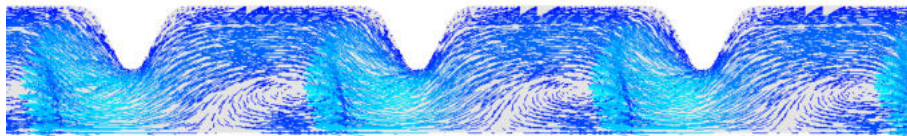
(a)



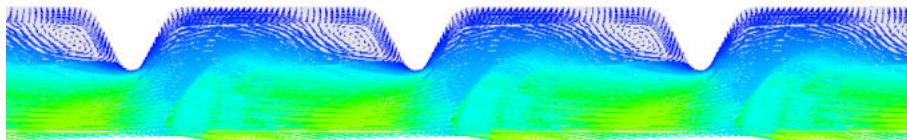
(b)



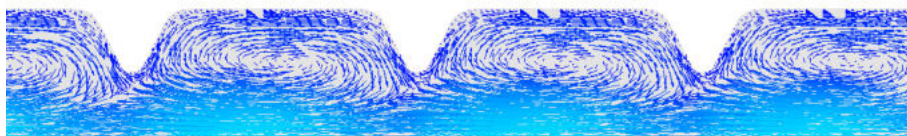
(c)



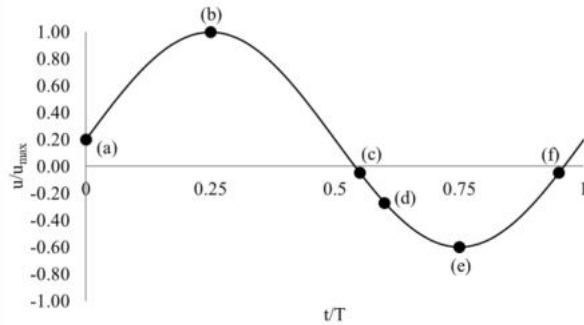
(d)



(e)

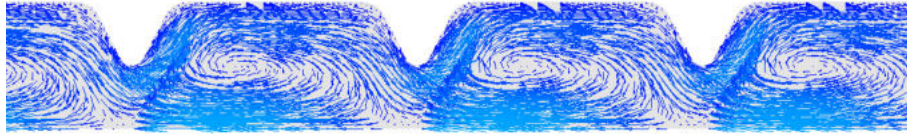
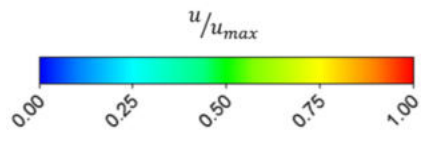


(f)

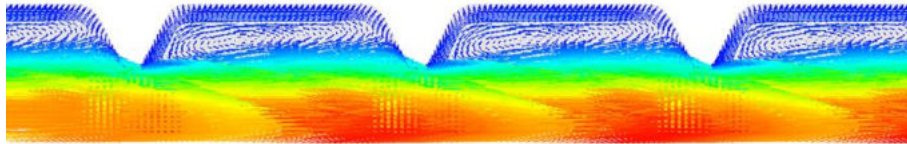


$u_{max} = 0.23 \text{ m s}^{-1}$
(g)

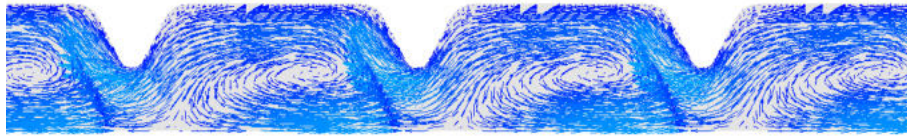
Case 6



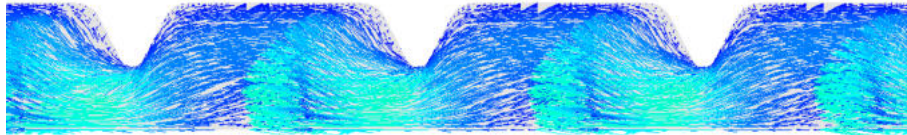
(a)



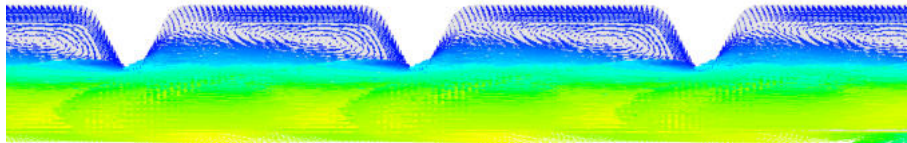
(b)



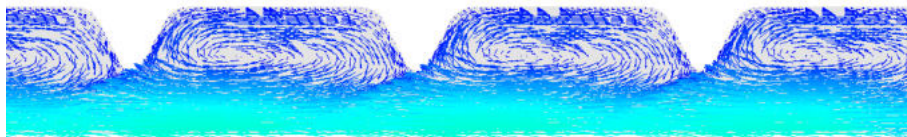
(c)



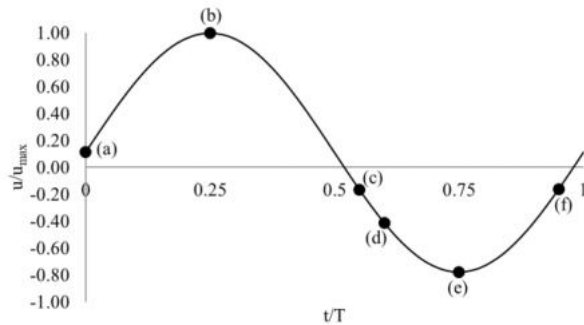
(d)



(e)

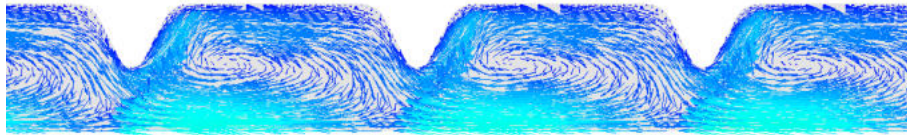
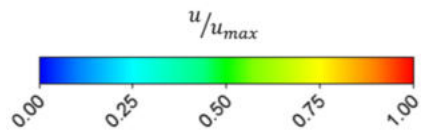


(f)

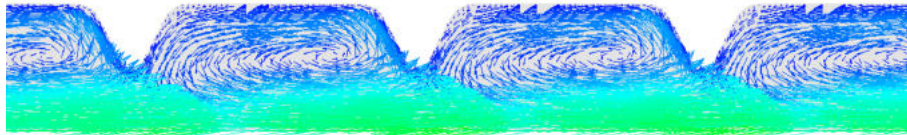


$u_{max} = 0.43 \text{ m s}^{-1}$
(g)

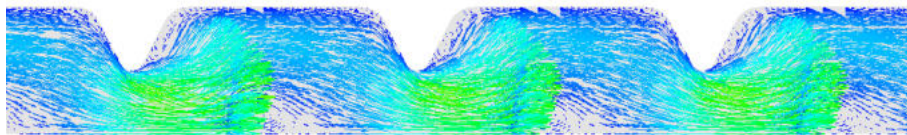
Case 7



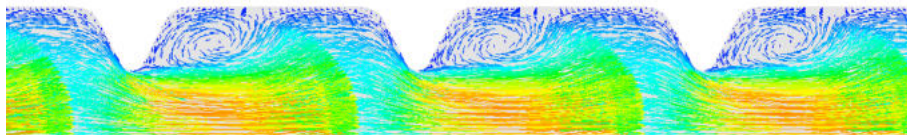
(a)



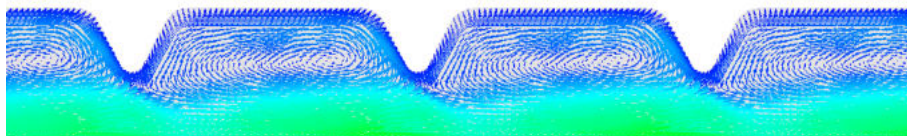
(b)



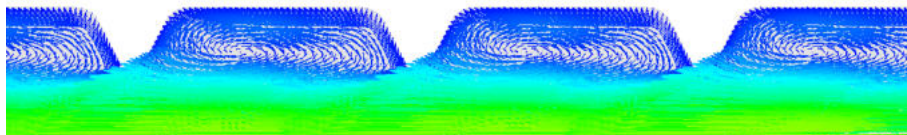
(c)



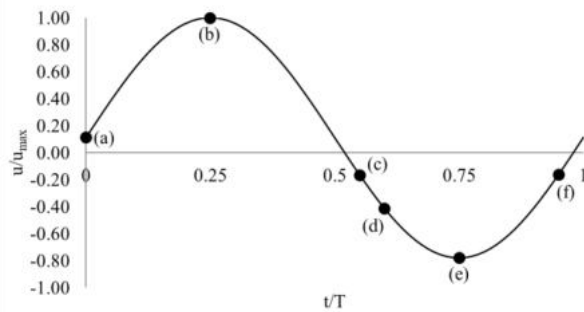
(d)



(e)

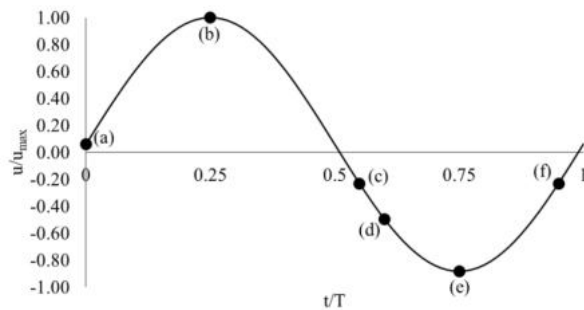
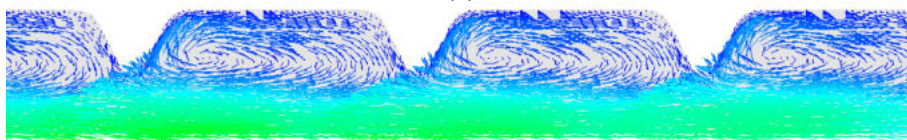
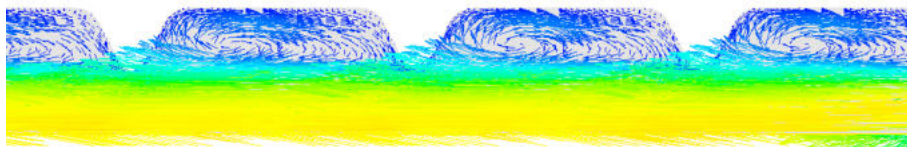
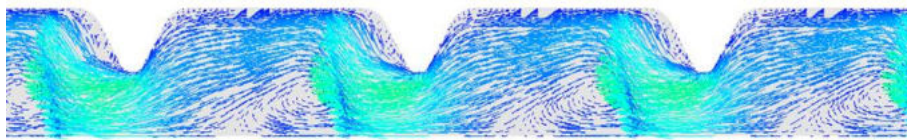
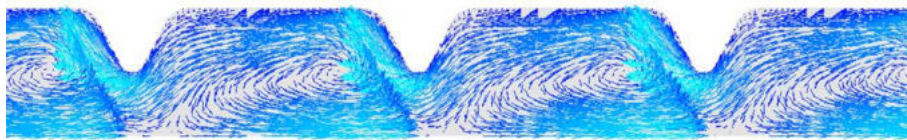
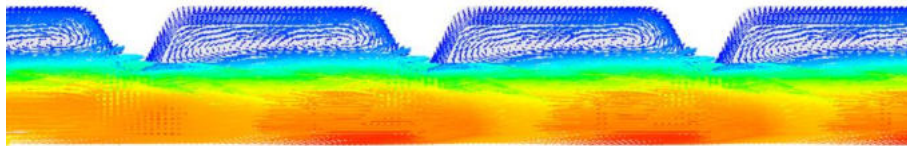
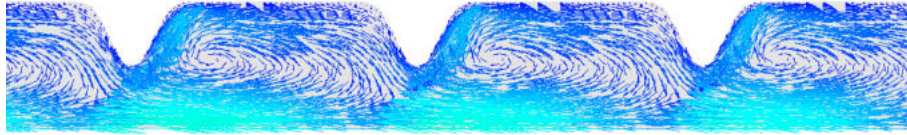
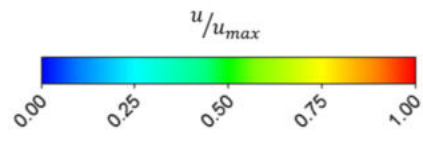


(f)



$u_{max} = 0.40 \text{ m s}^{-1}$
(g)

Case 8



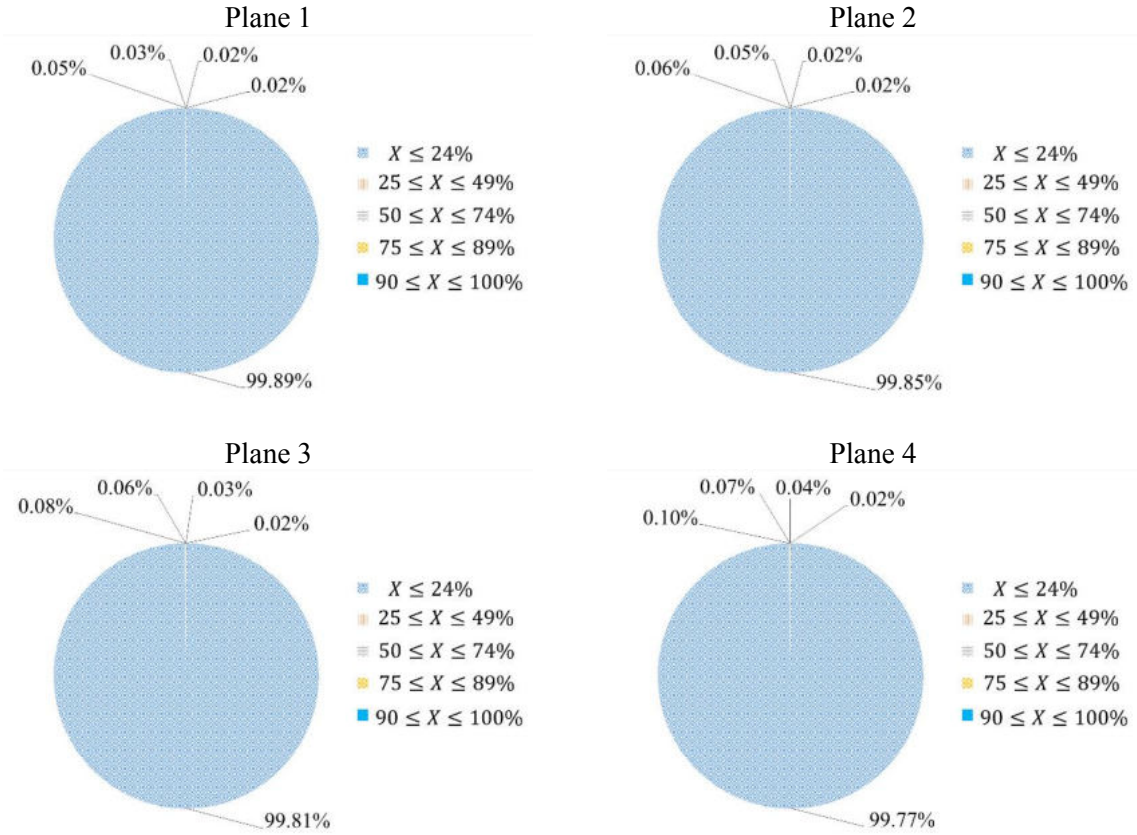
$u_{max} = 0.79 \text{ m s}^{-1}$
(g)

Appendix 2: Areal distribution of mixing intensity averaged over one oscillation period

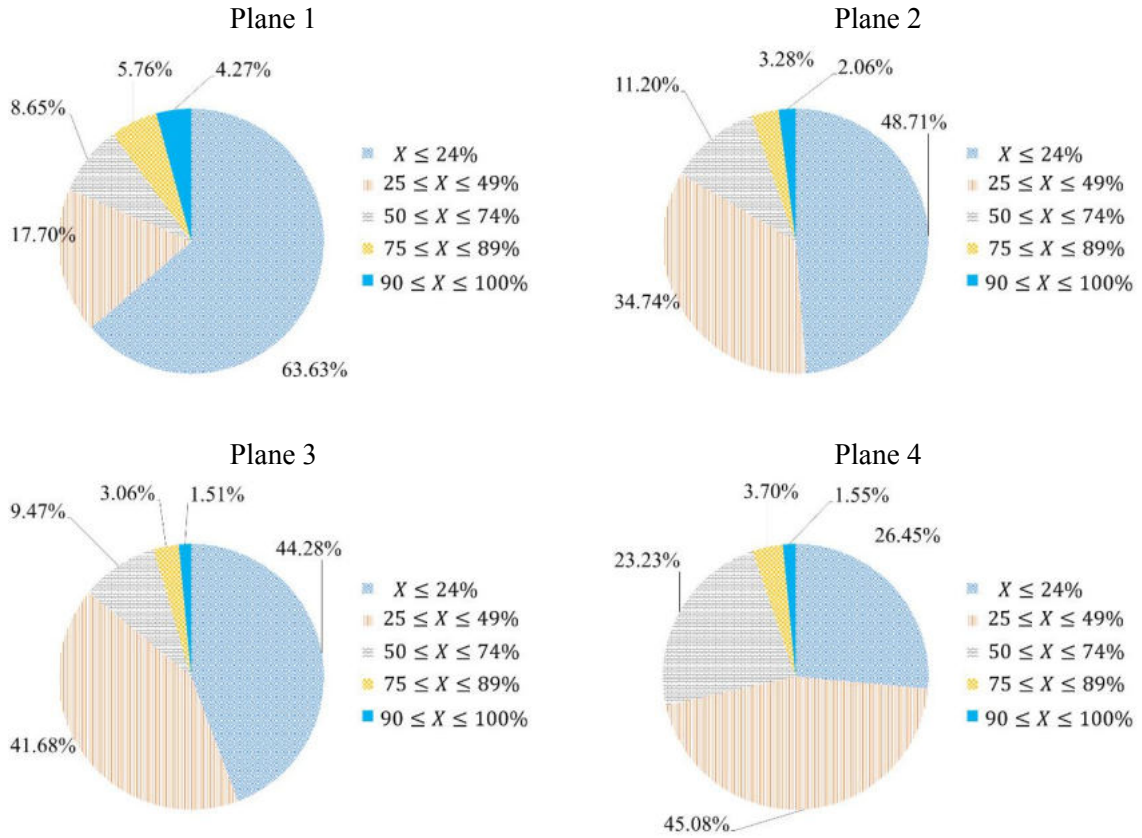
This appendix presents the charts of areal distributions of mixing quality averaged over one oscillation period for all planes and source positions for the different cases studied in Chapter 5, represented in Figure 5.1 and Table 5.1.

Case 1

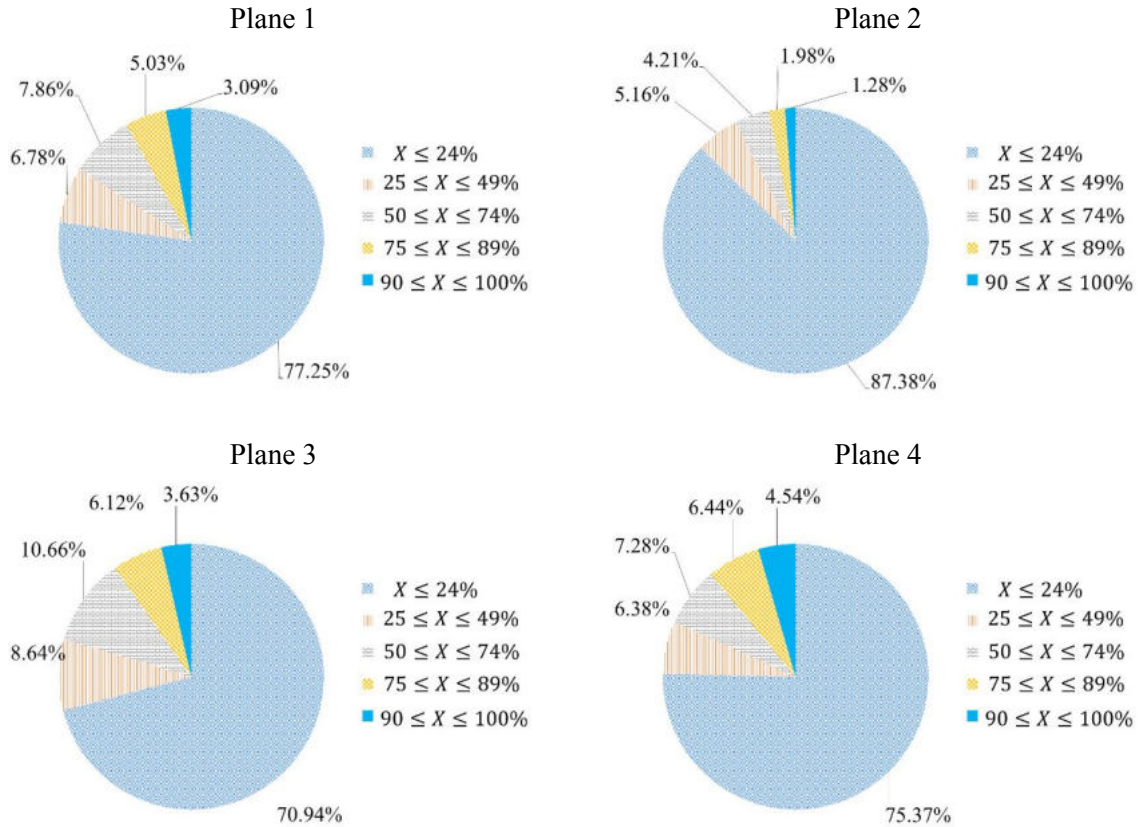
Source 0



Source 1

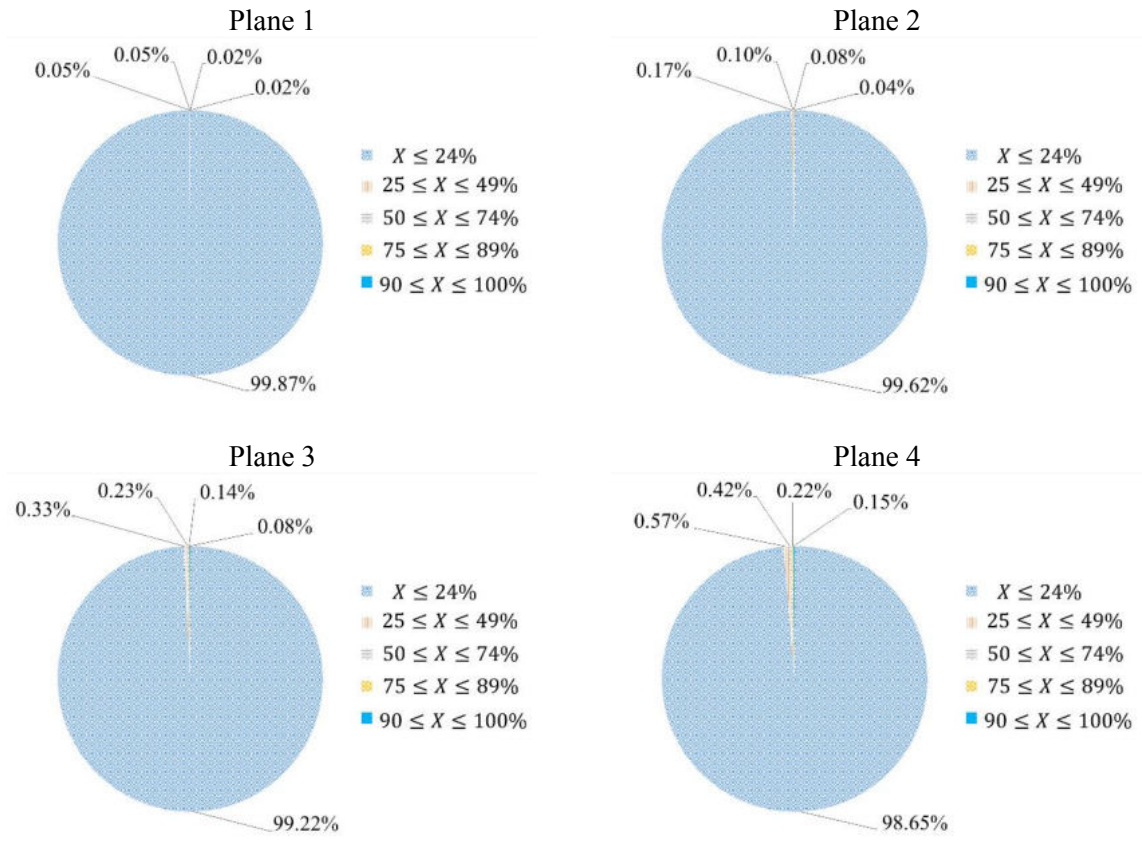


Source 2

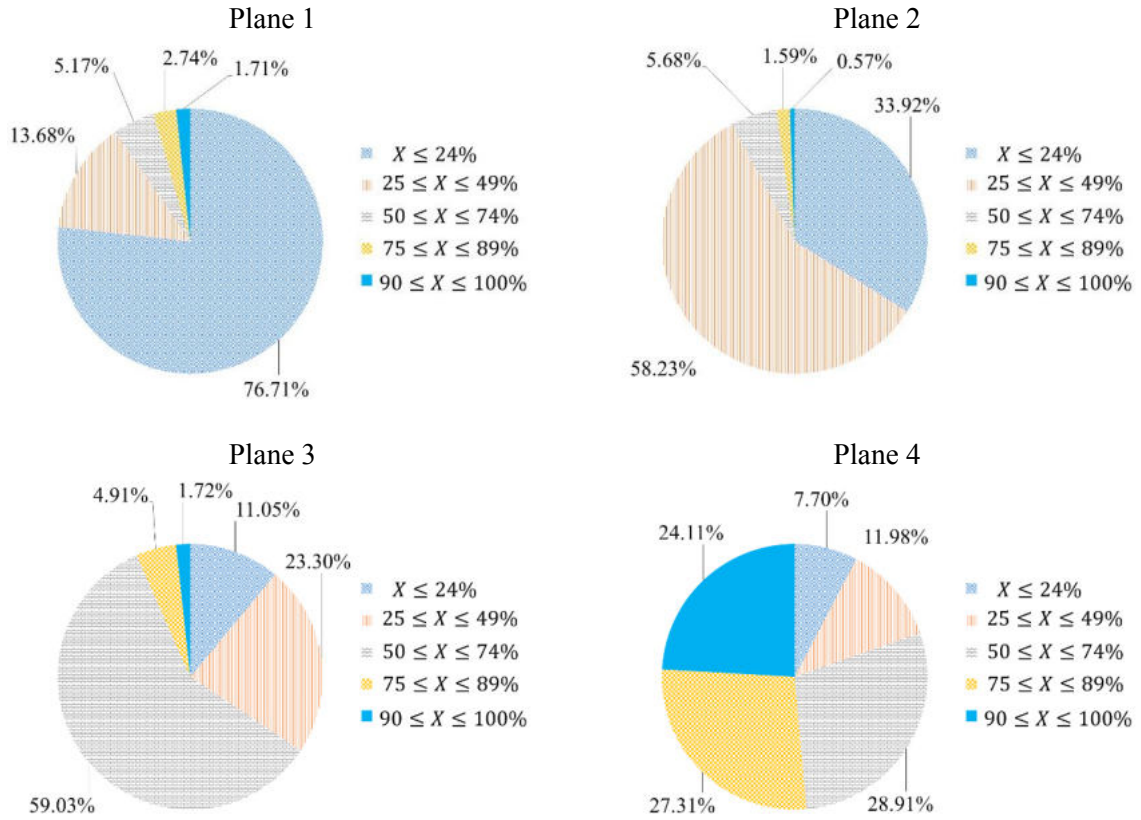


Case 2

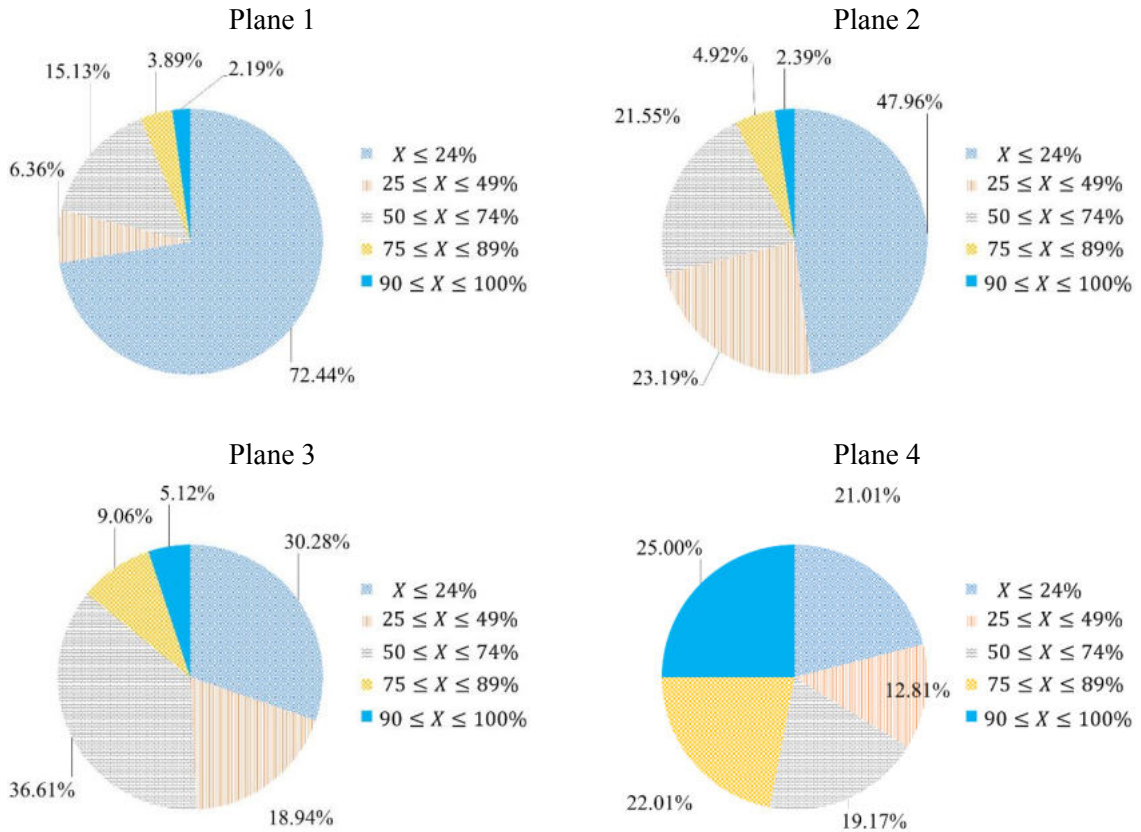
Source 0



Source 1

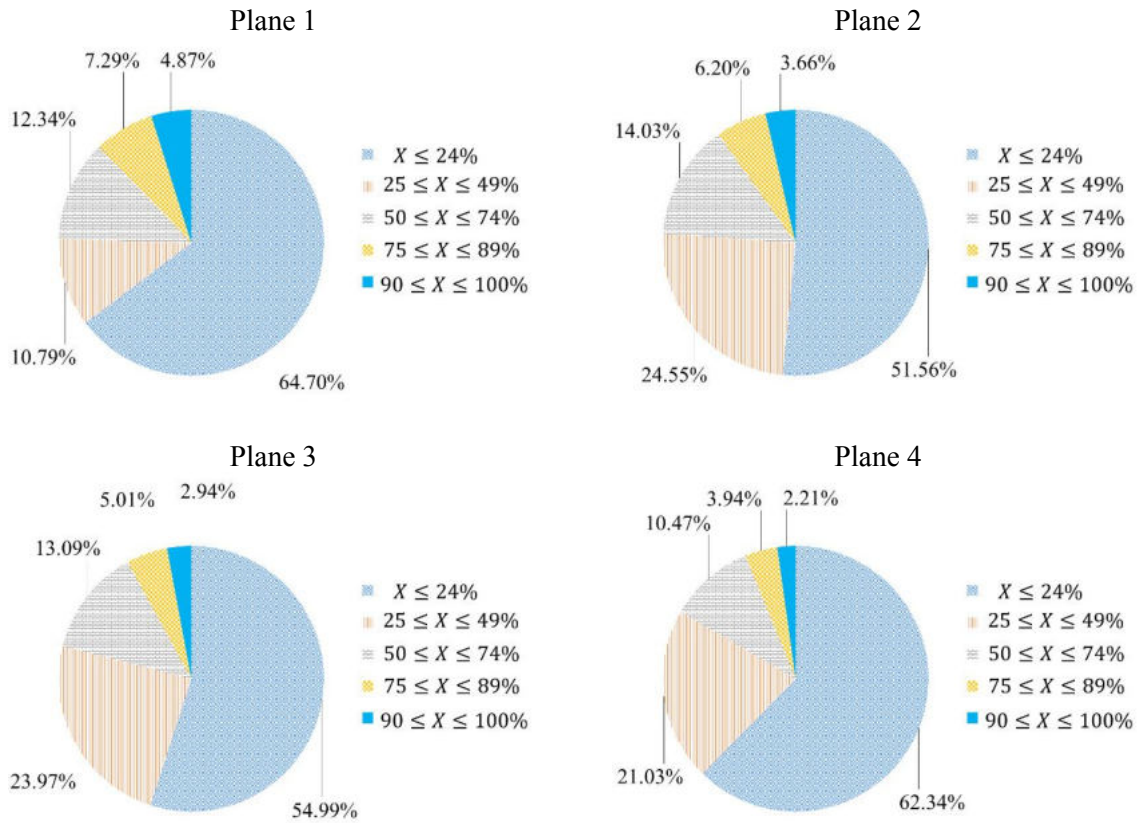


Source 2

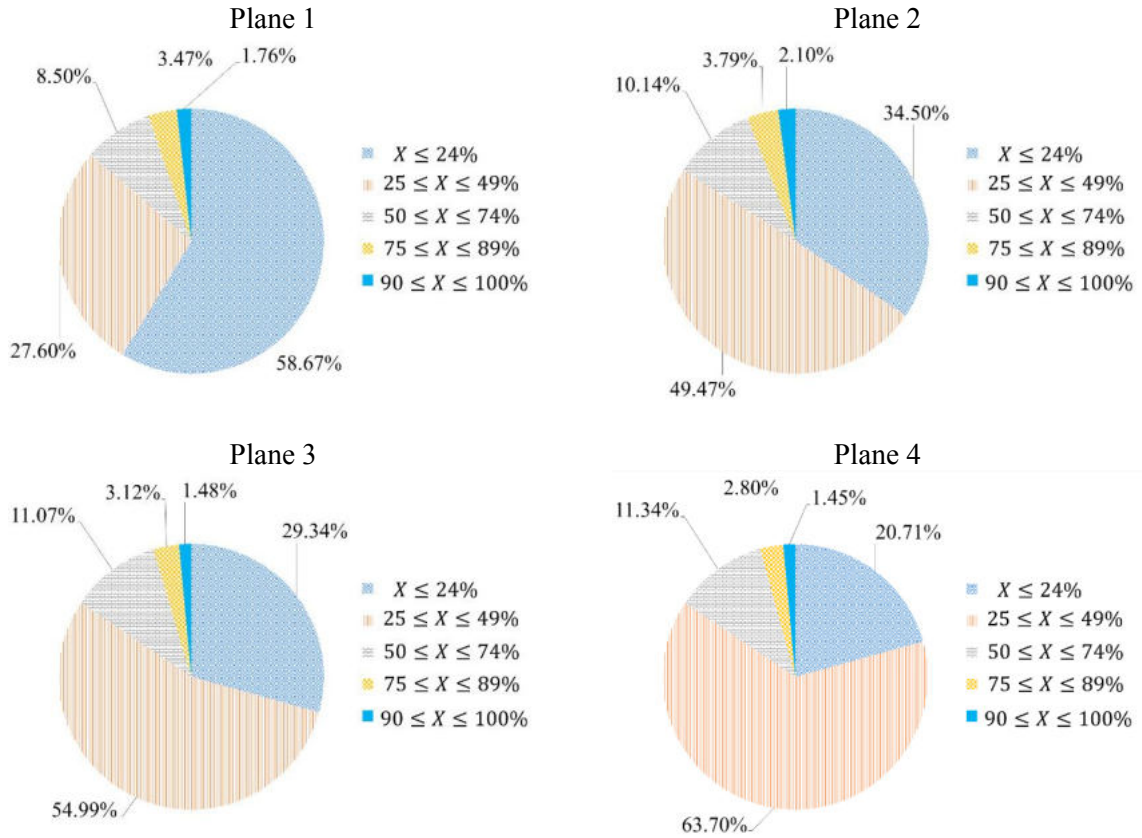


Case 3

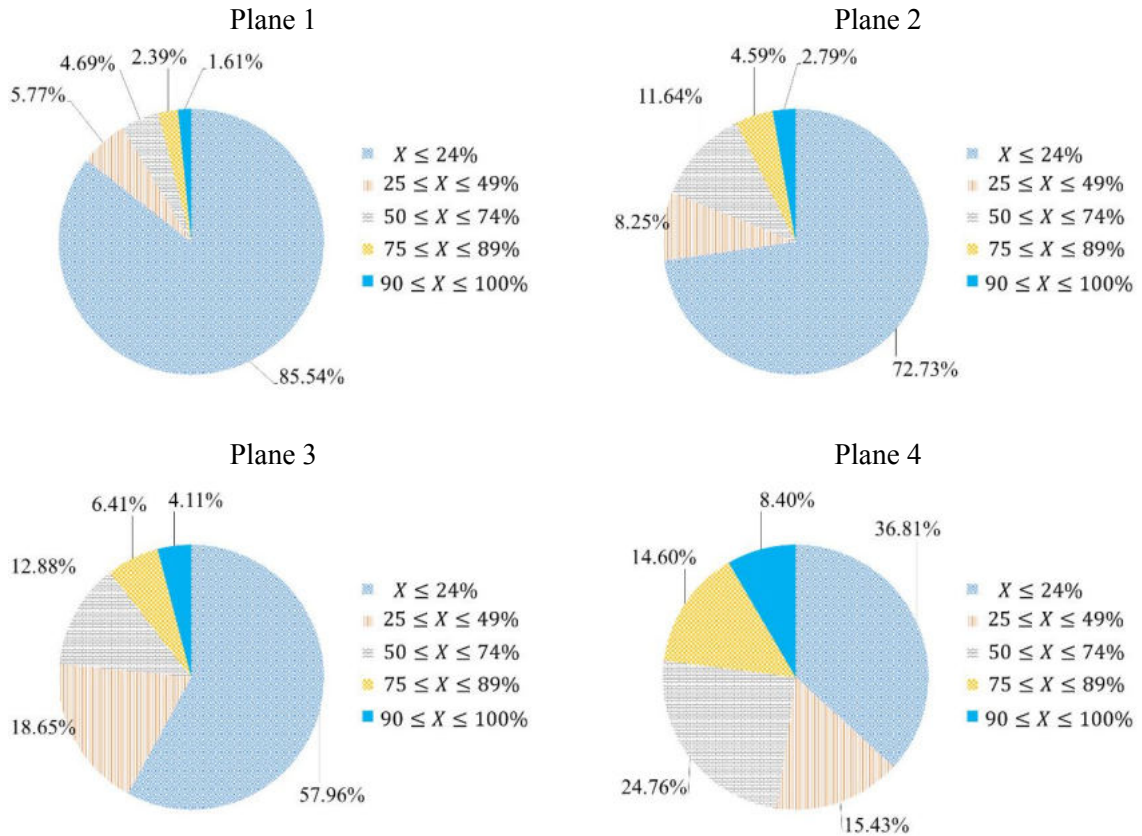
Source 0



Source 1

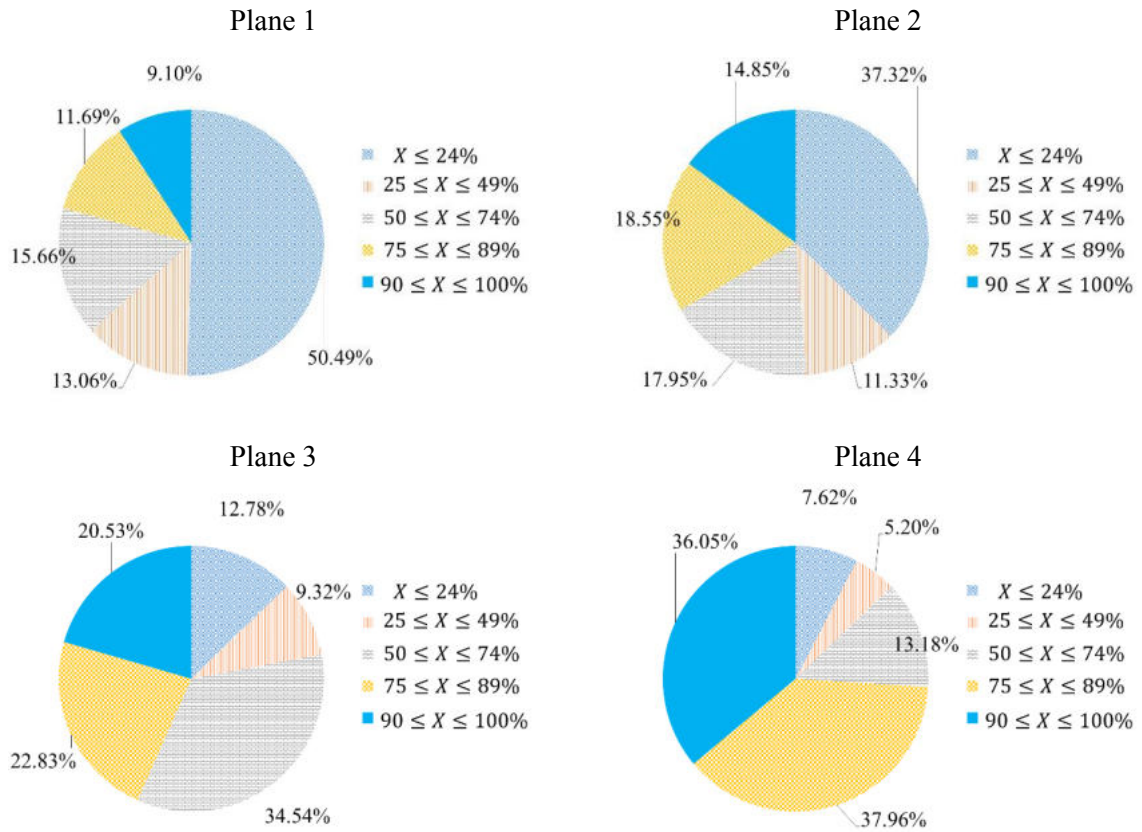


Source 2

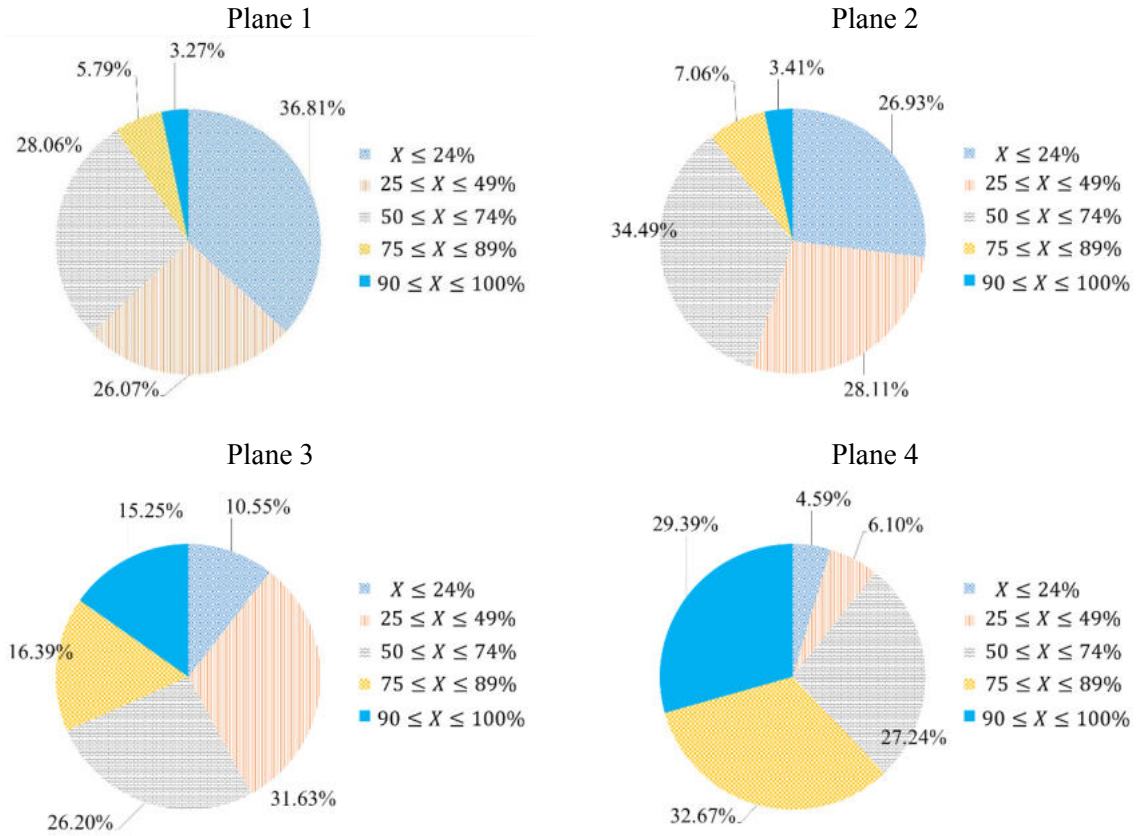


Case 4

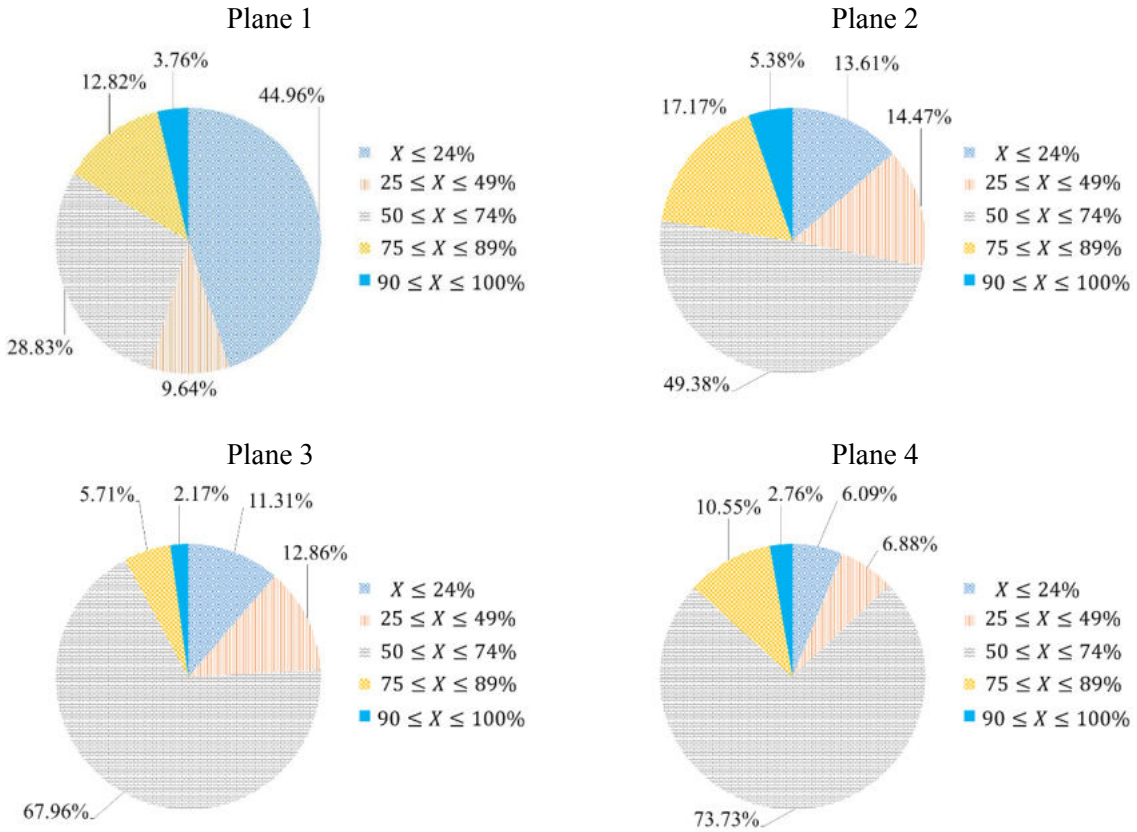
Source 0



Source 1

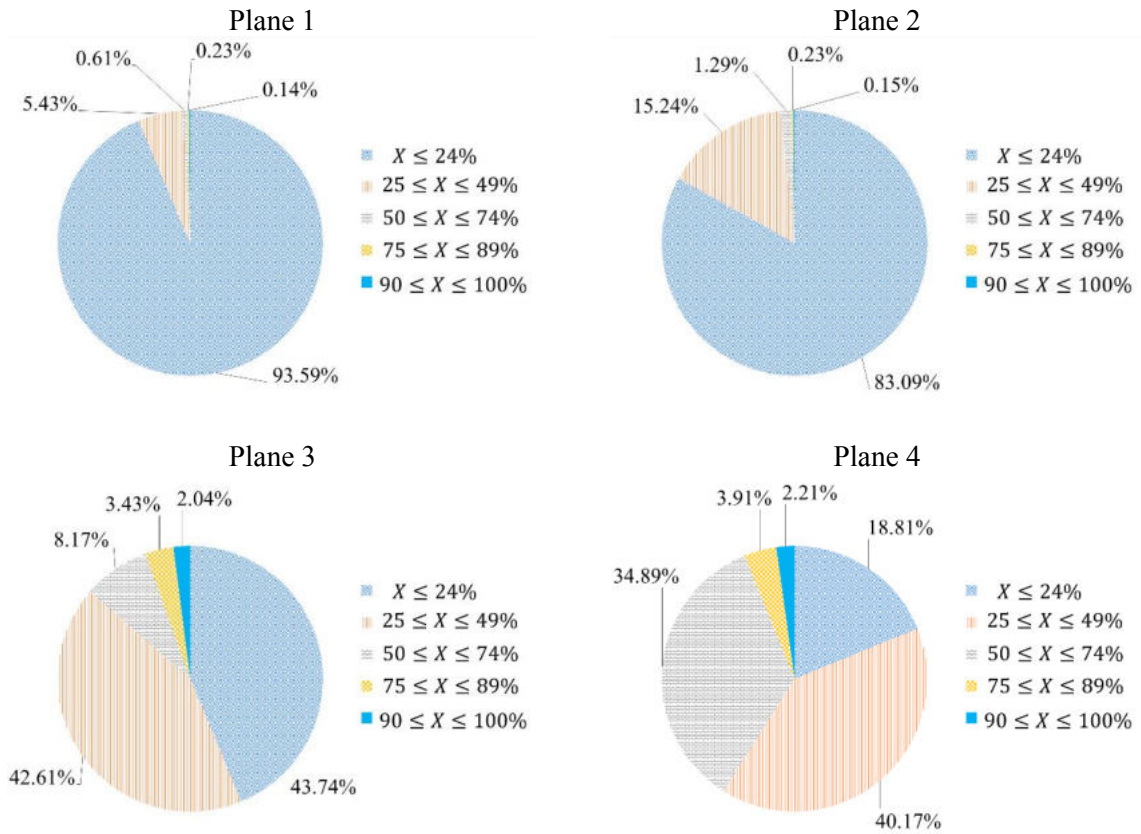


Source 2

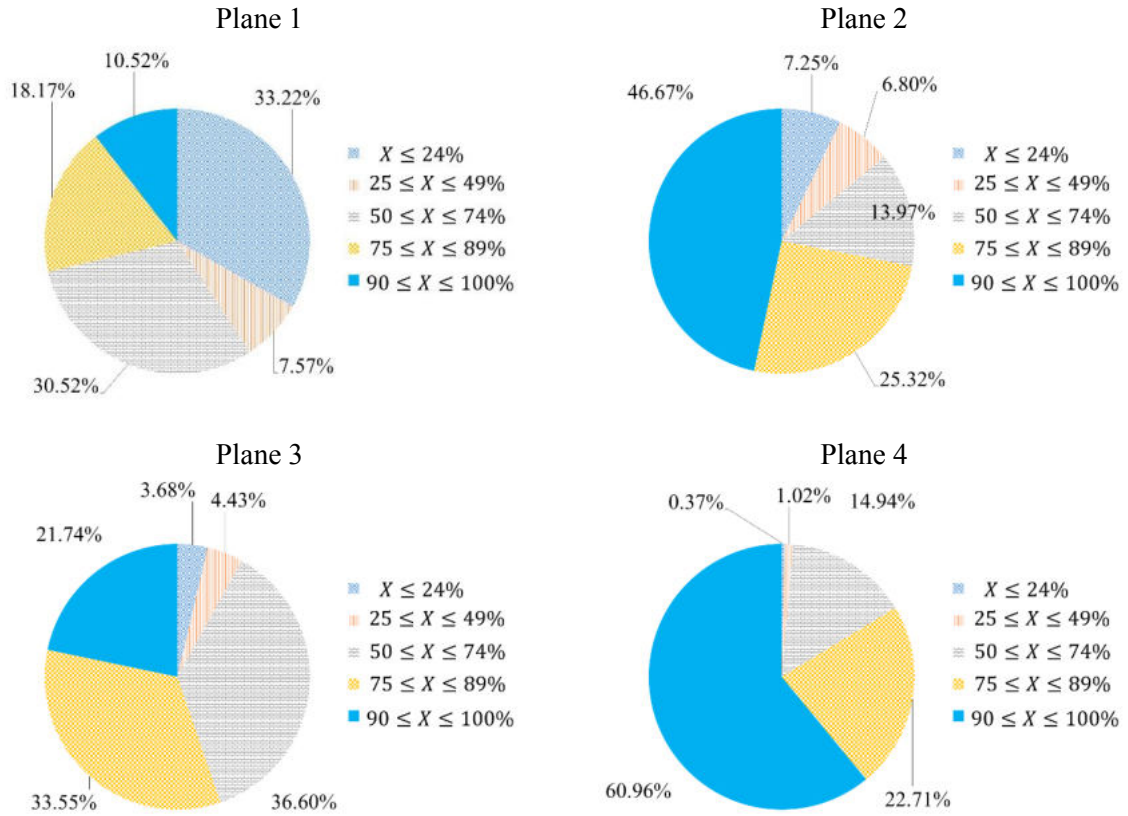


Case 5

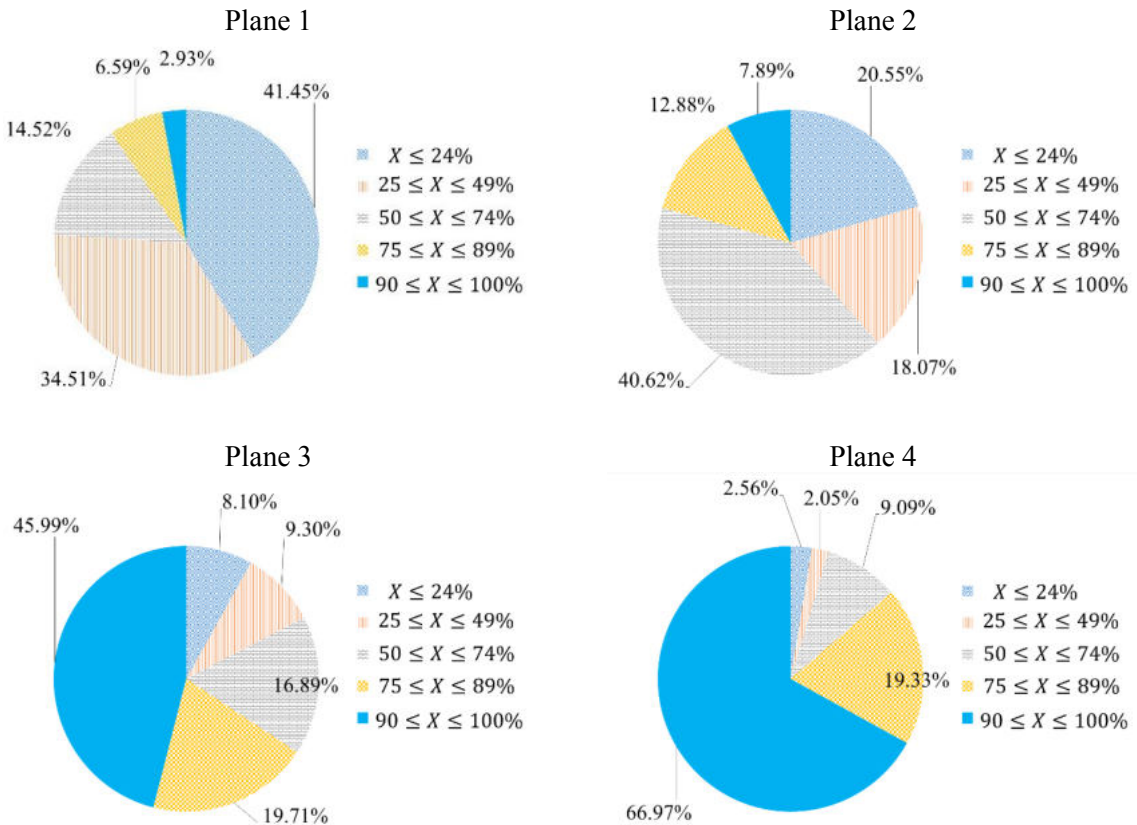
Source 0



Source 1

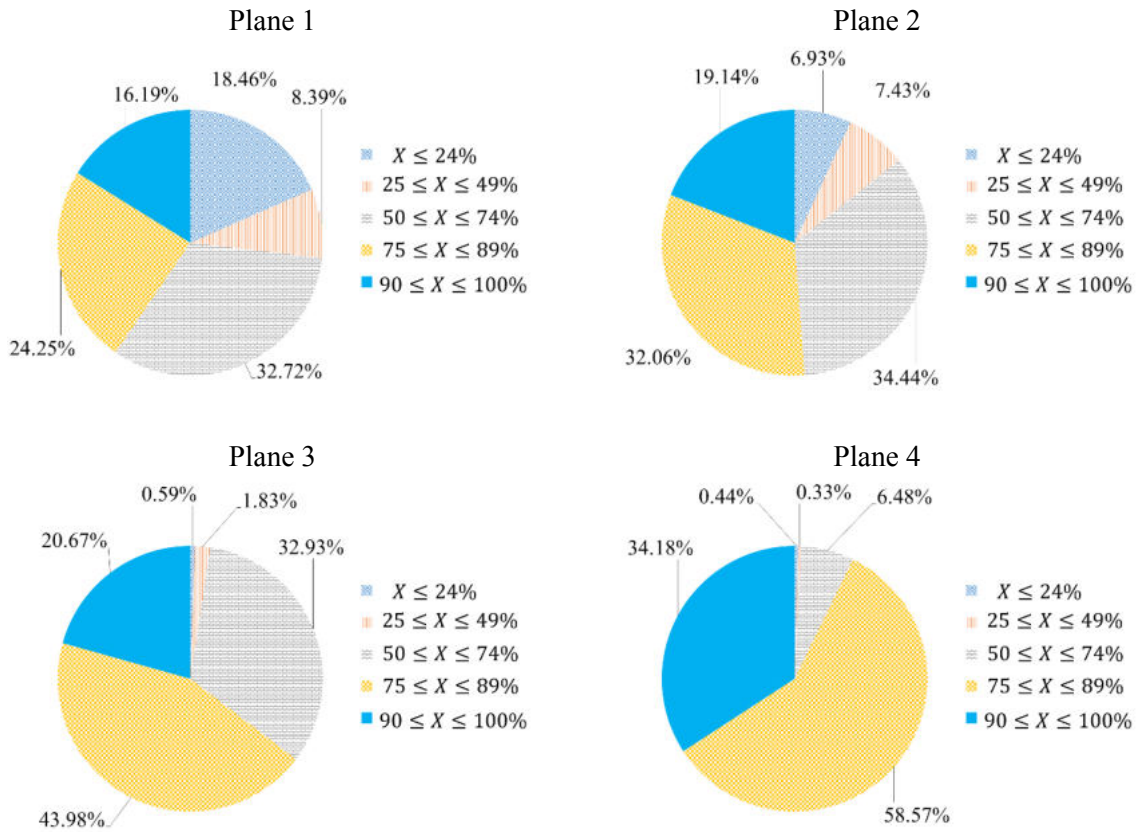


Source 2

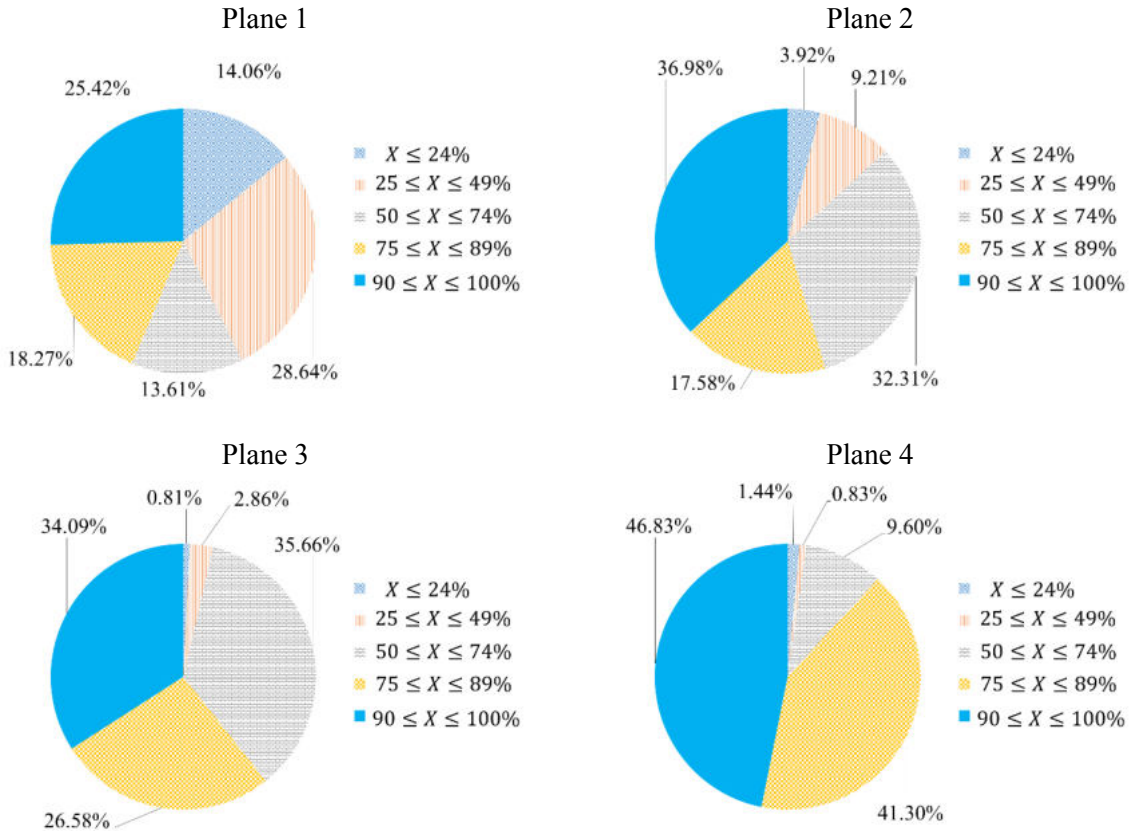


Case 6

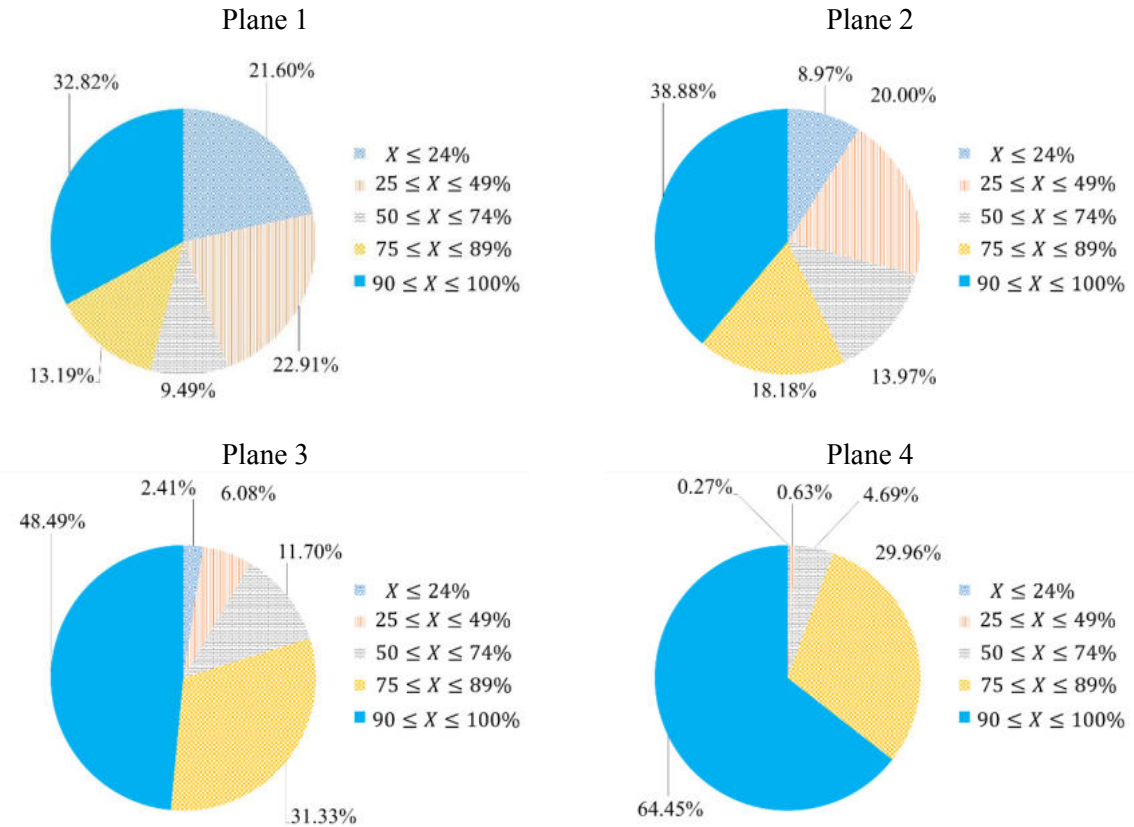
Source 0



Source 1

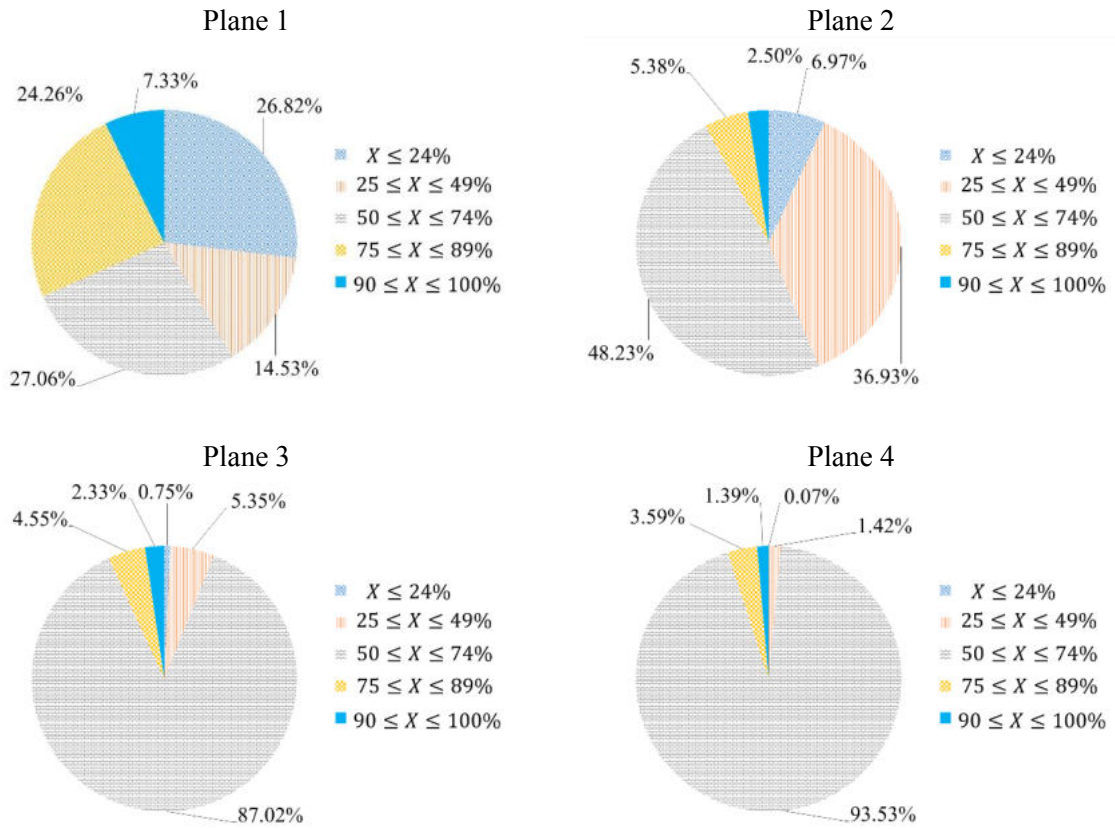


Source 2

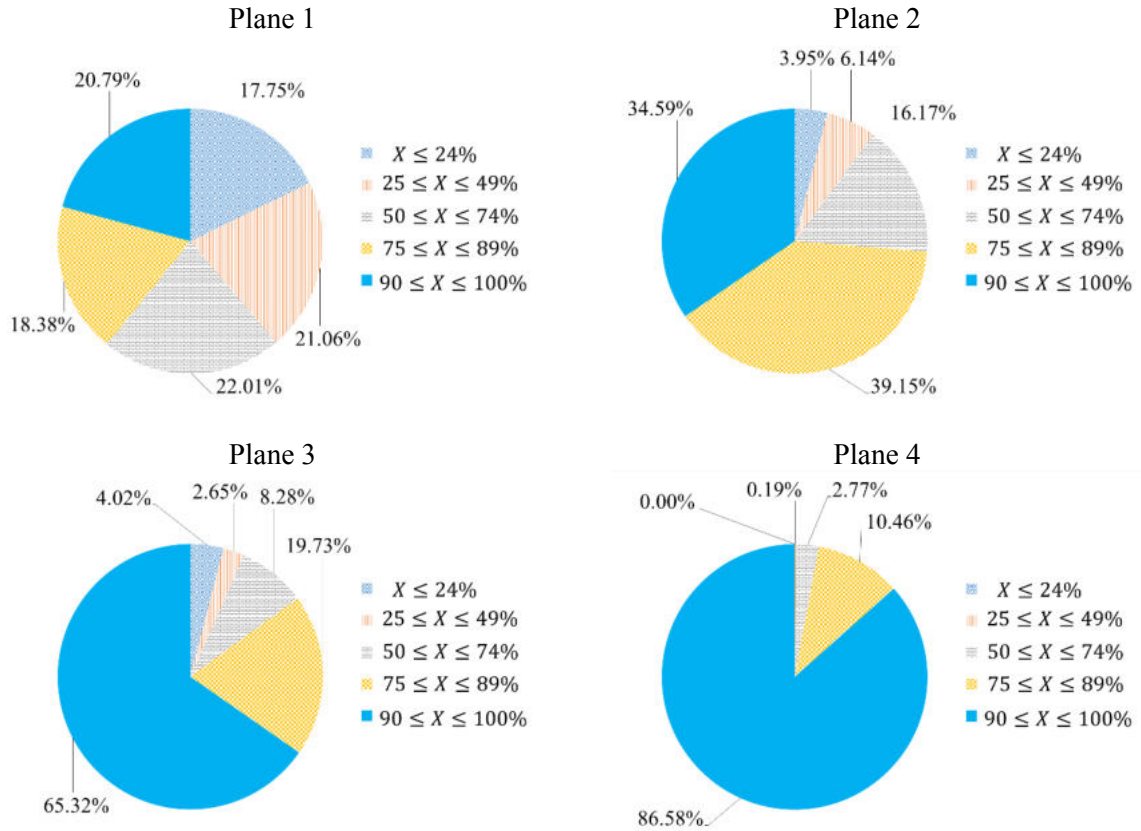


Case 7

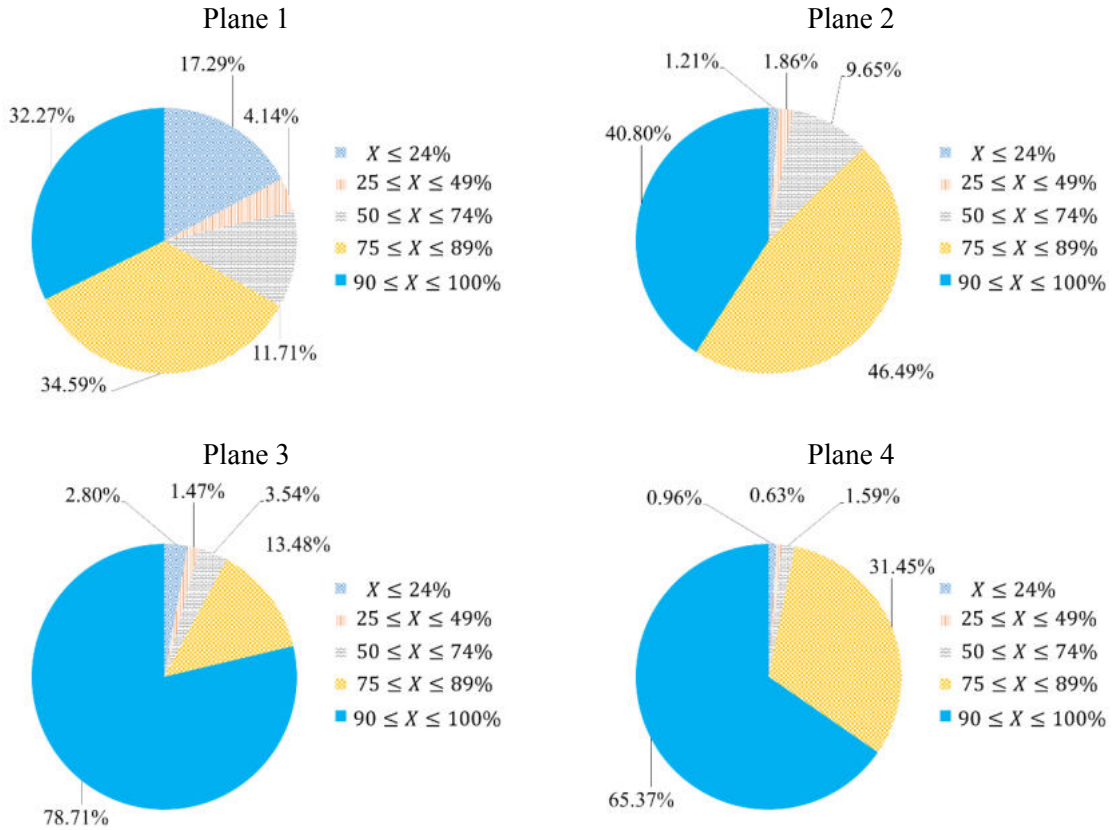
Source 0



Source 1

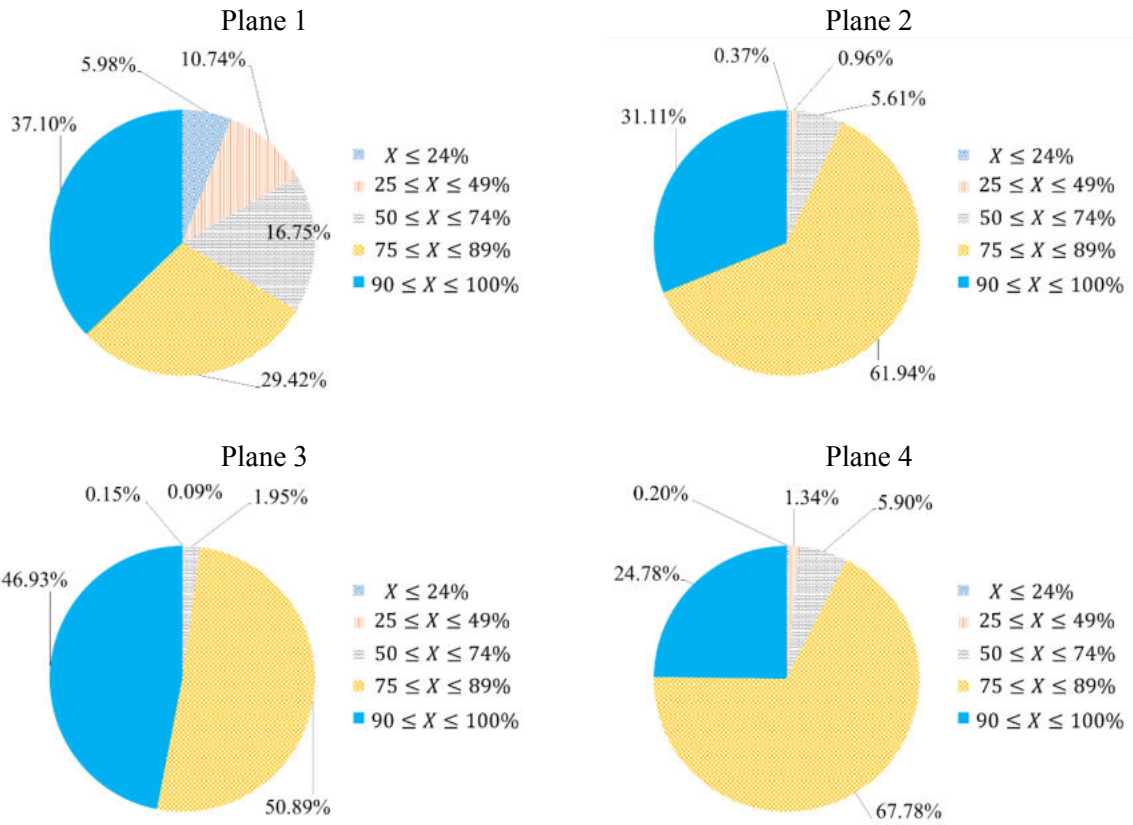


Source 2

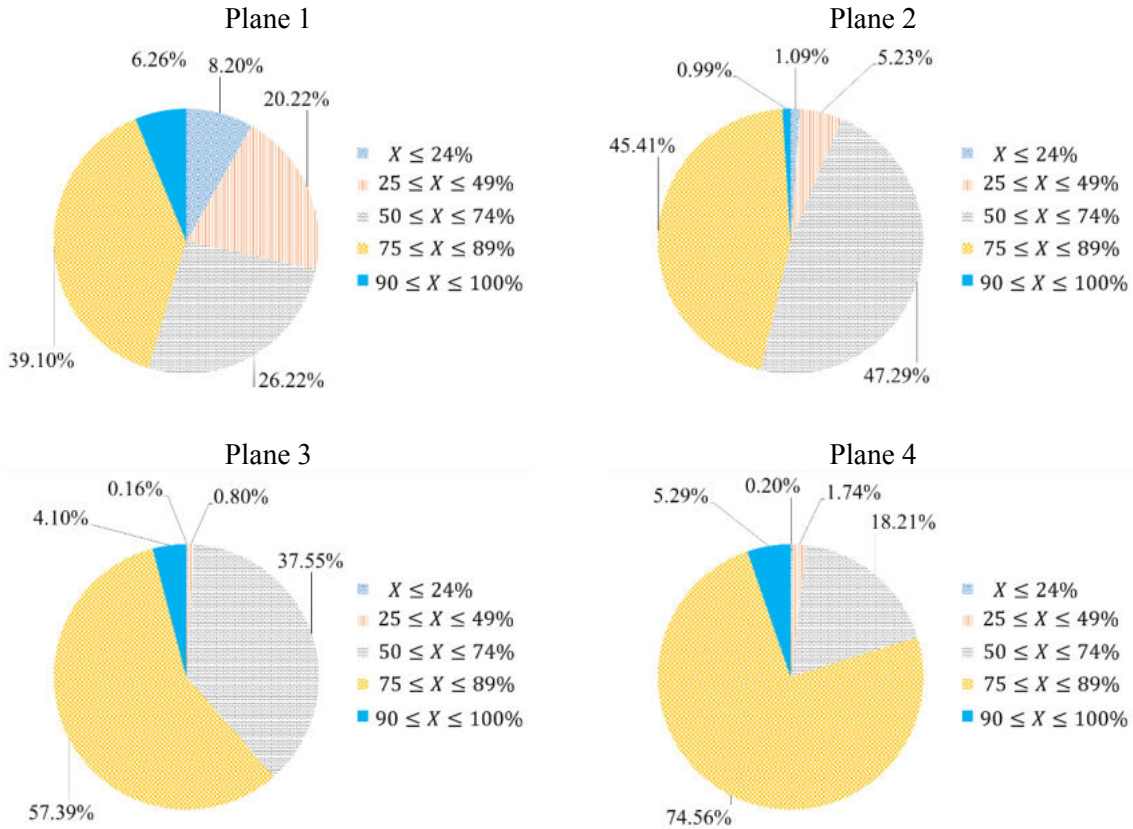


Case 8

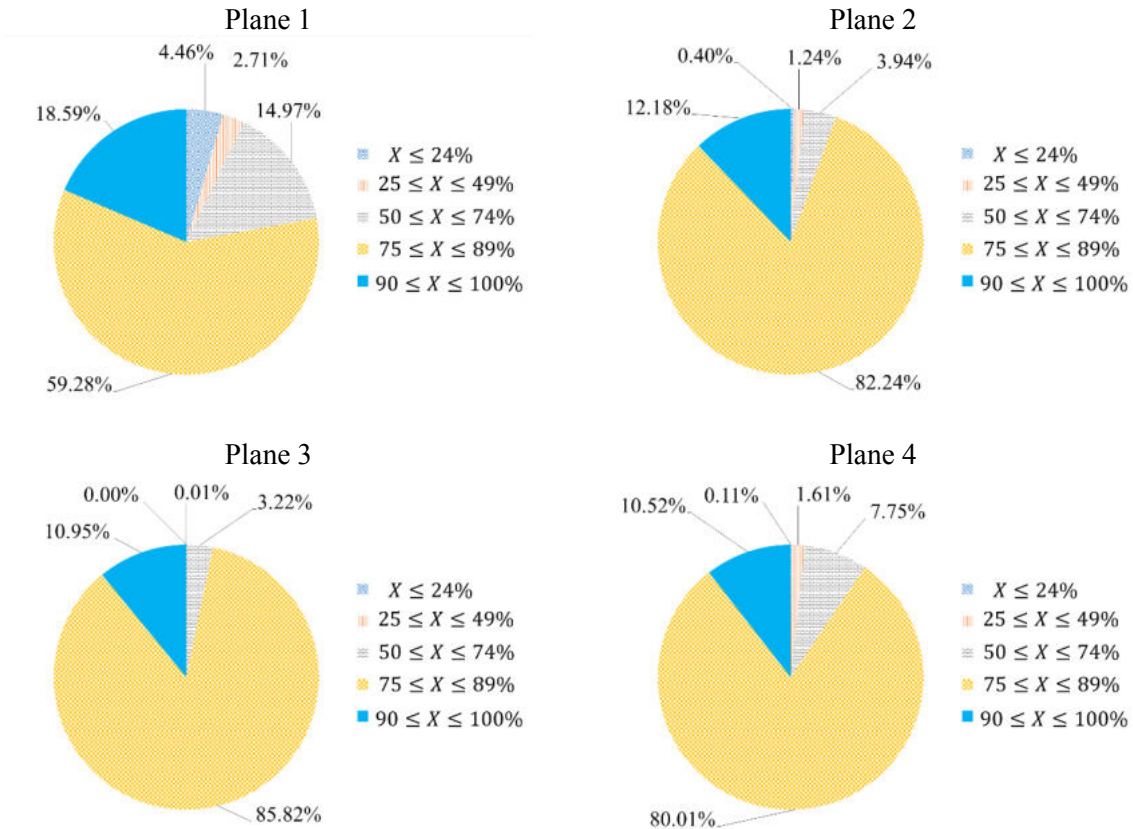
Source 0



Source 1



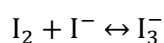
Source 2



Appendix 3: Absorbance calibration and experiments

Calibration plot

Calibration curve was realized using different concentration of a mixture of potassium iodide (KI) and iodine (I_2). These reagents will react according to the equilibrium reaction:



The equilibrium reaction should be done at the same temperature since the reaction is very temperature dependent. Concentrations of $[KI] = 3 \times 10^{-3} \text{ mol L}^{-1}$ and $[I_2] = 8 \times 10^{-4} \text{ mol L}^{-1}$ are used to prepared the $KI - I_2$ mixture. The concentration of $[I_3^-]$ is determined from the mass balance of the equilibrium reaction and its equilibrium constant K_B :

$$K_B = \frac{[I_3^-]}{[I_2][I^-]}$$

$$\log_{10} K_B = \frac{555}{T} + 7.355 - 2.575 \log_{10} T$$

Different concentrations of the $KI - I_2$ mixture are used in the determination of the optical density of I_3^- . Calibration curve between the optical density of I_3^- at 353 nm and $[I_3^-]$ is presented below, along with the molar coefficient extinction of I_3^- at 353 nm found in the literature.

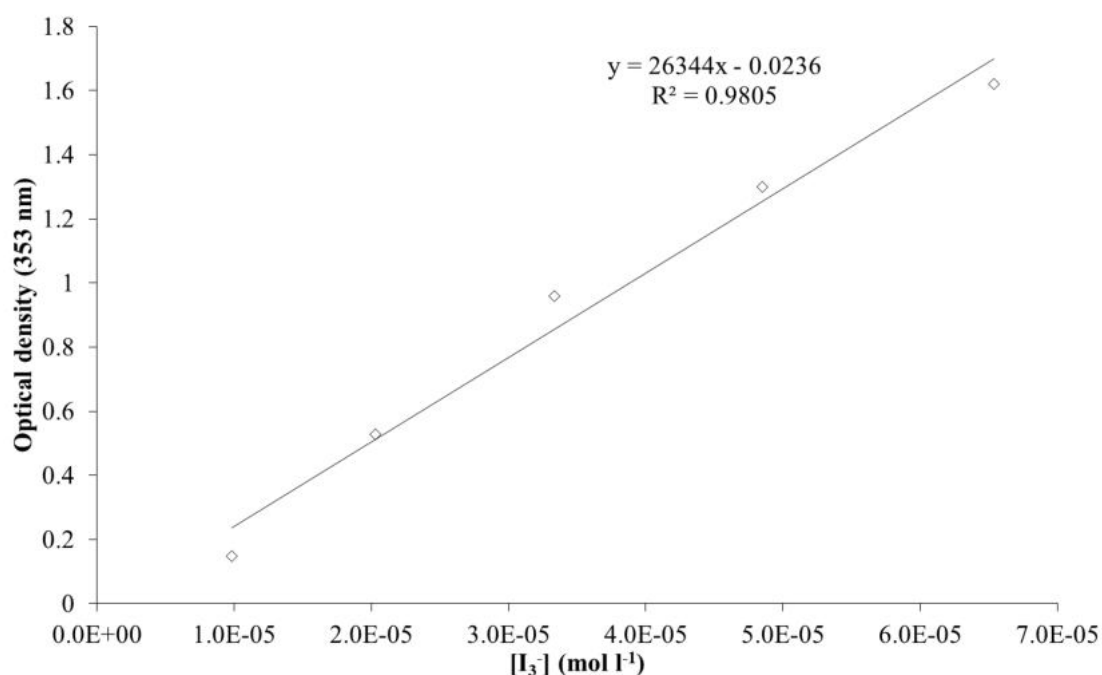


Table A.1: Molar extinction coefficient for I_3^- found in the literature

Wavelength λ (nm)	Extinction coefficient ϵ (L mol⁻¹ cm⁻¹)	Reference
352	25 900	(Custer and Natelson, 1949)
353	26 400	(Awtrey and Connick, 1951)
350	26 500	(Mayberry and Hockert, 1970)
350	25 750	(Palmer et al., 1984)
353	23 959	Single beam / (Guichardon et al., 2000a)
353	26 060	Double beam / (Guichardon et al., 2000a)
353	26 047	(Commenge and Falk, 2011)
353	26 240	(Yang et al., 2012)
353	26 080	Plastic cells / (Kölbl et al., 2013)
353	24 880	Quartz glass cells / (Kölbl et al., 2013)
353	24 620	(Wenzel et al., 2018)
353	26 344	This work

Absorbance Experiments

Absorbance spectra are a measure of how much light is absorbed by a sample. For most samples, absorbance is linearly related to the concentration of the substance. The software calculates absorbance (A_λ) using the following equation:

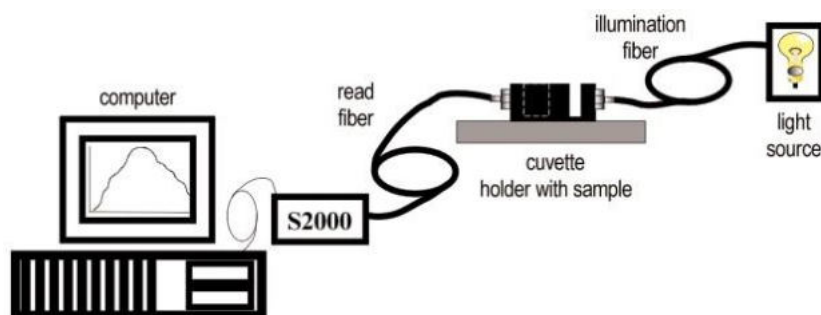
$$A_\lambda = -\log_{10} \left(\frac{S_\lambda - D_\lambda}{R_\lambda - D_\lambda} \right)$$

where S is the sample intensity at wavelength λ , D is the dark intensity at wavelength λ , R is the reference intensity at wavelength λ .

Absorbance can also be expressed as proportional to the concentration of the substance interacting with the light, known as Beer's Law. Common applications include the quantification of chemical concentrations in aqueous or gaseous samples. To take an absorbance measurement using OOIBase32, our spectrometer operating software, follow these steps:

1. Make sure you are in scope mode, by either clicking the scope mode icon on the toolbar, or selecting **Spectrum | Scope Mode** from the menu. Make sure the signal is on scale. The peak intensity of the reference signal should be about 3500 counts.
2. Take a reference spectrum by first making sure nothing is blocking the light path going to your sample. The analyte you want to measure must be absent while taking a reference spectrum. Take the reference reading by clicking the store reference spectrum icon on the toolbar or selecting **Spectrum | Store Reference** from the menu. (This command merely stores a reference spectrum. You must select **File | Save | Reference** from the menu to permanently save the spectrum to disk.) Storing a reference spectrum is requisite before the software can calculate absorbance spectra.
3. While still in scope mode, take a dark spectrum by first completely blocking the light path going to your sample. (If possible, do not turn off the light source. If you must turn off your light source to store a dark spectrum, make sure to allow enough time for the lamp to warm up before continuing your experiment.) Take the dark reading by clicking the store dark spectrum icon on the toolbar or selecting **Spectrum | Store Dark** from the menu. (This command merely stores a dark spectrum. You must select **File | Save | Dark** from the menu to permanently save the spectrum to disk.) Storing a dark spectrum is requisite before the software can calculate absorbance spectra.
4. Begin an absorbance measurement by first making sure the sample is in place and nothing is blocking the light going to your sample. Then choose the absorbance mode icon on the toolbar or select **Spectrum | Absorbance Mode** from the menu. To save the spectrum, click the save icon on the toolbar or select **File | Save | Processed** from the menu.

| If at any time any sampling variable changes -- including integration time, averaging, boxcar smoothing, distance from light source to sample, etc. -- you must store a new reference and dark spectrum.



A typical configuration for an absorbance experiment.

Appendix 4: Matlab script code for the determination of micromixing time

```
function Incorporationexp(dataq10, dataq20, datacH0, dataXS)

data.q10 =dataq10; %buffer vol rate
data.q20 =dataq20; %acid vol rate
data.cH0 =datacH0; %acid concentration

data.cH2BO30=0.0909;
data.cH3BO30=0.1818;
data.cIO30=0.00233;
data.cIO=0.0116;

data.qout=data.q10+data.q20;

data.cH0_matrix = data.cH0;
figure;
for k = 1:length(data.cH0_matrix);
data.cH0 = data.cH0_matrix(k);

%Rate constants
data.k3=5.9e9;
data.k3r=7.5e6;

NN=300;
XS=zeros(1,NN);
tm=logspace(-5,0,NN);

for i=1:length(tm);
data.tm=tm(i);
Con0=[data.cH0;0;0;0;0;0;0];

% 1=H+ 2=I- 3=IO3- 4=I2 5=I3- 6=H2BO3- 7=H3BO3

options=odeset('RelTol',3e-14,'AbsTol',1e-14);
t_max=data.tm*log(data.qout/data.q20);

[t,Con]=ode15s(@odefun,[0 t_max],Con0,options,data);

H=Con(end,1);
I=Con(end,2);
IO3=Con(end,3);
I2=Con(end,4);
I3=Con(end,5);
H2BO3=Con(end,6);
H3BO3=Con(end,7);

XS(i)=(2*((data.qout*(Con(end,4)+Con(end,5)))/(data.q20*data.cH0)))*(1+(dat
a.cH2BO30/(6*data.cIO30)));
end

colors = colormap(hsv(4));
loglog(tm,XS,'-o','Color', colors(k,:), 'DisplayName', sprintf('[H^+] =
data.cH0_matrix(%d)',k))
hold on
```

```

for h=1:length(dataXS)
plot([10^-5, 10^0], [dataXS, dataXS], '-o')
end
xlabel('t_m')
ylabel('X_S')
legend(num2str(data.cH0_matrix))
end
return

function dCon= odefun(t,Con,data)
Con(8:14)=[0;data.cIO;data.cIO30;0;0;data.cH2BO30;data.cH3BO30];

mu=1/2*(Con(1)+data.cH2BO30+data.cH0*2*1^2+(data.cIO30+data.cIO)+Con(2)+Con
(3)+Con(5)+Con(6)); % Calculating the ionic strength

global k2
if mu>0.166
k2=10^(8.383-1.511* sqrt(mu)+0.237*mu);
else
k2=10^(9.281-3.664*sqrt(mu));

end

dCon=zeros(7,1);
dCon(1)=-10^11*(Con(1)*Con(6))-(6*k2*Con(1)^2*Con(2)^2*Con(3))+Con(8)-
Con(1)/data.tm);
dCon(2)=- (5*k2*Con(1)^2*Con(2)^2*Con(3))-(data.k3*Con(2)*Con(4)-
data.k3r*Con(5))+((Con(9)-Con(2))/data.tm);
dCon(3)=- (k2*Con(1)^2*Con(2)^2*Con(3))+((Con(10)-Con(3))/data.tm);
dCon(4)=(3*k2*Con(1)^2*Con(2)^2*Con(3))-(data.k3*Con(2)*Con(4)-
data.k3r*Con(5))+Con(11)-Con(4)/data.tm);
dCon(5)=(data.k3*Con(2)*Con(4)-data.k3r*Con(5))+Con(12)-Con(5)/data.tm);
dCon(6)=- (10^11*(Con(1)*Con(6)))+(-Con(6)/data.tm);
dCon(7)=(10^11*(Con(1)*Con(6)))+(-Con(7)/data.tm);

return

```


Dissipation d'énergie et caractérisation du mélange dans des réacteurs continus oscillatoire

Résumé

Cette thèse de doctorat vise à étudier le micro et macromélange dans un réacteur continu à flux oscillatoire (COBR) lors de l'injection d'un composé secondaire dans l'écoulement principal. L'effet de la position de l'alimentation secondaire, l'influence des conditions oscillatoires et de la puissance dissipée sur les performances de macro et de micromélange sont analysés à l'aide de simulations numériques et d'expériences réalisées dans un réacteur commercial OBR Nitech® avec des constriction lisses.

La dissipation d'énergie est calculée par simulation numérique (CFD) en utilisant deux méthodes différentes - via la dissipation d'énergie visqueuse et par bilan de l'énergie mécanique, cette dernière étant préférée car elle est moins exigeante en terme de nombre de mailles. Un nouveau nombre adimensionnel caractérisant la puissance dissipée est proposé, outil spécifique de prédiction de la puissance dissipée dans les COBRs et indispensable pour l'extrapolation. L'analyse de la qualité spatiale du mélange a montré que, pour une position de la source d'injection correctement choisie, les performances du mélange s'améliorent considérablement en passant de 2% à 87% par rapport au système parfaitement mélangé lorsque le rapport des débits oscillatoire et net augmente. L'influence des conditions oscillatoires et du débit de l'alimentation secondaire sur la qualité du micromélange est analysée. Des amplitudes élevées et des fréquences basses sont préférables aux amplitudes basses et aux fréquences élevées et conduisent à une meilleure performance de micromélange.

Mots-clés : COBR, Dissipation énergétique, Macromélange, Micromélange, CFD

Energy dissipation and mixing characterization in continuous oscillatory baffled reactors

Abstract

The focus of this thesis is to study the macro and micromixing performance of a secondary component in the bulk flow and how it should be introduced into a COBR. The effect of the position of secondary feeds, the influence of the oscillatory conditions and power dissipation on the macro and micromixing performance is studied, using numerical simulations and experiments carried out in a commercial Nitech® OBR with smooth constrictions.

Energy dissipation is calculated through CFD simulations using two different ways – via viscous energy dissipation and the mechanical energy balance, the latter being preferred due to its lower demand for a refined computational mesh. A dimensionless power density number is obtained and proposed as a useful tool in the prediction of power density in COBRs. The impact of the position where a secondary feed enters the COBR on the spatial mixing quality is studied, and shows that when the source position is chosen correctly, an increase in the velocity ratio enhances mixing performance from 2% to 87% of the perfectly mixed state. The influence of the oscillatory conditions and flow rate of a secondary feed on the micromixing quality is analysed. Micromixing performance does not appear to correlate directly with power density. However, higher amplitudes and lower frequencies are preferred over lower amplitudes and higher frequencies to have a better micromixing performance. An attempt at characterising macromixing in the COBR experimentally using a coloured tracer was made however unexpected mixing performance was observed. Some preliminary experiments therefore focused on the behaviour of the tracer upstream of the COBR as a function of the oscillatory conditions.

Key words: COBR, Energy dissipation rate, Macromixing, Micromixing, CFD